NORTHWESTERN UNIVERSITY

Engineering Low-Dimensional Layered Structures

A DISSERTATION

SUBMITTED TO THE GRADUATE SCHOOL

IN PARTIAL FULFILLMENT OF THE REQUIREMENTS

for the degree

DOCTOR OF PHILOSOPHY

Field of Physics

By

Teodor K. Stanev

EVANSTON, ILLINOIS

September 2021

ABSTRACT

Engineering Low-Dimensional Layered Structures

Teodor K. Stanev

The highly flexible nature of 2D materials has led to them becoming fundamental building blocks for achieving novel device physics and potential breakthroughs in practical technologies. 2D layers can be interfaced in a wide array of methods with themselves, other 2D layered materials, or materials of entirely different type or dimension. As such, layered materials present themselves as good components for building towards goals greater than the sum of the parts.

In this Thesis, I will first present on a number of projects that utilize 2D materials in different configurations to achieve significant steps forward in 2D device fabrication. Of main focus, layered hexagonal boron nitride is utilized for its quality preserving properties. The first application was to greatly improve contact performance of an electronic 2D-2D heterojunction, allowing for more sensitive electrical characterization of the heterojunction. Secondly, hexagonal boron nitride was utilized as a protective layers around an MX_2 monolayer to achieve state of the art direct patterning without damaging the MX_2 layer and compromising its desired optoelectronic properties.

In the second half of this Thesis, focus will shift from 2D-2D layered combinations to 2D-0D mixed dimensional structures where monolayers are interfaced with the organic molecules of phthalocyanines and pentacene. Here monolayers serve as substrates upon which organic molecules can be deposited, and interfacial states that arise are studied as well as how these materials template upon deposition.

In the third and final main section, the topic will be of protection of volatile layered materials that rapidly decay in atmosphere. My contribution will mainly be focused on how these protected layers were measured for their magnetic properties using Magneto Opical Kerr Effect and its realization. The effects of different methods of protection on the magnetic character are also studied.

Finally, an extensive Appendix will highlight my work in developing the techniques for layer engineering as well as highlight several projects not part of the main Thesis that were enabled by my methods, including an all new in-situ TEM electrical measurement of suspended 2D materials.

Acknowledgements

This thesis is the result of many years of work and sometimes a loss of direction but I owe a great deal to Dr. Nathaniel Stern for not only being immeasurably patient with me but also a great guide along the way in going from our lab as a near-empty hole in the ground to the now highly developed, state-of-the-art lab that leads the way in certain types of magneto-optoelectronic measurements at Northwestern. I am thankful for all the time he made for me to discuss academic and lab work in your office. Dr. Stern was a great guide and mentor, and I hope to have left him with a great lab to build on his already excellent beginning.

I want to greatly thank Sam Amsterdam for being a great partner on several successful interdisciplinary projects over the years. He was an excellent, knowledgeable partner and together we made excellent strides in showcasing the interesting phenomena of mixed dimensional heterostructures. Where I brought mastery of 2D materials, Sam brought his endless knowledge of chemistry and organic materials. We proverbially put our heads together and produced a series of papers and projects now handed off to the next generation of students. It was a great partnership!

I also want extend immense gratitude to Akshay Murthy for his help with device fabrication and patterning, and skills with the electron beam systems at Northwestern. I learned a great deal from him in this regard. He was a great partner in several 2D material based projects that he brainstormed and put my skills of layer manipulation to

great use in realizing the ideas. We successfully designed a new method of measuring in-situ devices which, independently, would have likely never materialized.

I want to extend a highly appreciative thank you to all of the students we've had in the Stern Lab, they were great friends and partners in the lab and made for a great work environment. I want to specifically thank Erik J. Lenferink for his mastering of and then teaching of electrical device fabrication and measurement. Ying Jia for working with me on the first paper with my name on it and one that ultimately shaped a large part of my future, she was a great mentor. I also want to thank Peter Hwan Lim and Ethan Garvey for their work with me on building up and realizing MOKE spectroscopy and other optical measurements in the lab. I expect great things from both of them!

I'd also like to thank Northwestern University and the many great students and professors who served as great friends and teachers along the way. I'd also like to thank, specifically, the Physics and Astronomy Department and all of its helpful staff who helped keep everything in order through these years and for putting up with our non stop stream of orders as we built out our lab! I'd also like to thank the staff and organizers at MRSEC and the REU program which was a great experience for me in working with undergrads in the mentorship program.

Acknowledgements of Funding

This dissertation is based upon work that is supported in part by the Office of Naval Research (N00014-16-1-3055). Use of the Center for Nanoscale Materials, an Office of Science user facility, was supported by the U.S. Department of Energy, Office of Science, Office of Basic Energy Sciences, under Contract No. DE-AC02-06CH11357. The National Science Foundation by award DMR-1905986. Collaborative efforts of the MRSEC IRG-1 were supported by the MRSEC program (DMR-1720319) at the Materials Research Center of Northwestern University.

Table of Contents

List of Tables

List of Figures

A.1 Common preparation of micromechanical exfoliation tape, follows steps as described in the section list. (a.) Blank tape with folded edges for points of contact with gloved hands, helps to keep tape orderly and clear from contact residue. (b.) TMD crystal (MoS_2 pictured). (c.) The TMD crystal is pressed and pulled from the tape, leaving behind pieces of material residue. (d.) Tape is folded over on itself. (e.) The tape is slowly pulled apart, leaving two portions of tape with cleaved TMD layers. (f.) The process in (e.) is repeated until the material has covered the whole tape. 287

A.2 Heat and massage treated exfoliation for higher yield. (a.) A tape identical to the one made in Fig.[A.1] is placed atop wafer of SiO_2 thermal oxide of 285 nm thickness on p-doped Si. (b.) The soft guiding tool used to rub the backside of the tape. (c.) Gentle rubbing of the back side of the tape, done in strokes across the whole length of chips. A base plate as shown here made of aluminum is ideal for keeping chips from sliding or the tape from tearing. It is also a good thermal conductor for the healing step and prevents the tape from directly melting touching (contaminating) the hotplate. (d.) Samples are moved to a hotplate and heated at approx. 70 C for an hour or more. (e.) After treatment as described in this section, the tape is peeled off while still warm. (f.) The samples are moved to the microscope and can now be carefully examined for layers of desired

CHAPTER 1

Introduction

The simple isolation of 2D materials by the cleaving apart of bulk layered crystals weakly held together by van der Waals (vdW) forces has kicked off a revolution in the nanosciences because of their natural electronic confinement within a 2D plane, increase in tensile strength due to removal of weak vdWs bonds, and orders of magnitude increase in the surface to volume ratio at the monolayer limit, evidenced by the 2010 Nobel Prize for the isolation of 2D graphene by exfoliation reported in 2004. These desirable properties have made 2D materials of great interest in development of a new generation of transistor, photodetectors, topological insulators, and spin and valleytronics. Since the initial isolation of 2D graphene by exfoliation reported in 2004, which subsequently won the Nobel Prize, the field of 2D materials has bloomed with diverse and often unique layered materials such as hexagonal boron nitride, perovskites, and black phosphorus, and chalcogenides. With size scales of crystal unit cells, these materials have interesting optical, electronic, and magnetic properties that are often highly dependent on the number and configuration of individual crystal layers. Consequently, layer number and composition have become powerful tools for control of material properties in schemes not possible with bulk materials. For example, the electronic character of a material can be changed by altering its layer number, such as turning a bulk insulator into a monolayer semiconductor. Or, a magnetic materials can see its ordering transition from ferromagnetic to anti-ferromagnetic with alternating even-odd layer numbers.

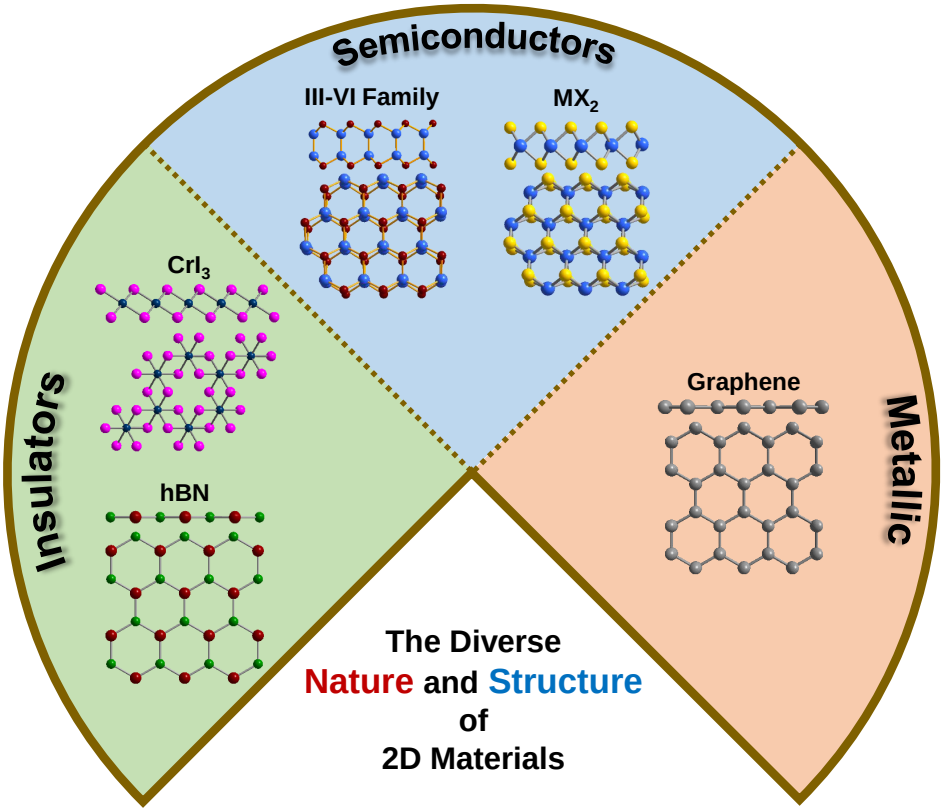

Figure 1.1. Example of the electronic nature and diverse crystal structure of 2D vdWs layered materials. Crystal structures are presented with a top-down and side-view to highlight the differences in atomic thicknesses and crystal unit cells. The materials highlighted here were the main contributors to the projects that will be detailed in up coming Chapters. CrI_3 is, additionally, an example of a magnetic 2D material.

Just as these layered materials can be peeled apart from bulk crystals to single layers, so too can they be assembled into completely new layered structures either with themselves, other layered materials, or even materials of completely different dimensions. This

new capability of layered assembly allows 2D materials to be fundamental building blocks of new composite materials that do not occur in nature.

Due to their atomic-scale thickness, 2D material layers are essentially all surface, and therefore highly sensitive to their environment. This sensitivity leads to advantages and disadvantages compared to other bulk or nanostructured materials. This sensitivity to their surroundings also further expands the possibilities for designing layered heterostructures or combining 2D materials with 0D organic molecules or other mixed dimensional systems with potentially novel emergent properties. By controlling the surroundings of 2D materials, it is possible to significantly alter their behavior (optical, electronic, or magnetic) or preserve their fragile atom-thick lattice from damage. This latter possibility opens the door on using otherwise unworkable materials that are too volatile to use outside of highly controlled, limiting environments such as a glovebox.

With these many possibilities for composite structures at our disposal, rapid advances have made 2D materials heterostructures a vibrant and fast-paced field with significant potential to tailor the properties of 2D materials and their heterostructures for new understanding of physical regimes and material applications.

1.1. Challenges of 2D Layer Manipulation

While these 2D materials, be they TMDs, graphene, hexagonal boron nitride (hBN) or volatiles like chromium iodide (CrI_3), are extremely tantalizing and show great potential for novel optoelectronic devices, there remain significant challenges in studying 2D materials that need to be addressed in most applications. Some examples include achieving high quality (single) layers [11], robust transfer of layers from one location to another [12],

protection of layer quality [13], and electrical contact interfacing [9, 14]. Isolating high quality layers and their robust transfer enables creation of homo- and heterostructures of high quality. Mastering the manipulation of layers in this fashion can also be leveraged for creating entirely novel measurement schemes or methods for interfacing layers with other systems such as waveguides or topological systems. Layer protection can allow for new measurements that were previously untenable for unstable materials or new methods for layer patterning that would have otherwise been destructive. Electrical contact engineering through layer interfacing allows for higher quality electronic measurements.

Tackling these challenges is paramount to fully utilizing 2D materials. Overcoming these hurdles and then applying them to novel devices is a recurring theme in this thesis, highlighting the type of impact of this work across several classes of 2D materials.

1.1.1. Achieving High Quality Layers

The first and most important challenge is obtaining monolayers of the desired materials. For many layers such as MoS_2 or WS_2 or selenide equivalents, there is an easy solution in chemical vapor deposition growth (CVD) or other growth methods of monolayers [15–18]. While often large and continuous, grown layers often have quality problems such as seed core centers, rampant sulfur vacancies and undesirable doping. For applications where crystal quality is highly important or structural engineering is intended, CVD sources will often not suffice. To that end, high quality crystals are best obtained from micromechanical exfoliation that cleaves apart layers leaving behind pristine, monocrystalline, smooth surfaces [11, 19, 20].

Traditional micromechanical exfoliation is well documented in literature but can be time consuming and arduous to undertake. Many of the original techniques were also interested only in achieving monolayers, not in their size, isolation, or shape. Refining old techniques and developing new methods to expedite and improve this process was of particular interest. Step-by-step details on the new and refined processes can be found in the Appendix. The majority of topics within this thesis utilized layers achieved from these improvements.

1.1.2. Robust Transfer of Layers

Using 2D materials as building blocks requires being able to pick them up, move them, and place them in deterministic ways such that a desirable end-product can be assembled [12]. This often requires different approaches and considerations for different materials, an important detail for *hetero*structures. The more precise the method, the better the end result.

However due to their thin nature, transfer of layers is prone to tearing, wrinkling, and other physical problems that can compromise the layers or the resultant structures. For example, assembly can create unwanted gaps or physical breaks in desired electrical pathways. Being able to successfully move layers while also preventing physical deformation is a key element to achieve high quality structures.

There are many approaches to tackle layer-by-layer transfer in the literature. In this Thesis, the approach used was informed by early literature [21], but has been developed and refined into an in-house procedure that can transfer layers onto a variety of surfaces and control layer rotation to within a degree. This robustness to target surfaces includes

difficult structures such as waveguides, electron microscope sample mounts, and more. The techniques as well as the robustness of transfer will be discussed in detail, step by step, in the Appendix.

1.1.3. Protection of Layer Quality

As mentioned previously, the atomically thin nature of 2D materials is both a great boon and bane due to their high sensitivity to their surroundings. In some materials, such as CrI_3 or BP, this sensitivity is normally crippling as even short exposure to ambient atmospheric conditions results in layer decay such as oxidation or reaction with water [22–24]. Even robust 2D layers that do not readily decay experience performance loss if left exposed.

In order to pursue more advanced and high quality measurements, and not be limited to extremely controlled and constraining workspaces such as a glovebox, it is necessary to protect sensitive materials from the environment. hBN and passivation techniques have presented themselves as tools to achieve this, allowing for the creation structures that preserve the pristine nature of 2D layers even when exposed or worked with in open ambient conditions [13, 22]. Several of the topics of this Thesis research deal explicitly with protecting 2D materials.

1.1.4. Electrical Contact Interfacing

Resistance formed at the interface of contact metals and 2D materials is a critical problem in nanoelectronics [5, 9]. Where conventional (bulk) semiconductors often have resistances

measures in single Ohms (Ω) [25], the contact resistances in TMDs and other 2D materials are of orders of MΩ or worse [26]. This significantly limits the capabilities of 2D nanoelectronics as it can cause problems such as little to no conductivity, sample heating at contacts, or poor sensitivity.

Common sources of this significant resistance are lattice damage from deposition of contact metals and trapped adsorbates in the lattice at the contacts [27], etc. By engineering the material surface it is possible to solve both of these problems at once! An example of this, which we will delve into further detail later in this Thesis, is to use very thin hBN as a tunneling barrier [9, 14, 28]. hBN provides protection for the sample surface both from adsorbates and from bombardment of high energy metal atoms, allowing us to smartly tackle both problems at once and enabling high-quality nanoelectronic devices.

1.1.5. Tackling The Challenges

These many challenges for utilizing 2D materials can appear daunting, but overcoming them is crucial for advancing our understanding of novel physics and measurements related to these materials. By mastering layer manipulation and preparation of numerous different material systems, I was able to tackle these limitations head on and harness 2D materials in developing new measurements and types of heterostructures. Moreover, these advances in handling materials opened up significant opportunities for large and successful interdisciplinary collaborations within Northwestern and beyond which depended on the layer manipulation techniques I developed.

For every challenge here, I found solutions to overcome via manipulation of and engineering with 2D materials and their environment. These topics will all be dealt with in

greater detail in the main body of this work. Although each specific project that follows has its own specific scientific focus, each of these studies is thematically linked by the idea that low dimensional materials can be engineered into configurations that enhance their properties. In my research, this is achieved through layered heterostructures (Chapter 4), lithography (Chapter 5), deposition of molecular layers (Chapter 6 and Chapter 7), and passivation (Chapter 8). Other opportunities such as utilizing layer manipulation for novel TEM experiments or waveguide-coupled layered materials are explored further in the literature and the Appendix, highlighting the general power of this line of thinking to enabling new explorations of materials. My work and mastery of layered material manipulation has helped illuminate these opportunities, enabling new studies based on my work.

1.2. Research Objective

2D materials are individually interesting but offer even greater flexibility and potential for interesting and novel physics when used as parts of engineered material systems such as creative heterostructures or layered structures interfaced with molecules or thin films [1, 2, 7, 10, 29, 30]. As such, being able to manipulate said materials has become a hot field of development in physics and material sciences. However, being able to build and measure these structures, some volatile while others only tens of nanometers in size, is no small feat.

The purpose of this thesis is to engineer the structural and electronic environment of 2D materials to study new properties. The main thrusts of this thesis exploit layer

assembly to study previously challenging systems and develop completely new measurement schemes for 2D materials. This general approach has resulted in significant advances across several classes of materials:

(1) Exploiting the 2D layer character/surfaces to access novel optoelectronic phenomena.
(2) Enhanced probes of optoelectronic properties through engineering of layered materials.
(3) Manipulating the environment to achieve new measurements on high volatile and fragile systems.

In Chapter 2 of this dissertation, I will present background on 2D Materials more generally, why they are interesting, and the challenges for working with these materials as parts of heterostructures. I will also discuss the new measurements and physics that can be achieved. In Chapter 3, I will present on homostructure engineering where I will be presenting on work with multiple layers and layer combinations of the same material, this chapter will showcase the layer dependent nature of these 2D materials. In Chapters 4 and 5, discussion will move to heterostructure engineering where multiple different material layer combinations are built into stacks and lateral structures. Of focus is utilization of hexagonal boron nitride (hBN) as a critical component for engineering the environment of TMDs and improving and preserving their desirable properties for optoelectronic use. In Chapter 5 and 6, heterostructure engineering will be expanded beyond layered materials and will delve into using 0D molecules as heterostructure components in the formation of mixed dimensional heterostructures, part of a large collaborative project. Chapter 6 will focus on phthalocyanine and 2D projects, while Chapter 7 will focus on pentacene and 2D

projects. In Chapter 8, I will discuss Magneto-Optical Kerr Effect Spectroscopy (MOKE) in the context of environmental engineering of 2D materials. This chapter builds off of the results in Chapter 5 and expands through collaborative efforts with the Hersam group to achieve a new type of environmental engineering that not only preserves the materials optoelectronic properties but also its magnetic properties.

Finally, in the Appendix, I will provide detailed technical details on realizing the development of technique to build and measure the structures in the preceding sections, sample fabrication, and the development of MOKE. The appendices will also highlight several projects to which my techniques and talents significantly contributed to but were not part of the main Thesis. While this section is distinct from the narrative thread of the primary dissertation results, these important projects and technical details provide a more complete picture of what has been achieved using 2D materials.

CHAPTER 2

Introduction to 2D Materials

Confining systems to lower dimensionalities has been a common goal towards reaching new regimes of physical phenomena and the quantum regime. One method of decreasing dimensionality in electronic systems is by creating 2D electron gas (2DEG) systems where electrons are confined to a narrow layer or interface of materials, confining their movement to effectively only two dimensions with their z-dimension effectively quantized. A common approach to realizing this is through the creation of metal-oxide-semiconductor (MOS) field-effect transistors (FET) (MOSFET) as seen in Fig2(a) [31–34].

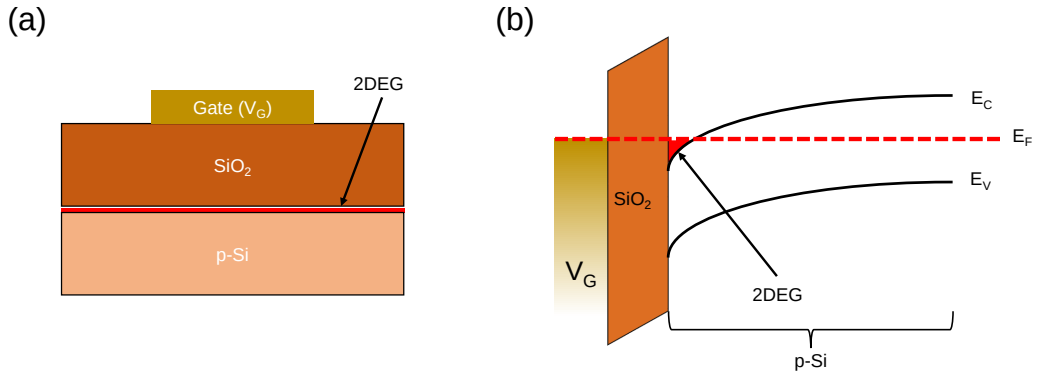

Figure 2.1. Creating a 2D electron gas at the interface of SiO_2 and Si by creating an inversion layer of trapped electrons. (a) Physical design of a gate-electrode atop slabs of SiO_2 and Si with the interface-2DEG marked in red. (b) Formation of the 2DEG by tuning the gate potential.

The gate contact (V_G) tunes the Fermi level and thus the electron density at the interface between the SiO_2 and p-Si, and by tuning the Fermi level above a certain threshold (V_T) defined by the depletion length such that $V_G > V_T$, can create an inversion layer of trapped electrons. These electrons are confined to a narrow region between the SiO_2 and Si, creating a quasi-two dimensional system.

While these systems have been extensively studied, they are quite complex to realize require many fabrication steps to develop a final 2DEG. Conversely the recent isolation of vdWs two-dimensional semiconductor provide these 2D systems intrinsically as they are only defined by their surface and edges [35–38]. By simply exfoliating or growing monolayers of vdWs 2D semiconductors, it is possible to realize 2D electronic systems without needing to define depletion layers. This leads to possibilities of combining and mixing 2D eletronic systems from different crystal layers. Moreover, many of these layered materials are stable in atmosphere [39, 40], and can be used utilized as 2D components in a variety of temperatures and conditions [41–43].

2.1. Transition Metal Dichalcogenides (TMDs)

2D materials have seen a rapid evolution in their usage and applications to new physics and material science breakthroughs. Throughout this rapid development, many different 2D materials have come to be used and studied extensively such as graphene [44], perovskites [45, 46], iodides [22], oxides [47], black phosphorous [48], and many, many other layered structures. These layered materials are held together as bulk via van der Waals forces (vdW) and why they can then be isolated down to single layers. For the purposes of this thesis the main focus will be on the chalcogenide family of layered materials, and more

specifically the transition metal dichalcogenides (TMDs) that take the form of MX_2 where commonly M = Mo, W, Re, etc. and X = S, Se, etc.. This family comprises the Group-VI semiconductors, a class of semiconductors that from the bulk or multilayer layer (>1L) to monolayer limit (1L), transition from indirect to direct bandgap semiconductors [35] with their band structure changing with layer number. An example comparison between Bulk, monolayer (1L), bilayer (2L), up to 5L can be seen in Fig.[2.2] [3]. These single layers are recognized by their three atom thick honeycomb array of an X-M-X structure as seen Fig.[2.3]. The exact nature of the optical bandgap, electronic properties, etc. varies between the different combinations of MX_2 as detailed previously [49].

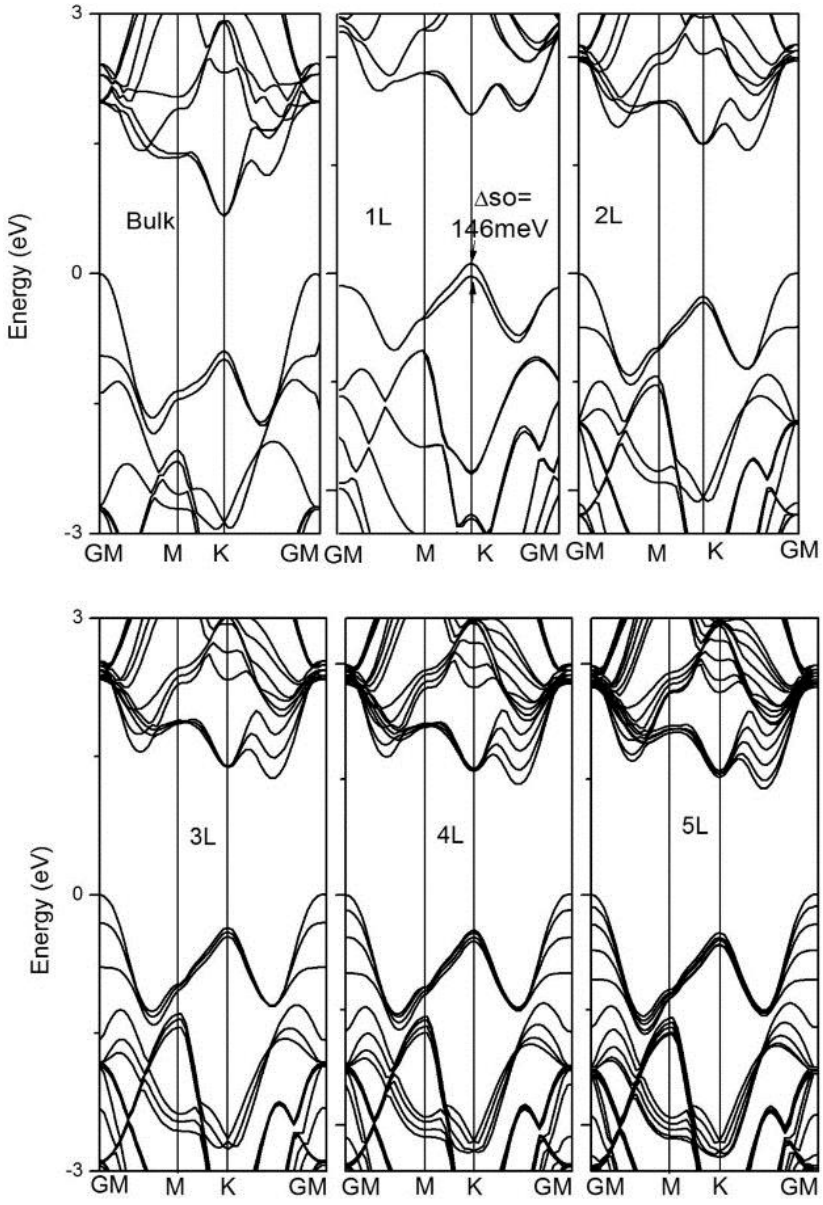

Figure 2.2. MoS_2 layer dependent bandstructure, highlighting the layer dependent nature of MoS_2 and optoelectronic properties. Depending on layer number, the MoS_2 transitions from a direct bandgap semiconductor at the K point, to one of indirect bandgap between the K and Γ points of the conduction and valence bands respectively. Adapted from [3], with the permission of AIP Publishing.

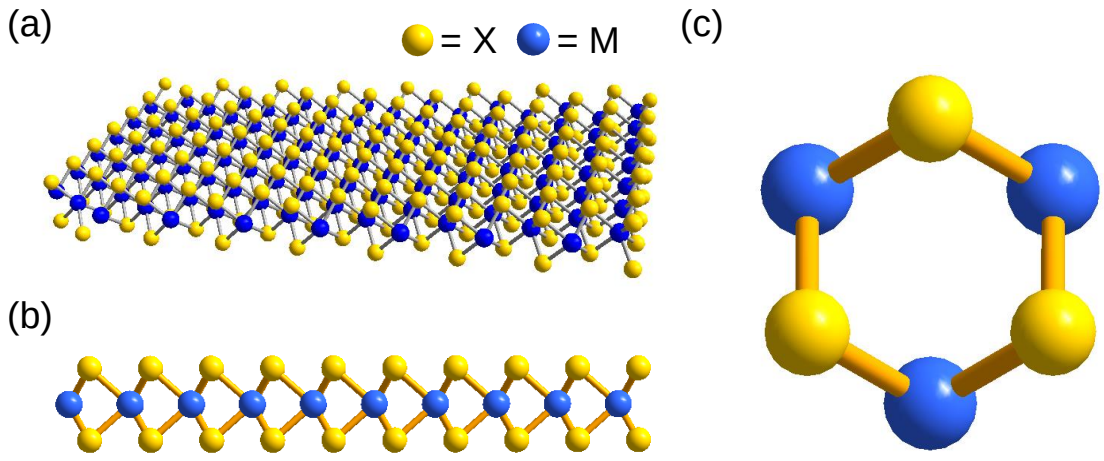

Figure 2.3. Example cystal structure of MX_2 monolayer as viewed from different orientations. (a.) A planar view of the crystal structure of a single layer of MX_2. (b.) Side-view of the MX_2 crystal structure for a monolayer. (c.) A single lattice of MX_2.

The first isolation of 2D TMDs came via the scotch tape exfoliation technique [50], a form of micromechanical exfoliation by cleaving layers apart from large source bulk crystals held together by vdWs forces into an array of many different thicknesses onto a suitable substrate such as SiO_2. Amongst the many exfoliated layers can sometimes be found isolated monolayers, confined systems where carriers are able to move along two dimensions (x, y) but confined along a third (z). These 2D systems have since been extensively studied for their direct bandgap nature [35], potential for high mobility electronic devices [51], applicability to spin and valleytronics [52–55], etc. And have been utilized to create novel optoelectronic devices that can study, for example, exciton lifetimes and formation [56–58], the formation of single-photon emitters [59], the valley-hall effect [60], and light-sensitive optoelectronic devices (such as photovoltaics, photo-transistors, light-emitting diodes, or solar cells) [61]. They have presented a great potential

for real world applicability in quantum application, light harvesting, information storage and other similar fields.

2.1.1. Achieving Monolayers

In the years following early work around TMDs, many different methods have been found for achieving the desired monolayers though no perfect technique exists that captures all of the highly desirable qualities at once such as: large size, monocrystalline, isolated, uniform, and defect free.

The standard approach to achieving all but the large requirement, is via micromechanical exfoliation where bulk crystal of MX_2 material is stamped onto an adhesive surface and exfoliated repeatedly across target wafers [35]. This leaves behind a rich array of various layer thicknesses including the rare but desirable monolayer. These exfoliated layers are usually quite small (few to few tens of microns) but of very high quality and their surfaces pristine prior to any processing. This type of layer makes for a great candidate for optoelectronic study and implementation in potential novel heterostructures. However, as noted, these layers are often very small using the very basic exfoliation techniques and as such much work has gone on in the field to develop updated methods of exfoliation that can maintain all of the high-quality desirables while also increasing the size Velicky2018. The progress on this and my own take on achieving the best and largest possible layers will be a major point of this thesis.

The desire for larger and larger sizes, not possible with standard micromechanical exfoliation, has been driven by an interest in real world, scalable electronics applications and has led to significant progress in growing monolayers of TMDs. This can be done in many

different methods, for example via chemical vapor deposition (CVD) where precursors of Mo and S are used to grown large triangular monolayers on target wafers which can merge to form large sheets of polycrystalline coverage of a substrate [15–17, 62]. While this technique and other similar methods (physical vapor deposition (PVD), atomic layer deposition (ALD), etc) can solve the problems relating to size, they are often of significantly lower quality than the layers achieved through exfoliation. Such layers are often plagued by vacancies of either the metal or chalcogenide or other unwanted adsorbates within the lattice that are potentially introduced and trapped during the growth process, making them highly defect rich. Moreover, as the growth process requires a point of nucleation from which a layer may grow, this often leads to the formation of large core-centers located at the center of any given flake of MX_2 or, if a film is grown, distributed randomly across the film. These seed cores impede the creation of heterostructures as they are vertically large (orders of tens of nanometers or more), result in point of stress when layers are transferred (the seed core will often not transfer and are not desirable to be transferred, ripping out a portion of the layer), and can be problematic for processing as they will deform mask dielectrics.

Grown layers are also prone to forming grain boundaries at intersections of two different nucleated layers growing into each other. These grain boundaries are rather fascinating as they are in fact a sort of heterostructure formed of two similar layers and have been shown to be exploited for interesting materials physics such as the creation of memristors or structural voids that can be generated under bias [63, 64]. And while these large layers are prone to problems as discussed above, they are still useful for studies that can work

on large ensembles and will be used in portions of this text where applicable for their best use.

2.1.2. Optical Properties of Monolayer TMDs, and Exciton Physics

An attractive and important feature of monolayer TMDs is their tightly bound exciton quasiparticles. These quasiparticles arise due to the 2D character of the monolayers and reduced Coulomb screening, allowing for photoexcited (or otherwise) electrons and holes to remain bound in pairs [65–67]. These bound pairs form one exciton specie and can recombine and emit light even at room temperatures and above. These excitons are bound tightly by high binding energies in the hundreds of meVs with very small Bohr radii on the scale of single nanometers.

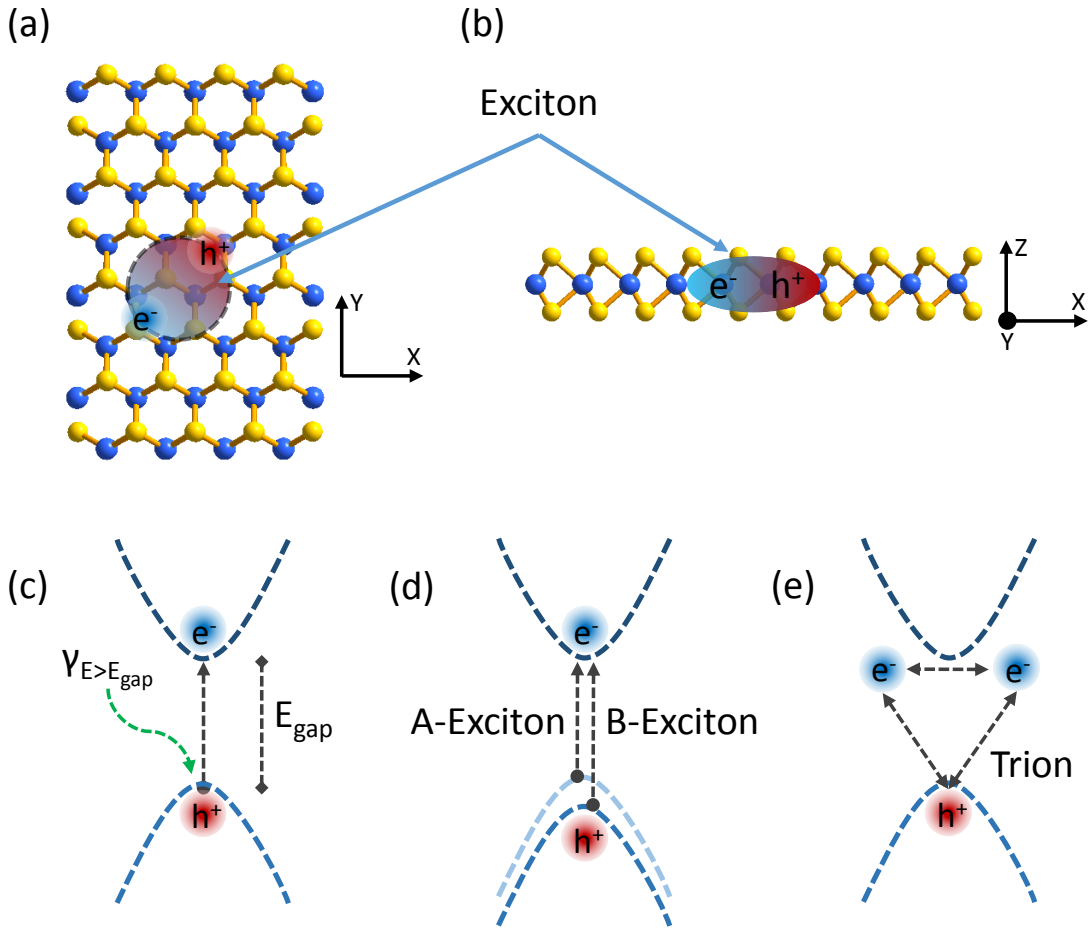

Figure 2.4. Excitons in a representive 2D lattice and their band energy formtion. (a) Shows exciton within the xy sheet of a TMD, showing its freedom in two dimensions. (b) A side view of the sheet in (a) showing a restriction in z-axis. (c-e) Exciton formation and examples of A-Exciton, B-Exciton, and Trion respectively.

Much of the optical behavior of 2D materials from room to low temperature is dominated by these excitons and other similar species. At room temperature, photoluminescence and absorption are dominated by the 1s exciton species (A and B), the former usually dominated by the A-exciton while the latter shows strong contributions from both

A and B-exciton species. For the extent of this thesis, I will be focusing on the A-exciton as it is the dominant specie in the majority of optical spectra and measurements detailed within this script. The A-exciton specie (from here on referred to as a generic exciton unless otherwise stated) is, for TMDs, within the visible to near IR wavelength ranges from approx 600 nm for WS_2 to 800 nm for $MoSe_2$ at room temperature. Dark exciton species also exist in TMDs, these are exciton species that are forbidden either due to momentum (electron-hole pair in different valleys) or spin (electron-hole pair with different spins), and cannot normally be stimulated via optical exploration due to a lack of momentum transfer or spin-flipping possibilities from photons. However, they can be stimulated using other methods and have recently become topics of interest in the field [68–70].

To better understand the exciton (and highlight a critical sensitivity of importance to this script), we look at the 2D effective mass Hamiltonian:

$$H = -\frac{\hbar\nabla_R^2}{2M} - \frac{\hbar\nabla_\rho^2}{2\mu} + V(\rho) \tag{2.1}$$

The equation is as follows: the first term is the center of mass Hamiltonian with M and R as the exciton effective mass and center of mass coordinate. The following terms make up the relative exciton Hamiltonian with μ the reduced mass ($\mu = \frac{m_e m_h}{m_e + m_h}$) and ρ is the electron-hole relative coordinate. More specifically and of interest, V(ρ) is the nonlocal-screen electron hole interaction potential defined as (from [3, 71]):

$$V(\rho) = -\frac{2e^2}{\epsilon_1 + \epsilon_2}\int_0^{\text{inf}} \frac{q_s J_0(q\rho)}{q + q_s} dq \tag{2.2}$$

With e as the electron charge, $J_0(q\rho)$ a Bessel function of the first kind, q is the electron wave vector, and:

$$q_s = \frac{1}{r_s} = \frac{\epsilon_1 + \epsilon_2}{\epsilon_r d} \tag{2.3}$$

Where r_s is the screening length and ϵ_r is the TMD relative dielectric constant. It is important to note the dependence on dielectrics (ϵ_n) of the interaction potential and screening length of the electron-hole pair. In standard applications, these terms are usually air and the substrate dielectric such as SiO_2, but it is because we can controllably vary these dielectrics around a monolayer via environmental engineering, that we gain significant influence over the exciton. Moreover, changing the environment of the TMD can be utilized to pick higher quality substrates such as hBN over the rough, amorphous surface of SiO_2 which not only modifies the dielectric consideration but removes local strain. These strain points have been shown to modify the electronic band structure from the theoretical expectation [4].

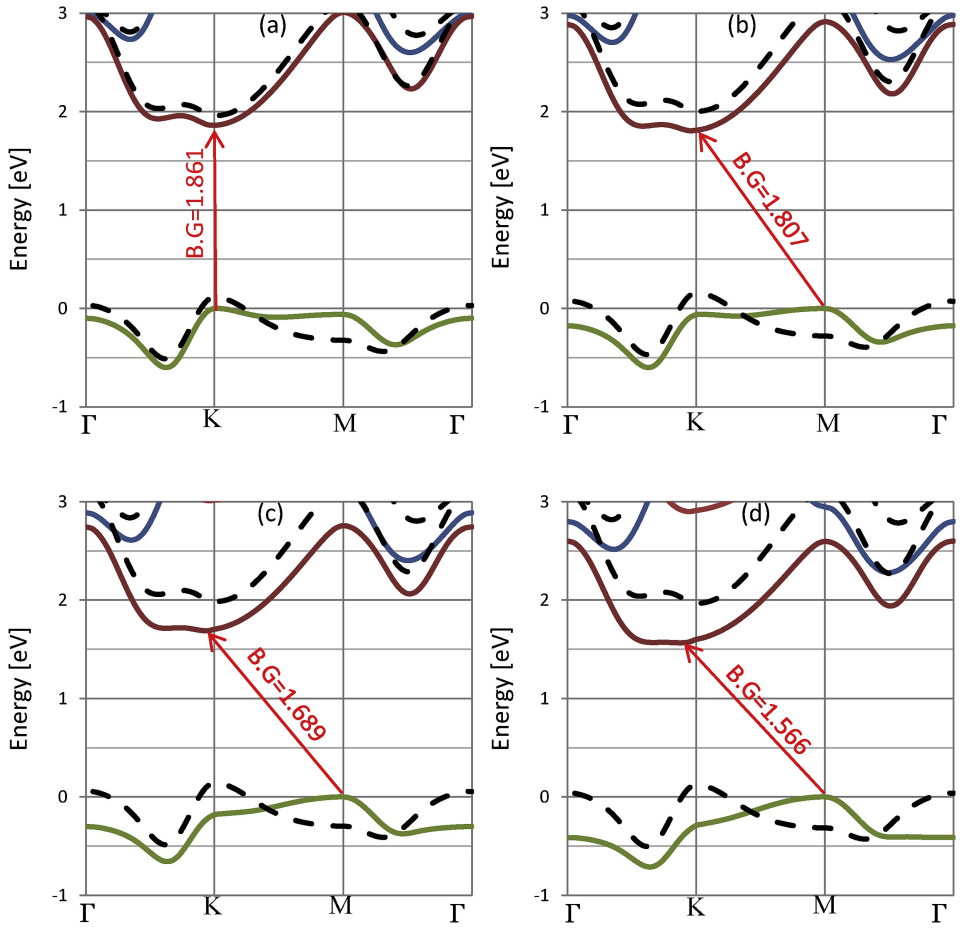

Figure 2.5. Example of strain modified MoS_2 bandstructure of a monolayer. It is possible to strain a layer, either intentionally or unintentionally, from direct to indirect bandgap. Adapted from [4], Copyright 2019, with permission from Elsevier.

Accompanying the charge neutral exciton (one hole, one electron), are also charged excitons (positive or negative) with either an extra hole or electron, and named positive trions or negative trions respectively [41, 66, 72–75]. The trion species are formed when the excited electron of the exciton pair interacts with a nearby charge carrier (hole interacts with a hole carrier), with notably smaller binding energies of a few tens of meV (for MoS_2 this has been found to be around 15 meV, an order of magnitude weaker than the

neutral exciton). These species are common, often even the dominant species, at room and low temperatures due to non-neutral doping of the TMD. In MoS_2, for example, due to the prevalence of sulfur vacancies and n-type (electron rich) doping [76], the negative trion is often the dominant emitter species at all temperatures without external influence on doping. The positive trion is extremely rare and difficult to realize in MoS_2 due to this inherent heavy n-type doping. Other TMDs, such as WSe_2 normally shows neutral excitons but can be externally tuned to show either species of trions. In either case, external tuning such as that afforded by local backgating can control the carrier populations and as such control which of the three species of exciton are the dominant specie [77].

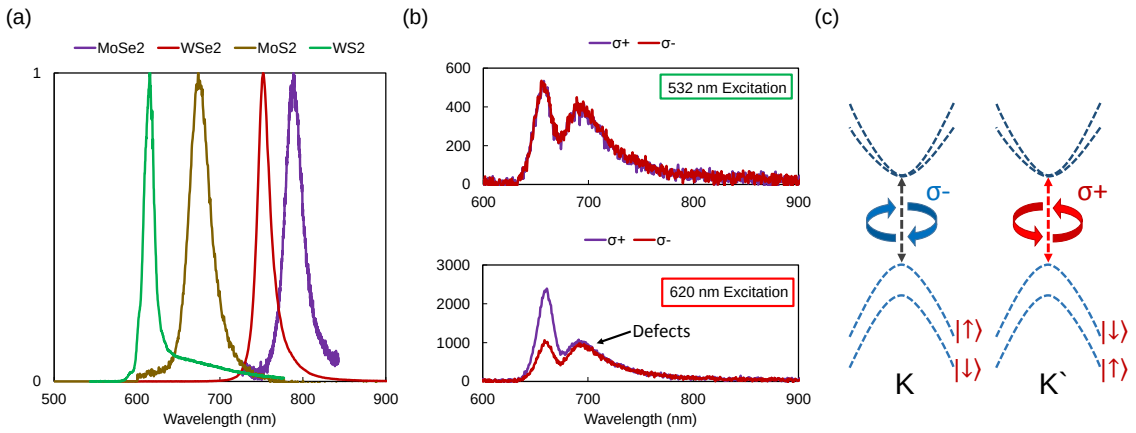

Figure 2.6. Exciton species in 2D TMDs. (a) Representative spectra of the exciton in MoS_2, WS_2, $MoSe_2$, and WS_2 at room temperature on SiO_2 wafers. This exciton emission is, for these materials at room temperature, comprised of the neutral and charged excitons and cannot be resolved directly without additional steps. (b) Exciton emission of MoS_2 at low temperatures showing circular polarized emission with near-resonance (620 nm) pumping $\sigma+$ and a lack thereof with off-resonance pumping. Defects are also labeled as an example, they show no circular polarization. (c) Valley polarization of the K and K valley in MoS_2.

Because of inversion symmetry breaking of monolayer TMDs due to a lack of an inversion center point (arising due to the M-X-M crystal ordering), normally degenerate valleys (such as in invertible graphene) become distinct and can be accessed in a way analogous to spin-dynamics. By use of right-handed or left-handed circular light excitation, it is possible to excite optical excitonic transitions specifically at either the K or K valley. This species of exciton is outwardly identical to the A-exciton and its trion subspecies but carries a distinct quantum character of the valley polarization and as such valley-dependent optical selection rules, resulting in circularly polarized emission matching the incident polarization [52, 53, 78]. In order to realize valley selectivity in TMDs, it is usually required to reach cryogenic temperatures and use near resonance excitation as to limit electron-electron scattering and resultant loss of the valley character. The quality of the valley selectivity is defined by the percent-polarization:

$$P = \frac{I_{\sigma+} - I_{\sigma-}}{I_{\sigma+} + I_{\sigma-}} \tag{2.4}$$

Where σ defines the handedness of the emitted light intensity (I) for a given polarized incident pump. Recently, methods have emerged to preserve valley properties up to room temperatures such as by putting a TMD within a cavity, opening this quantum character to new possibilities.

As temperatures drop and the exciton species emission begins to blue-shift, their linewidth narrow, and valley-properties become accessible, new exciton emitter species begin to appear as non-radiative recombination paths (for example Auger or phonon-assisted recombination) are closed off. The main focus will be on the defect (bound

exciton) emission state for this thesis but there are also other emitters such as high-energy 2s excitons and bi-excitons (quasiparticle state of two excitons) that become accessible. While not definitively understood in their origin, defect states are commonly associated with lattice defects such as sulfur or molybdenum vacancies in MoS_2 (also responsible for the formation of trions), lattice deformations such as folds or wrinkles or grain boundaries, impurities within the lattice, atmospheric absorptions, or lattice damage from etching or degradation [79, 80]. These defects form trap states often located within the bandgap potentially anywhere from just below the conduction band-edge down to the valence band-edge, and result in the creation of bound excitons which recombine through these trap states. The recombination emission from these defect-induced excitons are commonly characterized by their broad emission often many times broader than the exciton and made up of many different overlapping and convoluted states, lack of valley character, and high sensitivity to external manipulation such as local gating which can turn-off these features with sufficient doping[80].

These defect states are often unwanted but have been utilized in creative ways such as to realize the creation of single-photon emitters, magnetic sensitive quantum particles, and more [59]. For the purposes of this thesis, the focus will be on the avoidance of defect creation, minimization, and quenching as this state is generally undesirable in more classical applications. Control over potential imperfections or lattice quality as well as finding ways to mitigate defect optical contributions outright are tantalizing points of external control for the realization of higher quality optical devices.

2.2. Electronic Properties of Monolayer TMDs, and Contacts

In addition to their desirable optical and excitonic properties, TMDs semiconductors have also garnered considerable interest and study in their applicability for the creation of 2D electronic and optoelectronic devices [81]. TMDs have shown a remarkable quality of high carrier concentrations (10^{12}) [82], potential for high mobilities (50 to hundreds $cm^2V^{-1}s^{-1}$) [51, 83, 84], and high current on/off ratios (10^8) [85], as well as photosensitivity and creation of photoexcited carriers [86], making them prime candidates for optoelectronic device creation. Moreover, TMDs have proven to be remarkably robust over many cycles of on/off electrical usage even in atmosphere. Moreover, work has recently been done to harness the valley character of TMDs to create polarized emitters and other valleytronic devices [52, 53, 67, 87].

Much as with their optical properties, the exact behavior of TMD electronic devices can be modified by temperature, optical excitation (formation of photocarriers), and gating, as some examples. This affords a great degree of control over the properties of the layers characteristics.

2.2.1. Electrical Contacts

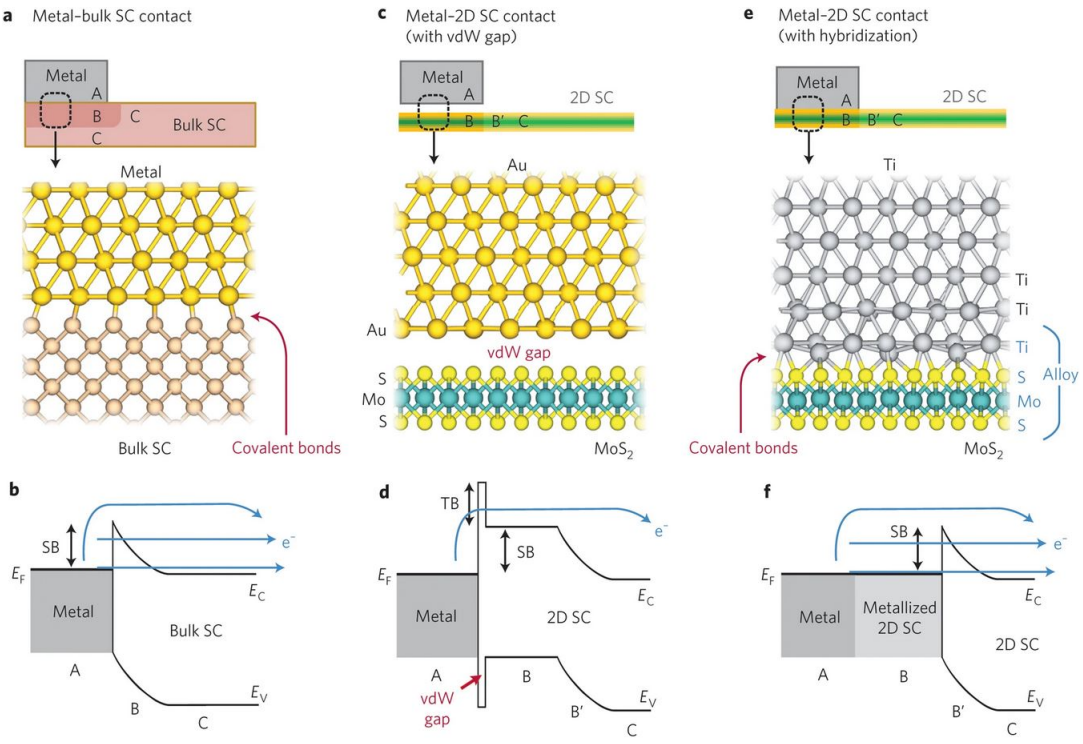

Figure 2.7. Contact interface examples. (a-b) Metal-bulk semiconductor interface and the resultant band configuration at the contacts. Band-bending at the interface results in the formation of a large Schottky barrier for the injection of electrons into the conduction band. (c-d) Metal-2D TMD gap interface by placing contacts atop of the 2D material directly rather than through deposition techniques, and the resultant tunneling + Schottky barrier. (e-f) Metal-2D TMD interface when metal is deposited directly, the underlying TMD is partially metalized by high-energy metal atom collisions, and the resulting barrier for carrier electrons injection. Reprinted by permission from Springer Nature Customer Service Centre GmbH: Spinger Nature [5], Copyright 2015.

One of the most critical components of creating an electrical device out of 2D TMDs is the formation of contacts and carries many of the difficulties in working with TMDs. Much of the performance of the resultant field-effect transistor (FET) is tied up at the contact interface between contact metal and 2D crystal lattice. Poor contact resistances

can arise for different reasons, here I will briefly discuss three major sources, the first is a physical problem while the latter two are problems in development and processing of 2D FET devices. The first is simply down to the interfacing of a metal with a semiconductor, resulting in a significant electron-flow barrier due to Fermi level pinning of the semiconductor by the metal. While the sensitive nature of 2D TMDs is one of its greatest strengths, here it is a major weakness as it results in a Fermi level pinned within the mid-gap. Second is due to an alloying (and deformation of the lattice) of the atomically thin 2D layer when bombarded with hot metal atoms during deposition of the contact metal. The third and final example arises from trapped adsorbates on the 2D layer surface, such as Oxygen or water vapor or chemical residues from processing such as MMA/PMMA residues from lithography steps used to define contact areas for metal deposition. In either of the latter cases, the pristine surface of the 2D layer is contaminated and compromised, resulting in significant loss or variability in performance.

Beyond the challenges of the contact and device fabrication, the resistance at the contacts can be understood as arising from a Schottky barrier, visualized in Fig.[2.7], which arises from a mismatch of work functions at the interface between the metal and the semiconducting TMD [5]. This barrier can be put in terms of the work functions as:

$$\Phi_{SB} = \Phi_M - \Phi_{TMD} \tag{2.5}$$

In a standard two-terminal FET, the contact resistance RC cannot be obviously extracted from the material performance R_M for $R_{Eff} = R_C - R_M$. This has significant ramification on the device performance as measured where the contact resistance plus

intrinsic Ohmic resistance of the metal can dominate the performance and result in observed low device performance. In TMDs, because of the low mean free path of electrons, the R_c can be understood by a transmission line model [5]:

$$R_C = \sqrt{\rho^{2D} r_c \coth l \sqrt{\frac{\rho^{2D}}{r_c}}} \tag{2.6}$$

With l is the contact length, ρ^{2D} is the TMD sheet resistance, and r_c is the contact/TMD interface resistance which is related to the Schottky barrier. Minimizing the contact resistance is a main focus of device creation in order to best extract the real material electronic behavior.

Traditionally, contacts are realized with use of masking (such as PMMA/MMA) and electron beam pattern writing to define a contact area on the target material. Metal is then deposited via thermal evaporation over the mask and defined regions, and then removed via a lift-off method that dissolves the resist mask. However, this technique is rife with short comings which tend to result in high contact resistances. As discussed previously, kinetic bombardment from the hot metal atoms induced damage as well as potential trapped adsorbates or resist residues are considered some of the main causes of the contact resistance problems [27, 88]. The former creates an unwanted alloying of the hot metal atom with the crystal lattice by displacing any given portion of the MX_2 crystal, creating MX-Metal for example. In the latter case, any form of processing will tend to leave behind unwanted residues on the exposed layer even with the best cleaning techniques. The best way to avoid this problem is to entirely remove or buffer out direct patterning and writing as we will see later in this thesis.

But aside from specific fabrication-induced limitations, the desirably sensitive nature of 2D TMDs is also a short-coming in realizing ideal contacts. Even if the metal contacts are realized through different methods without evaporation or similarly damaging methods (such as exfoliating directly onto contacts), the interface of metal-TMD causes Fermi level pinning due to a hybridization of the atomic orbitals of the metals and TMDs across the interface [89]. This pins the Fermi level within the bandgap at the contacts, creating a sub-optimal path (barrier) for electron (or hole) injection into the 2D material. By closely matching the work function of the metal with the TMD, it is possible to reduce this effect but never completely remove it. To that end, much work has been done in the field to find alternatives to metal contacts such as graphene contacts [90], 1D edge contacts [91], tunneling contacts [9, 14, 84], etc. In this work I will specifically focus on tunneling contacts.

2.3. Heterostructures out of 2D

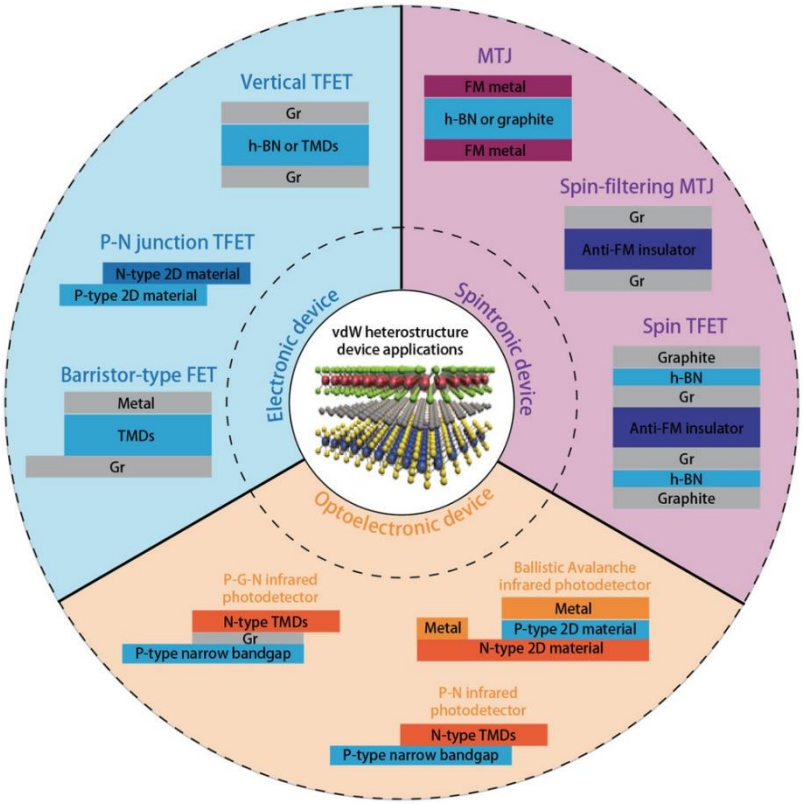

Figure 2.8. Examples of heterostructures built from 2D components, and the robustness of these building blocks in a wide array of applications. Adapted with permission from Wiley Advanced Materials [6], Copyright 2020.

While monolayer-only systems remain of interest, there are also many open questions and more recent discoveries based on the interactions of these layers with one another in more complex systems (2D-2D) [9, 29, 30] or with other types of dimensional materials such as molecules (0D) [2, 8, 10] or bulk dielectrics or insulators (3D) [1]. This later form of structure, still a heterostructure, is commonly referred to as a mixed dimensional heterostructure due to the combination of 2D with 0D, 1D, or 3D [7]. Much of the interest in these mixed dimensional structures comes from the fact that the 2D layer serves as an

all-surface substrate with effectively no thickness, as such it is wholly interacting with no need for considerations such as skin-depth or propagation through a medium.

These interactions are enabled by the creation of heterostructures by stacking layers atop each other, growing two different layered materials along sharp interfaces, depositing molecules or dielectrics over single layer substrates, or at the junction at the crystalline edge between a monolayer and bulk crystal. These exotic structures can have distinct physical and electronic properties on either side of the interface and, potentially and even more interestingly, at the interface. Or, conversely, these structures can be used to preserve or magnify the properties of the TMDs or other constituent layers used in their creation such as with hBN used to preserve and greatly improve the quality of encapsulated TMDs, or using molecular treatments to quench defect states out of the emission spectra.

2.3.1. 2D-2D Heterostructures

Creating 2D-2D heterostructures can be accomplished both out of-plane and in-plane. In the former case, this is done by either manually stacking layers atop on another via transfer technique or through growing layers atop of one another via CVD methods. In a way, this is similar to re-assembling the bulk crystal layer by layer but here we can control what layers are used [29] and their twist angles [92, 93] which are not variable in conventional bulk. Doing this in a controllable and reproducible fashion requires exceptional techniques that are not only precise to within microns of alignment and fractions of a degree but that can also gently handle the fragile 2D layers while also not contaminating their surfaces, a critical point of quality control that can significantly impact any layer to layer interaction

or layer to other material. A significant portion of my work was in designing techniques capable of this with robust applicability to many different types of heterostructures and device structures utilizing 2D materials as a component. Much of this is encapsulated in the two Appendixes of this Thesis.

By carefully assembling different monolayers into heterostructures, such as for example WSe_2 with $MoSe_2$, it is possible to create a brand new excitonic species across the interface with the electron-pair existing in part in the different layers [29, 94, 95]. This exciton is known as an interlayer exciton with the electron residing in the conduction band of one TMD and the hole in the other TMDs valence band before recombination. These interlayer excitons can be identified by their much lower emission energy, often several hundred meV from normal exciton emission of the constituent layers and have been shown to preserve valley characteristics [96]. These heterostructures can be further modified by specifically altering the twist angle between the constituent layers and can even be applied to homostructures using the same layer species as a heterostructure of sorts [92]. In mixed material heterostructures a small twist angle has been shown to create Moire exciton patterns in the heterostructure [30]. In twisted homostructures, it has been shown that is possible to preserve valley polarization in multilayer stacks even though standard bilayers and thicker do not shown valley polarization in TMDs [97, 98].

Another form of heterostructure is one built for functionality rather than direct realization of novel properties. Example of this are hBN used to encapsulate (a top and bottom layer sandwich) TMDs [13, 22], graphene-TMD interfaces for next-generation metal-free contacts [90, 91], hBN monolayer on TMD monolayer used as a tunneling layer for contacts [9, 28], etc. These heterostructures emphasize the power of being able to

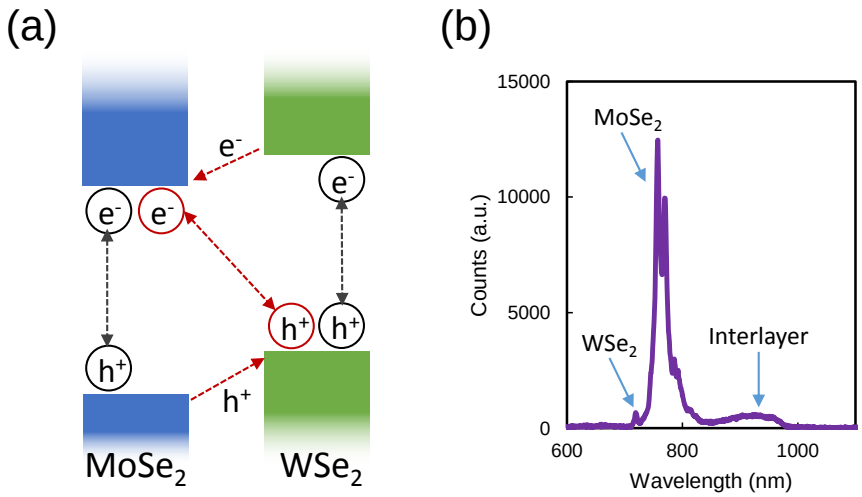

Figure 2.9. Example of an interlayer exciton. (a) Exciton band diagram understanding of the formation of an interlayer exciton. (b) Experimental realization of an interlayer exciton in the Stern Lab of WSe_2-$MoSe_2$ heterostructure at 10 K.

engineer the surroundings of TMDs to realize better environments, better device performance (optically or electronically), or the potential for previously unfeasible experiments. In the case of hBN encapsulation, it has been shown that the linewidth of TMD excitons can be reduced from tens of meV to that of a few meV, approaching the homogeneous limit [13]. This is due, in part, because hBN acts as an ideal substrates for TMDs freeing them from interfacial trap states and surface roughness of conventional substrates such as SiO_2. This linewidth reduction opens the way for more sensitive measurements of the exciton feature such as Zeeman splitting in a field [99, 100], particle-in-a-box quantum confinement tuning [101], and so on. Graphene contacts and hBN tunneling layers have been shown to greatly reduce or eliminate contact resistance in TMDs [9, 28].

For in-plane heterostructures, this is usually done via methods of CVD growth of specific species of TMDs in a sequence such that one layer is usually nested inside of

another in a triangle-within-triangle structure, but can also be more ubiquitous in the form of two sheets of TMDs interfaced at a 1D boundary. This form of structure creates a distinct grain boundary between the two TMDs that is often warped and deformed due to the different lattices mismatching at the boundary and has been shown to have distinct properties [9, 64, 71].

2.3.2. nD-2D Mixed Dimensional Heterostructures

Mixed dimensional vdW heterostructures have recently become a renewed point of focus and interest in the field of material science and physics[7]. While the basis of mixing dimensions for vdW materials or otherwise is one that has been established for years, combining nD + nD dimensions such as 3D + 1D or 3D + 0D, recent focus is explicitly in the combination of 2D + nD. Introducing 2D components to mixed dimensional heterostructures provides an atomically thin all surface component, as discussed previously 2D layers are defined only by their surface and edges, and as such a cleanly defined interface. This provides an interface of interactions that is not hidden away either physically or electronically within bulk components but is instead approximately directly quantifiable. Moreover, due to the thin and thus approximately transparent nature of the 2D substrate, the interface of 2D-nD can be electrically or optically stimulated via gate or optical excitation respectively, providing direct methods to explore its character.

A common example of mixed 2D-nD heterostructures is that of a 2D layer functionalized with organic molecules such as Phthalocyanine [2] or Rhodamine [8] dye molecules, Pentacene ring molecules [10], etc. Different molecules prove to have very different interactions with the surface of the 2D layer and have been shown to create novel interfacial

states or undergo self-assembly. Moreover, the individual components are modified with potential for improved light absorption or emission, doping, defect suppression, etc.

This combination proves robust but also scalable as it can be applied across large CVD growths, and can prove to be a potential avenue for significant improvements in photovoltaics and solar cells.

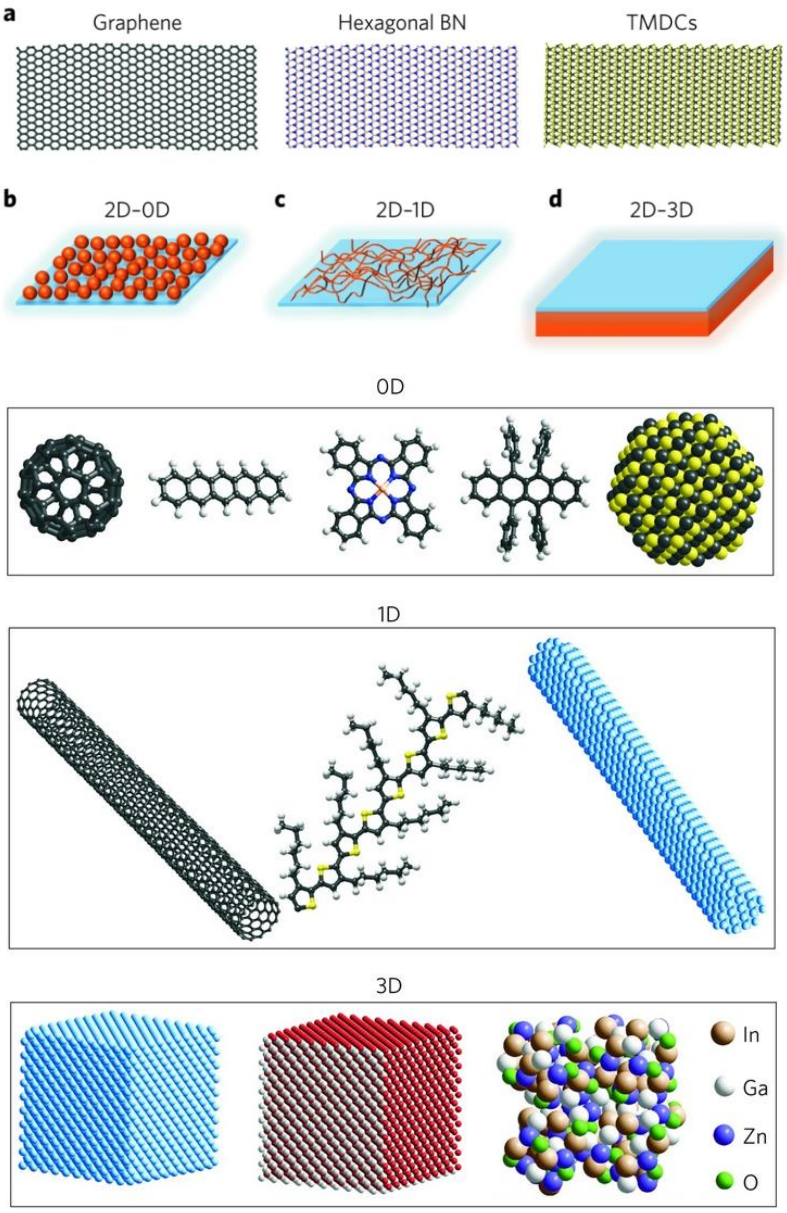

Figure 2.10. Examples of various mixed dimensional structures and representations of dimensionality (0D: organic molecule, 1D: Carbon Nanotubes, 3D: Bulk Semiconductors). (a) Shows examples of 2D sheets: graphene, hBN, and TMDs. (b-d) Shows mixed dimensions of 2D + nD where n=/=2. Adapted fromReprinted by permission from Springer Nature Customer Service Centre GmbH: Spinger Nature Materials [7], Copyright 2017.

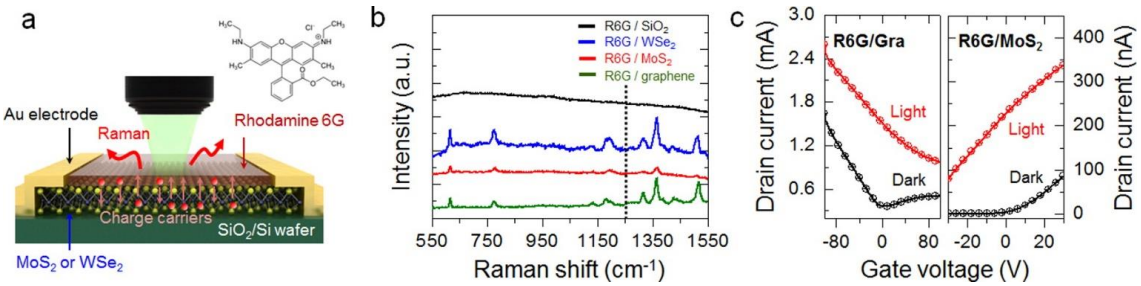

Figure 2.11. Light sensitized TMD with Rhodamine dye molecule functionalization. (a) Example device. (b) Raman enhanced response of Rhodamine on different substrates, showing significant enhancement from amorphous bulk SiO2 to 2D layer. (c) Significant light-sensitive improvement in electrical performance in part due to the Rhodamine functionalization, proving a possible avenue for creation of more efficient solar cell technology. Adapted with permission from [8]. Copyright 2016 American Chemical Society.

CHAPTER 3

Multilayer Homostructures: Engineering Electronic Properties with Layer Number

This first chapter will briefly go through my first projects with so-defined homostructures of like-like layered materials used in layered structures. While this work was primarily led by others, it was here that my introduction to material manipulation through layer numbers and achieving novel phenomena began and would influence many of the chapters to come after. As such it is the a proper introduction to my work.

While homostructures may appear less interesting than the heterostructures or mixed dimensional heterostructures that will come later, they are still quite important to consider. Particularly, just changing layer number can have a drastic impact on the optoelectronic properties of the material, such as the direct to indirect bandgap transition in TMDs. This means that even homostructures can be thought of as heterostructures! Rather than different atoms making up the mixture of materials, we instead have different electronic bandstructures.

3.1. Band Engineering with Monolayer/Multilayer Homojunction Interfaces

To begin, for homostructures discussed here, I will briefly go over band alignment and band bending to frame the discussion for mixing different electronic band structures in a homostructure. This will also be of importance in Chapters 4 through 7 on heterostructures as many of the principles apply there as well but rather than changing layer numbers,

we will be changing materials. The initial concepts of band bending were developed by Mott and Schottky [102, 103] to address the rectifying behavior at contacts between metals and semiconductors. I will look at it briefly in this context before applying it more broadly to semiconductor-semiconductor interfaces.

When metal-semiconductor contact is formed (a common theme in creating any semiconductor device with metal contacts either on top of or adjacent to the semiconductor), the work function (Φ) differences of the two materials lead to an exchange of free charge, the direction of which depends on the relative work functions. In the scenario where the work function of the metal is higher than that of the semiconductor,

$$\Phi_m > \Phi_s \tag{3.1}$$

Electrons will flow from the semiconductor and into the metal. This process continues until equilibrium is reached when the Fermi levels of the two disparate components align. In the region of the semiconductor nearest to the metal there results in free charge depletion, called the **depletion** layer. When the reverse is true and,

$$\Phi_s > \Phi_m \tag{3.2}$$

Charge flows from the metal and into the semiconductor, forming an **accumulation** layer.

Generally, when the Fermi level of the semiconductor is above that of the metal, free electron charge flows from the semiconductor, causing its Fermi level to decrease. When the Fermi level of the semiconductor is below that of the metal, charge flows into the semiconductor and its Fermi level increases. In the depletion/accumulation region, the charge transfer creates an electric field which causes a continuous shift in the energy band

edges of the semiconductor. As charge flows from the semiconductor, the Fermi level (of the semiconductor) bends upward towards and at the interface, and, as charge flows into the semiconductor, the Fermi level bends downward.

This is called band bending.

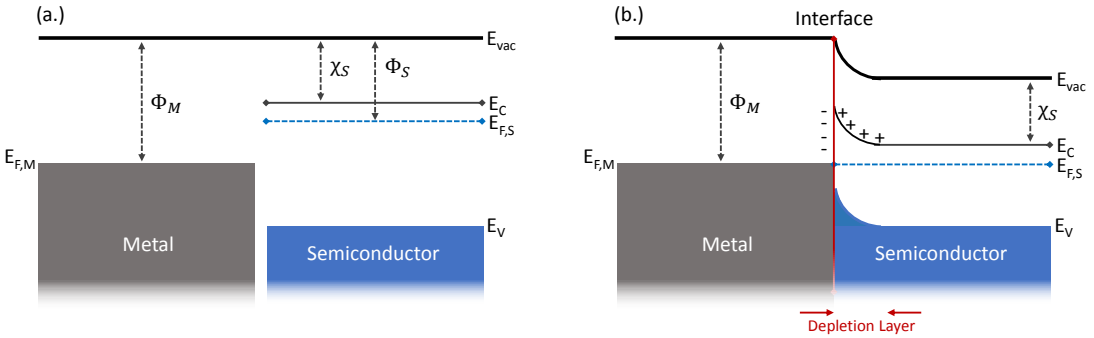

Figure 3.1. (a) Schematic of independent metal and semiconductor work functions, and unpinned Fermi level of the semiconductor. (b) Schematic of a pinned Fermi level of semiconductor when interfaced with a metal.

To create a simple picture of this like in Fig. [3.1], we look to electrostatics and consider what an electron experiences as it moves through from the semiconductor (metal) and into the metal (semiconductor) across the interface between them. At an established equilibrium, the regions just beside the interface are on one side negatively charged and on the other positively charged due to the electrostatic induction from the contact as previously discussed. As the electron moves to cross the barrier it will experience a repulsive force from the built up charge in the accumulated region and thus its potential energy rises and the band bends upward (downward).

Unlike the simpler case of metal-semiconductor, band bending between two semiconductors is dependent on many factors and both sides of the interface will experience band bending. The extent of the bending is dependent on numerous factors such as doping type (p, n, or undoped), crystal and particle sizes, surface interactions, etc. As both semiconductors see the interface, we must consider the picture to be two-directional unlike in the metal-semiconductor model where it was only the semiconductor side that experienced

any bending. How these bands bend on either side of the interface leads to three possibilities and junction types referred to as Type-I, Type-II, and Type-III as seen in Fig. [3.2], but all the same rules as were outlined in the metal-semiconductor case apply but now to both sides. This analogous to the behavior seen in 2DEG in $Al_xGa_{1x}As/GaAs$ heterojunction [104].

For the homostructure (and how we will look at it in ways very similar to heterostructures) we will now consider a Type-I, or n-n, junction as we saw in Fig. [3.2] at the interface between a monolayer and multilayer of MoS_2. Because we are working with single MoS_2 source and all exfoliated we can rule out disparate doping, changing particle sizes, lattice mismatches, etc. We are working with an effectively "perfect" interface.

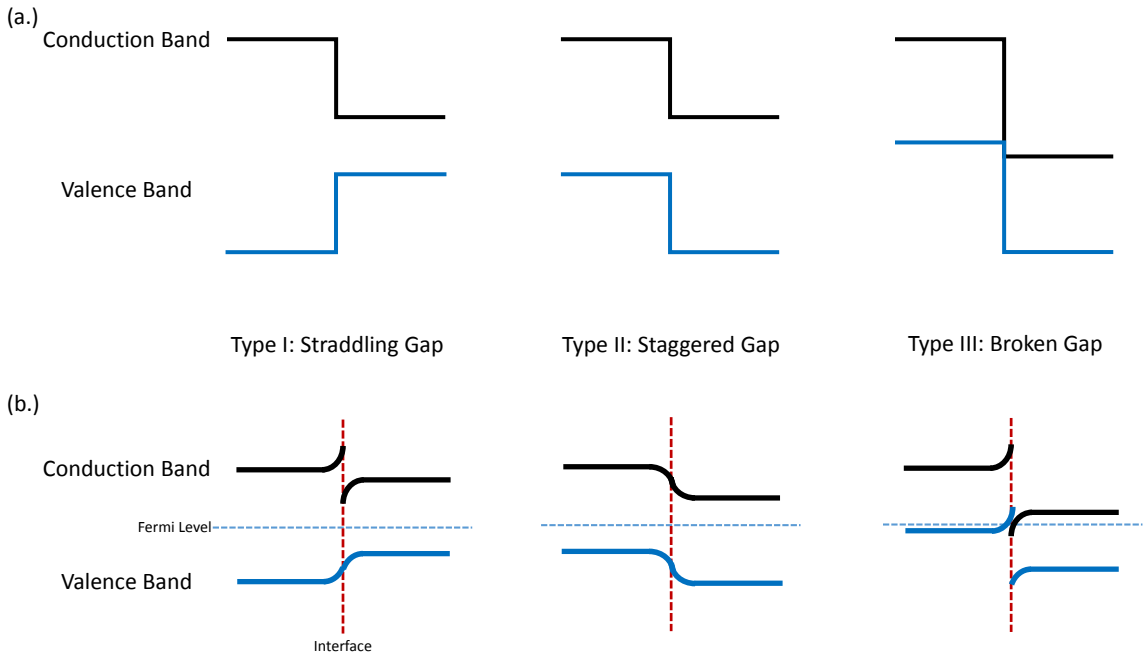

Figure 3.2. The types of (a.) band alignments for electronic junctions and (b.) resulting band bending in semiconductor interfaces. The red dotted line represents the interface. Blue dotted line represents a potential Fermi level placement within the midgaps of both sides of the interface.

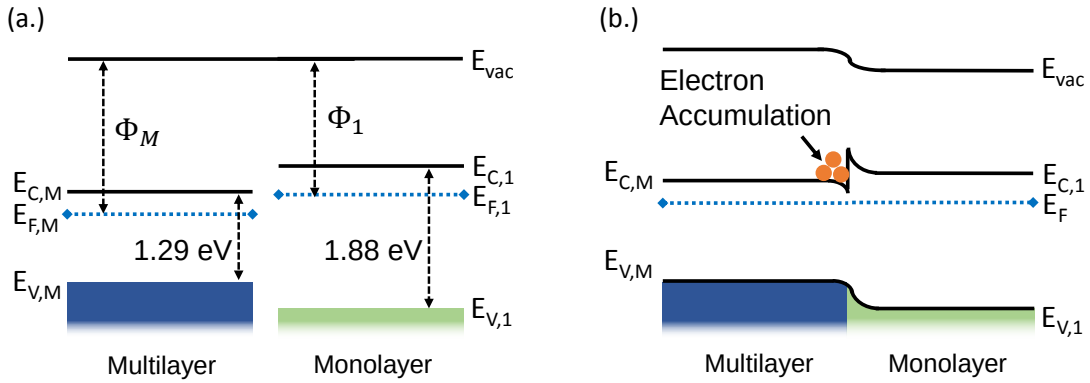

Figure 3.3. Band diagram of MoS_2 monolayer (1, right) and multilayer (M, left), (a.) before contact and (b.) after contact and equilibrium. Electron accumulation can be seen in (b.) where the band bends down in the multilayer. Adapted with permission from [1]. Copyright 2017 IOP Publishing.

To build a picture of the band alignment at the interface, we approach the problem with a similar starting point: we look to the work functions of each side of the interface. We define the work function of monolayer (1L) and multilayer (ML) as, respectively, Φ_{1L} and Φ_{ML}. In MoS_2 the monolayer and multilayer have different work functions with [105–107],

$$\Phi_{ML} \approx 4.59 \text{ eV} > \Phi_{1L} \approx 4.49 \text{ eV} \tag{3.3}$$

As before, electrons will flow from the material with lower work function to that of the higher, or, in this case, since $\Phi_{ML} > \Phi_{1L}$, the electrons will flow from the monolayer and accumulate in the multilayer. This creates an accumulation layer in the multilayer and a depletion layer in the monolayer. Recalling our picture of these two scenarios from the simple electrostatic considerations with metal-semiconductor interfaces. When a depletion

layer is formed, the band bends upward due to the build of negative charge across the interface that increases an electrons potential energy as it attempts to cross the interface. Conversely, when an accumulation layer is formed, the band bends downward due to the buildup of positive charges in the depletion region which decreases the electrons potential energy as it attempts to cross the interface, Fig. [3.3].

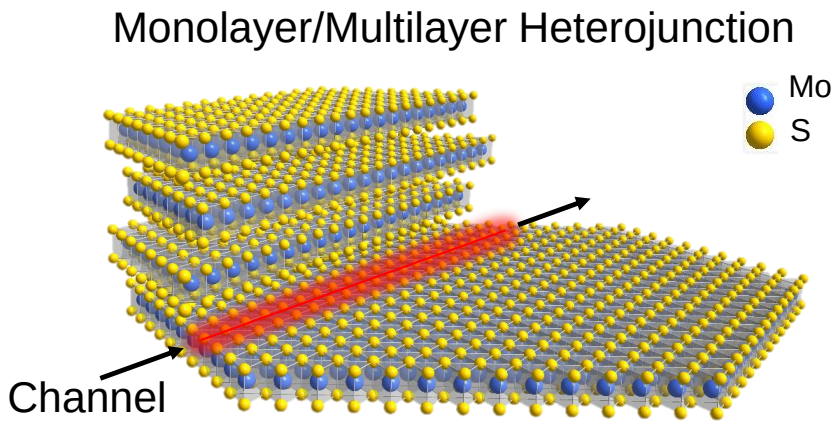

Figure 3.4. Monolayer/multilayer MoS_2 homostructure crystal example with a highlighted channel at the interface. Adapted with permission from [1]. Copyright 2017 IOP Publishing.

The combination of these two pictures results in an interface that, for the multilayer, bends downward towards the equilibrium Fermi energy, and, for the monolayer, bends upward away from the Fermi energy. It is this offset in the bents bands directly adjacent to the interface that creates a 2D channel in which electrons build up as seen in Fig. [3.3] and Fig. [3.4]. It is this picture that we wanted to probe.

We thus exploit the condition of differing, layer-dependent band structures and focus here on the homostructure formed at the interface between MoS_2 monolayer (1L) and multilayer (ML) pieces. This homostructure is convenient for a number of reasons: it forms

naturally at cleave-lines where the crystal has broken sharply along a lattice plane during exfoliation (almost every monolayer will be attached to some form of multilayer), it can be exfoliated from a single crystalline flake of MoS_2 (the aforementioned perfect interface!), and there is no need for secondary transfers or disturbing of the flakes to put them near or on-top of one another (unlike heterostructure designs, or twisted homostructures). The last point is especially important as transferred MoS_2 suffers from very pronounced strain-based defects, and in this way we avoid this problem entirely. As noted previously, strain can have a significant impact on the bandstructure and int his way is entirely avoided [4].

There are, however, disadvantages to this method in that there is no pre-exfoliation control on the number of layers that come in junction with a monolayer, and the layer thickness of MoS_2 can vary wildly from monolayer to over a hundred layers for any single exfoliation. An interface can be formed between hundreds of possible configuration of mono-to-nLayers, completely at random in the exfoliation process. The only way to create repeating devices is through trial and repetition in exfoliation which is of low yield. We also avoid thick MoS_2 of many layers (greater than 50 nm in size) to avoid any broken or uneven contacts. All of these factors significantly constrain device parameters and their realization.

To realize these devices, MoS_2 monolayer/multilayer flakes were exfoliated from un-doped MoS_2 crystals and deposited on heavily doped, 285nm thick SiO_2 substrates using the tape-exfoliation and gel methods, which are expanded upon in detail for methods in the Appendix. Please refer to the sections of interest for sample prep details. Samples were initially identified through standard optical microscopy where color-contrasts under white light at high magnification can distinguish monolayers (light brown/purple on SiO_2

depending on the thickness) from bilayer (darker light brown/purple) from multilayer (increasingly blue/yellow) and outright bulk (yellow/mirror like to the white light). Once a sample with a sharp, long edge between a monolayer of MoS_2 and suitable multilayer was identified optically, it was annealed at 400deg Celsius in an Argon/Hydrogen environment to burn away residuals from the exfoliation process as well as anchor the layers to the SiO_2 substrate (otherwise, it was not uncommon for devices to be washed away by acetone during lift-off). Cleaned devices were taken to be measured precisely with atomic force microscopy (AFM). Monolayers were identified, as expected, with a thickness of roughly 0.7-0.8 nm and $n*0.7$ for layer numbers (n) thereafter [108].

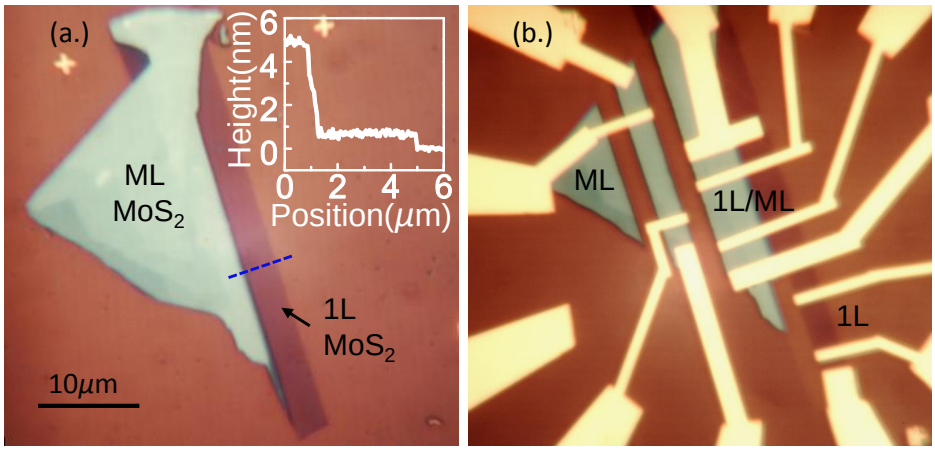

Figure 3.5. . Optical image of a device being processed. (a.) Initial optical identification and (inset) AFM height line scan confirming layer thickness. (b.) Post-etch and contact, fully fabricated device with monolayer (1L), multilayer (ML), and 1L/ML sections marked. Adapted with permission from [1]. Copyright 2017 IOP Publishing.

Devices were patterned into distinct individual rectangular slices (the importance of which will be made clear later) made from a single monolayer (1L)/multilayer (ML) flake: 1L-only, ML-only, and 1L+ML interface, using electron beam (e-beam) lithography and SF6 [109] reactive ion etching. Gold electrodes were patterned with a second step of e-beam lithography and gold was deposited to roughly 50 nm through thermal deposition. Electrode geometry was set to be perpendicular to the interface. The device, through the steps of identification and fabrication, can be seen in Fig. [3.5].

3.1.1. Results and Discussion

Initial measurements of the generation of carriers and band-bending at the interface were performed by scanning photocurrent microscopy (SPM) in high-vacuum (less than 1 mTorr) at room temperature under laser illumination from a pulsed femtosecond laser

system (OPO) with tunable wavelength. The SPM laser wavelength was varied to be below bandgap, at bandgap, and above bandgap energies, with average laser power limited to 70 μW. A backgate was applied through the underlying SiO_2 substrate and varied from 0 V to 40 V for repeated scans across the device and interface.

Subsequently, transport measurements were performed on each of the fabricated devices in parallel to the interface and characterized in similar conditions (no laser excitation was used in this part of the experiment and transport was measured in dark). Tests were performed at room and low temperatures (10 K).

In mono to multilayer MoS_2 the primary photocurrent mechanisms are exciton generation through higher-than-bandgap energy photon excitation and free carrier creation by electric field-assisted dissociation [110]. At the channel interface between the monolayer/multilayer, band bending would induce a high-local built-in e-field which can dissociate electrons and enhance photoresponse, and we looked to confirm this with SPM.

Photocurrent results are shown in Fig. [3.6] where the photocurrent is correlated with a spatial 2D reflectivity map, with three different laser energies used for excitation: 660 nm (1.88 eV) excitation, 680 nm (1.83 eV) excitation, and 700 nm (1.77 eV) excitation. All measurements were done with a 0.2 V bias across the V+ and V- contacts, and a 20 V backgate was applied.

Under 660 nm laser excitation, the exciting photon energy is very near to that of the optical bandgap of mono and multilayer MoS_2. In this regime, intensity contrasts of the monolayer/multilayer interface is greatly diminished due to other effects such as the creation of hot carriers and photo-thermoelectric effects. Under 700 nm laser excitation, the exciting photon energy is lower than that of either the 1L or ML optical bandgaps, and

as such fails to effectively create any excitons in MoS_2 leading to a reduced photocurrent intensity and no enhancement at the interface.

Under 680 nm laser excitation, we observe a region of current enhancement along the interface not otherwise seen at the other laser energies and a sharp I_{pc} peak is observed correlated to the interface. This result confirms that the band bending at the interface of the 1L/ML channel can increase the local generation of photocurrent.

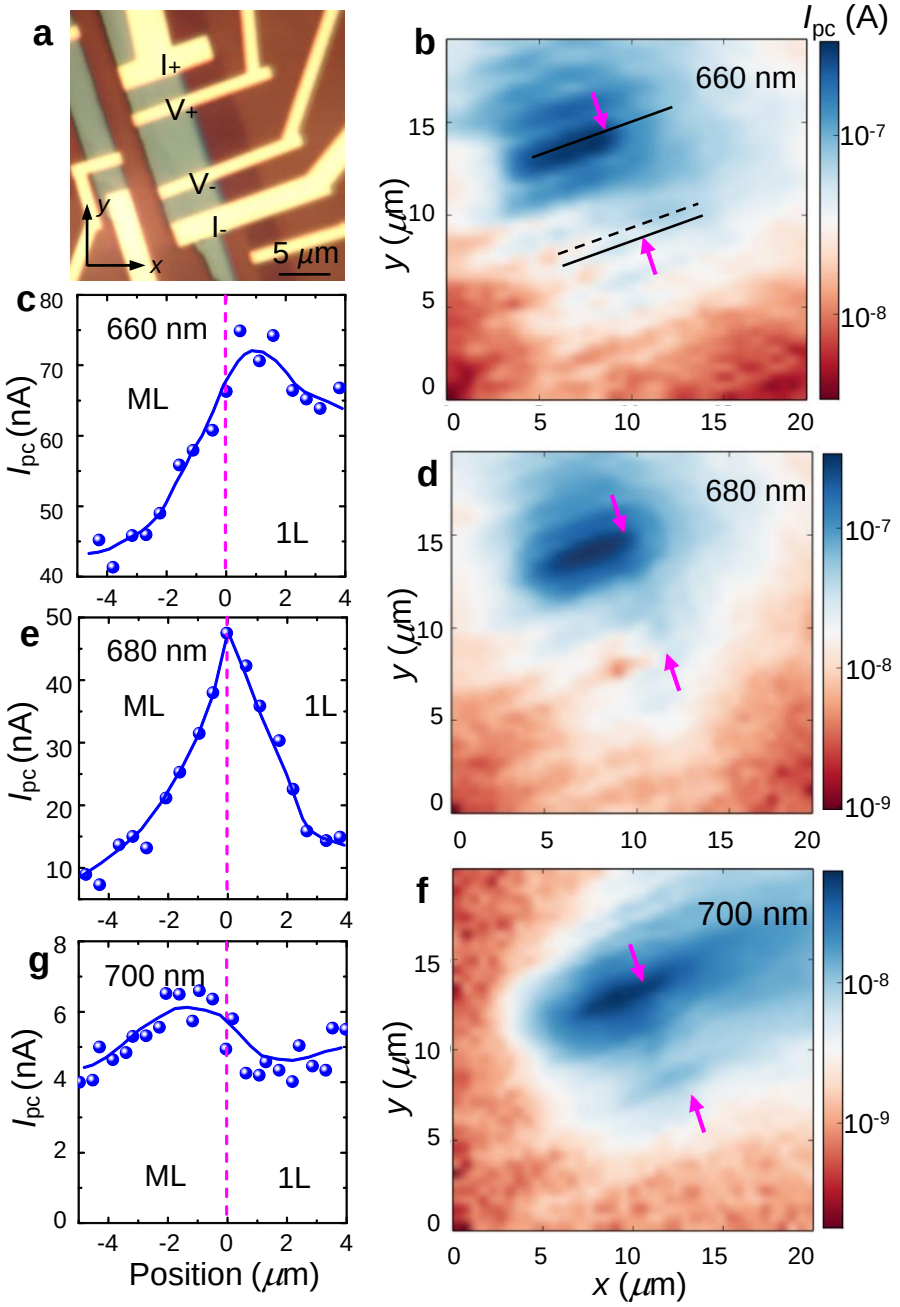

Figure 3.6. (a.) Completed device with Au-electrodes, mono-only and multi-only devices not shown in their entirety in this view. (b-c.) Photocurrent with a 660nm excitation source (pink arrows denote the location of the channel, to guide the eyes), (d-e.) with 680nm excitation, and (f-g.) with 700nm excitation. Dashed black lines on the line plots (c,e,g.) correspond to the spatial equivalent of the interface. The solid lines in (b.) correspond to the electrode contact edges. Adapted with permission from [1]. Copyright 2017 IOP Publishing.

To measure conductivity and the potential for a new conductive pathway along the interface, we performed transport measurements parallel to the interface at the 1L/ML boundary for our, as previously outlined, 1L-only device, ML-only device, and 1L+ML device. All devices, again, were fabricated from a single flake and preserve crystal orientation as parallel to the interface for all cases. This procedure was followed under the basis of the assumption that the conductivity of the 1L (or ML) flake equals that of the 1L (or ML) pathway of the 1L+ML interface device, allowing us to compare the effective conductivity of the 1L+ML device to that of the 1L and ML devices separately and in sum.

$$\sigma_{eff} = G\frac{L}{W_m + W_1} \tag{3.4}$$

where we define,

$$G = \frac{I_{sd}}{V_{sd}} \tag{3.5}$$

and so and all together,

$$\sigma_{eff} = \frac{I_{sd}}{V_{sd}}\frac{L}{W_m + W_1} \tag{3.6}$$

Where, as before, W_m is the width of the multilayer, W_1 is the width of the monolayer, L is the length of the device, and G is the net conductance of the 1L+ML device. Conductivity of the 1L and ML individual flakes were measured separately and are labeled σ_1 for a monolayer and σ_m for multilayer. If there is no change of the conductivity at the interface,

one should expect a result of,

$$\sigma_m \geq \sigma_{eff} > \sigma_1 \tag{3.7}$$

But in our tests we observe, instead a result that suggests an enhancement along the interface that cannot be explained by the sum of its constituents,

$$\sigma_{eff} > \sigma_m > \sigma_1 \tag{3.8}$$

Further analysis of the behavior of the channel can be done in calculating the effective field-effect mobility of the 1L+ML device and comparing it to similar values of the 1L-only and ML-only devices. To do this, the devices were measured for a series of backgate voltages, allowing for calculation,

$$\mu_{FE} = \frac{1}{C_i}\frac{\partial \sigma}{\partial V_g} \tag{3.9}$$

Where C_i is the capacitance per unit area of the SiO_2 and σ can be substituted with respective values for either the effective, 1L, or ML values for conductivity.

Examples of the results as calculated can be seen in Table 1, and in all cases we see an increased effective field-effect mobility along the interface that cannot be explained by a simple sum of the mobility of each individual channels.

Device #	# of Contacts	Layer #	$\sigma_{\#}$ at $V_G = 40$V ($10^{-6}/\Omega$)	$\mu_{FE-\#}$(cm^2/Vs)
1	4	1L	1.23	4.1
	4	8L	4.53	11.4
	4	1L/8L	7.87	20.2
2	2	1L	1.32	2.8
	2	2L	2.57	11.0
	2	1L/2L	4.41	15.2
3	4	1L	3.38	8.6
	4	2L	5.14	16.1
	4	1L/2L	11.58	31.1

Table 3.1. Table of device results from study of monolayer/multilayer interface with number of layers and contact number mentioned. Adapted with permission from [1]. Copyright 2017 IOP Publishing.

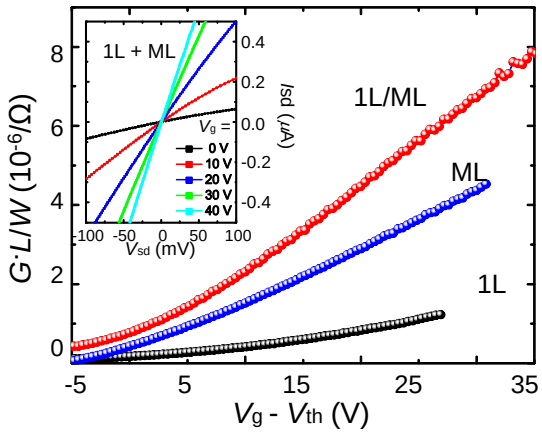

Figure 3.7. Electronic properties of backgated a monolayer/multilayer homojunction device. Effective conductivity is plotted as a function of gate voltage for 1L, ML, and 1L/ML. (Inset) IV characteristics of the 1L/ML device. Adapted with permission from [1]. Copyright 2017 IOP Publishing.

To summarize, our monolayer/multilayer homojunction of MoS_2 revealed an enhancement in photoresponse at the interface via SPM, owing to band bending. Transport measurements parallel to the interface provided further evidence, when compared to standalone monolayer and multilayer devices, that there was an enhanced conductivity along

the interface that could not be explained trivially as the sum of its constituents. These results together underline a new charge state that exists only at the interface.

This work can be seen in our publication: Ying Jia, Teodor K Stanev, Erik J Lenferink and Nathaniel P Stern; Enhanced conductivity along lateral homojunction interfaces of atomically thin semiconductors.*2D Mater.* 4 021012 **2017** [1].

3.2. Gate and Layer Dependence of Stark shift in Multilayer Molybdenum Disulfide

With an ability to control layer numbers as well as apply an external field, there exists an opportunity to study interlayer interactions and how they are affected by the aforementioned controls. Within the limits of field screening by increasing layer numbers, we can probe these interactions and their affects on the exciton.

The Quantum Confined Stark Effect has been a topic of interest in semiconductor devices since the mid-80s. GaAs and other such materials have been used to create quantum wells (or in other cases quantum dots) that have been extensively studied under the influence of external, perpendicular and parallel (to the material plane) fields [111, 112]. And as was discussed in Chapter 2, many of the ideas applied to 2DEG systems can be carried over to TMDs which are like quantum well systems of a finite thickness down to the monolayer scale. Recall the image of Fig.[2.4] where the exciton is confined in the z-axis but free in xy-axis.

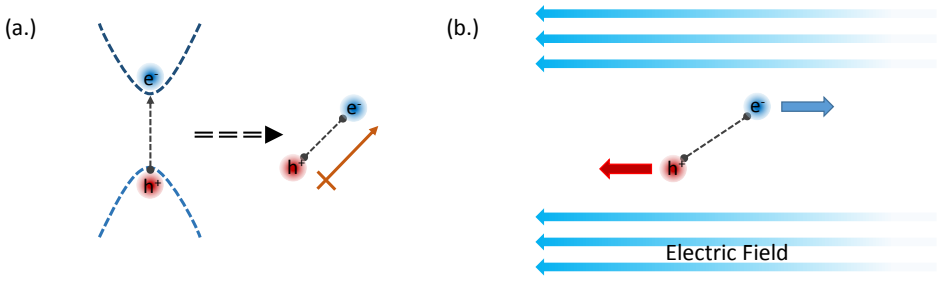

Figure 3.8. (a.) Approximating the exciton as a finite dipole with a moment. (b.) When the dipole experiences a field, the electron and hole will experience an field force in opposite directions, pulling them apart.

To frame our discussion, we can start by considering a very generic picture of the exciton that can be attributed to either a more traditional quantum well or TMDs. As the exciton is an approximation of an electron and proton (hole) pair, we consider the exciton to be a dipole with finite spacing or as picture in Fig. [3.8]. We further attribute to the dipole a polarizability, allowing for an externally applied electric field to manipulate the exciton formation energy. Provided that an exciton has a non-zero polarizability when the field is off (and in an ideal case of no extraneous doping by trapped surface charges or other sources of charge build up), then we can begin to build a picture for the exciton energy under an external electric field. Of course, in MoS_2 and other TMDs this is rarely the case of such a perfect condition and much of the interaction of excitons with external fields is also convoluted with formation or loss of the previously discussed trion species, due to changes in the Fermi level caused by the electric field. But for now we will consider an ideal case. In quantum wells, polarizability under a field can be obtained in the form of,

$$\Delta E = \frac{\mu_{eff} e^2 w^4}{\hbar^2} F^2 = \beta \cdot F^2 \tag{3.10}$$

Here w is the width of the quantum well, β is the exciton polarizability, F is the applied electric field, and the rest are standard constants. μ_{eff} is the reduced effective mass of the electron-hole pair,

$$\frac{1}{\mu_{eff}} = \frac{1}{m_{eff,e}} + \frac{1}{m_{eff,h}} \tag{3.11}$$

And in the case of a dipole in a field, we have that its energy is defined as,

$$E(F) = E_0 + U_p + U_\beta \tag{3.12}$$

Or with terms now added,

$$E(F) = E_0 - p \cdot F - \beta \cdot F^2 \tag{3.13}$$

Where E_0 is the zero-field exciton recombination energy, p is the dipole moment, and, again, β is the polarizability. By this simple expression, we would expect that increasing field strength should shift the exciton energy down (red shift) from the maximum at $F = 0$ due to non-zero dipole moment and polarizability. Emission energy would also be expected to go quadratic with increased field strength given a non-zero polarizability.

In quantum wells, this behavior has been observed and studied extensively with absorption and PL measurements, its dependence of field strength, thickness of the well, composition of the semiconductor structure, etc. We will, here, look at in the case of TMDC semiconductors and, specifically, MoS_2 [113].

3.2.1. Brief Discussion on Inter- and Intra- Interactions

Intralayer interactions we have already discussed are the formation of excitons, both direct and indirect, and trions. The single layer is also held together by intralayer bonds between the M-X atoms which are covalent in nature, though this is less interesting now but will be of importance in Chapter 4. But, very importantly, it should be noted that some of the intralayer interactions are themselves dependent on interlayer effects. For example, the case of monolayer vs. bilayer vs. few layers of MoS_2 highlights this intra-dependence

on interlayer interactions acutely. The intralayer formation of excitons in the monolayer is a direct transition between the K-points in the conduction and valence band, but due to interlayer interaction in the bilayer case the change in band structure leads to the formation of now-preferred indirect transitions from the K-point in the conduction band to the Γ-point in the valence band. This continues to evolve in the trilayer and thicker case where the transition point become the Λ-point in the conduction band and the Γ-point in the valence band. Subsequent layers change the exact energy levels of these transition points.

The first and most obvious sign of interlayer interaction is the very layered nature of these materials. Something is holding them together, that is weak vdW forces between the layers. Another example, is that of the changing band structure of MoS_2 discussed just above, and the stack of two layers results in the formation of the new system of the bilayer which is distinct from the monolayer in several ways: changes to the band structure energy levels, work function, formation of the indirect bandgap, a lack of inversion symmetry, etc. It is also easily observed in the quenched quantum yield of exciton emission with increasing layer number as seen in basic PL measurements, for example. And, as with the previous section on homostructures built from mono-multilayer interfacing, we begin to frame a layered homostructure in ways very analogous to heterostructures!

One way to study interlayer interactions (and a method that has recently become popular both for homo- and hetero- layer configurations, particularly for the formation and study of Moire Excitons [30]) is that of stacking (or folding) and twisting monolayers [92, 97, 98]. For convenience and simplicity, I will focus on the bilayer scenarios but discussion here may be extrapolated to n-layers.

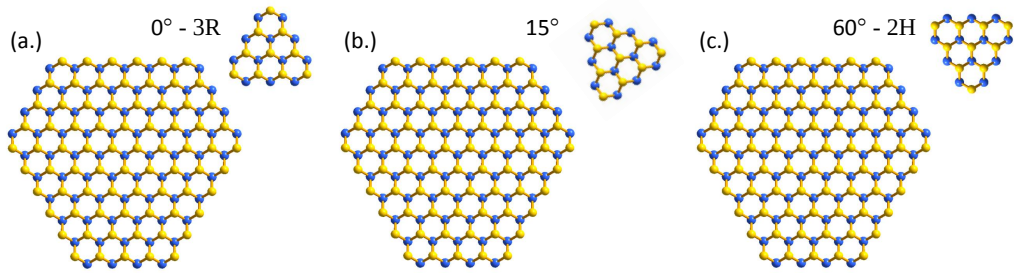

Figure 3.9. An example of rotation between layers when stacking monolyers to create bilayers. (a.) 3R stack when the two layers are the same orientation. (b.) Arbitrary rotation. (c.) 2H stack when the layers are reversed, a natural bilayer stack.

In a homostructure bilayer, twisting like-like layer orientations has been studied for its effects on the indirect exciton formation and valley-polarization. In its naturally occurring order, MoS_2 forms a 2H Z-stacking symmetry in which the orientation of the crystal lattices for each individual layer are exactly reversed every other layer. By twisting this symmetry through a manual stacking method (confirmed either by Second Harmonic Generations (SHG) study of the layer orientation or a more rough crystal approximation based on sharp edges/corners) we can alter the interlayer symmetry and, as has been shown, change the properties of the resulting bilayer. In the extreme case, we may fully rotate the top-most layer of a bilayer such that the molybdenum atoms and the sulfur atoms are aligned and the crystal axis is oriented in the same direction, this is called 3R Z-stacking. 3R-stacked bilayers are still characteristically bilayers in that they have an indirect exciton but there is a preservation of valley physics for such a device that would not exist in the naturally stacked 2H bilayer (nor does it exist, as has been shown, in a

likewise manually stacked 2H bilayer). Examples of these orientation-dependent stacks can be seen in Fig.[3.9].

In a heterostructure, the behavior of the resultant structure is highly material dependent as previously shown in Fig.[2.9], but is not of focus for this section.

3.2.2. Gate and Layer Dependence of Stark shift in Multilayer Molybdenum Disulfide

Individual monolayer properties and exciton formation are governed by intralayer interactions within the 2D system. But as layers are added, new interlayer interactions begin to affect the behavior of the crystal structure, its optical response, and the behavior of the formed excitons. As was previously discussed, MoS_2 has distinct electronic band structure changes with increasing layer number, owing to the strong interlayer interaction. Here we probe the interlayer interactions of MoS_2 by modulating an externally applied perpendicular field through varied layer thicknesses ranging from 3 layers to 11 layers. In doing this, we can compare the effects of increasing layer number on the optical response of MoS_2 in an external field. Depending on an observable increase or decrease in response with layer number to a finite gating, we can begin to draw conclusions on how interlayer interactions change with layer number.

Initial device fabrication for this device follows similar steps to those outlined in the previous section on the monolayer/multilayer heterojunction, and 285 nm SiO_2 for back-gating purposes. Of note, no visco-elastic stamping was used in this process and all devices were made from only tape exfoliated flakes as size was not a major hurdle for device realization but highest possible quality was of interest. Once again, post-exfoliation

transfer processes were avoided to avoid introduction of wrinkles, strain, and granular boundaries that could/would manifest as unwanted states at low temperature and under a depletion gating bias. Cleaning and AFM steps were also carried out in similar fashion to confirm the layer numbers for flakes of interest that were used for the measurement.

Samples were also optically characterized by their PL, at room temperature, in high vacuum, by a 532 nm laser, before fabrication was done to confirm good efficiencies and crystal quality. This extra step was performed in an attempt to avoid low-temperature defect and/or trapped states dominating the signal which can often times be diagnosed ahead of time by lower PL intensities, energy of emission, and wide line widths. There was also an interest in comparing across multiple devices and as such it was beneficial to pick out devices that had similar emission profiles for like-number layers across multiple chips.

Fabrication followed similar steps to those previously outlined with pure gold contacts used to make electrodes on the material, and a completed device can be seen as an example of identification and fabrication in Fig. [3.10].

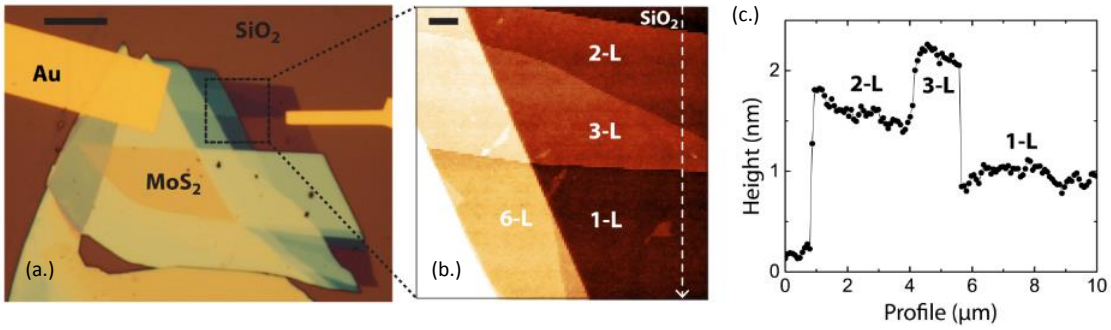

Figure 3.10. Example of a characterized and electrode-contacted device, (a.) an optical image, (b.) AFM 2D map and labeled layers, and (c.) a height slice from AFM scan with 1L, 2L, and 3L identified respective to the layers as labeled in (b.).

Once fabricated, devices were loaded into our cryostat, pumped down to high vacuum, and allowed to back-heat anneal overnight at 350 degrees Celsius to help remove atmospheric absorbents. At the same time, a 1 mW laser was left de-focused to roughly 100 micron spot, over the sample to laser anneal. The sample was then cooled to 10 K while continuously being laser annealed at gradually increasing power with temperature drop: 1 mW near 290 K, 2 mw below 200 K, and 5 mW below 100 K. This process was done to avoid trapped states from forming during the cooling process and the gradual increase in power was done to avoid potential optical laser damage to the devices. Once the sample achieved 10 K a final laser anneal at 5 mW with focused spot was done over the entire area of interest.

Low temperature was used to improve the linewidths of MoS_2 and, more specifically, to counter the quantum yield quenching with increased layer number in MoS_2. At room temperature, emission of higher order layer numbers drops substantially (orders of magnitude difference from monolayer to many (11L) layers) and makes reliable collection difficult.

MoS_2 layers of interest were studied with a 40 uW, 532 nm continuous wave (CW) laser with an applied backgate varied in steps of 5 V (or 10 V) from 0 V to -100 V, -100 V to 100 V, 100 V to 0 V, and repeated once more, for checks in hysteresis and data stability. This was repeated for 1 through 6, and 11 layer thick MoS_2. Monolayer data was used as a point of reference and comparison against literature where gated studied of MoS_2 monolayers are detailed for exction/trion behavior under gating on similar substrates and changing doping [52, 114], to help confirm similar and expected behavior in our device. Multiple similar layer-number configured devices were tested under as near-identical conditions and fabrication as possible.

As mentioned previously, much of the original framework is that of perfect materials with perfect excitons. But that is most certainly not the case in as exfoliated TMDs, where doping, strain, and other effects simply cannot be completely eliminated. In fact, MoS_2 is understood to be inherently n-doped from most commercial sources. This makes the measurement of the Stark Effect not a simple or clear task. We would expect our data to show detuning with a red-shift under an applied external field as can be seen in Fig. [3.11, a (left)], and for the PL intensity to drop with increasing field but this is not the case as seen in Fig. [3.11, a (right)]. Indeed, this suggests an incomplete picture if we want to only consider the Stark effect and other behavior is also contributing to the dynamics we have observed.

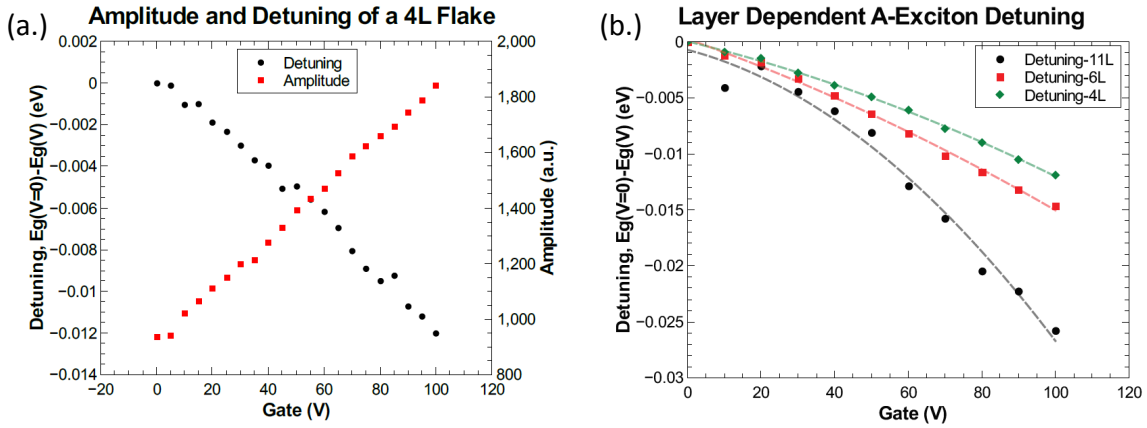

Figure 3.11. (a.) Amplitude and energy detuning of the exciton emission with gate for a 4L example case. (b.) Layer dependence of the detuning can be observed for 4L, 6L, and 11L with increasing layer number resulting in a distinct increase in slope and detuning strength. The quadratic nature of the data becomes clearer with increased layer number as the Stark effect emerges over Stokes.

Due to the presence of both the neutral exciton (X_A) and the charged exciton (trion, X_A^-), and their overlapped emission peaks in MoS_2 [52] we must consider their interaction and response to gating, changes in carrier concentration, and optical stimulation as we continue discussions. Work here will focus on the positive gating.

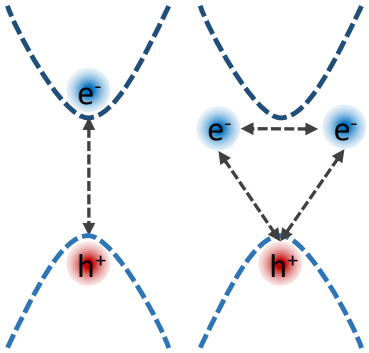

Figure 3.12. Neutral exciton (left) and charged exciton (trion, right) formation. Changes in doping (electron availability) directly affect trion populations. In a depleted conduction band scenario (Fermi level drawn towards the valence band), trions would become rare to nonexistent, and vice-versa when the doping level is conversely increased (Fermi level drawn towards the conduction band).

For both trions and the neutral exciton, it has been shown in monolayer MoS_2 that there is an observable Stokes shift that manifests as a red-shift detuning of the exciton peaks and an increase in quantum yield of the trion in PL measurements [52]. Behavior similar to this can be observed in Fig. [3.11, a], and this behavior is observed in all layers from mono to multilayer in our studies. (For a fully detailed measurement of the Stokes shift, an absorption measurement would have needed to be performed to observe the detuning between the absorption energies and the PL peak emissions for each layer.)

However, this behavior has been shown to be linearly dependent with gating and changes in doping, and as such fails as the only explanation for our observed behavior.

Where the Stark Effect enters consideration and what the Stokes shift fails to easily explain, however, is the layer dependence and quadratic nature of the applied fits as seen in Fig. [3.11, b] of the detuning strength with increasing layer number. The higher the layer count, the more noticeable the quadratic nature of the detuning (and the strength of the detuning becomes) becomes for our studied layer counts from 3L-6L and 11L.

As all flakes of interest in a given measurement session were from the same single crystal source, it is reasonable to believe that their doping level is not widely different per layer (and in fact should be on average the same) and so we would not expect disparate and uneven doping as a potential explanation for the increased effects with layer number. Moreover, the increasing thickness of the layers and increased screening per layer would negatively impact the field strength on the Fermi level and inherent doping strength of the backgate (especially so in the 11L case), as such making it harder still for only the Stokes Shift to explain our observed behavior.

All said, there is no compelling reason to believe that the layer dependent behavior arises from the Stokes Shift while said behavior and the quadratic nature of the curves strongly suggests the Stark Effect. Recent work on dual-gated multilayer samples of MoS_2 have similarly claimed the Stark Effect in conjunction with Stokes contributions [113]. This effect is potentially explained by an interlayer interaction, either from excitons or trions, that increases in field-sensitivity with layer number. Adjacent layers and their carrier wave functions' slight out of plane components could potentially 'see' each other and interact in a direction that is highly sensitive to field effects. In affect, it would be

a picture of displaced dipoles feeling the presence of each other and realigning because of this. This realignment, as it is vertical and in the same orientation as the field, would make exciton 'dipole' picture more responsive to an the effect of an applied field. From this we'd expect an increasing detuning with layer number and more pronounced quadratic, just as our data shows.

Still, it bears repeating that both effects of the Stokes and Stark effect are observed in the data and that they cannot be trivially separated completely without a much more robust measurement that includes absorption spectra for the few layer cases studied. This means that the strength of our Stark effect is at best a maximum for the applied field but is likely much less with some portion of the detuning coming from the Stokes shift.

This work can be seen in our publication: Kuang-Chung Wang, Teodor K. Stanev, Daniel Valencia, James Charles, Alex Henning, Vinod K. Sangwan, Aritra Lahiri, Daniel Mejia, Prasad Sarangapani, Michael Povolotskyi, Aryan Afzalian, Jesse Maassen, Gerhard Klimeck, Mark C. Hersam, Lincoln J. Lauhon, Nathaniel P. Stern, and Tillmann Kubis; Control of interlayer physics in 2H transition metal dichalcogenides. *Journal of Applied Physics* 122, 224302 **(2017)** [115].

CHAPTER 4

Layered Heterostructures for Improving Electrical Contacts

4.1. Introduction

As established at the onset of this Thesis, one of the powerful tools of engineering with layered materials is to build structures out of different layered materials [7, 13, 25, 29, 30, 36, 94–96]. These structures are called heterostructures. Generally, different materials are used to build these structures but can be built even from like-like material combinations so long as the natural order is somehow perturbed. An exampple of this is with twisted monolayers or mono-multilayer junctions that form type-I heterojunctions like the one presented in Chapter 3. These heterostructures often lead to novel emergent properties that are distinct from the constituent parts, one common example is the interlayer exciton [29, 96]. This layer-to-layer interaction leading to an exchange of electrons (still bound to their respective holes if optically stimulated) across the conduction bands of stacked materials in a type-II heterojunction. This results in excitonic recombination across the interace. That is the interlayer exciton as seen in Fig.[2.9] in Chapter 2.

Creating interlayer interactions is not the only way to utilize heterostructures nor does it require vertical stacking to achieve. hBN has emerged as a major component in heterostructures, not for its layer interactions but instead for being an ideal inert substrate for layered materials due to its smooth and pristine surface, layer-matching lattice, and insulating nature [116–118]. It is an excellent replacement for the amorphous

SiO_2, the surface roughness of which as well as penchant to charge-trapping, often results in inhomogenous broadening and excessive doping states in TMDs [119]. Thus, hBN makes for a great substrate to build upon and is itself a layered material that can be manipulated to build heterostructures as both a superstrate and substrate for various benefits [13].

As previously discussed, a major problem in TMD electrical device realization, is the formation of alloyed contact metal-TMD junctions resulting in compromised electrical performance and high contact resistance [5, 89]. A thin hBN superstrate, usually of 1 to 5 layers, can act as a tunneling barrier (ie. creating a tunneling contact) and protect the underlying TMD from alloying damage [9, 28, 84]. Likewise, engineering contacts with graphene or other conductors can also be utilized as a form of heterostructure building where graphene is used as the interfacial contact material that bridges TMD to metal, with graphene forming a direct conductive interface as opposed to a tunneling barrier [26, 90, 91]. My work will focus primarily on hBN as my dabbles in graphene contacts only manifest late into my career but much of the logic applied to hBN and hBN-based devices can be extended in a linear fashion to graphene or other layered materials for contact engineering.

In this chapter, we will look at a case of an in-plane heterostructure enhanced with hBN tunneling contacts.

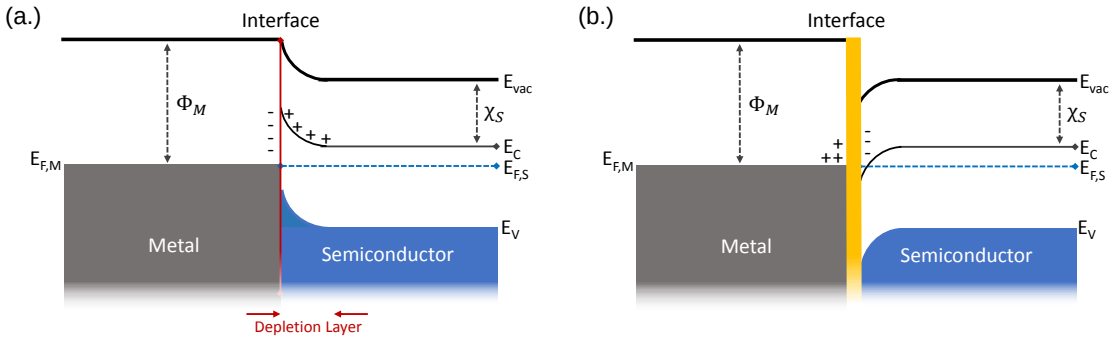

Figure 4.1. (a.) Band bending interaction of a TMD/Metal interface, which results in the formation of Schottky barrier. (b.) Introduction of an hBN intermediate tunneling layer. Ideally this results in the formation of Ohmic contacts. Adapted with permission from [9]. Copyright 2018 American Chemical Society.

4.2. Tunneling Contacts on 2D Heterostructures

The 2D nature that paves the way for novel phenomena and the ability to build elaborate, interacting heterostructures with TMDs also makes them susceptible to negative effects from their environments. This can take many forms, undesired doping from substrate or adsorbates [120–123], oxygen-reactive damage [124], or significant contact resistance due to allowing with contact metals or bad interfacing [5]. Of focus for this section will be the case of the interfacing of contact metals and 2D materials, which often leads to alloying and hybridization of neighboring orbitals. This adverse interaction results in a pinned Fermi level and the formation of significant barriers for electron conduction into the material, ie. Schottky barriers. By utilizing hBN as a tunneling layer on TMDs, it can serve as a protective buffer between metal and 2D material while still permitting electron flow [28]. A rough representation of this de-pinning can be seen in Fig.[4.1], comparing a pinned interface to that of an hBN de-pinned tunneling barrier.

This effort in contact engineering was initially put to use in conjunction with in-plane heterostructures as grown by Akshay Murthy in the Dravid Group as a collaborative project to study the interface characteristics of the in-plane heterojunction that forms between MoS_2 and WS_2 [125, 126]. The crystal growth (done through sequential growth operations, with MoS_2 acting as a nucleation point for WS_2) can be seen in Fig.[4.2a] with the resultant intended device with hBN encapsulation in Fig.[4.2b]. AFM and optical images of as-grown heterojunctions can be seen in Fig.[4.2c,d], slight decay of the lattice can be seen in the gaps at the MoS_2/WS_2 interfaces where voids form at the interface. This is caused for multiple reasons, for one, in transferring the CVD growth from a growth chip to a pre-patterned electrical device, the interface was prone to breaking in the process, requiring many attempts before a successful device could be realized. A second source of degradation was simple ambient exposure, likely due to poor lattice matching at the interface creating points where adsorbates can create points of lattice decay. A third likely source of degradation was the extended exposure to chloroform for sample cleaning post-stamping, chloroform is a highly reactive solvent and may have been a source of damage due to this but it was a mandatory step in the process. Due to this lattice breakdown, devices needed to be made quickly and handled carefully. hBN served a secondary purpose here, acting as a protection layer as well as a tunneling barrier, highlighting its robustness.

Following the necessary procedure for growing the needed in-plane heterojunctions, monolayers of hBN were identified from micromechanical tape exfoliation methods as outlined in the Appendix. An orange filter was utilized to identify the near-invisible monolayers on SiO_2. CVD grown heterojunction flakes were transferred first onto hBN "bottoms" of 5-10 layers thick, and then encapsulated on top with the monolayer hBN. The ideal

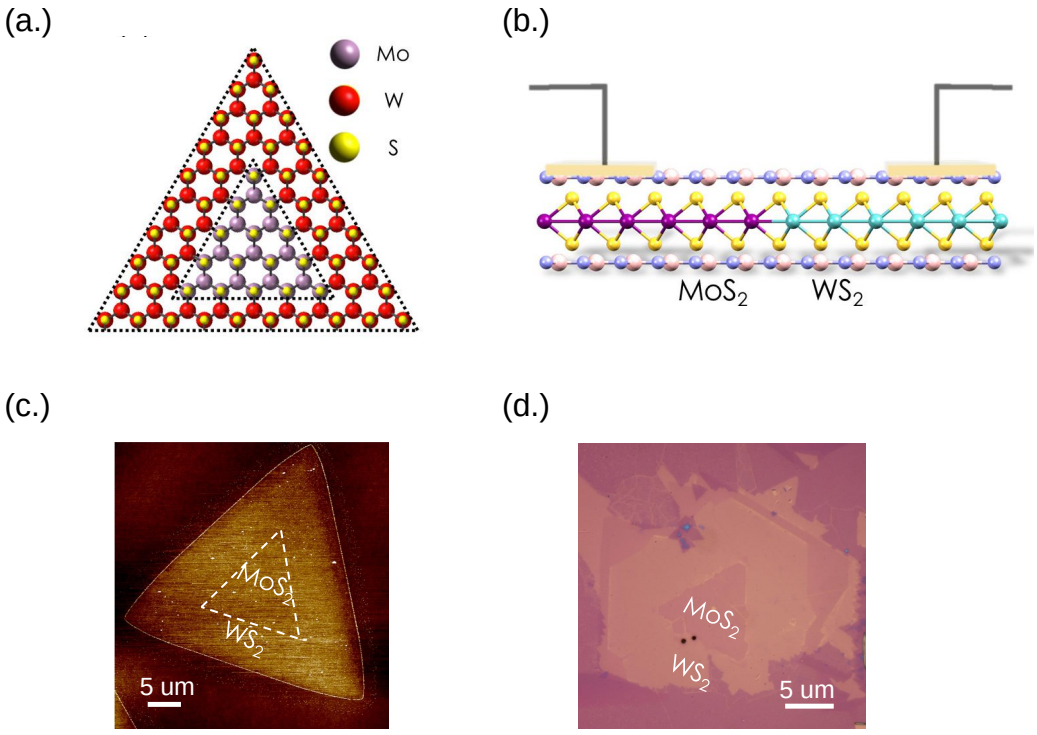

Figure 4.2. (a.) Crystal formation of in-plane heterostructure with MoS_2 acting as the seeding nucleation point for WS_2. (b.) Resulting device goal of an hBN-contact in-plane heterojunction. (c.) AFM of a heterojnction flake. (d.) Optical image of heterojunction, the slight contrast differences make identifying and "targeting" heterojunction interfaces straight forward for transfer processes. Gaps can be seen between the MoS_2 and WS_2 growths at points, this is break down of the lattice at imperfect growth points. Adapted with permission from [9]. Copyright 2018 American Chemical Society.

positioning is centering the monolayer hBN over an interface where the MoS_2/WS_2 meet creating an interface. This can be roughly identified optically under a microscope by slight differences in layer contrasts. Creation of a device is outlined in Fig.[4.3a-b], and the eventual e-beam mask for a device and a final example device of the heterojunction in Fig.[4.3c,d] respectively. Devices were developed with 5 nm Ni/50 nm Au metal contacts to form the electrical devices.

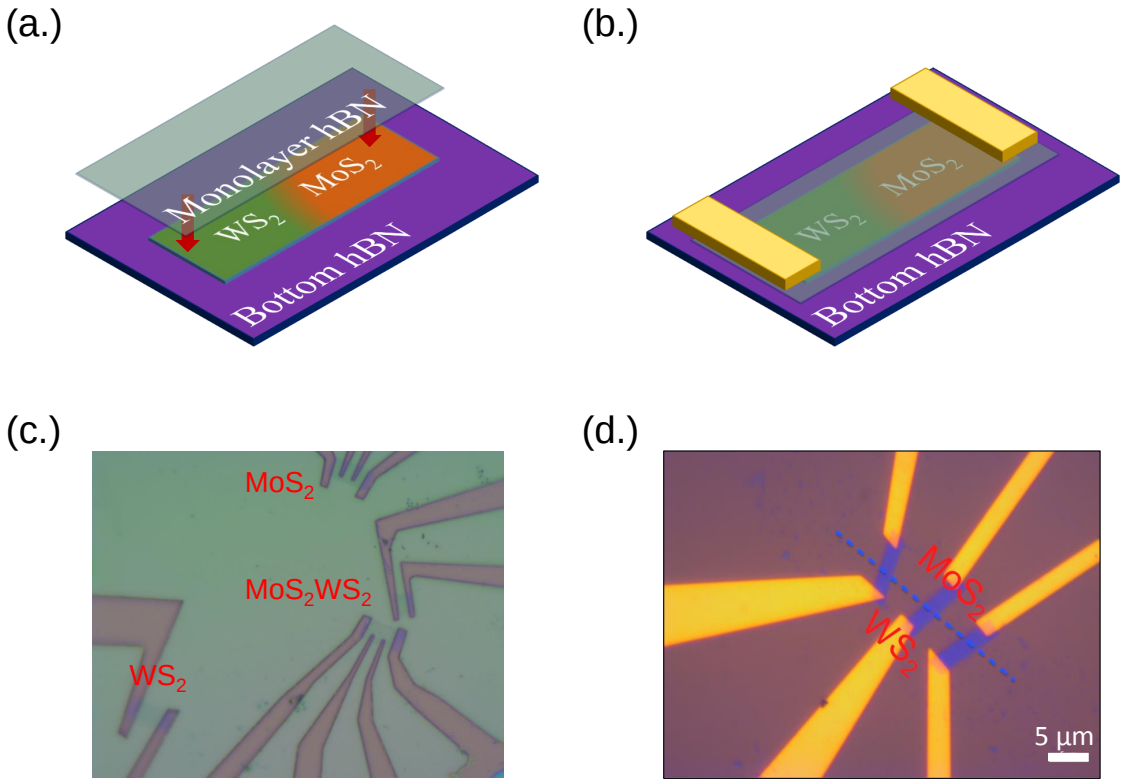

Figure 4.3. Device realization. (a.-b.) Show a simple representation of the assembly of a given heterojunction device, and can be applied to stand-alone materials as well. (c.) E-beam patterned mask of marked layers before deposition. (d.) Example of a finished device heterojunction.

Electrical tests of the individual layers were performed in the Stern group's ARS cryostat system under vacuum after the devices were baked out at 350 degC overnight in high-vacuum. First order of business was to confirm the realization of successful tunneling contacts and this can be seen in Fig.[4.4]. Without the hBN protection layer, MoS_2 and WS_2 show visible non-linear performance, indicative of a Schottky barrier being overcome before linear performance is achieved at which point the barrier is overcome. In the hBN tunneling contact case for WS_2, not only is the performance linear (Ohmic) at all biases, we can also see saturation. MoS_2 performs less ideally, still showing evidence of a small

barrier at small voltages, but otherwise exhibits linear and then saturation as well. This is indicative of high performance devices as previously shown in the literature [127, 128]. In both cases there is also a significant improvement in device performance for applied source-voltage, signifying the significant drop in contact resistance. The origin of the performance jump is attributed to the Fermi level de-pinning granted by the hBN monolayer tunneling barrier as previously described. Moreover, transfer curves of MoS_2 and WS_2 also show significant improvement, notably again is significant device performance improvement in WS_2 and significant reduction in hysteresis [127]. The hBN substrate and superstrate likely both play important roles in this significant drop in hysteresis, the substrate protects the TMD from charge trap states formed on traditional SiO_2 interfaces, as well as potential trapped absorbates under at said interface [27, 120]. The superstrate, as previously noted, helps protect from alloying damage of the TMD layer from metal bombardment as well as protects from absorbates by the layer [5].

With established success of the formation of Ohmic contacts and significantly improved device performance on stand alone individual material devices, next was probing of the heterojunction within the hBN-sandwich heterostructure. These were realized as separate devices but of the same growth as seen in Fig.[4.2]. The material interface is expected to form a Type-II heterojunction with the conduction band minima defined by the WS_2 and the valence band maxima defined by the MoS_2 though the exact configuration is set by the the applied bias which modifies the alignment specifics as seen in Fig.[4.5a] [125, 129, 130]. In theory, this alignment could also prove ideal for formation of in-plane "interlayer" excitons at the interface, though at the time of this project's work and eventual conclusion, we did not have sufficient resolution to see interlayer formation at the interface if it had

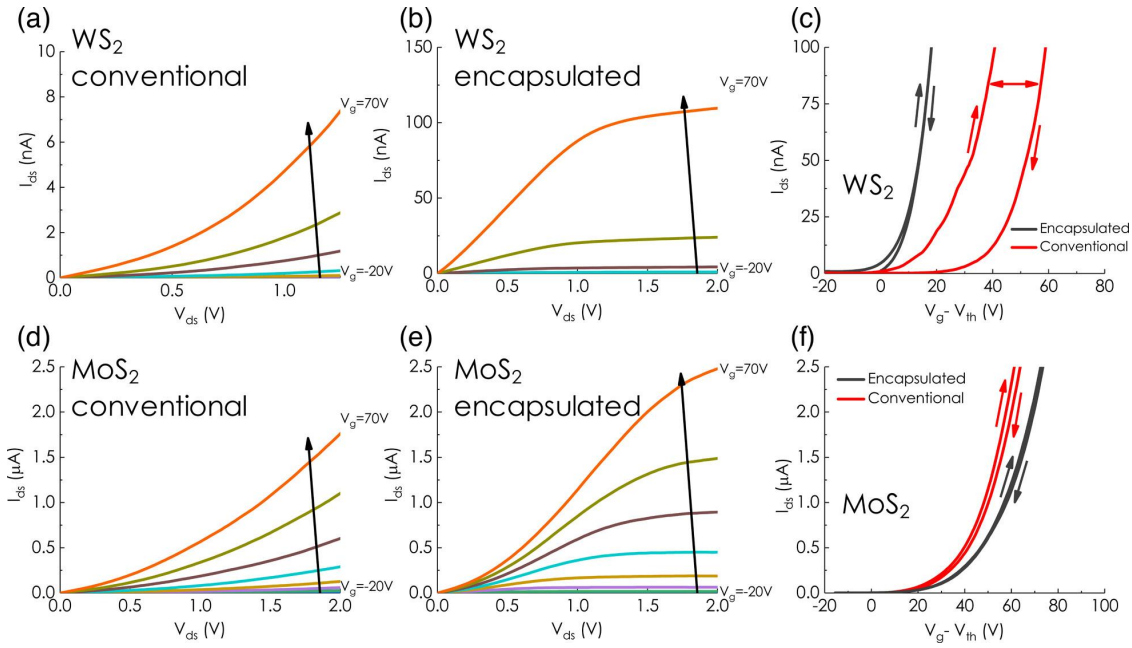

Figure 4.4. Tunneling contact testing. (a and d) Output curves across WS_2 (a) and MoS_2 (d) with varying gate bias using conventional contacts of direct metal deposition. (b and e) Output curves across encapsulated WS_2 (b) and MoS_2 (e) devices with varying gate bias. Current saturation is achieved in the encapsulated devices only. (c) Transfer curves across nonencapsulated WS_2 (red curve) and encapsulated WS_2 (black curve) and (f) transfer curves across nonencapsulated MoS_2 (red curve) and encapsulated MoS_2 (black curve). Vertical arrows indicate the direction that the gate voltage was swept. These sets of curves were conducted with $V_{ds} = 5$ V and display qualitatively similar responses, but the hysteretic component is eliminated in the encapsulated devices. Adapted with permission from [9]. Copyright 2018 American Chemical Society.

formed [131]. Though this could be an interesting point to investigate further in future projects! (Our new Attocube system would be a great system to review this device with in the future, as it is has high resolution, very low temperature scanning capabilities and may be sensitive enough to detect novel physics at this interface.)

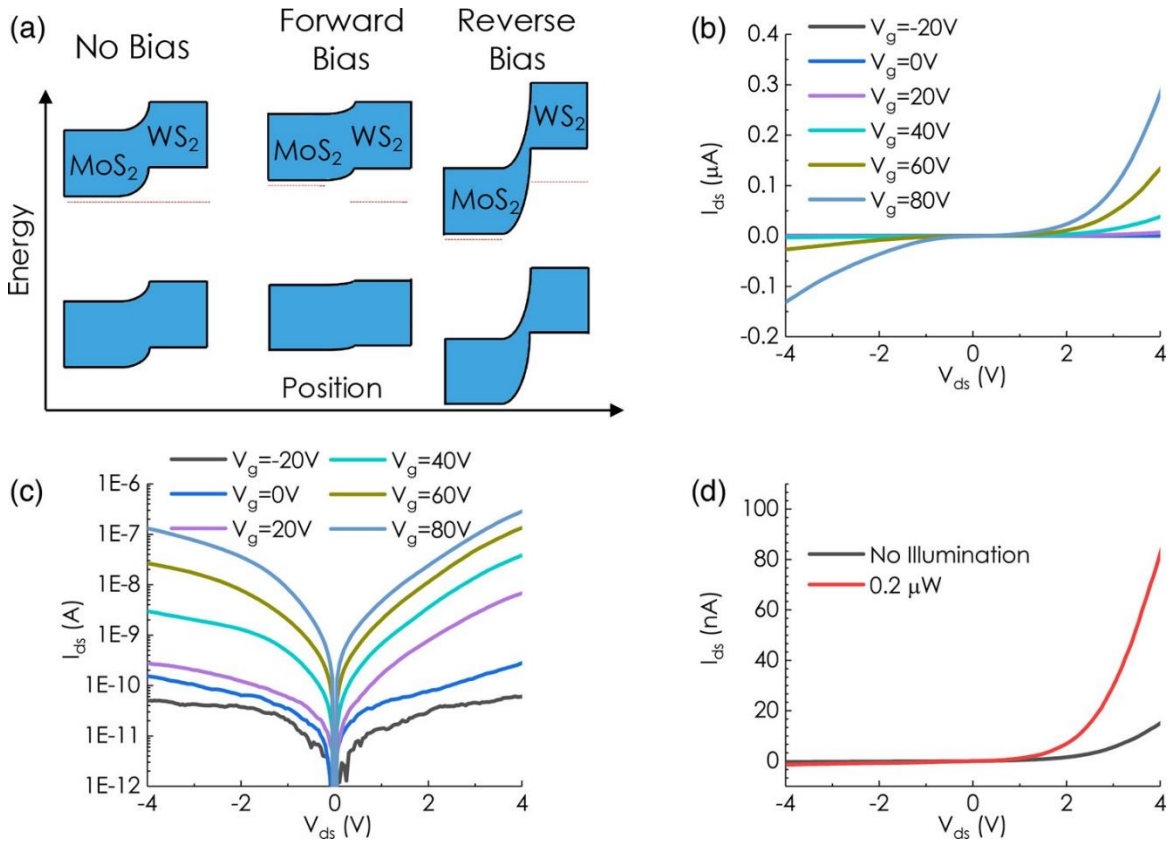

Figure 4.5. Encapsulated junction properties. (a) Schematic depicting the effect of various biasing schemes on band structures of MoS_2/WS_2. (b) Linear and (c) semi-logarithmic output curves across encapsulated junction for various gating conditions at 300 K. (d) Source-drain sweep across junction with and without illumination. Adapted with permission from [9]. Copyright 2018 American Chemical Society.

Testing of the heterojunction with tunneling contacts can be seen in Fig.[4.5b-d]. Notably, source-drain performance was not linear nor did it reach saturation. As has been shown that the individual components are either wholly-linear or near-linear with saturation in either case as seen in Fig.[4.4b,e], the non-linear behavior and lack of saturation is likely an interfacial cause. The rectification ratio is around 15 for Vg = 20 to 50 V and

diminishes to approximately 2 at the highest gate voltage ranges. Compared to nonencapsulated heterojunction devices that used the contacts whose behavior is demonstrated in Fig.[4.4a,d], the on/off ratios are almost 2 orders of magnitude smaller as can be seen.

A possible explanation is a "contact" resistance across the heterojunction as the interface will not be a perfectly matched growth. There will be defects, grain boundaries, and voids along the interface that can all significantly impede conduction and result in rectifying behavior that would not be present in stand-alone layers. Moreover, various theoretical and experimental reports have suggested that there exist large differences in the energy levels of the sulfur vacancy states in MoS_2 vs those in WS_2 [128, 132, 133]. Since these defects induce the aforementioned interfacial states such as voids and grain boundaries, this can lead to Fermi level pinning close to the middle of the midgap of WS_2 vs that of MoS_2 as can be inferred from Fig.[4.5a]. As such, the conventional contact geometry yields larger electron Schottky barriers in the WS_2 and as such create a new Schottky contact. Thus, by removing asymmetric Schottky barriers at the metal/semiconductor interface, we have achieved a more refined and informative electrical characterization of the material and potentially significant insight on the interface interaction. This proves a significant result brought on by tailoring the layered material heterostructure environment.

Furthermore, as we observed significant forward and reverse currents when testing our device structure, it is evident that there is a good natural contact formation at the interface. Otherwise, had the contact between MoS_2 and WS_2 at the heterojunction been poor, there would be a direction sensitive bias on currents. This was not observed, and this conclusion would not have been directly tested in the natural, direct-metal contact high resistance devices. Furthermore, the gate dependence on the rectification behavior of

our devices can be explained by the fact that the gating leads to an increase in available carrier concentrations in both materials. This results in an upward shift in the position of the Fermi level closer to and eventually into the conduction band of both materials. This permits much greater reverse currents through the drift of these electrons by the electric field. A representation of this can be seen in Fig.[4.6b].

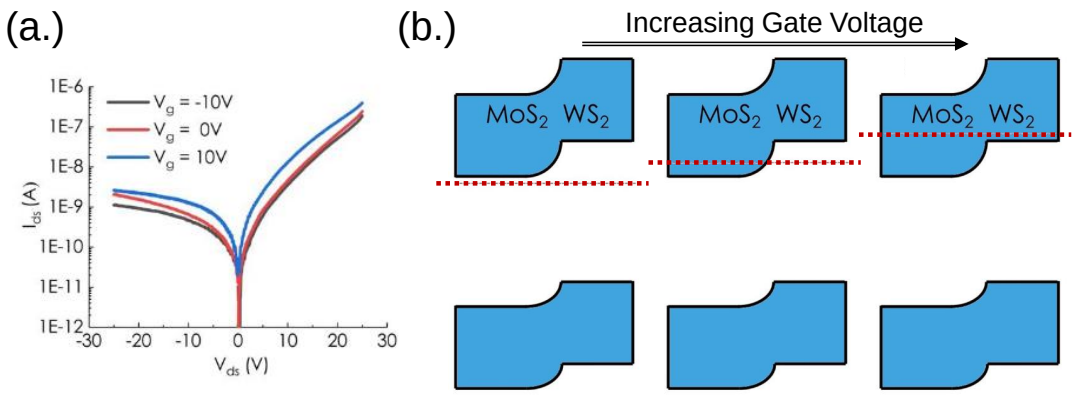

Figure 4.6. (a.) Non-tunneling contact device showing asymmetrical performance. (b.) As the gate bias is increased from left to right, the Fermi levels in both materials are moved closer to and then into the conduction band of one then both materials, resulting in increased conductivity. Adapted with permission from [9]. Copyright 2018 American Chemical Society.

To further study this now "isolated" contact interface of the junction, no longer blanked out by Schottky contacts at the metal/TMD interface, photocurrent mapping was used over the device and, specifically, the interface. This work followed my previous work on [1] and experience.

This approach was done in order to map the photocarriers as functions of source-drain and back-gate voltages. This was again done within the Stern Group ARS system, using a lock-in amplifier and current amplifier. A 532 nm chopped laser was rastered over the device while output current was monitored through a current amp sequenced

to a lock-in amplifier locked to the chopped laser frequency. This also allowed for 2D reflectivity mapping that could correlated specific points of photocurrent to regions of the device, allowing for correlation of response and location. This provides spatially resolved, electronic information at a junction [1, 134]. This mapping can be seen in Fig.[4.7] with contact representation and device location deviced by outlines.

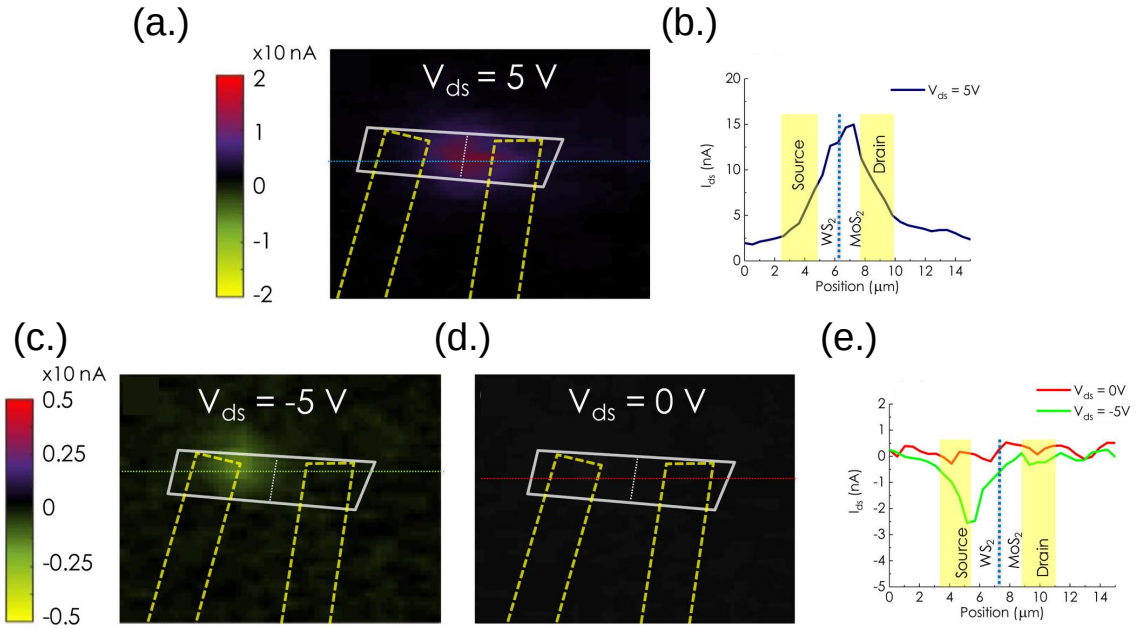

Figure 4.7. Scanning photocurrent mapping analysis. An optical image of the heterojunction device is provided in Figure S3a. Yellow dotted lines indicate contacts; white solid lines indicate material, and white dotted lines indicate junction. (a) Photocurrent generation map in forward bias (Vds = 5 V). (b) Line scan across the horizontal line in forward bias regime. The photocurrent maximum is located near the junction. (c) Photocurrent generation map in reverse bias (Vds = 5 V). The photocurrent in this regime exhibits a polarity opposing that seen in forward bias. (d) Photocurrent generation map with no bias (Vds = 0 V). No photocurrent is present. (e) Line scan across the horizontal dotted lines in reverse bias and no bias regimes. Measurements conducted at 350 K. Note that different photocurrent scale bars are provided for the top row vs the bottom row. Adapted with permission from [9]. Copyright 2018 American Chemical Society.

As previously mentioned and shown in Fig.[4.5a] the valence band maxima lies in MoS_2 and the conduction band minima lies in WS_2, and as such optically generated electrons and holes at the junction can be moved into the WS_2 and MoS_2 regions respectively by the built-in electric field via drift [79, 125, 135]. Photocurrent maps can be seen in Fig.[4.5], and it can be immediately noted that the observed drift is negative (against the field of at the interface) for all cases except for reverse bias. In the case of reversed bias, the drift and electric field align. For the case of forward bias, the photocurrent is seen to oppose the electric field at the junction which suggests a diffusion current. In the final, simplest case, when no bias was applied, no photoresponse is present which is expected as no carriers are being generated. All combined, these factors would suggest that the electric field of the junction due to the inherent mismatch of material electronic band structures is weak. This is likely linked to the junction's nature as an actual n+/n as opposed to a true p/n junction of the mismatched MoS_2/WS_2 in-plane structure. As such, while exciton splitting via the photovoltaic effect at the junction may explain part of the photoresponse, additional effects, such as the photothermoelectric or hot carrier effects likely play a role too [134].

The photothermoelectric effects can be ruled out quickly as a source of photoresponse as there was none at zero bias [134, 136] as the laser rastered over the device and junction. Moreover, the used laser power (20 μW with a spot size of excitation of only a micron) is much too low based on literature expectations [134, 137] to be expected as a relevant contributor. State of the art MoS_2 thermoelectric devices show performances of three orders lower than the observed regime [137]. Instead, it is likely that hot carrier generation, excited by the above resonance laser, is the major contributor in photocurrent

generation [134]. Electrons in the conduction band of MoS_2 are excited beyond the barrier between layers and the junction potential, and diffuse. For WS_2 it is the holes and the valence band. It is expected for conditions similar to those used here [134] for optically induced carrier concentrations to be roughly 10^{13} cm^2. Since these densities are comparable to the 2D Mott density of monolayer MoS_2, it can reasonably be concluded that the photoresponse measured is from free carrier generation, as opposed to photovoltaic splitting of excitons as previously discussed [134, 138].

It was possible to further rule out excitonic response,by utilization of sub-resonance excitation of the MoS_2 or the WS_2 with an excitation wavelength of 710 nm. Any response seen here in photocurrent could not be from excitons as none would be excited with such a lower energy. For context, laser excitation of 532 nm = 2.331 meV, 710 nm = 1.747 meV, MoS_2 Exciton 670 nm = 1.851 meV, WS_2 Exciton 610 nm = 2.033 meV. Despite the laser energy being insufficient to excite excitons in either the MoS_2 or the WS_2, the photocurrent maps show significant photocurrent generation at the junction as seen in Fig.[4.8]. This further supports the notion that hot carriers are involved in this photocurrent generation process at the junction. Once more, electrons (holes) are excited with the conduction (valence) band, along with trap states at the interface, and diffuse across the interface and generate a photoresponse. Further evidence to this conclusion comes from increasing the gate voltage and, by extension, the carrier concentration. Larger hot carrier photocurrents and generation regions manifest as the gate increases, and decrease as the gate decreases. Using this model of hot carrier generation, the observed forward bias photocurrent of 15 nA implies a hot carrier quantum efficiency of 0.05, within the established limits of

hot carrier quantum efficiency (0.1 to 5 percent) in comparable metal/semiconductor junctions.

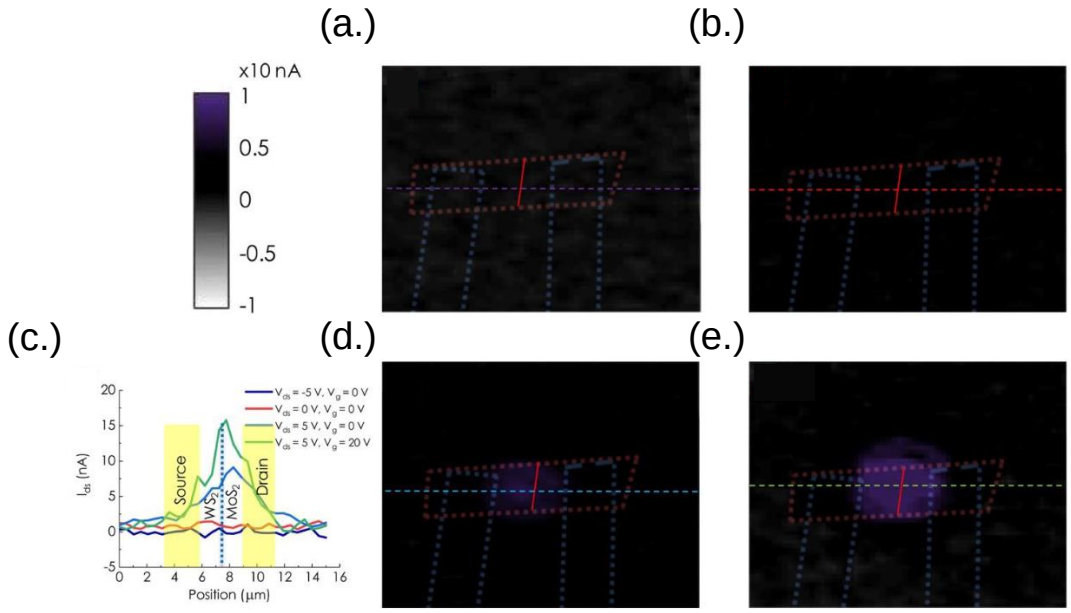

Figure 4.8. Sub-resonance excitation photocurrent, using 710 nm laser source. Blue dashed lines indicate contacts, red dashed lines mark the full device, and the red solid line denotes the junction. (a)V_{ds}= -5 V with V_g = 0 V, (b) V_{ds} = 0 V with V_g = 0 V, (c) Line scan of (a), (b), (d), and (e) through dotted lines. (d) V_{ds} = +5 V with V_g = 0 V, (e) V_{ds} = +5 V with V_g = 20 V. Adapted with permission from [9]. Copyright 2018 American Chemical Society.

It should also be noted that using sub-resonance excitation with 710 nm also removes the high photocurrent signal at the contact on the case of reverse bias. It is likely, given this result, that that signal was due to excitons tunneling from the semiconductor into the metal contacts across the small hBN potential barrier. By removing the excitation energy needed to generate excitons, this process naturally disappears. In previous reports [85, 139, 140], significant photocurrent generation was observed at the MoS_2 contacts with no

applied bias due to carrier separation by electric fields accompanying Schottky barriers at metal/semiconductor interfaces. In the case of this device, as there is minimalized tuneling of carriers without direct pumping of excitons which then tunnel across the barrier, there is no observed photocurrent at zero bias.

Further reading on this result as well simulation supporting information and detailed SI work can be seen in my paper with Akshay Murthy: **Intrinsic Transport in 2D Heterostructures Mediated through h-BN Tunneling Contacts**, Akshay A. Murthy, Teodor K. Stanev, Jeffrey D. Cain, Shiqiang Hao, Trevor LaMountain, Sungkyu Kim, Nathaniel Speiser, Kenji Watanabe, Takashi Taniguchi, Chris Wolverton, Nathaniel P. Stern, and Vinayak P. Dravid, Nano Lett. **2018**, 18, 5, 29902998 [9].

CHAPTER 5

Layered Heterostructures for Enabling Direct Nanopatterning

5.1. Introduction

Engineering of semiconductors in nanoscale structures is a powerful tool for optoelectronic applications. As we've seen, layered heterostructure engineering with 2D semiconductors like TMDs allows highly tunable optoelectronic properties of the composite structure. In a way, this is nanostructure engineering in the z-axis with layers only a nanometer or so apart, but lateral xy-axis nanoscale work using top-down patterning is not as straightforward. Previous work in the Stern Group pushed the limits of standard top-down patterning but those sizes were still relatively large compared to the small Bohr radius of TMDs (dots radii 20 nm or larger), moreover the linewidths at the time were broad and confinement effects vs. trion/exciton population dynamics were not clear [101].

In this chapter, I will present on how both of these problems were tackled to further push patterning capabilities as well as the application of these new techniques to electrical device creation for further quantum effects via constricted conduction channels.

5.2. Direct Nanopatterning via Encapsulation Protection

A variety of methods have been identified for realizing lateral TMD nanostructures, including chemically synthesized dots [141], sonicated and centrifuged flakes [142], helium ion-beam patterning [143, 144], direct femtosecond laser writing [145], laser ablation [146], electron beam (e-beam) lithography [101], and gate-defined quantum dots [147]. Of these

approaches, sonication and chemical dot synthesis have been shown to achieve TMD nanostructures on orders of nanometers with measurable confinement energy shifts. However, such methods are typically entirely random in size, placement, distribution, and yield. This makes them not only unscalable for potential broader applications but it also makes them nigh-impossible to utilize in more complex device realization such as electrical nanostructures.

Top-down methods based on electron-beam lithography are deterministic and reproducible, allowing for potential usage beyond only the realization of small nanodots, but face significant impediments for successful application to TMD-based nanostructures due to induced beam damage that can disrupt or out right destroy layer properties. Top-down techniques that utilize p-resist electron beam writing are a relatively safe approach to deterministic patterning, such as those of the aforementioned previous work in the Stern Group [101], in which the unexposed resist acts as an etch mask on top of the unetched material, and are common for field-effect transistor lithography (like that in the previous section's work). Such patterning can be used to pattern layered materials down to many tens of nanometers in size [101] and does not directly expose the material of interest (the resultant dot areas) to e-beam irradiation. However, the indirect nature of this patterning technique, represented in Fig.[5.1a], however, limits the ultimate nanostructure size to approximately 50 nm [148], much larger than the Bohr radii of TMDs. Conversely, negative resist (n-resist) techniques use direct writing, represented in Fig.[5.1b], and can produce patterns down to only several nanometers [149] but require orders of magnitude larger e-beam dosages (2,000 to 1,000,000 μC/cm^2 for n-resist, compared with 300 to 1,000 μC/cm^2 for p-resist).

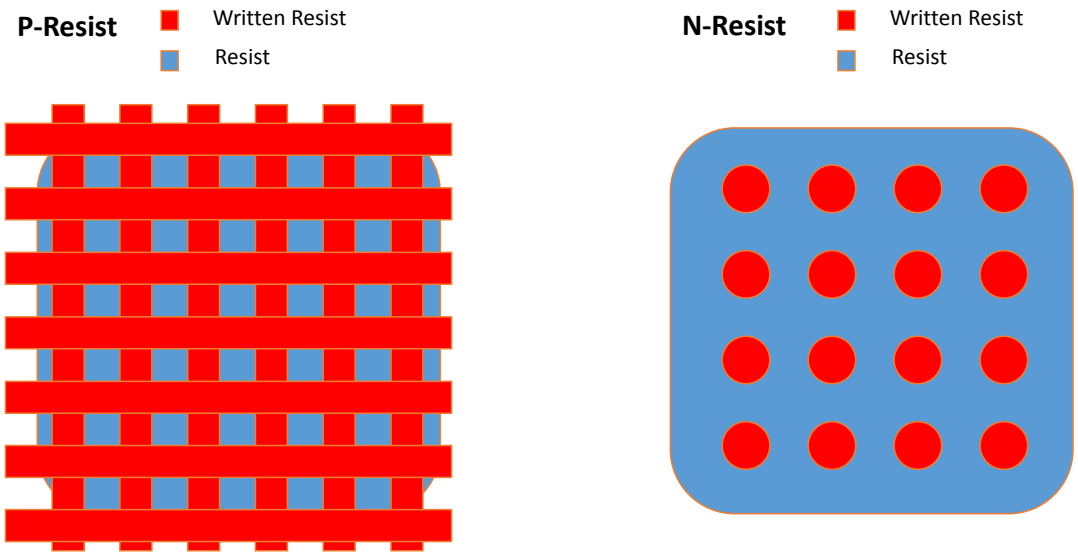

Figure 5.1. Comparison of resist approaches to patterning. P-Resist naturally requires multiple passes, and focuses on writing the area of non interest. Ideal for contact writing and larger structures (>1 μm) due to over-exposure, polymer linking, and over/undercut development if writing smaller sizes. N-Resist writes the structure desired, allowing for patterning as small as the development spot. Direct beam exposure, however, will damage unprotected layers.

Such intense and direct e-beam irradiation has been previously shown to cause destructive damage to the target layered crystal that degrades optoelectronic characteristics [150–153]. As such, n-resist techniques while tantalizing cannot be directly utilized for patterning of TMD layers. However, by developing ways to protect the TMD layers via structural and environment engineering, it is possible to leverage the advantage of n-resist patterning without the damaging consequences.

As we have already seen, hBN is a wonderful material for protecting the properties of more fragile materials. And, even here, it provides a solution to our quandary. We

utilized few layer hBN sandwiching of TMD layers as a means of protecting the TMD layers optoelectronic properties from direct, high dosage e-beam irradiation while applying n-resist patterning techniques.

To study layer damage and nanopatterning, monolayer flakes of $MoSe_2$ and few-layer flakes of high-quality hBN were prepared by micromechanical exfoliation on 285 nm SiO_2 on Si substrates and identified by optical contrast as shown in Fig.[5.2a]. Heterostructure devices of these components were assembled using the PC method as described in the Appendix with the on-stamp stacking approach. Following the creation of samples of standalone $MoSe_2$ and heterostructures of hBN/$MoSe_2$/hBN, samples were annealed in an Ar/H_2 environment to improve surface quality and layer adhesion. Following their preparation, heterostructures were characterized using PL to confirm good PL emission and narrow emission linewidths typical of hBN-encapsulated $MoSe_2$ before patterning [13]. Both the encapsulated and unencapsulated $MoSe_2$ monolayers were patterned with standard electron beam lithography using n-resist into squares with edge size 3 μm as seen in Fig.[5.2e,f]. The writing was performed using 100 keV e-beam lithography system with 10 nm hydrogen silsesquioxane (HSQ) as the n-resist with dosages varying from 5,000 $\mu C/cm^2$ to 50,000 $\mu C/cm^2$ to test layer damage thresholds.

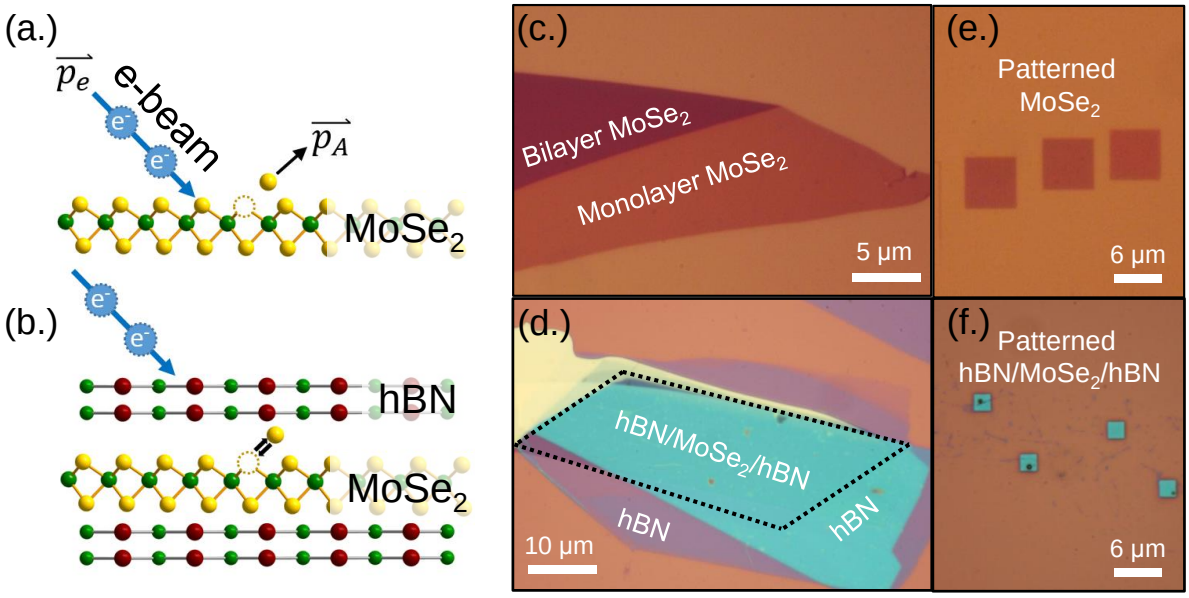

Figure 5.2. (a.) Cartoon of bare $MoSe_2$ being damaged by direct e-beam exposure. Atoms are displaced and the lattice distorted. (b.) Encapsulating hBN could protect the TMD layer from direct exposure, preventing the displacement of atoms and distortion of the lattice. (c.) Exfoliated $MoSe_2$ monolayer and adjacent bilayer. (d.) hBN encapsulated $MoSe_2$ layer achieved by visco-elastic stamping. Black lines outline the $MoSe_2$ under the hBN (teal). A bottom hBN layer (purple) can also be seen. (e.) Directly patterned $MoSe_2$ squares from the layer seen in (c). (f.) Directly patterned $MoSe_2$ heterostructure squares from the structure seen in (d).

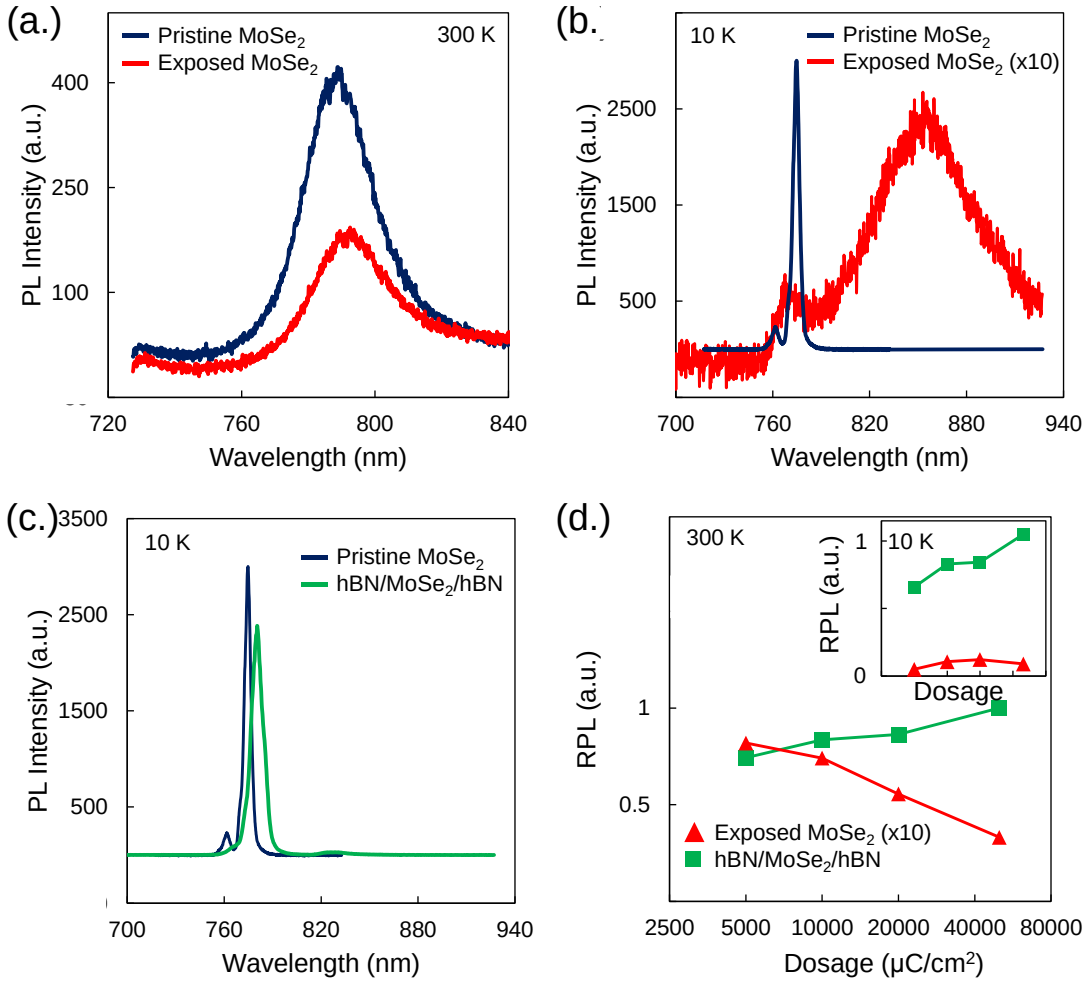

Figure 5.3. Comparison of PL from e-beam exposed, unencapsulated $MoSe_2$ (exposed) and pristine $MoSe_2$ layer (pristine) at (a.) T = 300 K and (b.) T = 10 K. At 300 K, e-beam exposure causes a 50 percent drop in PL intensity. At 10K, exposure quenches exciton PL by two orders of magnitude and induces a prominent broad defect emission. (c.) Comparison of PL from pristine $MoSe_2$ and exposed encapsulated hBN/$MoSe_2$/hBN. The encapsulated layer preserves excitonic emission without prominent defect emission. (d.) Relative PL (RPL), defined as the ratio of the integrated intensity of exposed layers with a given dosage to nearby unexposed layers, for exposed bare $MoSe_2$ and hBN/$MoSe_2$/hBN showing the impact of e-beam dosage for direct writing. Inset is 10 K, outset is 300 K; dosage axes are the same. The increased slope for hBN/$MoSe_2$/hBN is attributed to increasing trion emission likely due to charging induced by the intense beam exposure, a behavior very similar to n-type doping.

PL measurements were performed at temperatures of 10 K and 300 K for patterned encapsulated (hBN/$MoSe_2$/hBN), patterned unencapsulated, and pristine unprocessed $MoSe_2$, with results shown in Fig.[5.3]. Room temperature PL from unencapsulated monolayers shows a reduction in intensity compared to pristine unprocessed layers, while notable this is not yet a definitive result showing layer damage or otherwise as doping could potential explain minor changes in emissivity of layers [72, 114]. However, at low temperature, where emission from the exciton and trion in $MoSe_2$ correspond to distinct peaks as shown in Fig.[5.3b], the evidence of damage is no longer ambiguous as the PL intensity in the unencapsulated layer is quenched by two orders of magnitude and a broad emission emerges across the 800-900 nm spectrum [154]. This broad defect emission is orders of magnitude brighter than that observed for unexposed $MoSe_2$, and it is typically attributed to significant damage to the $MoSe_2$ crystal structure from the high dose direct e-beam exposure [153]. In contrast, the encapsulated structure of hBN/$MoSe_2$/hBN in Fig.[5.3c] shows no significant defect emission and a strong, narrow exciton PL peak even after direct e-beam writing. There is a notable increase in trions [153, 154] which is attributed to the high electron exposure which potentially charges the hBN or dopes the material directly which has been shown previously in graphene and 2D materials [155–157].

To further quantify the damage from the direct beam exposure, ratio of PL between exposed and unexposed regions was characterized by varying the dosage on multiple patterned squares. Unsurprisingly, increasing dosage rapidly degrades the unencapsulated layer, with 20,000 $\mu C/cm^2$ inducing a roughly 50 percent quenching of the PL in the unencapsulated layer at room temperature, further removing any possible doping ambiguity

on the quenching effect observed even at higher temperatures. At low temperature, because the damage is so significantly apparent even at low dosages, the damage vs. dosage is effectively flat at orders of magnitude because the layer is compromised even at small dosage exposure. Further visualizations of e-beam induced damage using 2D PL mapping before and after direct e-beam exposure are in Fig.[5.4]. The region marked off in a black outline goes dark after exposure, signifying the significant damage experienced by a monolayer under direct beam exposure. Thus it is evident that combining hBN encapsulation with high-dose direct e-beam writing allows for the potential for high-resolution top-down patterning of monolayer TMD nanostructures without significantly compromising optical quality.

A possible explanation for this conferred protection is that encapsulation could increase the threshold energy for chalcogenide atoms to escape the TMD monolayer, this prevention of atom knock-off was shown in Fig.[5.2a,b] [150]. In the unencapsulated material, a chalcogenide atom only needs to acquire enough energy to break the TMD covalent bond to escape, which can be readily provided by a 100 keV e-beam. The vacant atomic cite is then either filled by an adsorbate or the lattice deforms [152]. However, with hBN encapsulation, displaced atoms must also diffuse past the hBN layer or break the hBN covalent bonds to escape. The higher threshold energy prevents this from occurring, evidenced here by the preserved excitonic features in PL and the absence of strong defect emission at low temperature. The small reduction in PL intensity with hBN encapsulation and slight trion enhancement suggests that this protection is not perfect or that the electron bombardment can still cause charge doping [158].

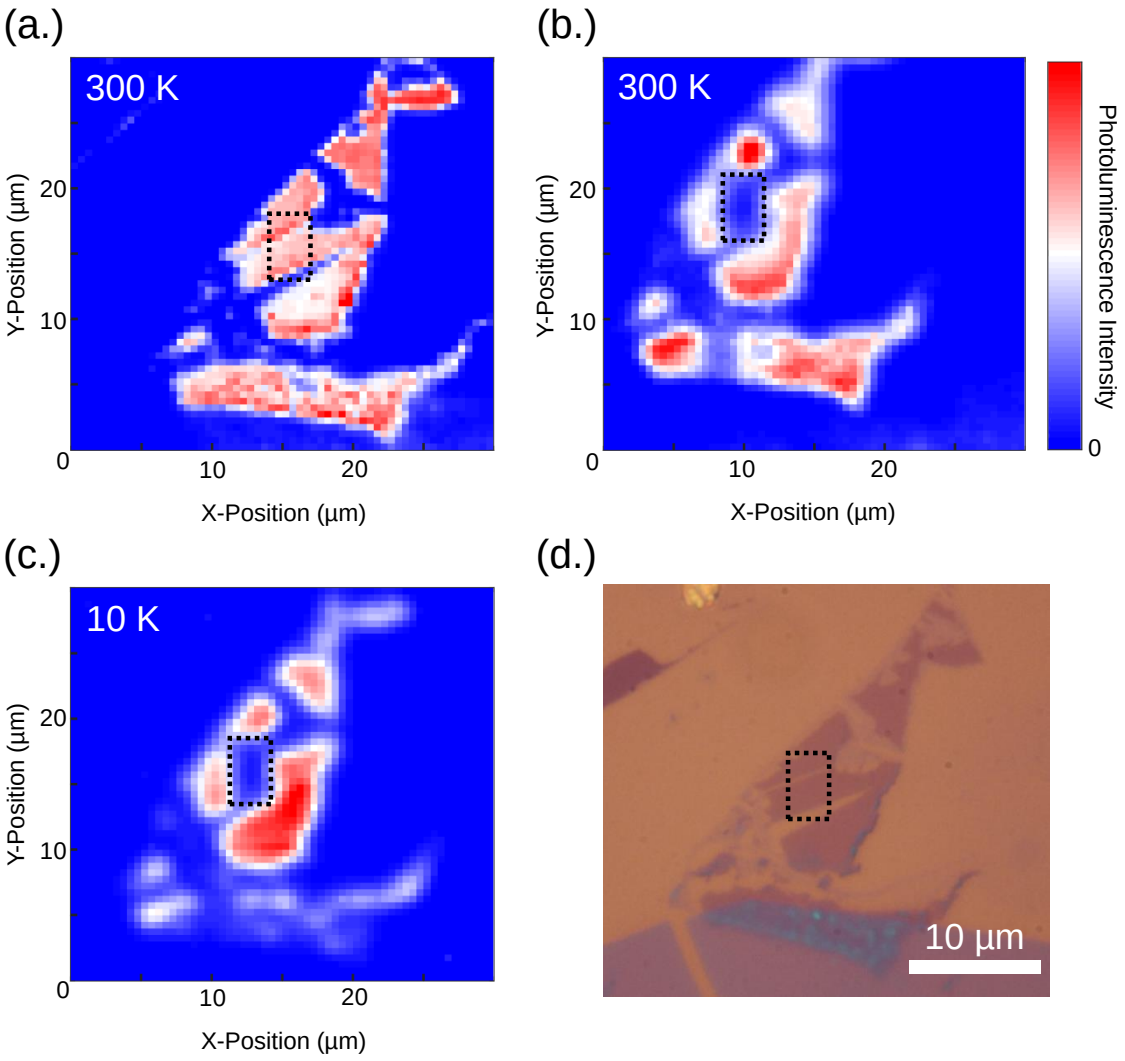

Figure 5.4. Bare-monolayer exposed (black dashed squares in (a-c) squares) to direct e-beam writing with dosage of 50,000 C/cm2. (a) Monolayer 2D PL map at 300 K before exposure. Dotted square indicates region that will be targeted for writing. (b) 2D PL map at 300 K after exposure, the indicated region has gone dark due to layer damage. (c) 2D PL map at 10 K after exposure, the target region remains dark. (d) Optical image of the layer, damage is not visible optically. Black outline is included in (d) to offer a reference to the written area and (a-c).

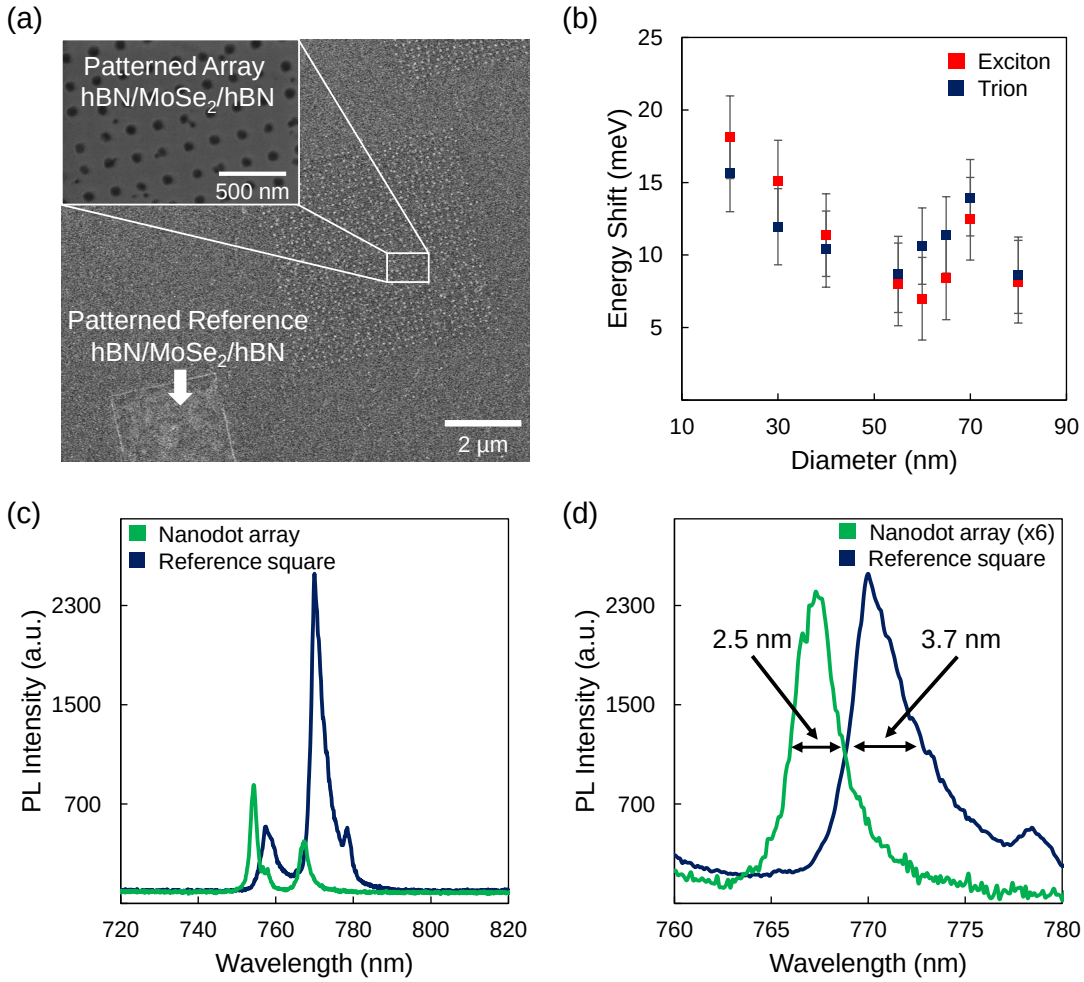

Figure 5.5. (a) Patterned array of $MoSe_2$ nanodots with diameter of 40 nanometers. A reference square of un-patterned hBN/$MoSe_2$/hBN is visible in the bottom left. (b) Average exciton and trion energy shift for different nanodot diameters, the shift is measured relative to an exposed reference square to rule out potential e-beam contributions. (c) Plot of PL of patterned dots of $MoSe_2$2 with a diameter of 40 nm and patterned referenced square of $MoSe_2$. (d) Zoom in on the trion photoluminescence of the patterned array of dots emitter (40 nm diameter, array in SEM image Figure 3a) to the reference square, showing an energy shift of 6 meV and a linewidth reduction.

With the layer protection established via hBN and enabling for use of more aggressive but finer n-resist paterning techniques, work was done to follow up the Stern Group's previous efforts in nanodot patterning and confinement [101]. We utilized the same writing techniques as in the previous section and studied dots of variable size arrays. Arrays of hBN/$MoSe_2$/hBN nanodots with diameters ranging from 10 nm to 80 nm were fabricated along with 3 μm squares for reference. The reference squares were exposed to the same e-beam dosage as the nanodots, allowing isolation of beam-induced effects from size and edge effects. Sub-10 nm nanodots with diameters down to 5 nm were also fabricated, but in these small nanodots, the n-resist typically loses adhesion to the layer surface, resulting in nanodot aggregation or complete pattern loss as seen in Fig.[5.6]. SEM images suggest that after etching, small diameter nanodots were still successfully created, but their position and separation are no longer controllable and repeatable. Further systematic study of resist and process steps could improve the surface adhesion and allow controlled patterning of sub-10 nm nanostructures without inducing layer damage, but this process development has not yet been done but is certainly a worthwhile project to tackle in the future as the Stern Group's ability to pattern nanoscale devices evolves further!

Following fabrication, PL was measured from the arrays in vacuum at temperatures of both 10 K and 300 K. Room temperature PL was utilized mainly as a check on nanodot integrity after writing and etching, a lack of PL at room temperature would strong indicate damage due to etching or other problems. The emission at room temperature is too broad to be of significant use for small energy shifts due to confinement or edge effects. As noted, this was a previous short coming that needed to be overcome and as such

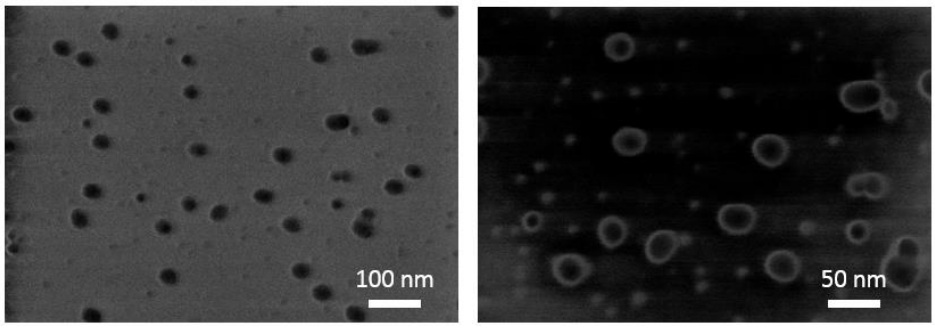

Figure 5.6. Two SEM images of arrays where migration could be observed clearly in the dots due to loss of surface adhesion during development. (Left) Patterns of 20 nm sizes could still show issues of surface adhesion, but did not show mass aggregation and thus reliable for measurement. (Right) Patterned nanodots down to diameter 10 nm or smaller resulted in aggregation and clumping.

this room temperature PL is merely a tool for confirming functionality but not ideal for further confinement analysis. At low temperature, as previously shown, $MoSe_2$ has distinct exciton and trion peaks and that is where the interests lie! Indeed, $MoSe_2$ can approach single-digit meV scales at low temperatures, distinctly separating out the exciton and trion species and enhancing sensitivity to small energy shifts [13]. PL results with narrow linewidths and clearly defined excitons (<760 nm) and trions (<780) at 10 K can be seen in Fig.[5.5c,d].

Naively, the expectation would be that confinement takes the form of particle-in-a-box potential. For a 2D quantum dot, this takes the form:

$$E_{QD} = E_0 + \frac{\hbar^2 \rho_0^2}{2M_{eff}^* R_{QD}} \tag{5.1}$$

where E_{QD} is the expected confinement energy for a given size, E_0 is unconfined energy of the exciton, R_{QD} is the effective nanodot radius, $\rho_0 = 2.4048$ is the first root of the zero-order Bessel function, and M^*_{eff} is the effective mass of the exciton [101]. Measuring our dots, we see that for nanodots with diameters from 80 nm down to 20 nm there is an apparent shift toward higher energy for the individually resolved excitons and trions with notably reduced linewidths. This, at least, removes ambiguity between exciton and trion population changes when peaks are convoluted [101]. Moreover, as we compare patterned dots vs. a similarly patterned but unetched, no-confinement reference square we do not expect the e-beam or lattice damage to play a role in the results that are observed. This shifting can be seen in Fig.[5.5b], and a more specific view of the shift in a 40 nm dot pattern array is shown in Fig.[5.5c,d]. Evidently, at least at 50 - 80 nm sizes, there's no obvious size-dependent shifting which immediately causes problems for simple particle in a box analysis as even at these length scales we would have expected noticeable shifting. There is however a significant background shift that is unchanging, and this shift is unlikely to be related to exciton confinement as it can be observed that both the exciton's normal emission and a shifted emission are observable for larger sizes as seen in Fig.[5.7]. One possible cause for this double emission and shift is an edge effect [159, 160]. Unlike the reference square which shows no such behavior, the reduced size of the nanodots significantly modifies the ratio of crystal edge-to-surface area. Contributions from edge states or charging created through the etching process may be non-negligible in nanodot PL, and could be sources of doping that cause the background shift seen in all patterns.

At smaller dot sizes, under 50 nm, there is a small, linear shift to higher energy with smaller dots. As our radii are still far larger than the 1 nm Bohr Radius of the exciton,

these nanodots would be in a weak confinement regime. The origin of the smaller size-dependent energy blue shift is not conclusively identified by these experiments done at the time. All that said, utilizing hBN and layer engineering with heterostructures allowed for the creation of even smaller dots than before and the observation of new behavior in PL and energy shifts not previously reported!

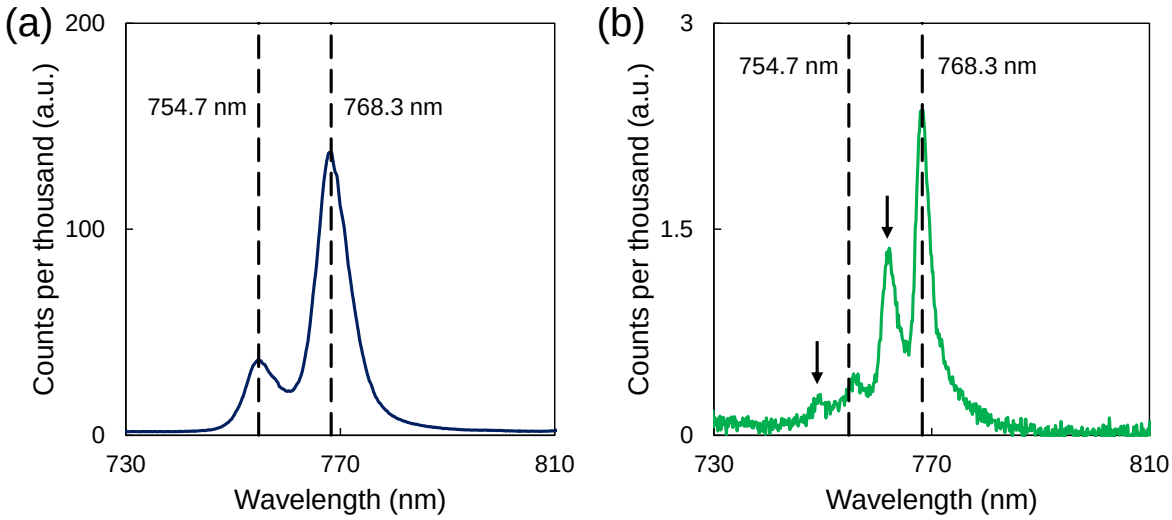

Figure 5.7. Comparison of photoluminescence at 10 K of a patterned reference square (a) and a nearby 70 nm nanodot array (b). The higher wavelength (lower energy) peaks of both the exciton (755 nm) and trion (768 nm) closely match the reference square PL as shown by guiding dashed black lines. The lower wavelength peaks (higher energy) are likely due to a modified edge contribution on PL introduced by the nanodot patterning. This dual peak feature disappears as the nanodot size shrinks and the edge becomes the dominant emission feature, showing only the lower wavelength (higher energy) peaks in the patterned arrays.

Following the work of successfully patterning layers into nanodots for optical study, the utility of the protective heterostructure approach was tested for its potential in quantum electrical device creation. Much as with the case for optical performance, direct e-beam

writing of a 2D TMD layer would normally degrade electronic performance of TMDs [161–163], preventing direct writing of nano-scale electronic devices. Thus the next step was to test the potential to realize nano-scale electronic devices and quantum conductance channels. Quantized conduction in TMD devices has previously been achieved using optical doping [164] and gate-defined constrictions [165] but not in selectively and directly patterned nanostructures which opens new device potential in the future with possible quantum wires [55, 166], for example. For this section, work was done utilizing MoS_2 instead of $MoSe_2$ due to the depth of literature for MoS_2 FETs reporting high mobilities [51, 83–85], to demonstrate the creation of quantized conductive channels. We also utilize the tunneling contact work presented in the previous section for the realization of high quality contacts.

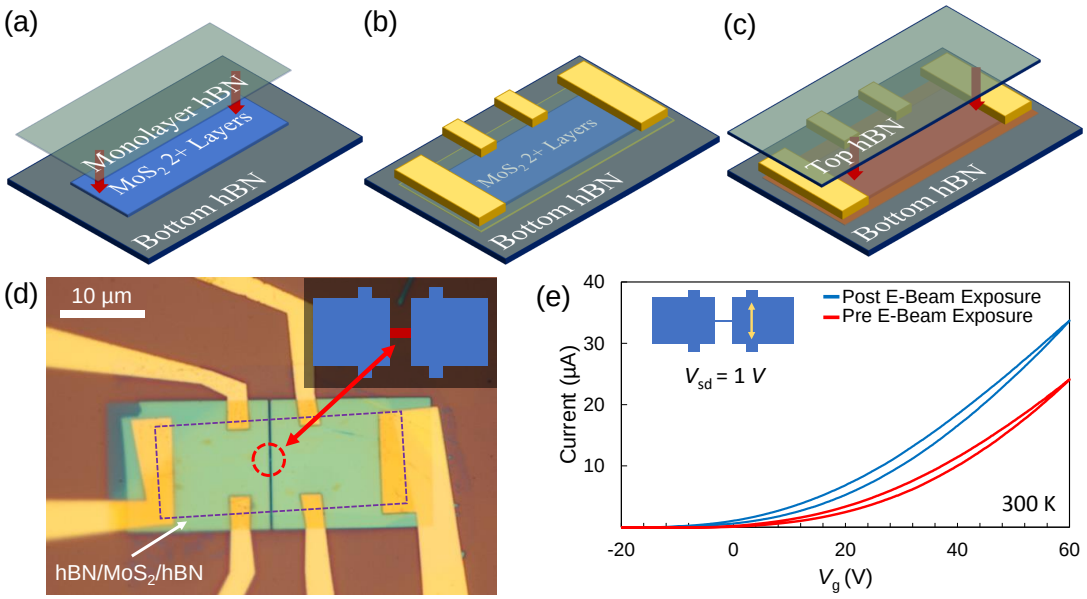

Figure 5.8. (a-c) Preparation of MoS_2 layer for electrical device. (a) Few-layer MoS_2 is transferred onto an hBN bottom layer, followed by a multilayer of hBN on top to serve as a tunneling layer. (b) Contacts are deposited on top of the monolayer of hBN. (c) A final multilayer of hBN is transferred on top of the completed structure for protection. (d) An image of a completed electrical device, represented schematically in the inset. The patterned conduction channel is highlighted red. A purple dotted line outlines the monolayer under the hBN. (e) Current vs. gate voltage (VG) performance before (red) and after (blue) e-beam exposure for hBN/MoS_2/hBN heterostructure for a two-terminal non-channel test as the inset shows. The higher current response suggests an increased n-type doping of the material after exposure, but there is no reduction in electrical performance that would indicate layer damage from exposure.

For this experiment, samples were made of hBN/2L-4L MoS_2/1L hBN heterostructures patterned with e-beam lithography. The single layer of hBN on top serves as a tunnel barrier for Ohmic electrical contacts as established in the previous section on contact engineering while also protecting the TMD layer from external adsorbates and perturbations. Few-layer MoS_2 was used rather than single layers to more repeatedly achieve

high mobilities as has been shown in literature [51]. A second flake of few-layer hBN was transferred on top of the fully fabricated contacts and un-patterned MoS_2 to ensure sufficient protection for the nano-channel region, we did not test if a single layer of hBN was sufficient protection. The conducting channel device was then patterned with direct n-resist lithography using the same procedures from $MoSe_2$. The stacking and contact process and final device can be seen in Fig.[5.8].

A control sample of hBN encapsulated MoS_2 heterostructure with no direct patterning was electrically tested before and after direct e-beam exposure (rastering over the entire device area, exposing everything equally as best as possible) to test any potential for obvious electrical damage. Two-terminal conductivity showed no appreciable electrical-impacting damage caused by direct exposure, as the overall field-effect mobilities at room temperature (45 cm^2/Vs before to 48 cm^2/Vs after) and low temperature (43 cm^2/Vs to 50 cm^2/Vs) were largely unaffected. The turn-on threshold gate voltage of the encapsulated device was larger after writing, which follows from the previous results in optical behavior showing increases in trions. It is understood that electron bombardment is a source of doping and this result is in agreement [150, 156, 157].

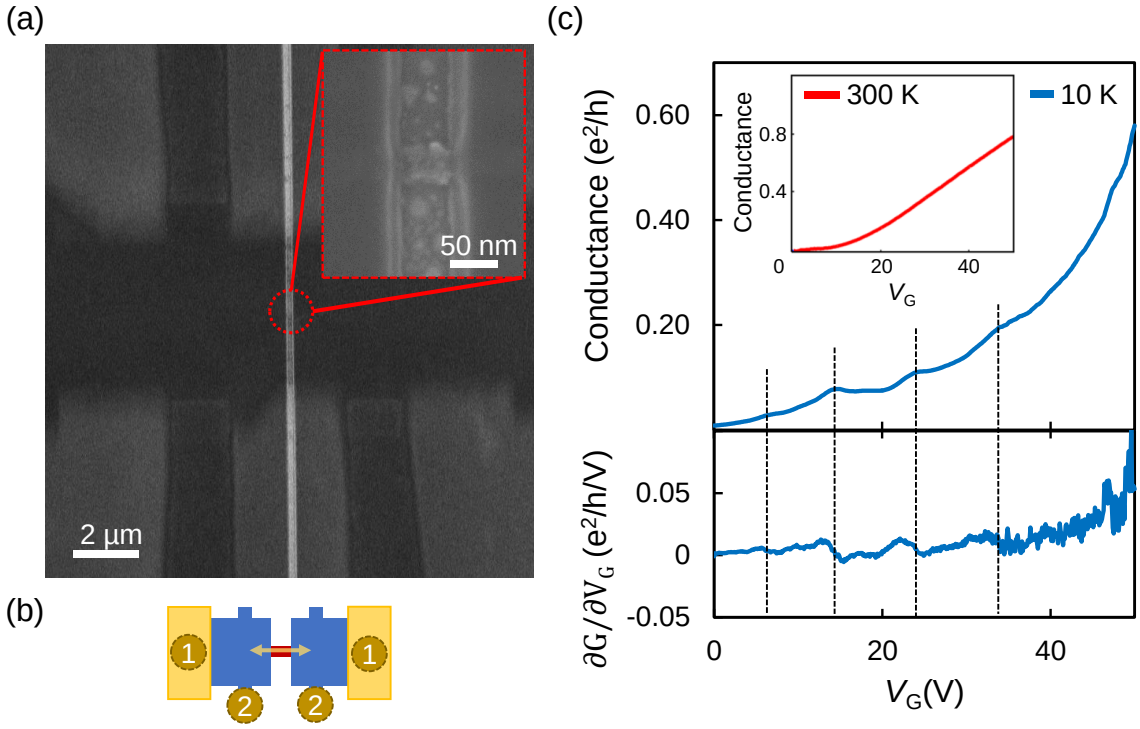

Figure 5.9. (a) SEM image of patterned device with narrow channel at center. (Inset) Zoom in on channel. (b) Simple cartoon representation of device measurement from (a) in a four terminal arrangement. Contacts 1 are used as source and drain for current, and Contacts 2 are used for sensing in a four-terminal experiment. (c) Measured conductance as a function of gate voltage across a 50-nm wide channel etched into an hBN/$_2$/hBN heterostructure as seen in the inset of (a). Inset is 300 K, outset is 10 K. Step-like behavior can be observed at 10 K but no such features can be seen at 300 K. (Bottom) Derivative of the conductance with respect to the applied gate voltage. Peaks and dips correspond to the step-like transitions. Black dashed lines serve to guide the eye.

In a subsequent full device, conduction channels of 50 nm width and 100 nm length were fabricated as seen in a representative SEM image of a channel in Fig.[5.9a]. Four-terminal conductance measurements were performed across the channel using the source and drain leads and their corresponding adjacent sense-leads on either side of the channel.

At cryogenic temperatures (10 K), the channel shows discrete steps in the conductance at regular gate voltage intervals (V_G 6.7 V, 14.5 V, 24.9 V, 34.5 V), a hallmark of quantized conduction.

These conductance plateaus in Fig.[5.9c] are however not integer values, less than the ideal integer steps of the conductance quantum e^2/h. The origin of this can be understood due to the limitations of the material and device geometry. In an ideal channel conductance experiment, only the narrow channel region would be measured. In such a scenario, it would be expected that the device will exhibit expected integer steps for conductance as conducting channel states are filled. However, the FET fabrication was limited by the required contact spacing using standard need for PMMA/MMA e-beam lithography and thermal metal deposition. Therefore, in practice, the FET devices had large regions of unexposed MoS_2 between channel and contacts. Experiments do not directly measure the channel conductance, but rather the conductance of the entire device. This reduces the conductance plateaus to sub-integer values.

A simple model can intuitively explain this by considering the device as consisting of three conducting components in series represented by the regions 1, 2 and C as shown in Fig.[5.10]. Regions 1 and 2 are the unpatterned encapsulated MoS_2 material. Region C at the center is the patterned channel. G_i is the conductance of each part (1, 2, and C) measured in the experimental geometry. Because 1 and 2 are the same material and not treated differently in processing, it is assumed that they have similar conductivities, mobilities, and carrier concentrations (while ignoring possible differences caused by processing variability at the contact interfaces).

The channel C is patterned down to a size of 50 nm by 100 nm with conductance G_C. Because we were not able to directly pattern contacts to such a small channel, the measured device conductance G_{eff} arises from the combination of all three components. The effective conductance can be estimated from a simple circuit model approximating this device geometry. Assuming these three regions form a simple series circuit between the relevant contacts, the effective conductance is expressed as:

$$\frac{1}{G_{eff}} = \frac{1}{G_1} + \frac{1}{G_C} + \frac{1}{G_2} \tag{5.2}$$

If $G_1 = G_2$ as assumed previously, then:

$$\frac{1}{G_{eff}} = \frac{2}{G_1} + \frac{1}{G_C} \tag{5.3}$$

Regions 1 and 2 do not have any quantization phenomena, so only G_C has interesting features. If G_1 and G_C are at all comparable in scale, then the plateau values will be sub-integer. Interestingly, if the channel conductance is much higher than the rest of the material, then the plateau behavior will be suppressed. In order to achieve integer values of conductance $G_C << G_1$ or G_2, or more specifically:

$$\frac{L_C}{\sigma_c W_c} >> \frac{L_1}{\sigma_1 W_1} \tag{5.4}$$

The geometric factors are approximately one for the device in question, leaving:

$$\frac{1}{\sigma_c} >> \frac{1}{\sigma_1} \tag{5.5}$$

Achieving this regime such that integer values of conductance plateaus are recovered requires mobilities of hundreds of thousands for carrier concentrations approximately 10^{12} as is typical of MoS_2 devices in the G_1 and G_2 parts of the device. Therefore, sub-integer values of the conduction plateaus are expected for the device material and geometry studied here. Although it ignores contacts and quantitative details, this simple model effectively explains the observations as the result of measuring more material than just the patterned nanochannel.

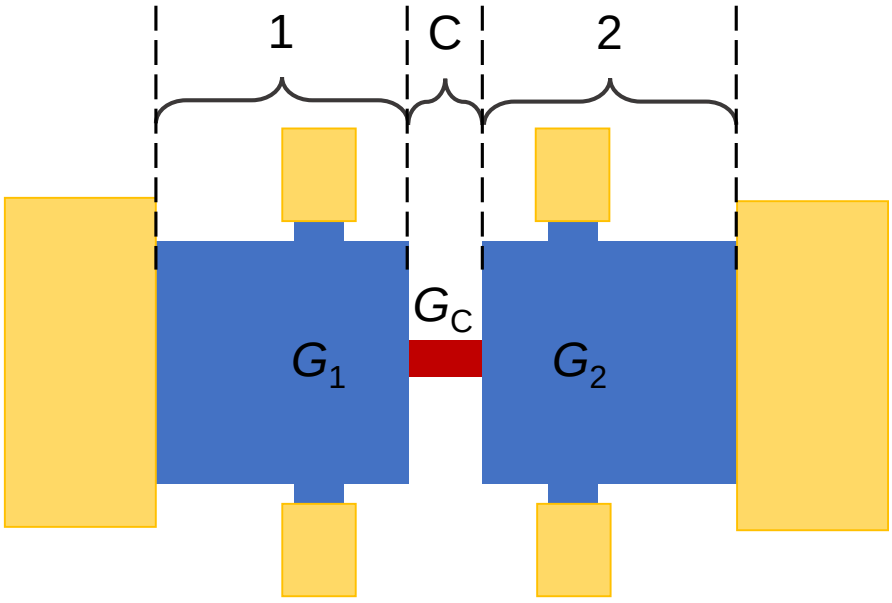

Figure 5.10. Simple representation of the composite device previously shown in Fig 5. The device is segmented into representative parts 1, 2, and C for the unpatterned MoS_2 on each side (1,2) and the channel (C) respectively. Each of these segments is given a corresponding conductance G_1, G_2, and G_C.

In summary we have utilized hBN as a powerful tool to engineer protected heterostructures first in the case of creating next-generation, high-quality contacts and subsequently for new techniques for more direct, more fine patterning of TMDs without layer destruction. The latter has allowed for the controlled and repeatable patterning of monolayers at the 10 nm and higher scale with good opto-electronic properties. Please look forward to this work being published in the near future!

5.3. Future Work

Following the patterning work in the previous section, a new project has been started on nanopatterning Moire heterostructures (twisted layers), and creating isolated nanodots of Moire potentials in TMDs. As discussed at the start of this thesis, angle twisting is a powerful tool in layer manipulation. In vdWs materials the twist angle between two layers can be adjusted arbitrarily between the crystal axes of stacked layers. This opens the door for creating Moire Superlattices, a heterostructure with a larger spatial structure than either of the constituent layers. As this project overlaps with twist angle control techniques that I developed, the project and my early work on creating Moire heterostructures is discussed in greater detail in the Appendix.

CHAPTER 6

Mixed Dimensional Heterostructures: Electronic Coupling of Organic Molecules and 2D Materials

6.1. Introduction

The building of van der Waals structures need not only use layered materials stacked on each other in various configurations or combinations as was the topic in previous sections. In fact, many surfaces will interact through van der Waals (vdW) forces, allowing for the creation of vdW heterostructures combining different dimensionalities [7]. A multitude of configurations can be attained in combination of nD + n'D where $n = 0, 1, 2, 3$ in the general case, with an example of some of these dimensionalities presented in Fig.[6.1]. Optical images of realized mixed dimensional heterostructures, mixing 0D and 2D, can be seen as well. These mixed dimensional heterostructures have been of particular interest over the past decade [167–172] in the quest to create ever more efficient and capable photosensors [173], photovoltaics [174], solar cells [175–177], and diodes [176, 177], making them an extremely tantalizing field of study for application in modern technology and energy harvesting.

For the discussion here, I will be building off of 2D materials as the basis of these mixed heterostructures, reducing the previously mentioned array of combinations to: 2D + nD where $n = 0, 1, or 3$, and more specifically we will be considering specifically 0D: phthalocyanines and pentacene molecules.

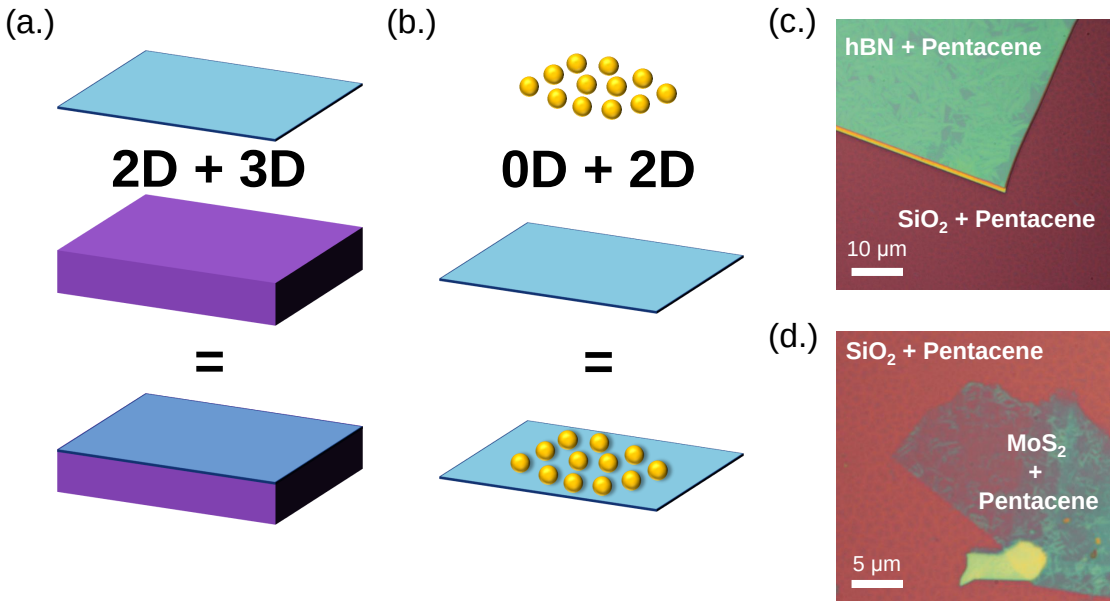

Figure 6.1. Examples of mixed dimensional heterostructures. (a.) $2D + 3D$ mixed dimensional heterostructure, such as a TMDC (2D) and a bulk semiconductor (3D). (b.) $0D + 2D$ heterostructure, such a molecule of phthalocyanine or pentancene (0D) and a TMDC (2D). (c. and d.) Optical images of Pentacene on two different layered van der Waals materials hBN and on MoS_2, and contrasted with SiO_2 a bulk 3D material.

The utilization of 2D materials as a component in mixed heterostructures has brought quite significant breakthroughs due to their well-defined surface and atom-thick nature. In other cases involving non-2D combinations, the junction at the surface was difficult to study directly as it would be obscured. This left many unanswered questions as to the dynamics occurring at the interface, or how either component was modified. By comparison, a 2D layer is atomically thin and the entire layer is the surface, and can directly be characterized. Moreover, any interactions or emergent dynamics of the heterojunction can be characterized as arising purely from the surface. The thin nature of the 2D layer

also allows for modification through the layer such as normal electric and magnetic fields, optical stimulation, and doping.

6.2. Electronic Coupling in TMDC-Phthalocyanine Mixed Dimensional Heterojunction

Mixed dimensional heterostructures built off of 0D organic dye molecules and 2D TMDCs offer a wide array of combinations (such as Rhodamine 6G [8, 170], Pentacene [10, 178], Phthalocyanine [170, 173], etc.) that have drawn extensive interest in the field. Previous works in the literature have focused primarily on application and the creation of more sensitive photodetectors and photovoltaic devices, where the 0D dye molecule is used to enhance and modify the photosensitivity of the underlying TMDC. These results have underscored the interesting and flexible capabilities of mixed heterojunctions built from 0D+2D, but understanding of the interactions had been limited.

In collaboration with Sam Amsterdam from the Hersam and Marks Groups, and Qunfei Zhou from the Darancet Group, I set out to investigate the interaction of phthalocyanine (Pc) dye molecules interfaced with 2D TMDCs as functions of the transition metal identity (M) of the Pc molecule and layer number of the TMDC. MPc, specifically, were of particular interest due to their ease of processing and significant optoelectronic tunability as functions of the their metal M core. This made them an ideal use case for producing many different combinations with significantly tunable electronic properties as a function of the M metal while maintain similar molecular geometries and surface chemistries. Our work systematically probed the $MPcMoS_2$ heterojunctions with ultravioletvisible (UVVIS) optical absorption spectroscopy and Raman scattering.

6.2.1. Results and Discussion

MoS_2 samples were prepared in two ways. For MPc-MoS_2 comparisons, MoS_2 films were grown by chemical vapor deposition (CVD) growth on single-crystal sapphire substrates. Samples for layer-dependent interactions of MPc-MoS_2 were produced manually by micromechanical Scotch Tape exfoliation from MoS_2 bulk crystals onto SiO_2 substrates as shown in the Appendix. All samples were characterized first via optical microscopy, atomic force microscopy, photoluminescence and Raman spectroscopy to confirm their quality as well as layer number. Films of various metallophthalocyanines (CoPc, NiPc, CuPc, ZnPc) and metal-free phthalocyanines (H_2Pc) were purified by vacuum temperature gradient sample sublimation and then deposited by thermal evaporation on the MoS_2 substrates as well as on clean reference SiO_2 and single-crystal sapphire substrates. Films were deposited by thermal evaporation at a pressure below 10^{-5} Torr at a rate of 0.1 0.2 $\AA$/s, monitored by a calibrated quartz crystal microbalance, to a thickness of 2 to 20 nm. After deposition, on all chips of interest with and without TMD layers, the presence of the Pc was confirmed via Raman and served as a check of thickness [167]. Sample preparation and end result can be seen in Fig.[6.2].

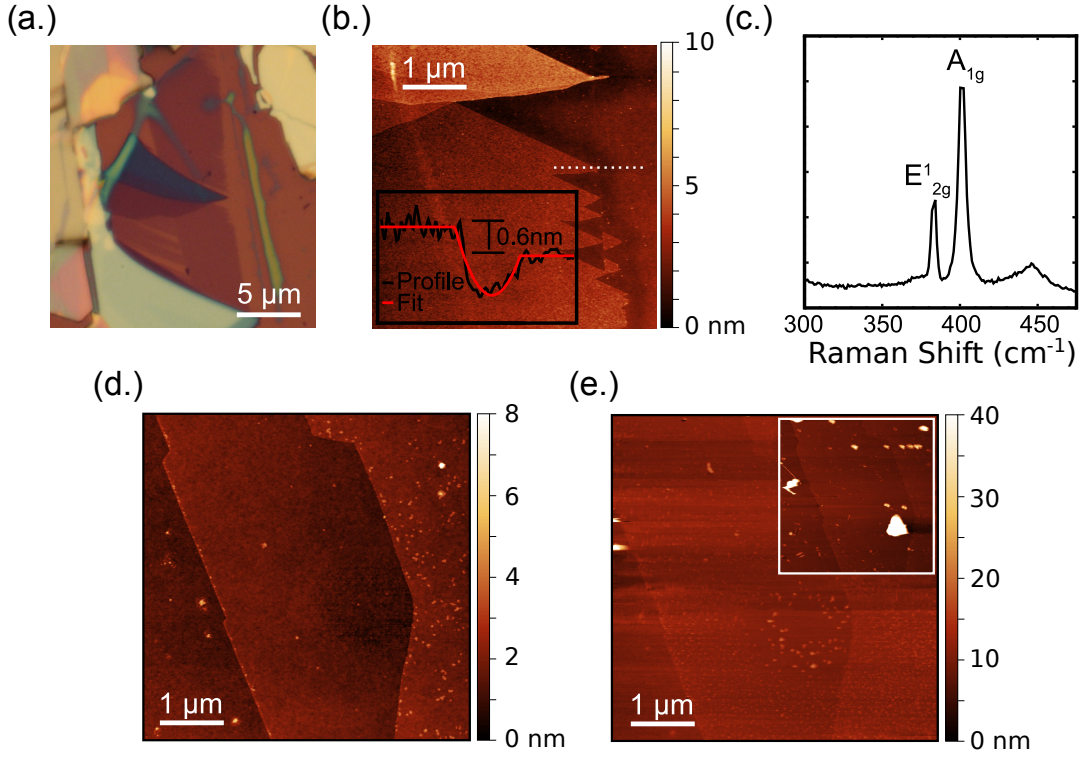

Figure 6.2. Sample prep example and post-Pc deposition on SiO_2. (a.) Exfoliated layer of MoS_2 as found on SiO_2 pre-anneal, there is evident tape residue that must be removed by annealing to prepare a pristine surface for building a heterojunction. Residuals on the surface can comprise a heterojunction formation and can complicate later characterization by acting as dopants, absorbates, etc. (b.) Post-anneal AFM of the same layer, the pristine surface is evident. (c.) Raman further confirms MoS_2 monolayer. (d.) A large, clean monolayer and bilayer structure before deposition. (e.) The same layer, now with CuPc molecules deposited over the surface of the layer, creating an MoS_2/CuPc heterojunction. (Inset) Shows the affects of overheating the CuPc on MoS_2 and, in part, why the layer and heterojunction cannot be cleaned after deposition. This also highlights the delicate nature of these heterojunctions. Adapted with permission from [2]. Copyright 2019 American Chemical Society.

Following the preparation of an MoS_2/MPc heterojunction, such as the one seen in Fig.[6.2e] and the simple cartoon representation in Fig.[6.3a], several measurements were planned out and performed. All measurements sought to compare the heterojunction with the individual components, this would highlight any novel dynamics that arose due to the interface.

The first of the series of tests was done via large area UV-VIS optical absorption of MoS_2, MPc, and the MoS_2/MPc heterojunction all on a sapphire substrate. Sapphire was used in this case specifically for its transparent nature, making it ideal of transmission based optical absorption (over reflection based absorption common for SiO_2/Si substrates which are complicated by thin film signal from the SiO_2). To make the junction comparison as direct as possible, we did absorption first of the MoS_2 (pre-deposition) and then deposited MPc on the MoS_2, this would rule out variations in absorption spectra of different growths of MoS_2 being convoluted with any potential novel behaviors.

Absorption spectra of the heterojunction show a strong feature arising between 700 nm and 750 nm, with the exact wavelength position of the peak dependent on the MPc metal identity. The new peak, coined A_CT in Fig.[6.3b-f], MPc metal identity can be tracked from NiPc at approx 700 nm to CuPc at 720 nm, and the metal-free case of H_2Pc shows this feature at 740 nm. This feature is not present in either the original, pre-deposition MoS_2 (blue) or on MPc (green) deposited on bare sapphire as seen by the accompanying spectra in each part of Fig.[6.3b-f].

$$\text{Abs}\%_{Diff} = \text{Abs}\%_{MoS_2+MPc} - \text{Abs}\%_{MoS_2} \tag{6.1}$$

Following Eq.(6.1) and subtracting the spectra of the pre-deposition MoS_2 absorption from that of the heterojunction built atop the same MoS_2, we see clearly in Fig.[6.4b] (dashed purple) that the novel, strong feature at wavelengths of 700 nm and higher is distinct to the junction. There are minor features in this difference-spectra similar to those seen from the absorption of the MPc (seen in dashed purple between 600 to 700 nm with the latter appearing as a shoulder on the A_CT peak) deposited on bare sapphire, which was to be expected. The Type-II band-alignment of the MPc orbitals (gas-phase) with respect to the MoS_2 bands [35, 171, 179, 180] suggests that this A_CT feature is a charge-transfer transition from the MPc highest occupied molecular orbital (HOMO) to the MoS_2 conduction band minimum (CBM) as represented in Fig.[6.4c]. As previously mentioned, the A_CT peak has a strong metal-identity dependence but remains visible in the metal-free H_2Pc case, this suggests that the MPc HOMO participating in the charge transfer have a primarily π-character. The roughly 20 nm shift in the A_CT peak suggests a strong correlation to the frontier Pc metal d-orbitals, with Co and Ni (d^7 and d^8 respectively) absorbing at similar wavelengths. Likewise, Cu and Zn (d^9 and d^10 respectively) have similar wavelengths, all tracked in Fig.[6.3b-f]. The observed dependence on orbital filling indicates that d-electrons, while only weakly involved in the A_CT transition, play a significant role in the electronic band offsets between the MPc and MoS_2. Similar results have been observed previously with MPc and other semiconductor surfaces [181].

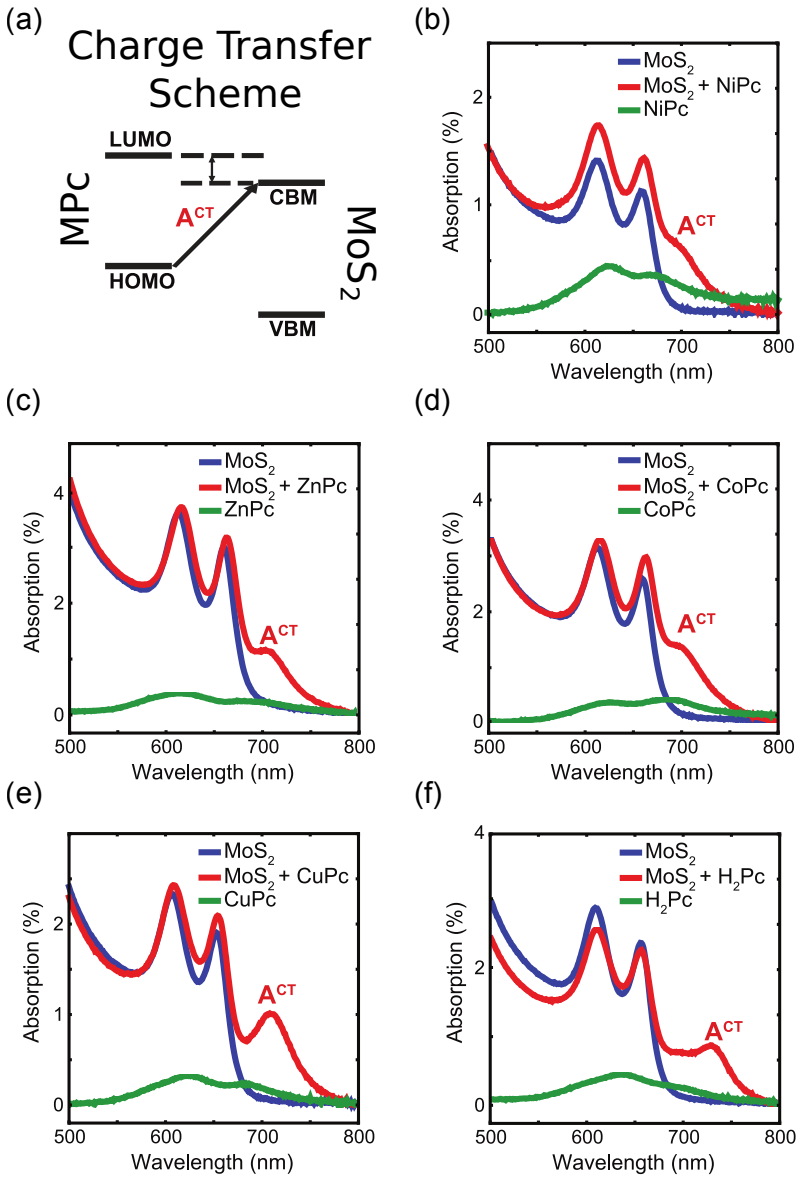

Figure 6.3. Series of absorption spectra of MPc + MoS_2 heterojunctions with varied M-core identity. (a.) Shows a simple representation of the MPc molecule, MoS_2 crystal structure, and their combined heterostructure as measured under white-light illumination. (b.-f) Absorption spectra of MPc (NiPc, ZnPc, CoPc, CuPc, and H_2Pc, respectively) on MoS_2 CVD monolayers. The A_CT peak shows an evident metal-identity dependence including the case of metal-free for H_2Pc. Adapted with permission from [2]. Copyright 2019 American Chemical Society.

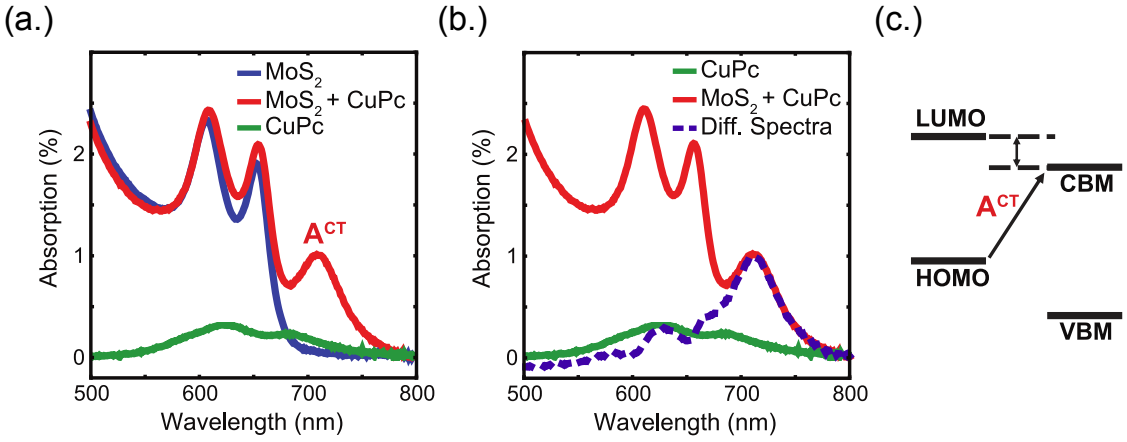

Figure 6.4. (a.) CuPc + MoS_2 heterojunction absorption, shown again for convenience of comparison. (b.) The difference of CuPc + MoS_2 spectra and MoS_2-only spectra from (a.) shown in dashed purple. Features similar to those of the CuPc can be seen in the difference spectra between 600 to 700 nm with a shoulder manifesting on A_CT. The A_CT is a novel dynamic from the junction. Similar results were found for all other MPc + MoS_2 combinations and difference spectra. (c.) The charge transfer picture that creates the feature A_CT, via a direct transition from the HOMO of the MPc molecule to the CBM of the MoS_2. Adapted with permission from [2]. Copyright 2019 American Chemical Society.

Further analysis of the MPc-TMD junction was done via Surface Enhanced Raman Spectroscopy (SERS) analysis of MPc deposited over exfoliated mono to few layers of MoS_2. SERS has been observed in similar organic/MPcMoS_2 systems and as such was a well established tool for studying charge transfer sensitive systems [8, 167, 170, 172, 182–187]. The shift to exfoliated layers from CVD was done to remove the inhomogeneity of CVD grown layers, their uncertain doping (often arising from an overabundance in sulfur vacancies in as-grown MoS_2) [188], and introduce more layers in a straight forward way. Without a need for transparent substrate and large-scale layer for absorption measurements, there was no further advantage in using CVD growths. In fact, sapphire

substrate, due to its lack of a back-reflection plane, can make it difficult to collect sufficient Raman without extended exposure or long collection times. This is non-ideal due to the aggregation previously detailed (Fig.[6.2e] which can also be triggered by laser heating.

Raman spectra from our MPc/MoS_2 heterojunctions on SiO_2/Si (detailed at the start of this section) were collected with power under 150 μW and under 60 s of exposure. These parameters were tested and found to no laser-induced bunching. These conditions were arrived at by exposing test heterojunction spots with laser light for discrete periods of time and subsequently performing AFM (and optical) checks on those locations.

The SERS intensity enhancement factor, E_{REL}, is calculated by dividing the signal intensity of a given MPc vibrational mode on the MoS_2 by that on nearby bare SiO_2 (6.2).

$$E_{REL} = \frac{I_{MoS_2}}{I_{SiO_2}} \tag{6.2}$$

To confirm that any signal differences we observe are not due to differences in thickness of deposition of MPc on MoS_2 vs SiO_2 we performed XPS on the sample as detailed in our paper. It was found that the morphology and surface coverage were similar, and as such any signal differences between the heterojunction and the reference SiO_2 were not from deposition differences but from the junction.

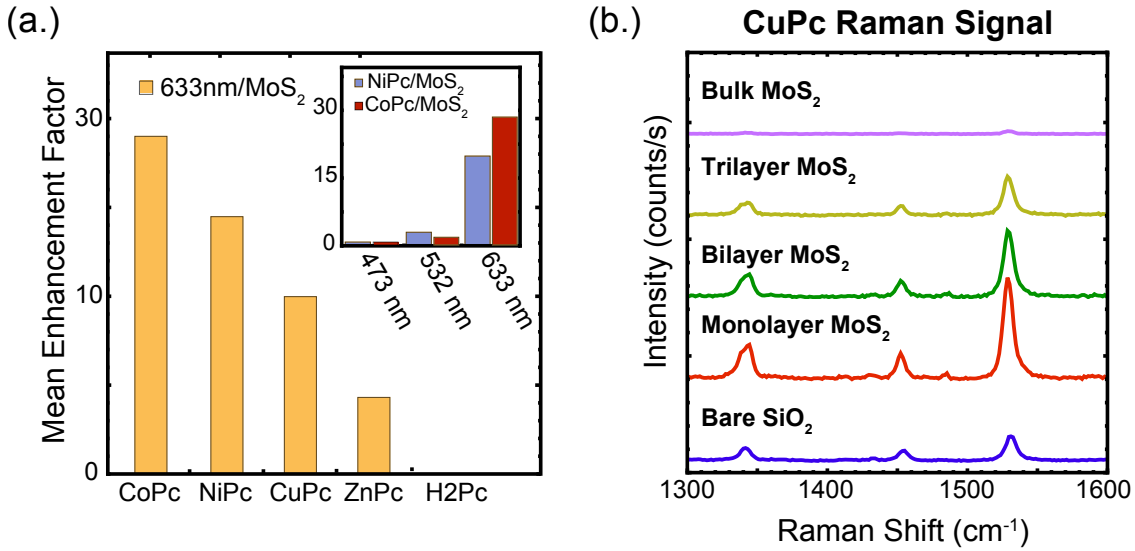

Figure 6.5. Surface Enhanced Raman Spectroscopy of the MPc + MoS_2 heterojunction for varied metal identity, layer number, and laser excitation. (a.) Metal-identity dependent enhancement of the Raman modes on MoS_2 at 633 nm excitation, showing an enhancement decrease with increasing M atomic number. (Inset) Laser excitation dependence on the enhancement: wavelength-dependent enhancement shows an increase as the wavelength shifts from non-absorbing (473 nm) to on-resonance with the MPc Q-band $\pi \rightarrow \pi^*$ absorption and the MoS_2 exciton absorption (633 nm). (b.) Layer dependent enhancement (532 nm excitation source) of CuPc on MoS_2 of N-layers. Mono to trilayer show a decreasing enhancement factor with increasing layer number, but bulk MoS_2 quenches the MPc Raman modes. Adapted with permission from [2]. Copyright 2019 American Chemical Society.

Results of the Raman tests on MoS_2 of different layers with different MPc metal identities can be seen in Fig.[6.5], showing a dependence on laser excitation, layer number, and M-core identity. This enhancement closely follows an M atomic number trend with decreasing enhancement with increasing atomic number. Put in other terms, following the Table of Elements, CoPc shows the highest enhancement factor E_{REL} at nearly 30x the signal on SiO_2, followed by the E_{REL} of NiPc at 17x, and decreasing further to CuPc and

ZnPc. H_2Pc exhibits essentially zero enhancement factor. The enhancement factor also shows a noticeably significant dependence on the laser excitation wavelength, increasing with increasing wavelength. At 473 nm the the Raman modes of MPc are very weak on either substrate and show no evidence of enhancement from the MoS_2 vs SiO_2, at 532 nm excitation the MPc Raman modes are strong on SiO_2 and show enhancement of 3-4x when moving to the MoS_2 heterojunction, see Fig.[6.5a(inset), b]. At 633 nm, when the laser excitation is close to resonance with the MoS_2 and MPc absorption features from Fig.[6.3b-f], we see a sharp increase in enhancement factor up to 30x with CoPc, an order of magnitude increase from 532 nm excitation, see Fig.[6.5a, a(inset)].

The trend in E_{REL} is not correlated with the MPc optical absorption trends from those seen previously in Fig.[6.3b-f] (where we observed a trend roughly from NiPc $\rightarrow$ CoPc $\rightarrow$ ZnPc $\rightarrow$ CuPc) but, as mentioned in the previous paragraph, follows the Table of Elements transition metal progression with a maximum enhancement for CoPc $\rightarrow$ NiPc $\rightarrow$ CuPc $\rightarrow$ ZnPc $\rightarrow$ $E_{REL} = 0$ for H_2Pc. This trend can be understood in terms of the decreasing energy of orbitals with strong out-of-plane d-character (i.e., d_{xz},d_{yz}, and d_{z^2}) lying below the predominantly π-HOMO band. The critical role of metal d-orbitals is further confirmed by Raman spectroscopy of H_2Pc on MoS_2, which shows negligible enhancement of the Raman signal despite 633 nm being resonant with the H_2Pc optical absorption as seen in Fig.[6.3f] [185–187].

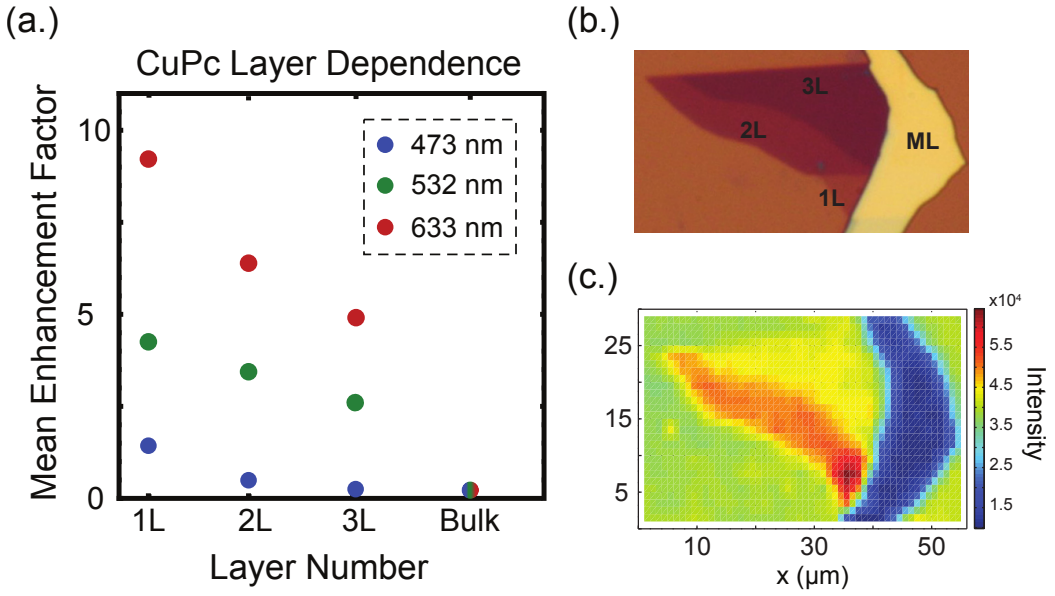

Figure 6.6. Layer dependent behavior of MPc/MoS_2 heterojunction. (a.) CuPc on MoS_2 layer dependence with three different excitation lasers. In all three cases, the increasing layer number diminishes the enhancement factor of the junction. Bulk quenches Raman outright. (b.) Optical image of a flake of MoS_2 with several different layer numbers before CuPc was deposited. (c.) 2D Map of Raman intensity, the monolayer shows the strongest enhancement, then bilayer to trilayer and bulk acting like a quencher. This map highlights that this behavior is largely uniform across the heterojunction and not caused by clumping or location specific interactions. Adapted with permission from [2]. Copyright 2019 American Chemical Society.

Table 6.1. Layer dependent enhancement E_{REL} (st.dev) on MoS_2 layers for each metal identity MPc at 633 nm excitation. (*) corresponds to signals that were too low to be measured or compared. Adapted with permission from [2]. Copyright 2019 American Chemical Society.

	Monolayer	Biayer	Trilayer	Bulk
CoPc	25.8 (3.2)	48.2 (10.2)	14.8 (2.1)	1.7
NiPc	23.4 (3.6)	26.5 (7.2)	14.1 (1.3)	0.5
CuPc	9.2 (0.9)	6 (0.8)	5.1 (1.0)	*
ZnPc	4.9 (0.7)	4.9 (1.7)	2.1 (0.3)	0.6
H_2Pc	*	*	*	*

Table 6.2. Layer dependent enhancement E_{REL} (st.dev) on MoS_2 layers for each metal identity MPc at 532 nm excitation. (*) corresponds to signals that were too low to be measured or compared. Adapted with permission from [2]. Copyright 2019 American Chemical Society.

	Monolayer	Biayer	Trilayer	Bulk
CoPc	2.5 (0.3)	2.1 (0.1)	1.7 (0.2)	*
NiPc	2.9 (0.2)	1.8 (0.2)	2.2 (0.1)	*
CuPc	3.9 (0.1)	2.7 (0.2)	1.6 (0.1)	*
ZnPc	0.6 (0.1)	0.5 (0.2)	*	*
H_2Pc	1.6 (0.4	1.4 (0.6)	0.9 (0.3)	*

The surface dynamics also depend on the underlying layer number of the MoS_2 as seen in Fig.[6.6b]. Monolayer of MoS_2 shows the strongest enhancement for CuPc with 532 nm excitation with it decreasing with increasing layer. Bulk shows an inversion of the enhancement behavior and actively quenches the Raman modes of CuPc. At 633 nm excitation, notable exceptions arise to this trend with CoPc and NiPc + MoS_2 heterojunctions showing significantly increased enhancement on bilayer MoS_2, to 48.2 and 26.5, respectively. Trends can be seen in detail for various layers and MPc in **Table 1** and **2**. The trend is the same following this with increasing layer number resulting in decreasing signal and, ultimately, quenching in bulk. It is likely that this divergence is due to particularly favorable charge transfer between Co/NiPc and bilayer MoS_2, similar to previous results on Rhodamine 6G on MoS_2 layers [8].

These results point to the critical role of the metal core identity and, further, the non-frontier orbitals in mediating the exchange of charge across the interface of the MoS_2/MPc heterojunction. Further reading on this and the highly useful simulations results done by Qunfei Zhou to support our data-drawn conclusions can be seen in our published paper: Electronic Coupling in MetallophthalocyanineTransition Metal Dichalcogenide Mixed-Dimensional Heterojunctions, ACS Nano 2019 13 (4), 4183-4190 [2].

6.3. Defect Quenching in TMD-Pc MDH

In follow up to our findings in SERS of the MPc component of the MPc/MoS_2 heterojunction, our collaborative efforts moved into studying the impact of the junction formation on the underlying MoS_2. Specifically, our work focused on defect states of MoS_2 at low temperatures with additional room and variable temperature studies to understand the underlying dynamics.

Deciphering the mysteries of defects in TMDs remains a hot topic in 2D layered materials, and being able to control their contributions is essential in optoelectronic devices [189, 190], and they remain a major impediment in high quantum yield photoluminescence at room and low temperatures [38]. These defect states are known for their roles in electronic transport [9, 191], exciton recombination [192], doping [193], and general lattice quality and characteristics (such as grain boundaries) [194–196]. At room temperature, defects are optically dark as their recombination is blocked by processes such as phonon scattering but still play a role [197, 198]. They do not become optically active until cryogenic temperatures (<150 K). This temperature dependent optical activity can be seen in Fig.[6.7a], as well as the thermal shifting of the exciton state from 670 nm to 650 nm. The defect becomes optically active under 100 K at 700 nm. While this behavior is ubiquitous, the exact structural and chemical origin remains unclear and a point of interest [141].

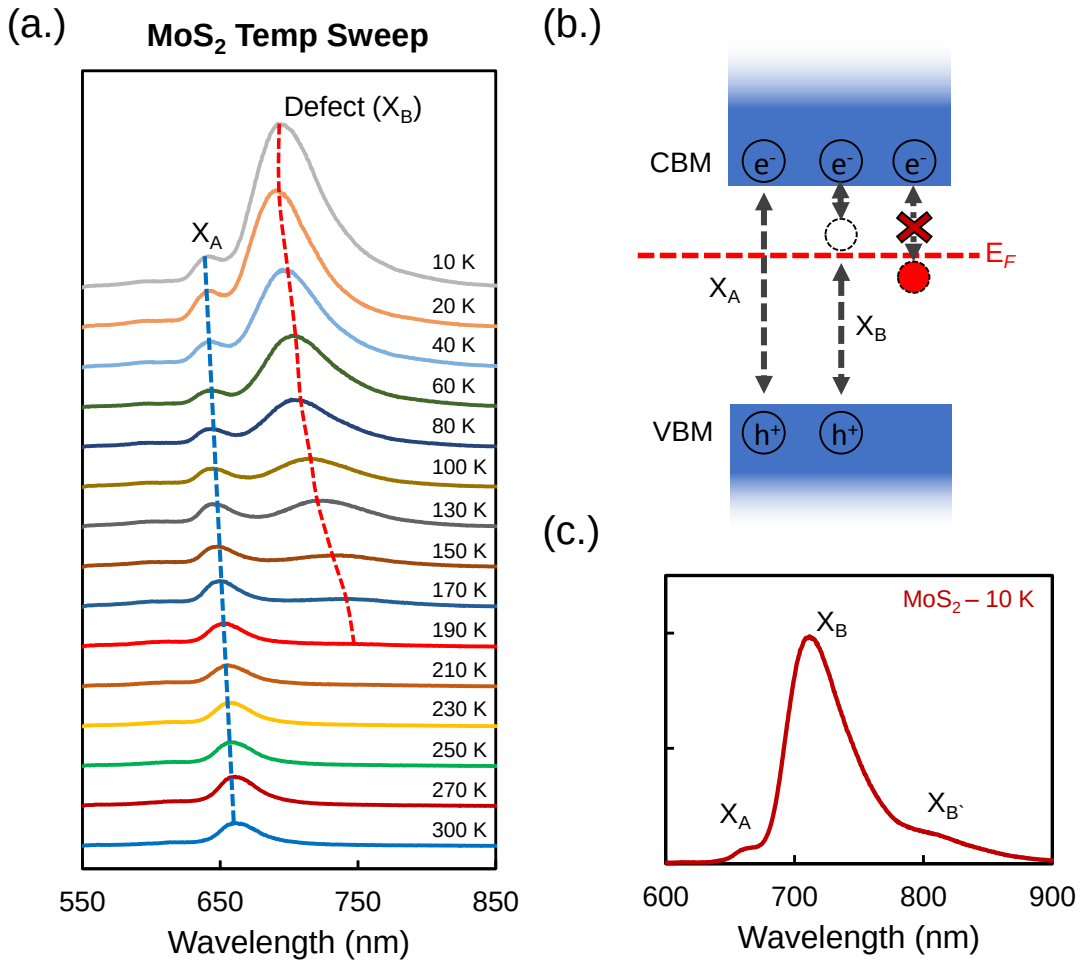

Figure 6.7. (a.) Temperature dependent behavior of MoS_2, the emergence of the defect state can be clearly seen starting at approximately 150 to 170 K. (b.) Simple representation of defects and exictons in the bangap, and the role the Fermi level can play in defect recombination. (c.) Low temperature PL of MoS_2 with emission peaks labeled. X_A is the MoS_2 A-exciton, and X_B and $X_{B'}$ are two defect states.

Based on their lower energy emission and theoretical predictions, majority of MoS_2 (and TMD in general) defects arise from sulfur vacancies (S_{vacs}) (in selenides, it would be selenium vacancies or Se_{vacs}, but for this work focus will be on S_{vacs} only) [143, 144]. This leads to the formation of localized bound states near the conduction band edge within the gap. A simple representation of these bound states at and near the conduction band edge (not exhaustive) can be seen in Fig.[6.7b], and the resultant emission at low temperature in Fig.[6.7c] with peaks labeled as X_A for the A-exciton and X_B for the bound defect state.

However there are other sources of defects such as the recently shown oxygen substitutions [145, 146], but here the focus will be on Svac defects, generally considered the dominant defect state. Encapsulation with hBN can reduce the background defect PL but is a non-scalable approach with considerable labor intensity and time requirements. Molecular approaches to MoS_2 defect passivation have been explored [142, 199, 200] but these strategies do not efficiently quench the defect PL. Defects have also been used as useful tools for novel physics such as in their recently shown potential for creating single-photon emitter sources in TMDs [59, 200].

Moreover, it is possible to control defect populations through simple gating procedures such as backgating common in any electronic devices [80]. The backgate tunes the Fermi level, showing it plays a critical role in the quantum yield (QY) of defects. Lowering the gate potential tunes the Fermi level lower towards the valence band, and increasing the gate tunes the Fermi level higher towards the conduction band. The former increases defect emission as midgap states are de-occupied and become pathways for emissive recombination, and the later quenches defect emission as the midgap states are filled [201].

Because MoS_2 is usually n-type [123], it can be tuned well into the conduction band and defects quenched out entirely with just the gating. A rough approximation of this filling/depletion of states can be seen in Fig.[6.7b].

6.3.1. Results and Discussion

Phthalocyanines interfaced with MoS_2 provide a powerful system with which to explore optical defects, their identity, and modification. The electronic structure of MPc, as noted in the previous section, is a powerful tool due to the ability to be readily altered by changing the metal core while retaining their aromatic macrocycle framework [149], providing a systematic point of study. To accomplish this, layers and the subsequent junctions were made in similar fashion to the previous section for exfoliated layers of MoS_2. For side-by-side comparisons, MoS_2 was also grown via CVD on SiO_2/Si thermal oxide substrates, and different metal-core identity MPc (Co, Cu, Zn, H_2) were deposited in differing quadrants of the growth. Deposition of Pc was identical to that discussed previously though limited to only 1 nm of deposition for all tests. Samples were then loaded into our Advanced Research Systems cryostat and pumped down to a vacuum.

To study the impact of the junction on the MoS_2, photoluminescence was utilized as the measurement method for study. Measurements were done with 532 nm excitation laser for all measurements. Samples were measured room to low temperatures before and then after deposition on exfoliated flakes. This can be seen in Fig.[6.8]. Raman was used to characterize and confirm deposition of MPc on the MoS_2, showing enhanced Raman signal as is expected based on the previous work in the previous section [2, 159, 189].

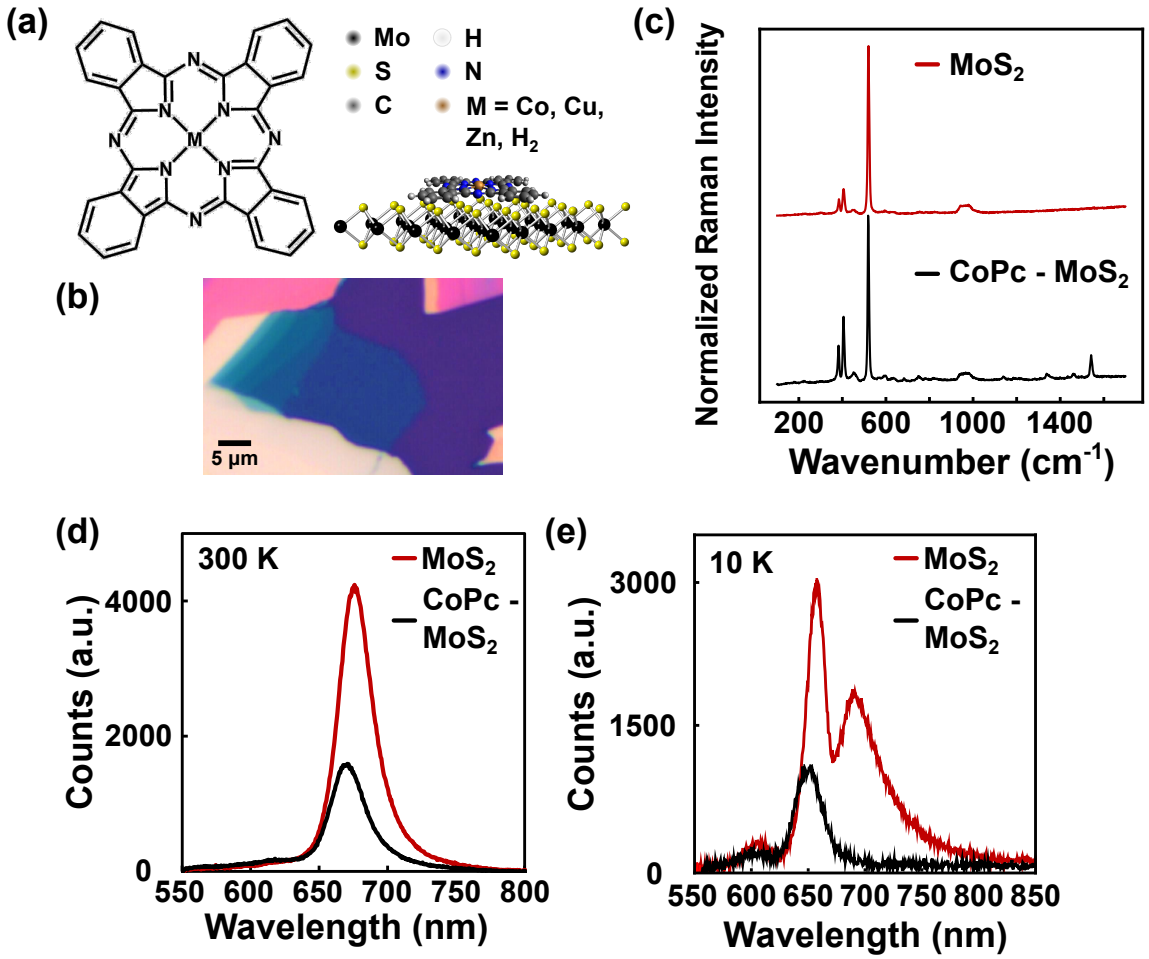

Figure 6.8. (a) Simple representation of MPc (M = Co, Cu, Zn, H_2) on MoS_2 layer. (b) Optical image of MoS_2 layer on SiO_2 with MPc deposited over the surface. (c) Raman on/off MoS_2 of CoPc, a familiar enhancement from the first work on MPc-MoS_2 of the Raman (SERS) can be seen. (d) PL comparison of MoS_2 exciton before and after CoPc deposition at room temperature (300 K). (e) PL comparison of MoS_2 exciton before and after CoPc deposition at low temperature (10 K).

Room temperature measurements (300 K) are shown in Fig.[6.8d] for a representative CoPc example of the MPc + MoS_2 heterojunction before and after deposition on an exfoliated flake. There is an obvious quenching by roughly a factor of two times of the exciton signal of MoS_2 under the junction. It is likely that this quenching arises from the formation of a Type-II heterojunction [152] at the interface and subsequent charge transfer between the MoS_2 and CoPc. This charge exchange also likely results in p-doping of the underlying MoS_2. Evidence of this can be seen in the slight blue shift of the MoS_2 exciton under the junction which suggests an increase in neutral exciton relative to negative trions [72].

As temperature drops defects emerge in the MoS_2 layer, as was previously shown in Fig.[6.7a]. Once CoPc is deposited on the surface, we see, again that the exciton is quenched and slightly blue shifted, however, the defects are now quenched out entirely. A further example of this is shown in Fig.[6.9] where linescans across a partially coated MoS_2 with 5 nm of ZnPc. This thicker film was used to exaggerate the effects of the quenching. The same quenching can be seen at room temperature of the exciton, though no meaningful energy shift is observed in the case of the ZnPc influenced exciton as seen in the normalized comparison Fig.[6.9c]. A linescan of 200 microns across the junction interface over MoS_2 shows the quenching at room temperature. Low temperature comparison and low temperature linescan shows a significantly stronger quenching at low temperature due to the high defect quenching in the MPc+MoS_2 heterojunction.

To better probe the MPc impact on defects as well as the generality of the process, PL and defect quenching were compared over a range of MPc: Co, Cu, Zn, H_2. To facilitate this comparison and rule out layer-to-layer differences, samples were instead made from

CVD grown films and MPc (Co, Cu, Zn, H_2) were deposited in quadrants over the film. Regions of uncoated MoS_2 similar to the deposition shown in Fig.[6.9a] were left as nearby references to each quadrant. By comparing MPc-MoS_2 heterojunction to adjacent bare MoS_2 film inhomogeneity would be minimal making for the best possible comparisons. Another advantage for this study of CVD grown layers is the expected higher defect density, resulting in much higher defect PL emission at lower temperature and making for an excellent comparative base for quenching efficacy.

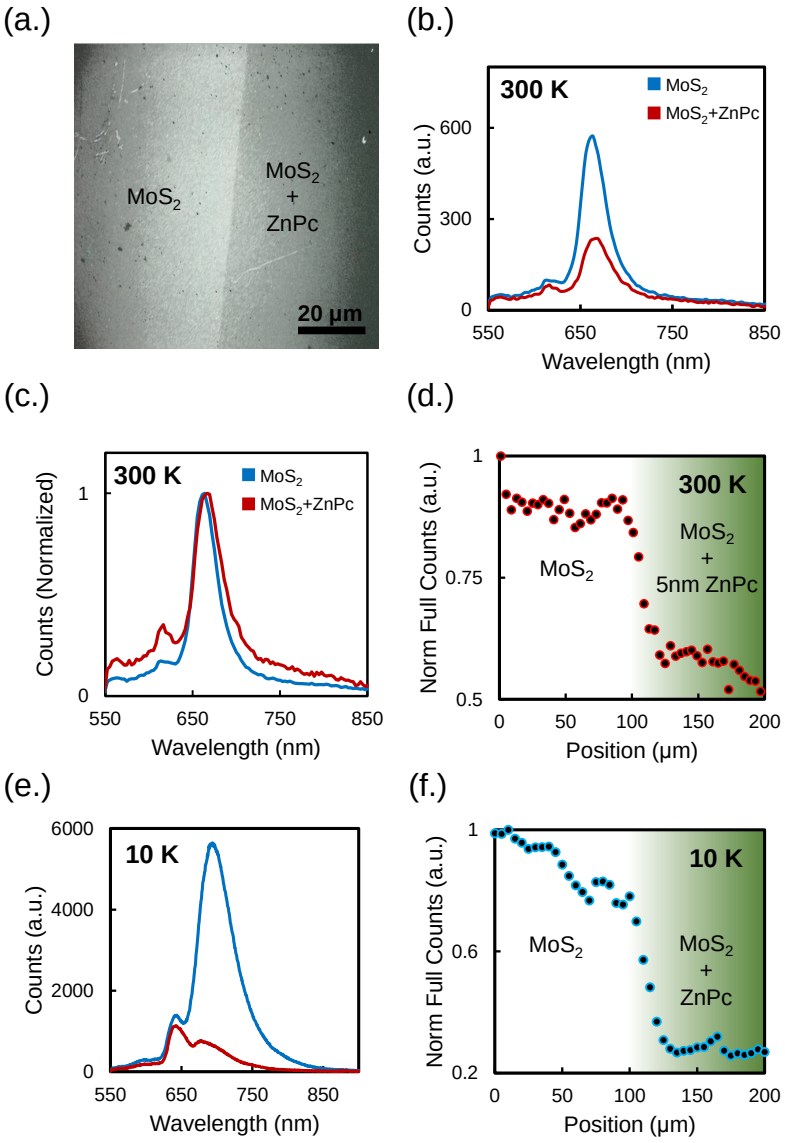

Figure 6.9. ZnPc-MoS_2 scans. This sample used 5 nm ZnPc for exaggeration of effects. (a.) Optical image showing the bare MoS_2 and heterojunction adjacent to it. (b.-c.) Room temperature PL of MoS_2 and the ZnPc-MoS_2 junction, raw and then normalized respectively to show no meaningful energy shifts. (d.) Room temperature line scan across the threshold. (e.) Low temperature PL, showing significant quenching of the defect peak of MoS_2 under the heterojunction. (f.) Low temperature line scan across the threshold.

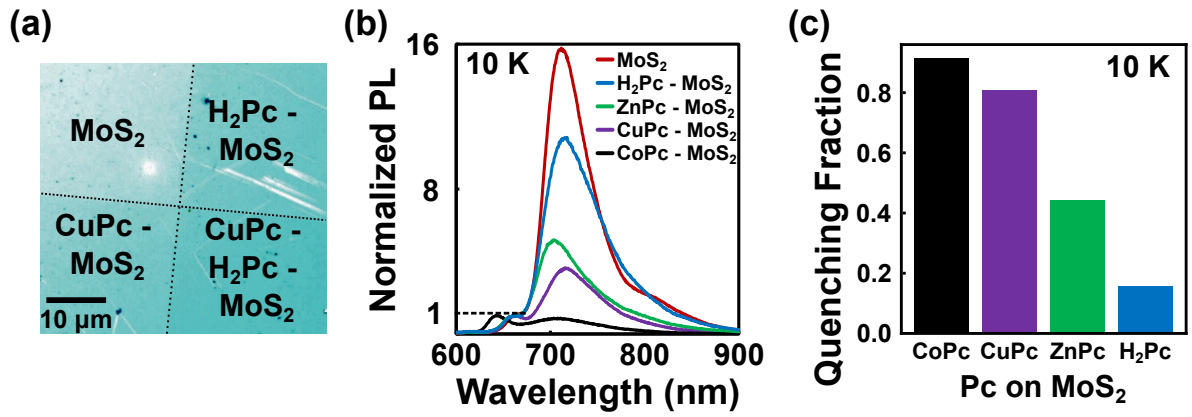

Figure 6.10. (a) Microscope image of MPc films on monolayer MoS_2 grown via CVD. PL spectra in (b) and used to generate (c) were done as linescans across the boundary interfaces between MoS_2 and respective nearby MPc. (b) Low temperature photoluminescence spectra of MoS_2 with H_2Pc, ZnPc, CuPc, and CoPc heterojunctions, normalized to the neutral exciton.(c) Comparison of quenching fraction of each MPc.

The differences in quenching behavior of the MPc-MoS_2 heterojunctions can be seen in Fig.[6.10], done with close proximity linescans from nearby MoS_2 and respective MPc. It is evident there is a clear trend, very similar to the Raman trends in the previous section, that related to the metal core identity of the MPc with CoPc showing the strongest quenching then CuPc, ZnPc, and H_2Pc. The comparison is captured in bar graph comparison in Fig.[6.10c] using:

$$QF = 1 - \frac{\Sigma PL(MPc - MoS_2)}{\Sigma PL(MoS_2)} \tag{6.3}$$

Where QF is the Quenching Fraction and achieving a fraction of 0 means no quenching and 1 means total quenching of the defect emission. The quenching fraction follows CoPc > CuPc > ZnPc > H_2Pc.

To better understand the quenching behavior, devices with electrical backgates were made from tape-exfoliated MoS_2 flakes and measured before and after deposition of CoPc. This was done compare, pre to post deposition of MPc, Fermi level dependence (and therein doping changes) brought on by gate tuning [148]. For negative gate: in the bare MoS_2 case it is seen (and expected) that the gate has a significant impact on defect emission, with the defect dramatically increasing in emission strength as the gate is pulled to high negative values thus moving the Fermi level well into the midgap. Unlike the bare MoS_2, however, the CoPc-MoS_2 heterojunction shows a persistant quench of the defect state even out to very high negative gate voltages and only reaching a significant contribution at the limits of SiO_2 breakdown voltages. This result shows the CoPc introduction has significantly shifted the on-state of defects by over 70 Vg. This behavior is captured in Fig.[6.11].

For positive gate: there is limited difference between the MoS_2 and CoPc-MoS_2 heterojunction cases. In this positive gate regime, emission is quickly dominated by negative trions becoming the main emitter species [72]. It is this neutral exciton vs. trion population that also shows the most obvious distinction in a more pronounced shift in the exciton state over the gate voltage range of the CoPc-MoS_2 heterojunction. This is due to the intrinsically higher neutral exciton state density of the CoPc-MoS_2 heterojunction vs that of the bare MoS_2 in their respective 0 V gate states. This can be seen in Fig.[6.10b] where the exciton of the CoPc-MoS_2 junction is shifted to bluer energy significantly from other heterojunction cases. The end state of both the heterojunction and the bare MoS_2 at high positive gate is nearly identical, showing that eventually the CoPc-MoS_2 heterojunction also becomes heavily trion dominated.

This result from the gate sweeps rules out a simple doping picture for the extinction of MoS_2 defects in the heterojuction. It can be seen that the CoPc-MoS_2 junction does not behave like a heavily n-doped system analogous to the bare MoS_2 in high positive gate voltages where the defects are quenched. Indeed, it appears that the MoS_2 in the junction exhibits a more p-type behavior with significant increase in neutral exciton populations and requiring significantly higher positive gate voltages for trion populations to become the dominant emitters. However more p-type, again analagous to the bare monolayer case, would have suggested an increase in defect emission which is not the case! This inconsistency with simple doping expectations rules out that the MPc is merely acting as a surface dopant for the mechanics of defect quenching. In fact, as it is evident that the CoPc is actually contributing some degree of p-doping to the system via exciton analysis, the extent of quenching seen is even more significant than initially thought.

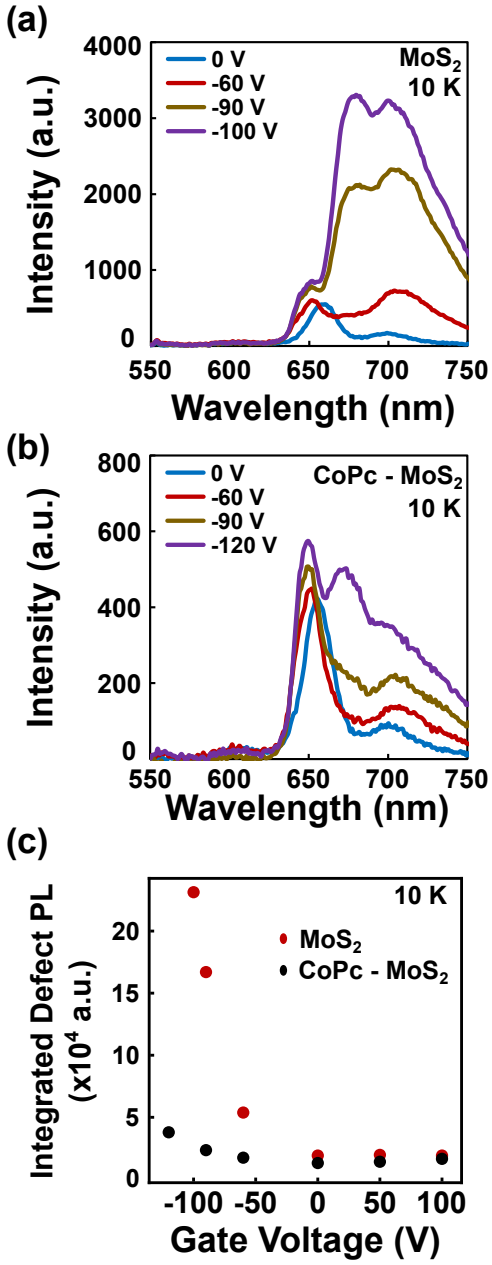

Figure 6.11. Low temperature PL with applied backgate voltages. (a) Exfoliated MoS_2 alone in negative gate regime, showing an explosive growth in defect emission with increasing negative gate. (b) $CoPcMoS_2$ heterojunction in the negative gate regime, the defect and gate amplification at high negative voltages are suppressed by CoPc. (c) Comparison of defect PL integrated defect intensity for MoS_2 and $CoPcMoS_2$ at the measured gate voltages.

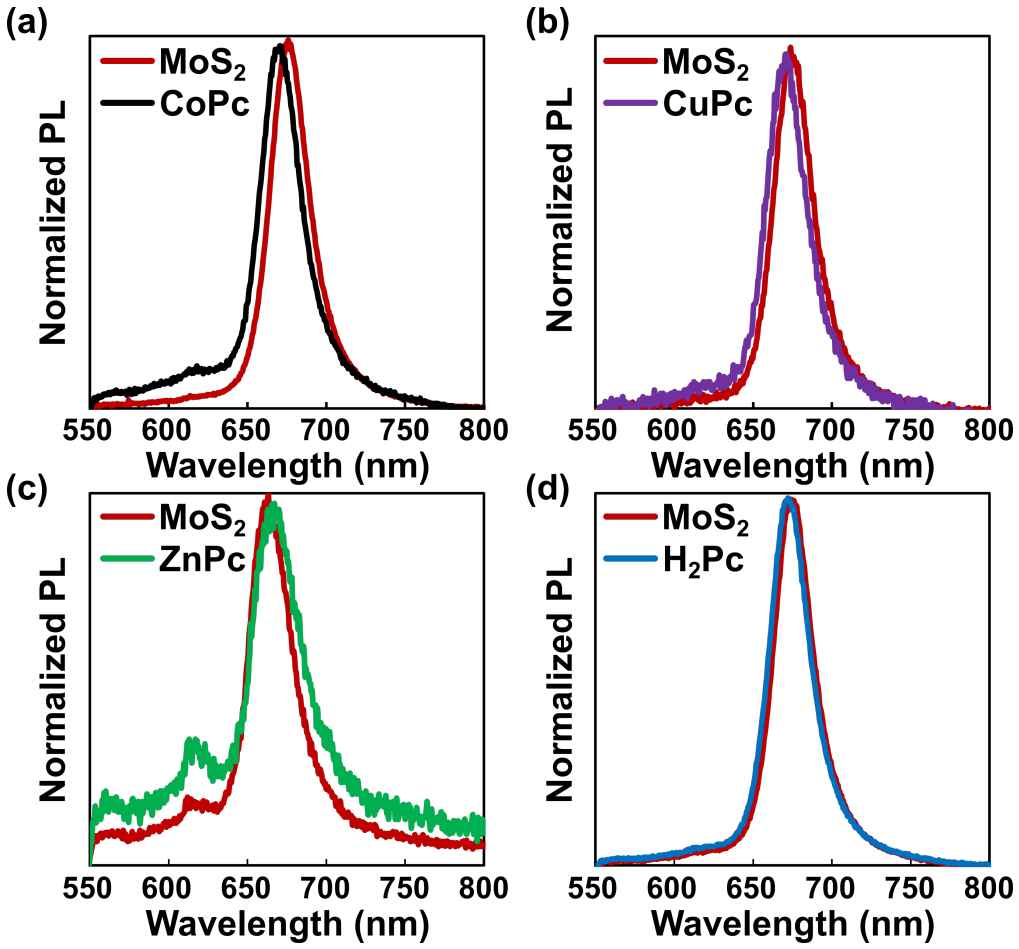

Figure 6.12. Room temperature comparisons of the utilized MPc-MoS_2 heterojunctions' PL, normalized to show no significant doping changes observed.

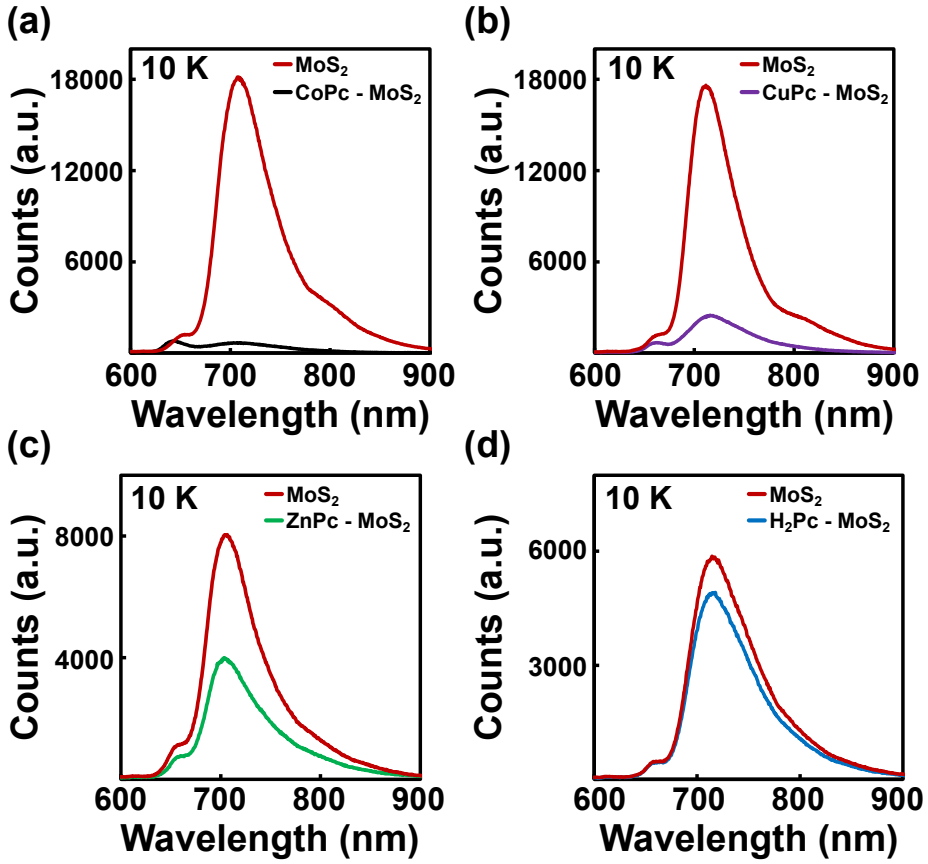

Figure 6.13. Low temperature comparisons of the utilized MPc-MoS_2 heterojunctions' PL, showing the MPc-dependent quenching.

Comparing the excitons of all MPc at room and low temperature shows that none of the MPc selected act in a way that would agree with the doping picture. None of the excitons show n-type doping: red shifting to trion dominated/contributing regimes. Instead, most show slight shift to the p-type regime. And it is in fact expected that the MPc would act as p-dopants from literature [153, 202, 203]. This can be seen in detail in Fig.[6.12] and Fig.[6.13].

To further investigate the extent of the defect quenching, time-resolved photoluminescence was carried out on the heterojunctions and bare MoS_2 via low temperature time-correlated single photon counting (TCSPC). In bare MoS_2 it is expected for the defect to have a long, several microsecond lifetime [192]. And to within the limits of available instrumentation this can be seen in Fig.[6.14]. As the exciton has lifetimes on the order of hundreds of picoseconds, it is not expected to be a contributor to the long tail component of the MoS_2 signal which can be taken as the defect lifetime past 100 ns [192]. By fitting the trace of TCSPC past 100 ns, we can extract a qualitative estimate of the lifetimes of the MoS_2 defect state and, more importantly, that of the different MPc treated heterojunctions. Doing so, shows that the MoS_2 exhibits the expected microsecond decay times with H_2Pc-MoS_2 showing a decreased slope, and the three metal core (Zn, Cu, Co) Pc cases showing no long lifetime slopes at all. That is, they show no microsecond decays associated with defects in MoS_2. This result suggests that the MPc are either providing a new, non-radiative decay path that outcompetes the radiative path or are entirely eliminating radiative decay outright.

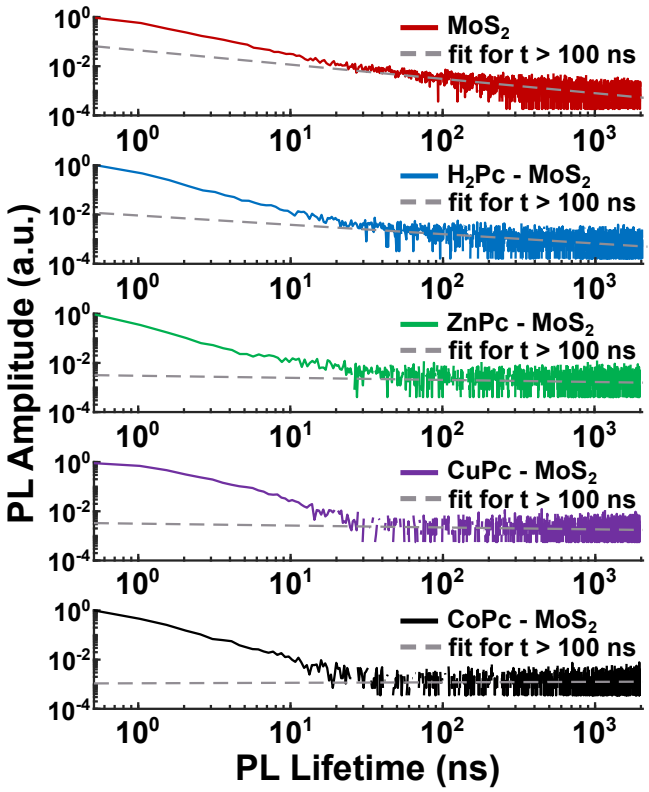

Figure 6.14. Time correlated single photon counting traces collected at 10 K with a 450 nm laser showing the photoluminescence decay for MoS_2 and the MPc-MoS_2 heterojunction. Due to instrumentation limits, we cannot accurately fit the s-scale decay of the defect emission but can qualitatively compare it by using a linear fit to the median intensity for times greater than 100 ns.

To better narrow in on potential mechanisms of this powerful defect quenching, we worked with DFT analysis and simulation provided by Qunfei Zhou and Luqing Wang. Their simulation work generated the energies of formation for defects with and without MPc heterojunctions, and the formation of charged defects which may play a pivotal role in our observed dynamics. Fig.[6.15] shows these results for S_{vacs} of different charges as a function of Fermi energy and simple band diagram of the CBM and VBM. The major

change induced by the introduction of MPc is a shift in the Fermi level where the lowest energy defect charge changes from 0 (neutral defect) to -1 (charged defect of one extra negative charge). Svac defects in bare MoS_2 show this crossover from 0 to -1 charge when the Fermi level approaches the CBM. Whereas in the $CoPcMoS_2$ case that the 0 to -1 crossover occurs at a lower Fermi levels than the bare MoS_2 case, with H_2Pc-MoS_2 between the two cases.

Based on the gated PL results in Fig.[6.11] there is a transition from dark to bright defects as the Fermi level is lowered by decreasing the gate voltage, which corresponds in the formation energy calculations in Fig.[6.15] to the transition between negatively charged defects and neutral defects. Thus we can conclude that the -1 charged defects are poor emitters and the neutral defects are the primary source of defect PL. Furthermore, we observe that the CoPc lowers the energy of the negative defect more than H_2Pc, in agreement with our observed trend in quenching efficiency shown in Fig.[6.10] (Co > Cu > Zn > H2).

Another potential mechanism of defect quenching is charge transfer. While thermally activated charge transfer processes are typically phonon-coupled and thus require more thermal energy than is available at 10 K, charge transfer can still occur by tunneling mechanisms [204]. PL quenching by tunneling has been studied extensively in coupled semiconductor quantum wells and heterostructures, and found to occur most efficiently when the energy levels of the quantum wells are in resonance [164, 205]. To investigate this possibility, calculations were done by variation in the energies of localized defect-related states with respect to charge, Fig.[6.16] shows the pDOS this calculation. Both the 0 and -1 charged Svac has localized defect states within the bandgap near the CBM.

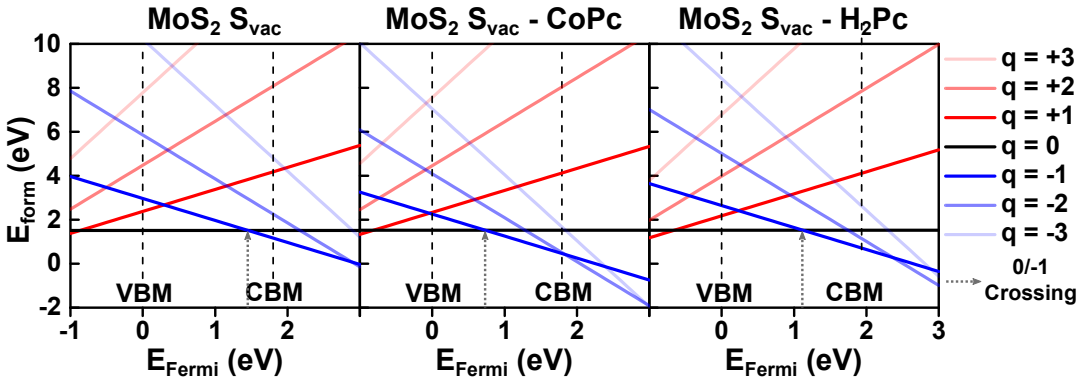

Figure 6.15. Formation energy of neutral and charged Svac vs Fermi energy for MoS_2 alone, CoPc - MoS_2 and H_2Pc - MoS_2. For a given Fermi energy, the dominant defect state will be the charge corresponding to the lowest energy line. For the MoS_2 case, at the VBM this is neutral, while at the CBM this is -1. At a Fermi level near the CBM the energy of formation of the negative Svac is CoPc < H2Pc < MoS_2 only. The Fermi energy where the defect charge changes from neutral to negative is highlighted with a gray arrow.

If the MPc is acting as a charge acceptor, the orbitals involved must be close to the defect states both energetically and spatially. Calculation of the orbital energy of the different MPc-MoS_2 heterojunctions, seen in Fig.[6.16], shows no orbitals of similar energy to the mid-gap S_{vacs}. We do however note a clear trend in the energy of out-of-plane MPc HOMO−1 or HOMO−2 d_{xz} and d_{yz} orbitals that follows our observed quenching trend from before in Co > Cu > Zn > H_2Pc. The energy of these orbitals moves from the VBM in the case of CoPc to lower energy in the case of CuPc and ZnPc, while H2Pc has no such orbitals. We note that S_{vacs} have localized states near the VBM, where the hole of a defect-bound exciton would likely exist. This suggests the possibility of resonant tunneling of defect-bound holes to the MPc HOMO−1 or HOMO2 orbitals as a competing process to radiative recombination, and a potential mechanism of defect PL quenching.

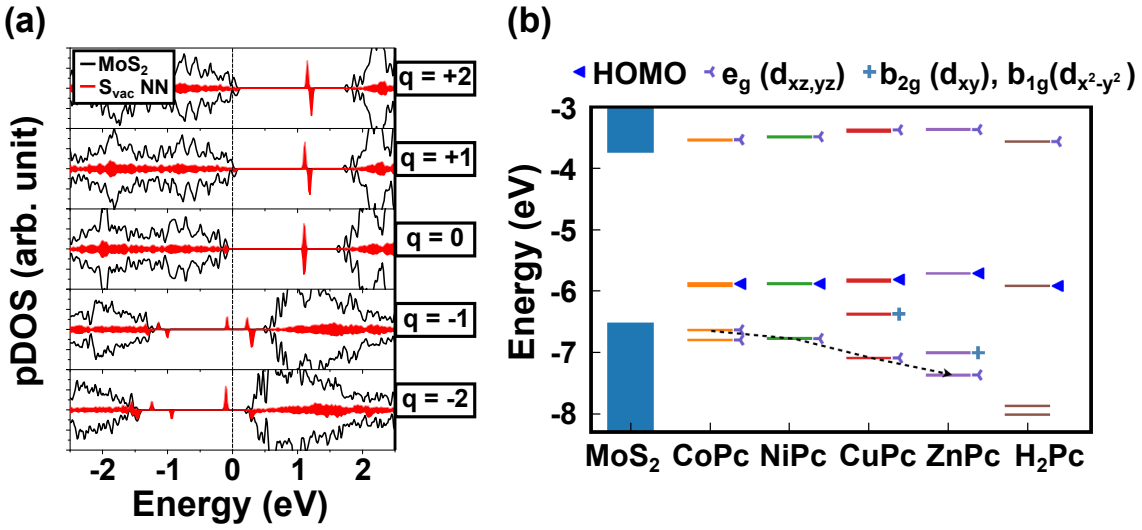

Figure 6.16. (a) pDOS of Mo_2 with sulfur vacancies of different charge. The Svac nearest neighbor (NN) orbitals correspond to the localized states induced by the Svac. (b) Band alignment diagram showing the energy of the out-of-plane MPc d_{xz} and d_{yz} orbitals moving from the valence band edge in the case of CoPc to lower energy in the case of CuPc and ZnPc, while H_2Pc has no such orbitals.

This explanation also matches with the observed trended in quenching factor, with the CoPc HOMO1 being in close resonance with the VBM, and this resonance decreasing following the quenching trend of Co > Cu > Zn > H2. This is also consistent with the gating results in Figure 4b, where the defect PL returns in CoPcMoS_2 below -100 V as the resonance between the MoS_2 VBM and CoPc HOMO−1 is reduced by the large electric field, resulting in less efficient tunneling and thus less quenching. A notable feature of this mechanism is that it is controlled by the non-frontier orbitals of the MPc, rather than the HOMO and LUMO that typically dictate charge transfer processes in heterojunctions. This points to the possibility of using molecular synthesis to control the excited-state charge transfer dynamics of an organicMoS_2 heterojunction through tuning of its HOMO

and LUMO energy while independently controlling defect quenching by tuning of the non-frontier orbitals.

This project is in the process of draft editing and review, and will soon be submitted for publication with a tentative title: Mechanistic Investigation of MoS_2 Defect Photoluminescence Quenching by Metal Phthalocyanines. Please look forward to it!

6.4. Future Work

Moving forward, MPc-TMD heterojunction offer other potential points of interest to pursue for study. Notably, can MPc with a ferromagnetic metal identity such as iron, be used as a vehicle to impart magnetic properties onto non-magnetic TMDs such as MoS_2 [206–208]. One possible approach to accomplish this, is to utilize circular polarization probing in conjunction with external fields and a magnetic Pc molecule. By pumping the TMD with circularly polarized light, we would naturally excite spins in one valley, depleting them in the valence band due to the spin-valley degeneracy in TMDs. Interaction with a coupled magnetic material could potentially result in re-population of this spin-valley depletion in the TMD as spin-doping has been a tantalizing property of magnetic phthalocyanines [209, 210]. This then effectively results in spin-accumulation in the MPc, which can be monitored via polarized absorption analogous to Optical Kerr Effect measurements [211]. The TMD would be pumped, and the MPc would be probed. If this works, one could expect this absorption to then be a function of the pump polarization as the pump is rotated between valleys, creating a figure-8 shape of polarization.

An external field could also be utilized and Magneto-Optical Kerr Effect (MOKE) measurements could also be attempted [212–214]. This is a still-new capability of the

Stern Group that I had a pleasure of bringing to fruition in my last year, and much on MOKE success will be discussed in its Chapter coming up. MPc-TMD would be another potentially interesting system to test this way in either Polar or Voigt geometries for the creation of novel magnetic heterojunctions. This project has recently started but will not finish before my tenure has concluded but please look forward to potentially exciting results!

Another project recently starting, following initial planning by Sam Amsterdam and me, is the utilization of MPc defect quenching capabilities to modify and potentially advantageously isolate Single Photon Emitter (SPE) states from defect emitters [59, 154]. These emitter states exist surrounded by and often obfuscated by broader defects such as those seen in MoS_2, by functionalizing the surface of a strained TMD it may be possible to quench these defects while leaving only visible SPEs. This would potentially open the way for novel organic-2D optoelectronic structures with SPE as dominant emitters. There is also a possibility of further insight on defect interaction with MPc depending on how the SPEs and defect states from strain interact with the functionalization. This project has recently produces some early results but the fruits of this labor will be realized after my tenure, hopefully they continue to be exciting!

CHAPTER 7

Mixed Dimensional Heterostructures: Organic Self-Assembly of Pentacene on 2D Substrates

As we saw in the previous sections optical properties of organic thin films have a very strong dependence on the substrate, and as we modify the surface we can observe significant differences. These changes arise in part from orientation changes of the molecule on different substrates [215]. In the case of MPc, previously, our films were very thin and we observed no obvious structural changes when optically observing the samples. We could trigger clumping behavior by overheating MPc regions but this was surface independent behavior and did not change the behavior of the MPc but simply made it a thicker, localized deposit.

However, pentacene deposited by thermal evaporation (like MPc), is found to form large grain crystalline films with a face-on orientation on layered materials, compared to the dendrite-like thin-film phase found on SiO_2, making it distinct from our previous work with MPc [216–218]. This structural change is most obvious on hBN, but can also be seen forming on MoS_2 and WS_2, highlighting the importance of the substrate on the structural orientation of how organic molecule self-assemble.

This set our work with Pentacene apart from MPc which looked more at the dynamics arising at the junction, while Pentacene allows us to observe the impact on substrate on the organic molecule.

7.1. Pentacene Ordering on vdW Surfaces

Similar to MPc, pentacene is a technologically relevant organic semiconductor, both for its high mobility in thin film transistors [219] and as a model system for for carrier multiplication in organic photovoltaics [220]. Since optoelectronic properties of pentacene thin films strongly depend on film morphology [221–223], control over the growth of pentacene thin films has been of particular interest and research focus for the last few decades [224–227].

Work on this project began first on MoS_2 following the work done on MPc and previous work by the Hersam and Weiss groups on charge transfer between the Pentacene and MoS_2 [178, 228]. However, it was quickly (and in part by coincidence in the process of making higher quality layers of MoS_2 on hBN for cleaner substrates) found that many of the same phenomena observed on MoS_2 were observed much more obviously on hBN layers in particular with the morphology changes of the pentacene film on hBN vs. MoS_2 vs. SiO_2, recall the previously presented example of this in Fig.[6.1c-d]. To that end, the focus will initially be on pent-hBN heterostructures and will then briefly discuss results on MoS_2 at the end.

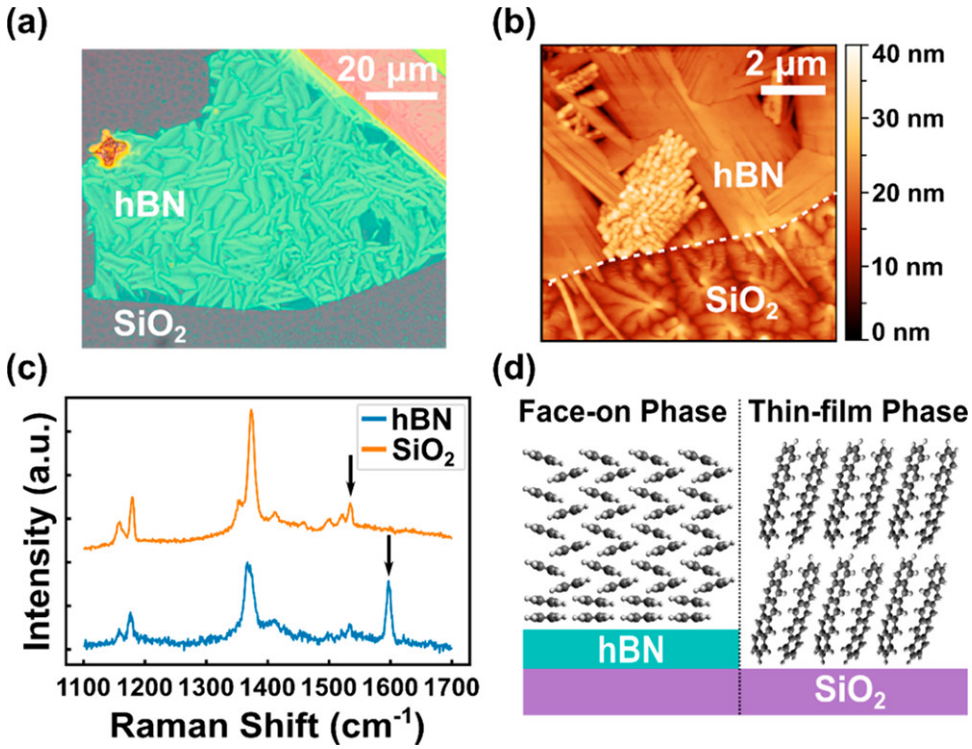

Figure 7.1. (a) Microscope optical image of an hBN on SiO_2 with pentacene deposited over the entire area. The dendritic structure of pentacene vs. the needle-like formation on hBN is clearly seen. (b) AFM map showing the fine structure not clear in optical imaging, and the abrupt transition from hBN to SiO_2 in phase formation of pentacene. (c) Raman spectra of pentacene on hBN and SiO_2 via 532 nm excitation, normalized to their respective maxima at 1370 cm^{-1} and offset to highlight the different modes that are visible. Arrows indicate the Ag vibration at 1533 cm^{-1} in pentacene-SiO_2 and the B_3g vibration at 1597 cm^{-1} in pentacenehBN. (d) Schematic illustration of the face-on orientation of the pentacene film on hBN and the edge-on orientation of pentacene of the typical thin-film phase on SiO_2. Adapted with permission from [10]. Copyright 2021 American Chemical Society.

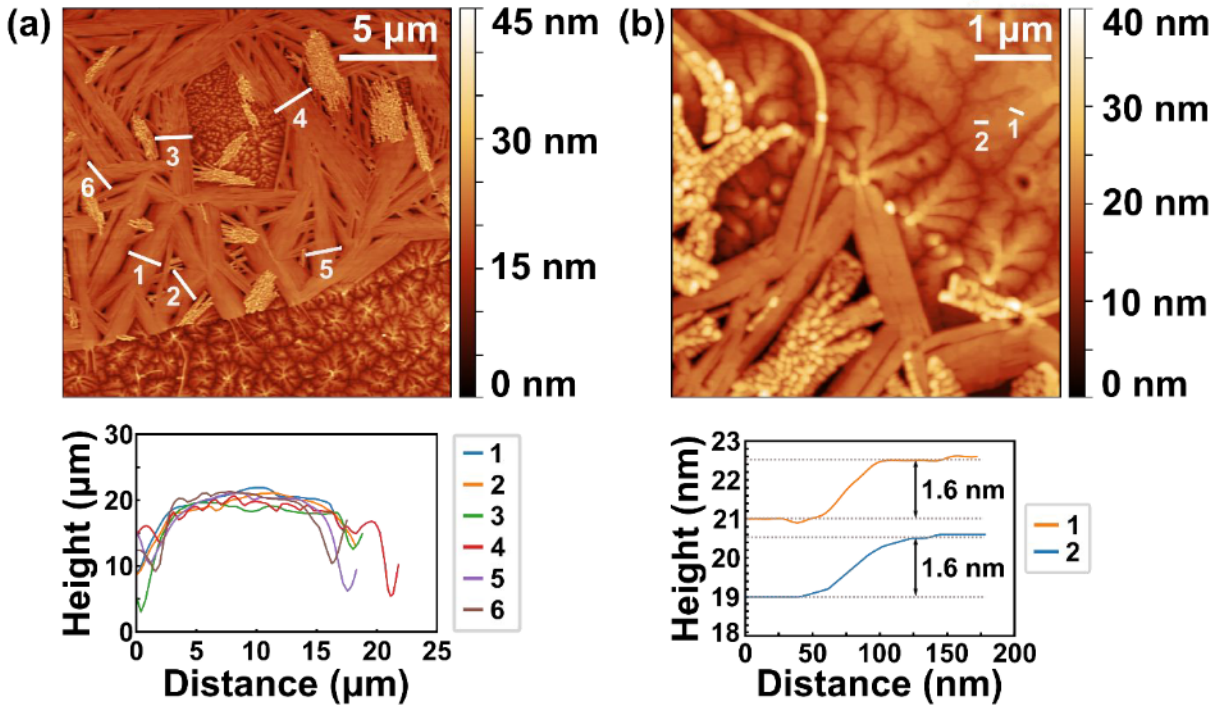

Figure 7.2. AFM mapping on pentacene-hBN and interface of hBN/SiO_2 on different hBN showing the same sharp transition from needle-like to dendridic structures. (a) Shows that dendridic structures can also form on hBN. (b.) SiO_2 dendridic structures. (Bottom) Respective profilometry of the marked structures in (a-b). Adapted with permission from [10]. Copyright 2021 American Chemical Society.

As seen optically and in high detail with AFM in Fig.[7.1a,b] pentacene films on hBN have a very distinct morphology from that observed on SiO_2. On hBN, the pentacene forms very long needle-like structures that appear to form in large bundles. Conversely, on the SiO_2 the pentacene forms expected dendrite pyramidal structures. These dendrites are well studied at room and low temperatures [222, 229] but the needle-like morphology on hBN is novel and required investigation. A precise understanding of the differences in optical properties between these two morphology phases can facilitate design of emerging

optoelectronic devices with the prototypical pentacene as a component in organic-vdW heterostructures.

To do this, photoluminesence measurements were done from room to low temperatures on pentacene on both hBN and SiO_2. To fabricate the samples, hBN was mechanically exfoliated onto standard thermal oxide substrates (285-300 nm SiO_2/Si) and then coated with 20 nm of pentacene by thermal evaporation. AFM of the hBNSiO_2 edge in Fig.[7.1b] shows an abrupt change in pentacene phase between the two substrates. The dendritic structures on the SiO_2 are typical of the thin-film phase of pentacene. Additionally, it can be seen that the coverage of the needle-like structures on hBN is not complete, and the gaps between the crystals show either a dendritic thin-film phase or nanoscale grains of indeterminate phase.

Raman spectra seen in Fig.[7.1c] of the two pentacene phases shows the ratio of intensity of the two highlighted vibrational modes. These modes help us deduce the orientation of the pentance on hBN vs SiO_2. The modes highlighted, B_{3g} (1597 cm^{-1}) to A_g (1533 cm^{-1}) are determined by the orientation of the pentacene with respect to the surface normal. The dominant B_{3g} mode in the case of hBN indicates that the pentacene is lying flat/face-on whereas, on SiO_2, the A_g phase indicates the pentacene is edge-on [230, 231]. From this we construct the understanding of the differing orientations of pentacene on the two different substrates as seen in Fig.[7.1d]. It should be noted that no changes were needed in the growth process (a common tool for manipulating growths on a singular substrate) but instead by simply varying the substrate we can modify the growth significantly, keeping everything else the same. This will be further seen in the case of MoS_2 and WSe_2 where the growth shows further dependence on the substrate.

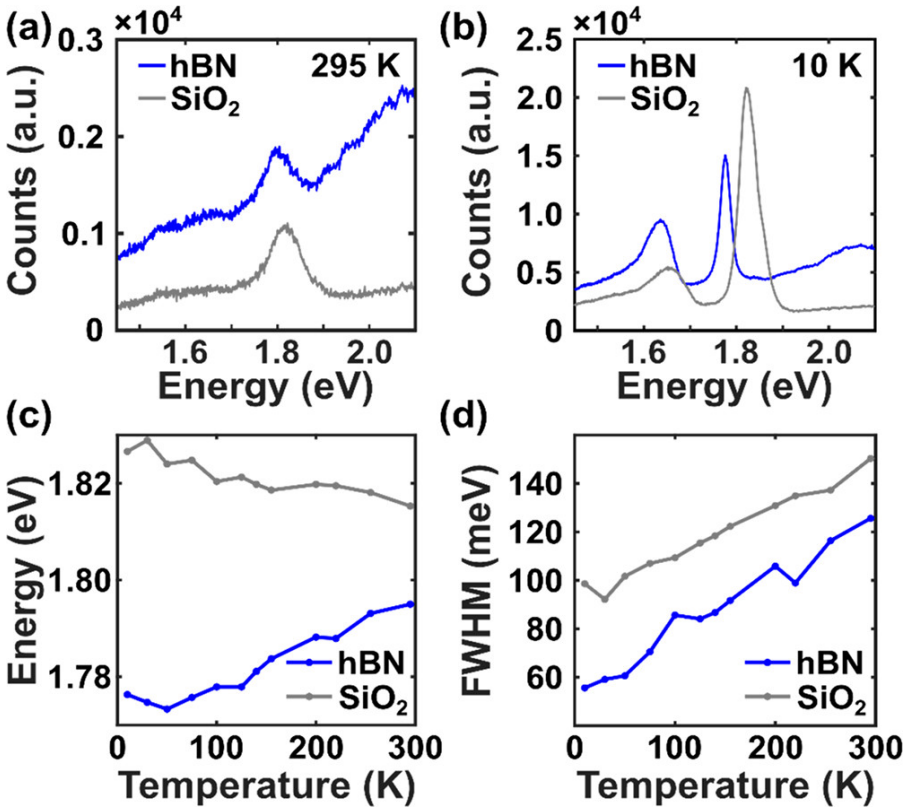

Figure 7.3. (a) Room temperature (300 K) PL comparison of pentacene on hBN vs. SiO_2. (b) Low temperature (10 K) PL comparison of face-on and edge-on pentacene on hBN and SiO_2 respectively. The higher energy peak is the pentacene free exciton (FE) emission and the lower energy is self-trapped excitons (STE) in the pentacene films. Emission from the face-on phase on hBN (blue) exhibits reduced line width and a lower energy relative to emission from the thin film phase on SiO_2 (grey). (c) Temperature dependence of emission energy of the FE for the two phases of pentacene. The face-on phase lowers in energy with low temperature while edge-on phase increases in energy. (d) Temperature dependence of emission full width half maximum (FWHM) showing that both phases show narrower emissions at lower temperatures. The face-on phase emission is narrower than that from edge-on phase at all temperatures. Adapted with permission from [10]. Copyright 2021 American Chemical Society.

At room temperature, the emission path for pentacene is dominated by ultrafast singlet fission [232], resulting in the observed low emission on either substrate. This recombination is highly inefficient. However, as temperature drops the recombination path becomes increasingly dominated by free exciton (FE) and self-trapped excitons (STE), at 1.8 and 1.65 eV respectively, and at 10 K the emission is clear and strong [233, 234]. Additionally, there is a broad low-energy shoulder extending through 1.5 eV., owing to pentacene defects [233]. The face-on phase FE and STE emission is at 40 meV lower energy relative to the edge-on PL on SiO_2 [222].

Temperature sweeping further shows that the two phases show distinct behavior with changing temperatures. hBN pentacene shows a significant red shift in energy with decreasing temperatures from room to low temperatures. This behavior is similar to previous work done with pentacene [223, 229], where when grown on polyethylenterephthalate (PET), it exhibits similar energy shifts. It is important to note that hBN and PET have similar thermal expansion coefficients, 5-15x10^{-5} K^{-1} for PET [235] and 2-4x10^{-5} K^{-1} for hBN [236]. In the case of SiO_2, it can be seen that the temperature behavior shifts in the opposite direction (lower energy) and with much less of an overall shift observed. This can potentially be attributed to two possibilities: the lower coefficient of thermal expansion of SiO_2 (5x10^{-7} K^{-1}) [237] and relatively weaker interactions between substrate and molecule. Both phases show similar temperature dependence of their linewidths, with the face-on phase is narrower at all temperatures. This suggests a higher degree of ordering and fewer defects in the face-on phase. The narrower linewidth and lower energy FE emission suggest that the face-on phase of pentacene on hBN is optically similar to pentacene single crystals.

These results point to the important role of the substrate on molecular ordering and significant impact on observable exciton dynamics. Further reading on this and time-resolved analysis can be found in our published work:Tailoring the Optical Response of Pentacene Thin Films viaTemplated Growth on Hexagonal Boron Nitride, J.Phys.Chem.Lett. **2021**, 12, 2631 [10].

7.2. Pentacene on TMDs, and Defect Interactions

Analogous to the dynamics seen in phthalocyanine-MoS_2 heterojunctions in the previous chapter, pentacene also modifies the underlying TMD and is seen to similarly have defect quenching dynamics as well as influence on exciton recombination. First and foremost, however, just as in the case of hBN discussed above, pentace on TMDs takes on a different phase from that on SiO_2 as seen in Fig.[7.4] [226, 231]. It is notable that the exact structure appears to be consistent across the tested layered materials, forming into long needle-like growth phases. However the exact size of the growth is evidently dependent on the exact material chosen. hBN as per the previous section showns very large needle-like growths, followed by WS_2 with smaller needle-like growths and, finally, MoS_2 showing the smallest needle-like growths. Dendridic structures can still be seen in all growths and the SiO_2 consistently forms dendrites, ruling out variations in pentacene growth.

The exact origin of these differences has not yet been studied systematically but is a potentially interesting project for consideration by future students in these fruitful collaborations between the Stern Group and Hersam and Weiss Groups.

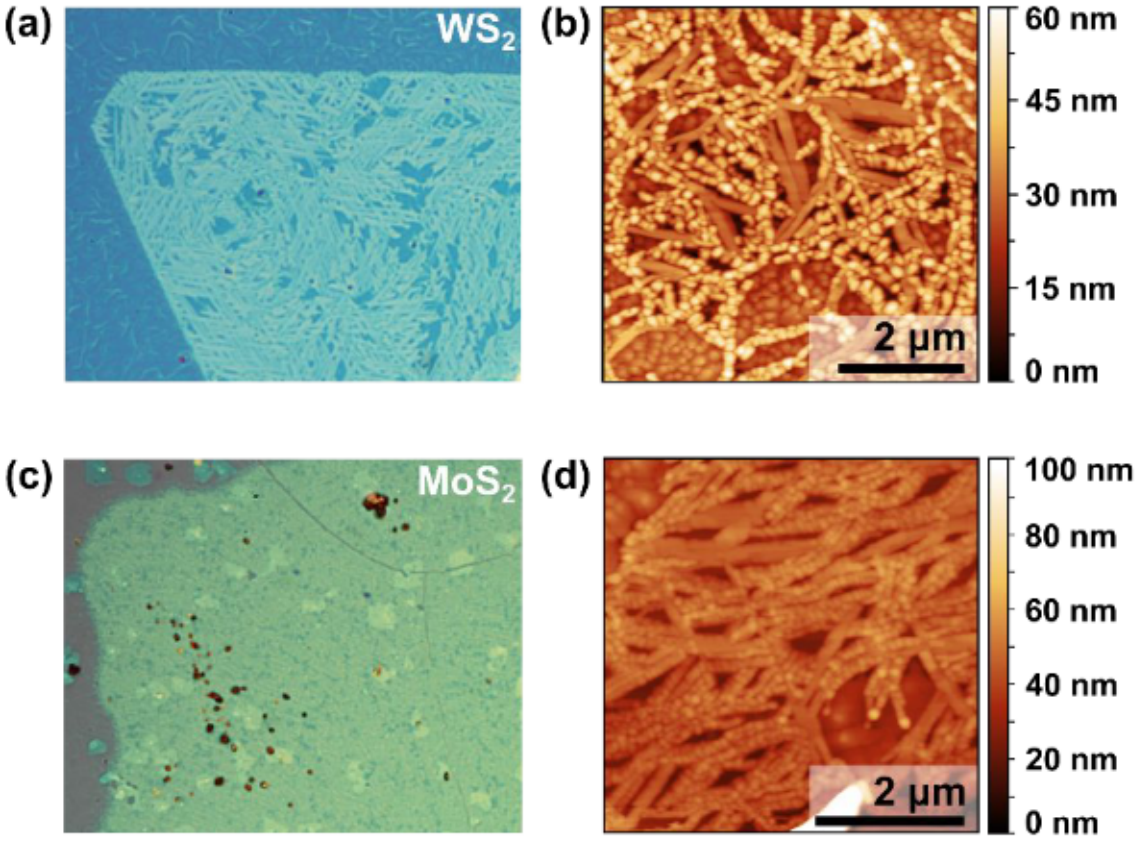

Figure 7.4. (a) Pent-WS_2 heteorjunction (surroundings are SiO_2) shows similar formation of needle-like structures on WS_2, there are notably much smaller however. (b) AFM of (a.) showing the needle-structures. (c) Pent-MoS_2 with even smaller needle-like structures. (d) AFM of (c). Adapted with permission from [10]. Copyright 2021 American Chemical Society.

As previously mentioned, the heterojunction has a noticeable impact on the underlying material by the pentacene [178, 228]. In hBN, this is difficult to quantify as hBN is a non-emissive insulator, but by utilizing WS_2 and MoS_2 we can look at exciton dynamics in the visible spectrum as influenced by the pentacene. At room temperature, the Pent-MoS_2 junction was observed to be a convolution of pentacene PL and MoS_2 PL, with a notable quenching of the MoS_2 PL while the pentacene showed no significant changes. This is

shown and further discussed in Fig[7.5] of room temperature PL of the MoS_2, pentance, and the heterojunction with fits to extract the convoluted data. Fig[7.5d] compares the extracted fit PL of the heterojunction MoS_2 vs. the standalone layer, showing the clear quenching observed. There is also a notable blue shift of the exciton peak, which can be understood as p-doping from the pentacene, in analogue to what we saw before with phthalocyanines.

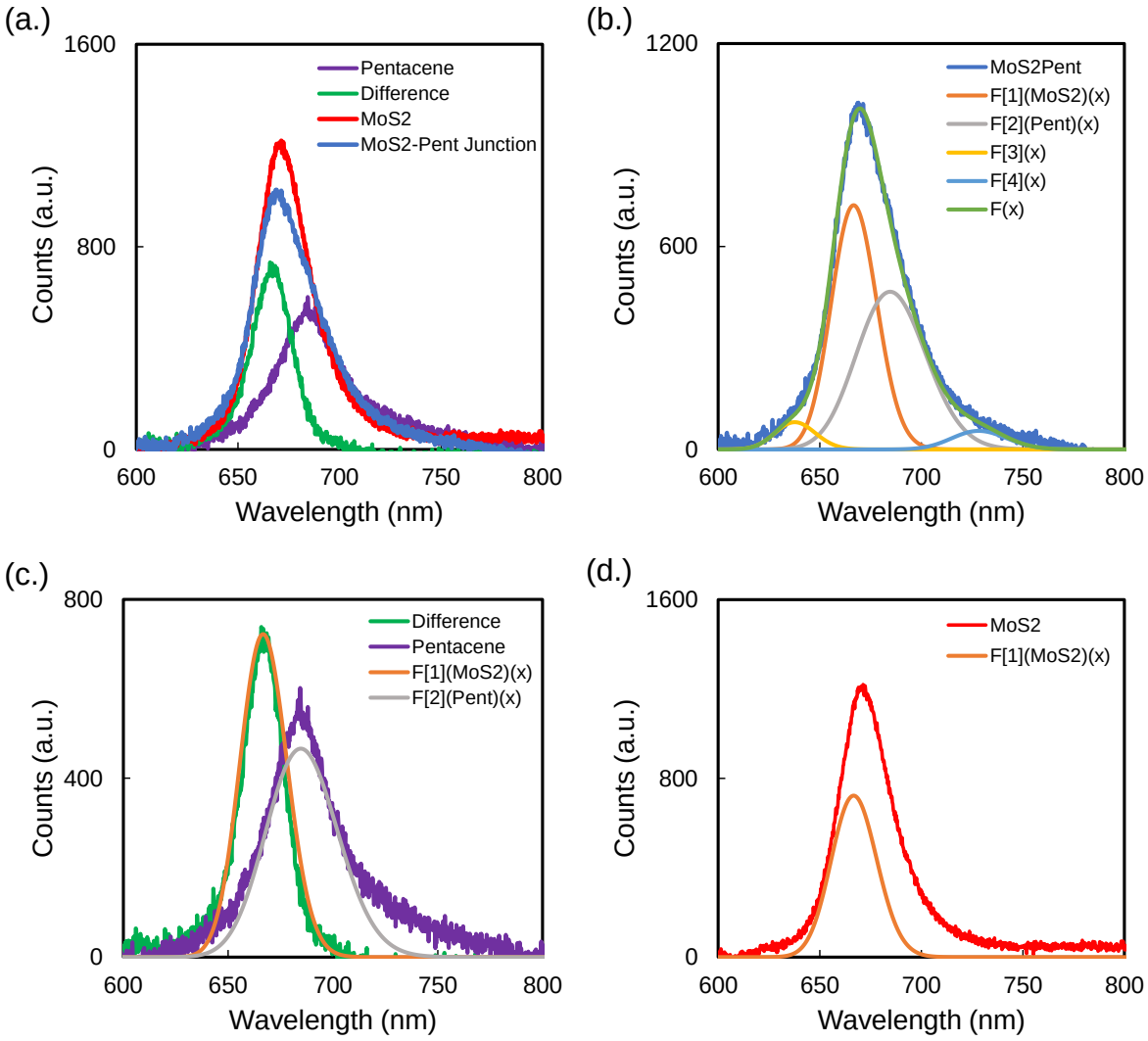

Figure 7.5. (a.) Room temperature comparison of MoS_2, Pentance, and Pentacene-MoS_2 heterojunction in Red, Purple, and Blue respectively. Subtracting the raw pentacene signal from the Pent-MoS_2 junction is shown in Green, suggesting a quenched, blue-shifted exciton. (b.) Fits of the Pent-MoS_2 heterojunction. (c.) Comparison of the extracted fits from (b.) to the difference spectra and pentacene-only spectra from (a.). (d.) Comparison of the MoS_2 to the fit (and difference signal) from the heterojunction, showing the quenching and blue-shifted signal.

At cryogenic temperatures (10 K), the interaction becomes more complicated. The first main difference observed is the large quenching of MoS_2 defect states. This defect quenching can be seen in Fig.[7.6], where it is clear that the defect state (X_B) is completely suppressed in the junction. Curiously, at low temperature, the exciton of MoS_2 no longer shows any significant doping with the exciton of MoS_2 only and of the heterojunction lining up at X_A. Moreover, the pentacene exciton (X_P) is also suppressed and a new peak can be observed at X_J. To confirm that this new peak is not the defect state but shifted, power sweeps were done on the sample and can be seen in Fig.[7.7]. The MoS_2 excitons (bare and in the junction) and X_J show linear response to power but defects show the expected non-linear, saturation response. This is an expected outcome as there are a finite number of mid-gap defects that can act as pathways for recombination and can be saturated with sufficiently high power of excitation [158, 238, 239]. Moreover, a power fit produces x^n with $n = 1$ for the excitons as expected, defects also show an expected $n << 1$. This indicates that the new peak is excitonic in behavior.

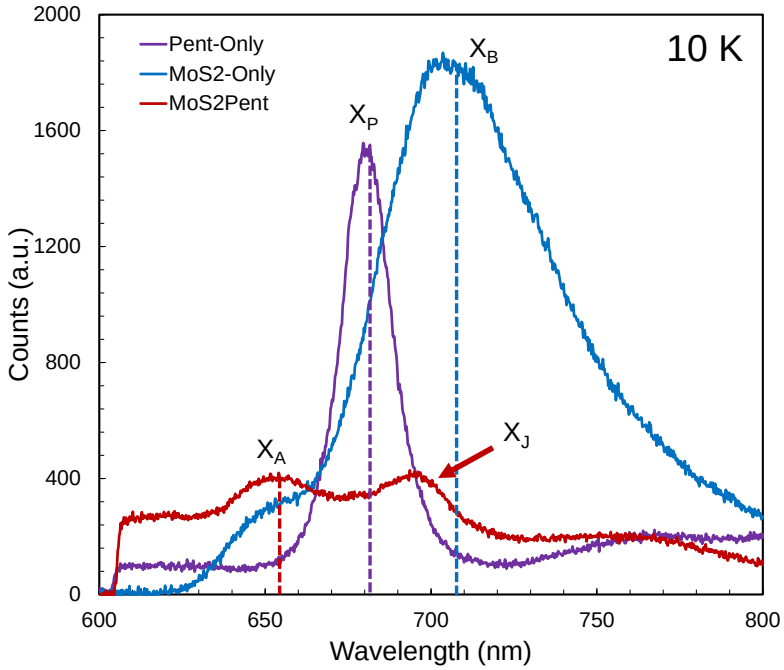

Figure 7.6. MoS_2, Pentacene, and Pent-MoS_2 heterojunction PL at 10 K. The quenching of defects X_B are quenched in the junction and a new peak X_J is visible.

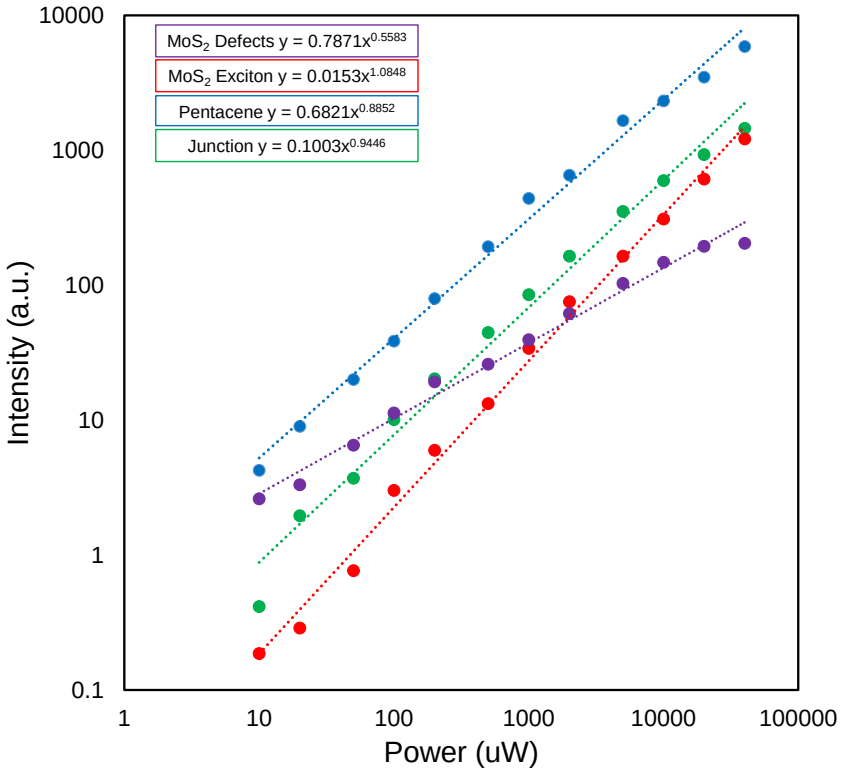

Figure 7.7. Power sweep on MoS_2, Pentacene, and Pent-MoS_2 emission to quantify defect and excitonic behavior.

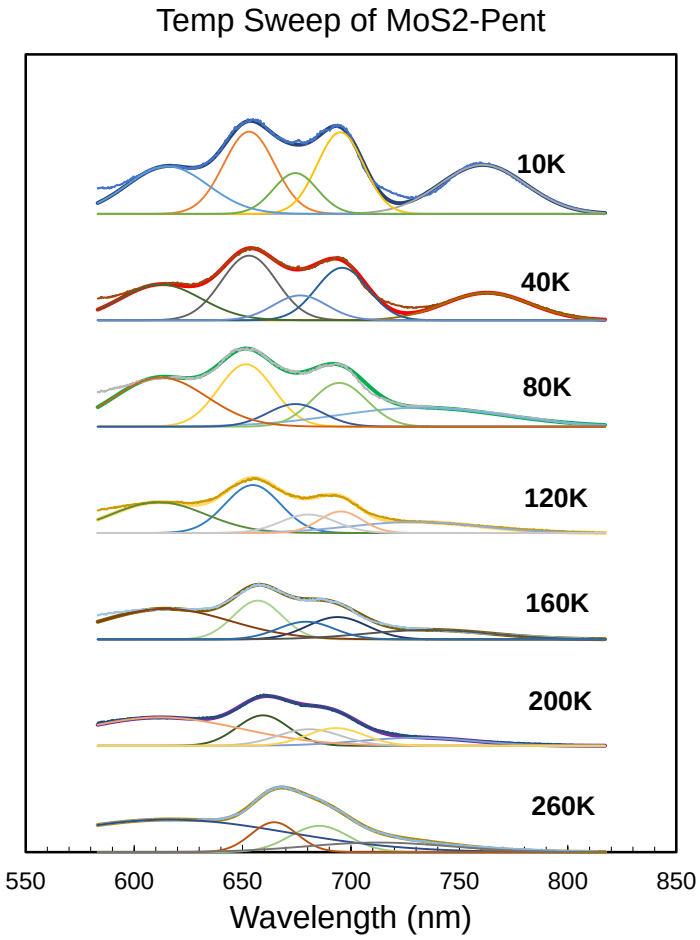

Figure 7.8. Temperature sweep of Pent-MoS_2. Fits were attempted to track the peak X_J as discussed in Fig.[7.6]. It is unfortunately the exact origin in MoS_2 is not clear due to the convolution of emission of MoS_2 and that of Pentacene itself.

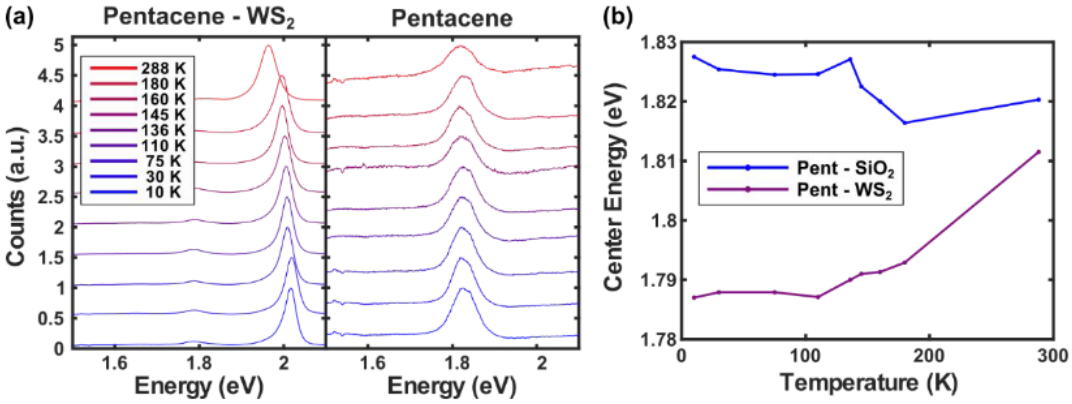

Figure 7.9. Temperature-dependent PL of Pent-WS_2. (a) PL plots of the pentacene thin films on WS_2 and SiO_2. (b) Energy of pentacene free exciton emission versus temperature. The film on WS_2 behaves similarly to the film on hBN, although with a lower overall energy shift. Adapted with permission from [10]. Copyright 2021 American Chemical Society.

Indeed, recalling the behavior of pentacene on hBN we expect that it's emission red shifts with decreasing temperature. It is very likely that this X_J is the pentacene emission but shifted at low temperatures. Temperature sweeps on MoS_2 and WS_2 were done to try and quantify this. In MoS_2, the excitons and pentacene are highly convoluted and it is very difficult to say with certainty what peak is shifting at X_J, this can be seen in Fig.[7.8]. Fits were done to best try and extract likely peak positions but due to the heavy convolution is heavily guess-work based. The MoS_2 exciton and X_J are very obvious at low temperature but the exact evolution of the latter is unclear. Nevertheless, the lack of defects is evident and consistent here as well.

However, in the case of WS_2 it is very clear that the pentacene is red shifting on the WS_2 as expected unlike on SiO_2 as seen in Fig.[7.9]. The exciton emission of WS_2 is not convoluted with pentacene, being approximately 170 meV blue shifted from the MoS_2 exciton and 250 meV from that of pentacene. This makes it an ideal study case and, indeed, we see that the pentacene emission clearly red shifts. This is in fact a similar overall shift (100 meV) as seen in MoS_2 if we assume X_J is a modified pentacene emission. This shift is smaller than that observed on hBN but it is nevertheless a common quality and different from the observed trend on SiO_2, likely owing to the similar overall needle-like growth. MoS_2 and WS_2 have smaller thermal expansion coefficient factors approximately 10^{-6} K^{-1} [240–243], which may explain the lower thermal shift.

7.3. Surface Quality and Film Growth

As a brief final comment and the wrap up of this section, Fig.[7.10] shows the importance of a clean substrate. Even with the ideal substrate of hBN used as well as WS_2,

after exposure to patterning techniques which often leave behind resist residue [244–246] and other contaminates the entire sample behaves similarly with formation of globule-like structures rather than dendrite or needle-like substrates.

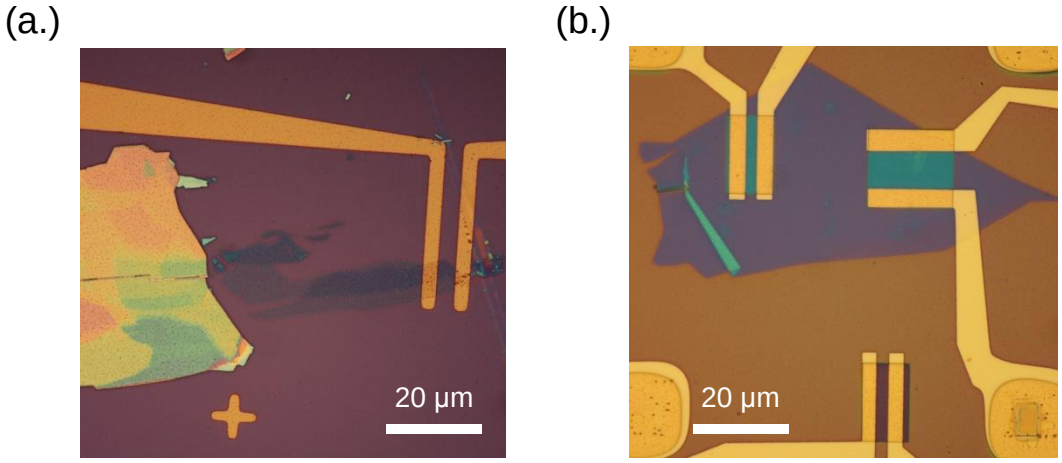

Figure 7.10. Evidence to the importance of surface quality on pentancene growth. (a.) WS_2 sample with contacts developed via PMMA/MMA patterning, due to surface residue left by the process the entire sample is coated in dendritic structures of pentacene with no visible needle-like formations. (b.) As with (a.) now demonstrated on hBN with windows defining gaps of resist where the hBN and SiO_2 are exposed. Due to residue from the processing, growth does not form into needle-like structures.

All in all, these results highlight the flexible, powerful capabilities of layered materials as substrates for novel mixed dimensional heterostructures. The substrate layer as well as the molecule chosen can have significant effects on the behavior of the resultant heterojunction.

CHAPTER 8

Probing Passivated Magnetic 2D Materials with Magneto-Optical Spectroscopy

8.1. Introduction

Magnetic 2D materials offer attractive platform for spin and spin-control properties opening up a new degree of freedom in 2D material physics and the realization of spintronic devices [247–249]. These new options for devices can be built atop the already versatile platform of 2D materials leveraging all previous advantages.

While theoretical simulations can often predict magnetic properties of materials, experimental work is necessary to confirm and realize those properties in a lab environment, and capture any nuances such as localized domain effects [250] and strain or field dependent properties [251]. To accomplish this several experimental techniques can be used but for this section I will focus on magneto-optical Kerr effect (MOKE) spectroscopy [212, 252].

Specifically, I will be discussing the realization of MOKE spectroscopy [253–255] in the Stern Lab in co-partnership with my undergraduate understudy and lab partner Peter Gilhwan Lin, and the breakthroughs we made in our successful quest to make a robust, high-signal to noise experimental set-up. Our successes have made the Stern Lab one of the main leaders in magneto-optical capabilities at Northwestern University and the go-to for many collaborative efforts. Subsequently I will then discuss how I leveraged MOKE

spectroscopy to investigate and confirm the robust protection of a novel encapsulation technique of volatile magnetic layered materials, and studied the magnetic properties of several new interesting candidates for layered 2D magnetic materials. Which paves the way for work on magnetic mixed dimensional heterojunctions.

8.2. Magneto-Optical Kerr Effect

Magneto-optical Kerr effect (MOKE) is the change in polarization of linearly polarized light as it undergoes reflection off a magnetic material surface [253–255]. When incident linearly polarized light is reflected from the surface of a magnetic material, the axis of polarization will rotate and become elliptical with respect to the strength of the magnetic field. The degree to which the polarization rotates and becomes elliptical is Kerr Rotation and Kerr Ellipticity, respectively. The Kerr Rotation Angle, encompassing both Kerr Rotation and Kerr Ellipiticity, can be defined as follows:

$$\Phi_k = \theta_k + i\phi_k \tag{8.1}$$

with the real component θ_k representing Kerr Rotation and the imaginary component ϕ_k representing Kerr Ellipticity. The dependence of the Kerr Angle on an externally applied magnetic field can provide key insights into the magnetic nature and ordering of the material being tested. Kerr Angle can highlight ferromagnetic or anti-ferromagnetic ordering, domain formations or uniformity, and even the number of layers being studied.

Naturally, this also allows MOKE to be used as a method of probing the magnetic properties of unknown or unconfirmed magnetic materials. A simple diagram of the measurement is presented in Fig.[8.1].

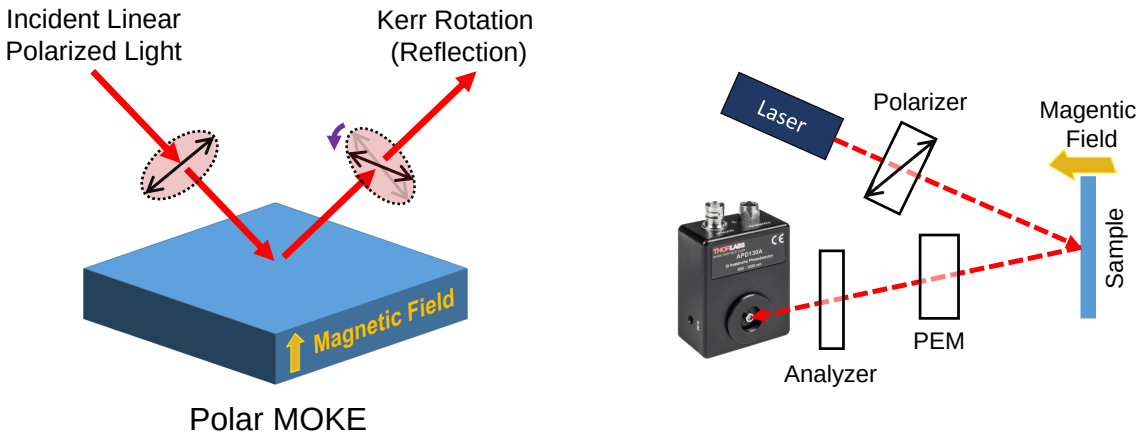

Figure 8.1. (Left) Simple example of polar-MOKE, where incident linear polarized is reflected off the surface of interest and experience a rotation of polarization that is captured as Kerr Rotation. The sample is modified by a magnetic field normal with the plane of the surface. Note, light-angles presented in this diagram are purely for demonstration. The measurement is performed at normal incidence with a lens and not a sharp angle. (Right) Simple measurement set-up used for measuring polar-MOKE for the work presented. A linear polarizer (Glann-Thompson) is used to polarize light from a tunable laser source (visible) with a high extinction ratio. The reflected light is then passed through a PEM (Photoelastic Modulator) and then a subsequent linear polarizer-analyzer on to a photodiode (Avalanche Si Photodiode).

The theoretical origin of MOKE is caused by energy level splitting of the material's band structure when a material is exposed to a sufficiently strong external magnetic field (Zeeman Splitting). In a magnetic material such as CrI_3, when this splitting occurs the off-diagonal terms of its permittivity tensor changes. In the polar-MOKE geometry, this can be written as [256]:

$$\epsilon = \begin{bmatrix} \epsilon_{xx} & \epsilon_{xy} & 0 \\ -\epsilon_{xy} & \epsilon_{yy} & 0 \\ 0 & 0 & \epsilon_{zz} \end{bmatrix} \tag{8.2}$$

That is to say, the speed at which light propagates through the material in different directions changes. This is commonly stated as:

$$v_p = \frac{1}{\sqrt{\epsilon\mu}} \tag{8.3}$$

Where ϵ is the aforementioned permittivity tensor, and μ is the magnetic permeability. Because linearly polarized light is a superposition of circularly polarized light, the change in the permittivity tensor alters the propagation of the component circularly polarized light through the material, creating circular birefringence in the material. This manifests as phase-shift between the components and a change in the linear polarization of the light that returns from the material in reflection. This change, or rotation, is the measured Kerr Rotation by MOKE.

All discussion on how MOKE spectroscopy was achieved and the work that went into getting the set-up operational can be found in the Appendix.

8.3. MOKE of Chromium Iodide

There have been a wide variety of layered magnetic materials that have drawn attention for potential monolayer-magnetic properties. A standout candidate that is now well

studied in literature is chromium triiodide (CrI_3) which has been shown to have ferromagnetic ordering to the monolayer limit below its Curie temperature (T_c) of 61 K for bulk and 45 K for monolayers [206, 212, 213, 252, 257–259]. As such, it has made a great candidate for testing novel encapsulation techniques as well as the robustness of our MOKE capabilities in the Stern Lab. The need for these techniques and their development is the volatile nature of CrI_3 which can, under air and light exposure, rapidly decay and as such MUST be carefully handled and protected [260]. One possibility is limiting all work with CrI_3 and other similarly volatile magnetic materials to only within the confines of a glovebox but this would impede and significantly limit any scientific study.

The common solution to this volatility and limitation on CrI_3 has been hBN encapsulation, a common technique in layered materials that is known to help protect materials from the environment and decay [261, 262]. More importantly, the hBN has not been shown to adversely affect the magnetic properties of the layer and as such has be used as a building platform for building magneto-optical or magneto-electronic devices with CrI_3 [212, 252]. However, this technique is neither scaleable nor thoroughly robust. For the former, hBN encapsulation requires normal exfoliation and transfer of individual hBN parts for both a top and bottom sandwich of hBN around the layer of interest, and building a stack of hBN/CrI_3/hBN heterostructures all within a glovebox environment. While this approach is great for the making of and study of one device, it becomes an increasingly impractical method for rapid production or increasing layer sizes and films. For the latter, we have observed that the hBN encapsulation does in fact still lead to decay after several months of atmospheric exposure which is not ideal as can be seen in Fig.[8.2].

These limitations and more make for finding a new, more practical, scalable, and robust method of protecting volatile magnetic layers tantalizing.

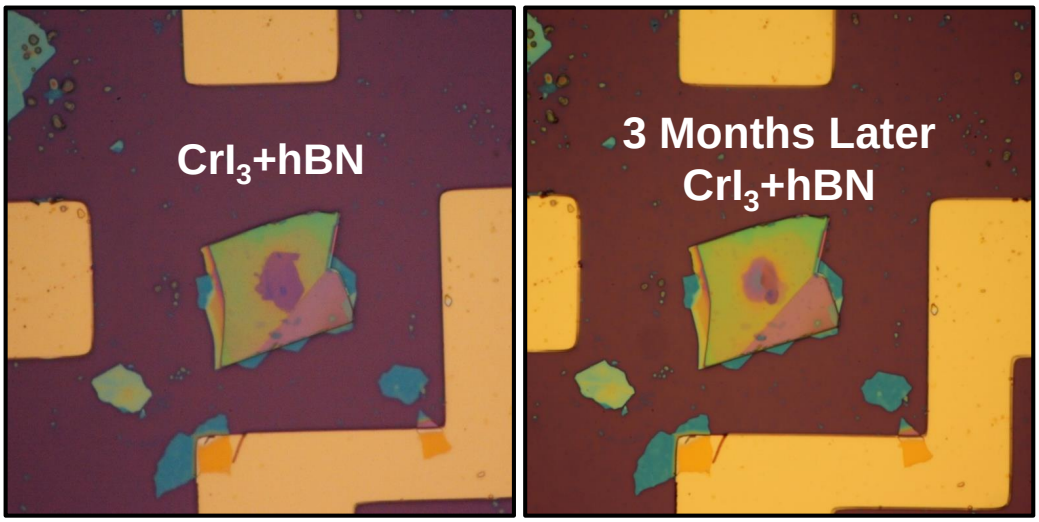

Figure 8.2. (Left) Bulk (10L+) CrI_3 encapsulated in hBN on top and bottom, on a SiO_2 substrate. Picture was taken shortly after the structure was finalized and prepared. Gold alignment markers created through e-beam lithography can be seen on the periphery to allow for finding of the sample after it has been inserted into a cryostat. (Right) After three months of exposure to ambient and light, the CrI_3 has visibly decayed under the hBN encapsulation and only traces of the structure can be seen with the rigid, crystal lattice mostly lost. This highlights a long-term limit on hBN encapsulation, likely arising from gaps at the interface of the layers that arise during the transfer process.

In collaboration with the Hersam group, alumina (Al_2O_3) based passivation of CrI_3 using atomic layer deposition (ALD) was studied. This technique offers scalable longterm protection of CrI_3 from atmospheric decay as well as the preservation of its magnetic properties without damaging the material [263]. If successful, this technique would open the way for a scalable, robust approach to protecting CrI_3 or other layered magnetic materials which would have significant impact in possible broader applications for magnetic

layered materials in application to modern technology. To accomplish this, samples of monolayer to trilayer to bulk CrI_3 were prepared by the Hersam group with ALD Al_2O_3 encapsulation alongside several hBN-encapsulated samples for comparison.

8.3.1. Bulk Chromium Iodide

Initial work with CrI_3 began with bulk Al_2O_3 passivated and bulk hBN encapsulated CrI_3 as strong anti-ferromagnetic signal was expected and would serve as a good initial barometer on the capabilities of passivation. All sample preparation and measurement details discussed here will hold true for thinner materials as well and will not be repeated unless important differences need to be identified and highlighted. In this section, focus will be on bulk material of 10+ layers and their results.

Samples were prepared by micromechanical tape exfoliation on orders of 10+ layers on amorphous SiO_2 substrates and either used to create hBN-CrI_3 heterostructures through viscoelastic stamping (see Appendix for techniques on hBN stamping) or directly passivated with ALD. Once protected either by Al_2O_3 or hBN, electron beam lithography was performed to create large gold guiding leads that created a recognizable pattern around the target in order to facilitate finding and measuring the specific layers. An example of this patterning can be seen in Fig.[8.2], the image is of hBN/CrI_3 with nearby gold patterning but the designs were the same for alumina capped layers. Following preparations and successful lift-off of 50 nm of gold deposition for the markers, samples were then transferred to a glovebox for storage until tested. Following a first testing, samples were allowed to sit in ambient within a climate-controlled environment (25% humidity, 20 degrees C).

To probe the magnetic ordering of the passivated (alumina) and encapsulated (hBN) CrI_3 samples, we measured their MOKE response as a function of applied external magnetic field. The samples were placed inside a variable-temperature cryostat (Attocube AttoDRY2100, details on sample loading are in the Appendix) that ranges between 1.6 K and 300 K, with a variable-field magnet that ranges from 0 T to 9 T. The measurement employed a Faraday geometry, in which the applied field is perpendicular to the sample, and utilized a polar-MOKE scheme in which the probe laser is incident normal to the sample plane. This scheme allowed for probing of the out-of-plane magnetization of the sample, which is what CrI_3 is known to exhibit [212]. The optical probe was a tunable Ti:Sapphire laser (M Squared SolsTiS) with wavelength capabilities from 530 nm to 660 nm. The probe laser was delivered by fiber to the measurement setup and was first chopped by an optical chopper to modulate the intensity at a particular frequency (1033Hz) and linearly polarized at 0 deg with a Glan-Thompson linear polarizer (LP). The beam was then transmitted through a 70:30 non-polarizing beamsplitter down into the cryostat onto an aspheric lens of $f = 7.5$ mm in a custom-built adapter to achieve a small spot size with minimal stray field effects.

The polarization of the light reflected off of the sample was modulated by the photoelastic modulator (PEM) at a resonant frequency of 50 kHz. The PEM was oriented parallel to the Glan-Thompson LP at 0 deg. The modulated beam was then polarized at 45 deg by a final linear polarizer before collection. Finally, the modulated output beam was focused onto a fiber coupled to an amplified photodiode for signal detection. A two lock-in amplifier scheme was used for detection, to measure the signal modulated at the first and second harmonics of the resonant frequency as well as the reflected intensity of

the chopped beam. Kerr Rotation is proportional to the ratio between the intensity of the beam modulated at the PEMs second harmonic and the reflected intensity. Similarly, Kerr Ellipticity is proportional to the ratio between the intensity of the beam modulated at the PEMs first harmonic and the reflected intensity.

Kerr angle as a function of applied field was measured. In addition to the CrI_3, we also measured the signal of only the Al_2O_3 or hBN stack in order to subtract this as background from our actual data. This background signal was a location-independent, reproducible sloped line. Similar response was observed on the nearby gold alignment marks, suggesting that this background was due to magnetic effects on the lens and not from either test locations.

Comparisons between hBN (the sample previously shown in Fig.[8.2] before decay was used) and Al_2O_3 passivated samples can be seen in Fig.[8.3], showing our measurement capabilities with either protection scheme, as well as the successful signal preservation with alumina passivation. As the samples are not identical, specific signal behavior is hard to compare directly but there is a general similarity between the results under different conditions for bulk CrI_3.

8.3.2. Mono to Few-layer Chromium Iodide with Buffer Layer

A key question in developing and testing the passivation technique of alimuna, is whether or not the method causes damage to the layers it is trying to protect and potentially compromise their optical and, more importantly, magnetic properties. This is especially important for few layer materials, and doubly-so when there are layer dependent orderings such as in CrI_3, where monolayers are ferromagnetic ordered, bilayers exhibit

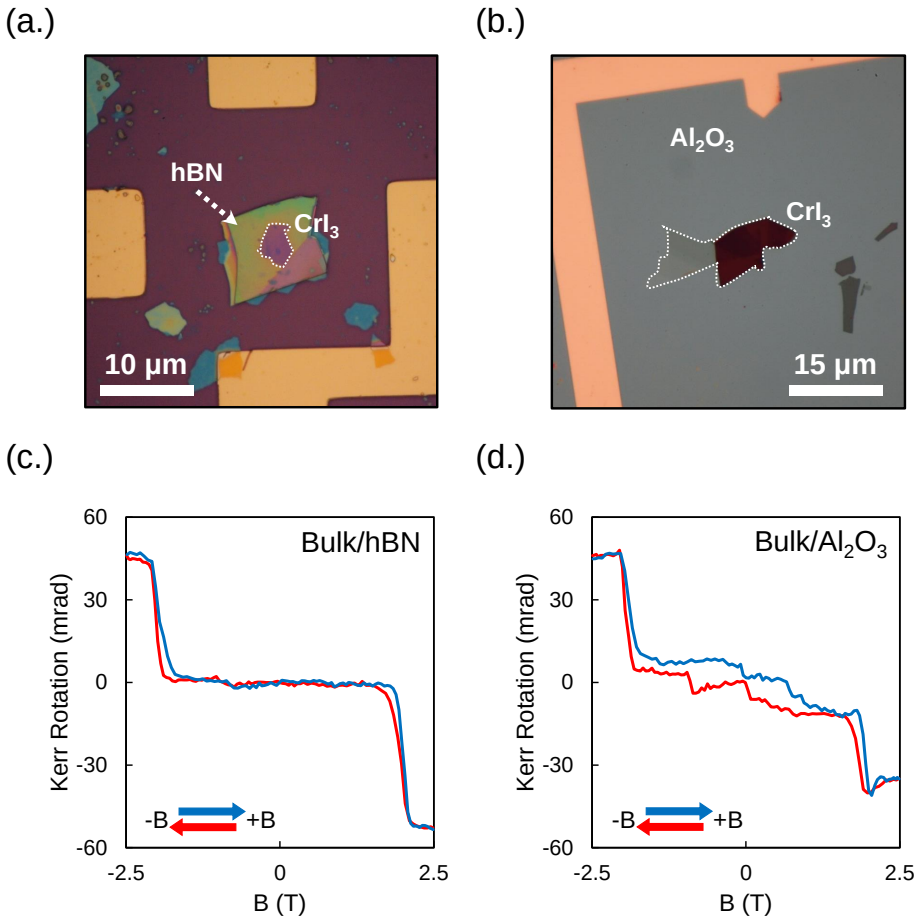

Figure 8.3. Comparison of protection techniques for CrI_3. (a.) Optical image of hBN encapsulated CrI_3, the CrI_3 is outlined by a white dashed-line to guide the eye. (b.) Optical image of alumina-passivated CrI_3, the CrI_3 is outlined to help guide the eye. There are thinner layers present but data was collected on the dark bulk. (c.) MOKE of the hBN encapsulated CrI_3. (d.) MOKE of the alumina-passivated CrI_3. While there are signal differences between (c.) and (d.), the overall behavior is very similar, suggesting the techniques are comparable for bulk.

anti-ferromagnetic order, and trilayers and thicker can show a mixture of ferromagnetic and anti-ferromagnetic orderings. Each layer has ferromagnetic ordering but the layer to layer coupling causes these changes from ferromagnetic to anti-ferromagnetic. Due to the

atomically thin nature of monolayers, they are highly susceptible to damage from external sources. Damaging these layers could result in total loss of magnetic ordering. In the case of an n-layer thick sample, if the top most-layer is compromised only, the ordering would correspond to that of an n-1 sample.

One such source of concern with alumina growth is the use of H_2O and Ozone as part of the cycle for growth of the alumina [264]. It was not previously known if this exposure can damage the layers much like atmospheric exposure can. In the cases of bulk studied in the previous section, potential damage to the top most-layer or the crystal-edge would not be obvious as the signal would have been dominated by the many other n-1 layers comprising of the bulk. It is also not obvious how we could test or observe crystal-edge damage at the very periphery of a bulk stack of many layers. To avoid these potential issues and uncertainties in sample preparation, a "seed" layer of perylenetetracarboxylic dianhydride (PTCDA) [265] was used initially in the case of all thin layers. It was deposited after exfoliation but before ALD deposition of alumina, serving as a buffer between the CrI_3 and potentially damaging alumina growth and H_2O exposure.

As monolayers and bilayers are harder to identify optically whether under a standard microscope or in the AttoCube, gold contact patterning needed to be improved from the examples shown in Fig.[8.2]. This was accomplished by patterning the gold adjacent to the layers of interest with V-groove shapes surrounding the layers and making it a straight forward task to identify position relative to this landmark, greatly simplifying the process of finding layers with very minimal signals. Samples made this way can be seen in the insets of Fig.[8.4].

These are the only major differences in preparation of thin (monolayer to trilayer) CrI_3 samples for this section, and all other discussion will proceed with prep identical to that discussed in the bulk case in the previous section. Because monolayer and bilayer signal was expected to be very low (single digit millirad rotations) compared to bulk (tens to hundreds of millirad), the photodiode used for detection was upgraded from an amplified photodiode to an avalanche photodiode. These gains proved critical in the observation of monolayer signal.

Results of these measurements can be seen in Fig.[8.4] where monolayers, bilayers, and trilayers of CrI_3 passivated with alumina and protected by PTCDA are shown. The monolayer exhibits clear results that closely match those seen in literature for similar thicknesses, confirming that the passivation technique we utilize does not compromise the layer or damage its magnetic properties. This is a major success in realizing large-area capabilities for application of volatile magnetic materials.

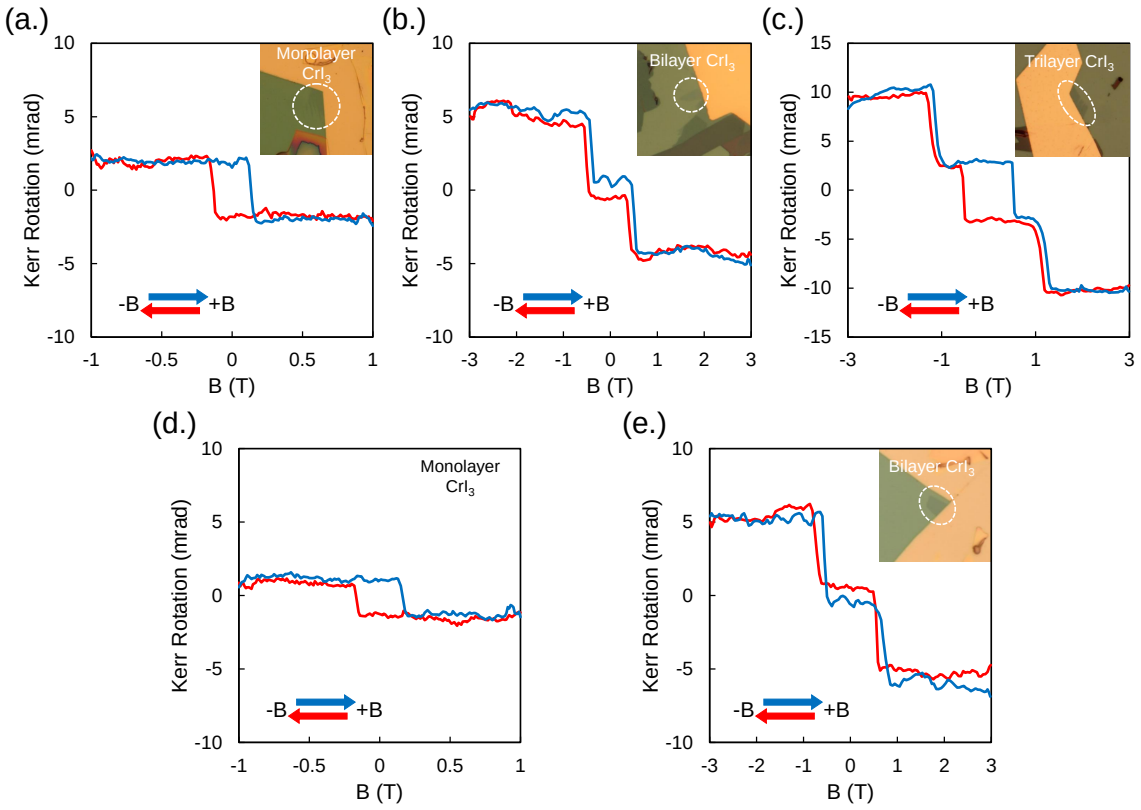

Figure 8.4. Thin flakes of CrI_3 prepared and protected with alumina ALD under a seeding layer of PTCDA. Large gold alignment markers help to identify the locations of these nearly transparent flakes for study inside of a cryostat. White circles were added to guide the eye to the location of the layers, and colored arrows indicate the field sweep direction for the respective colored data lines, highlighting the hysteresis depending on the direction of the field sweep in all layers sampled. All measurements were performed at 1.6 K in a Helium environment. (a.) Monolayer CrI_3 showing characteristic ferromagnetic behavior. (b.) Bilayer CrI_3 showing anti-ferromagnetic behavior. (c.) Trilayer CrI_3 showing both a ferromagnetic response around zero and anti-ferromagnetic behavior at higher fields. (d-e.) Monolayer and bilayer CrI_3 in a second batch of prepared samples showing similar behavior as previous runs, indicating that the ALD method is repeatably robust. There is also no apparent damage to the thin layers, especially in the monolayer, and magnetic properties are preserved.

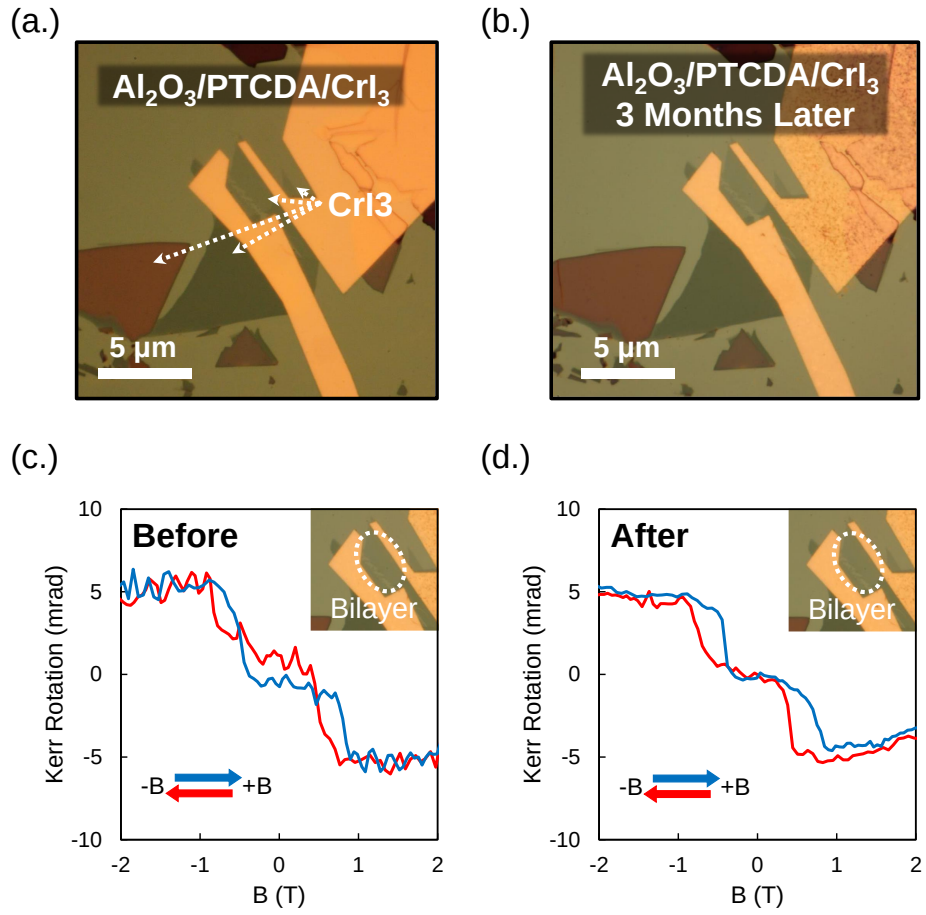

Figure 8.5. Passivation long-term stability. (a.) CrI_3 sample shortly after fabrication. (b.) The same sample, three months later after being left in ambient under a protective cover to avoid dust accumulation. The gold is visibly damaged from exposure but the underlying layers show no optically-obvious signs of decay. (c.) The bilayer sample as measured originally from (a.), the location of measurement is marked by a circle in the inset. Expected anti-ferromagnetic switching is observed. This measurement was done before the photodiode was upgraded, showing a worse signal-to-noise. (d.) The bilayer as measured three months later after ambient exposure. The signal shows no significant changes nor evidence of decay. This measurement was done with the APD, improving the signal-to-noise significantly.

To further test the robustness of this passivation, some samples were allowed to sit exposed (but protected from dust) in ambient for several months similar to the hBN protected layers in Fig.[8.2]. As expected, no decay was observed after months of ambient exposure in the layers of any thickness. Fig.[8.5] shows a several month comparison of the passivated sample before and after. The gold contacts and their visible clumping (they are above the alumina and so exposed to ambient conditions) serves as a good reference for the passage of time, clumping can be seen occuring on the gold in Fig.[8.5b]. While the gold suffered during its exposure, the underlying CrI_3 showed no obvious signs of damage optically nor in MOKE measurements performed after the exposure as seen in Fig.[8.5c, d]. In comparison, the hBN sample previously shown had completely decayed in the same time period. Attempts to measure the hBN-encapsulated sample proved unfruitful after decay but this was an expected null, showing that the layer had completely decayed.

These results show that we have achieved a robust, scale-able method of protecting volatile layers such as CrI_3 from ambient decay while also preserving their magnetic properties. This work has been successfully published in ACS Nano. Ambient-Stable Two-Dimensional CrI_3 via Organic-Inorganic Encapsulation, ACS Nano 2021 5 (6), 1065910667 [266].

8.4. Direct Alumina Passivation

To better capture the beneficial impact of the PTCDA layer, samples were prepared without addition of the PTCDA layer buffer, and alumina was directly grown on bilayers and trilayers of CrI_3. Monolayers were not used because of their weak signal relative to thicker materials (approx. 4 mrad vs. approx. 10 mrad) and difficulty to locate. Searching

for a possible null case (if alumina destroys the top most layer) in such a delicate layer would be difficult to separate from other potential complications. Instead, work was focused on bilayers and trilayers and expectations were set to observe 'damaged' layers behaving as n-1 of their expected thickness.

Layers were prepared in the same way as in the bulk discussion previously, however patterning techniques for finding the layers from work with the thinner layers and PTCDA were applied to allow for ease of sample identification.

The first sample (a bilayer) that was tested behaved as expected in ordering, displaying anti-ferromagnetic (AFM) coupling at the applied fields. Signal from the layer can be seen in Fig.[8.6**a**] with marked off expected AFM transitions. It is important to note that the signal is significantly lower than that observed repeatedly in previous bilayer and PTCDA measurements as seen in Fig.[8.4**b,e**], suggesting a possible loss of signal due to the direct passivation. Strikingly, after extended exposure and measurement, the signal began to steadily decrease with each successive test. On the third and final day of testing, no signal could be located anywhere on the thin device though nearby bulk was tested as a sanity check to confirm that the system was still functioning normally; no unexpected results were seen from the bulk showing standard bulk behavior, ruling out a measurement issue. This loss over three days of measurement is represented in Fig.[8.6**a-c**], where an obvious loss of clear AFM transitions is visible. By the final day, there is only a faint hint left of any distinct AFM transition in the sample. This behavior, combined with the lower-than-expected signal observed initially suggests strongly that the layer had been compromised by direct alumina growth.

One possible explanation for this decay is that small molecules of H_2O, a precursor for the alumina growth, were trapped during the growth process of the alumina between the alumina and the CrI_3 layers. When cooled down and exposed to our focused laser light, these small water molecules began to interact with the layer as they would for CrI_3 under ambient exposure, and lead to the observed decay and eventual loss of magnetic (and likely crystal) ordering. This process was likely going on (very slowly) while the sample was exposed to ambient light during loading into the AttoCube and would help explain the lower-than-expected signal at the very start of our measurements.

A follow-up sample of bilayer and trilayer of CrI_3 was subsequently tested for a fuller set of data under these new conditions with the intent to capture any reproducible deviations in expected signal due to direct alumina growth on CrI_3. The sample and its results can be seen in Fig.[8.6**d-f**], where we observe strong signal **but** not the signal expected! Here we observed FM transitions for a bilayer, and multiple unexpected AFM transitions in the trilayer at higher fields which had not been previously observed.

First, discussing the FM behavior in the bilayer, this behavior matches what was originally expected as n-1 behavior in directly alumina capped layers. The top most layer of the bilayer is damaged, and the sample is reduced to one good layer. However, there are small shifts in the data seen in [8.6**e**] marked by arrows that suggest some segments of the top layer may have survived and are creating a response very similar to that of AFM bilayer switching but nearly an order of magnitude suppressed. The layer was investigated post-measurement with our optical microscope but no damage or decay (such as that seen in Fig.[8.2]) was evident. This was not surprising, however, as due to the poor contrast of thin layers of CrI_3 under the alumina it is unlikely we would be able to see any but the

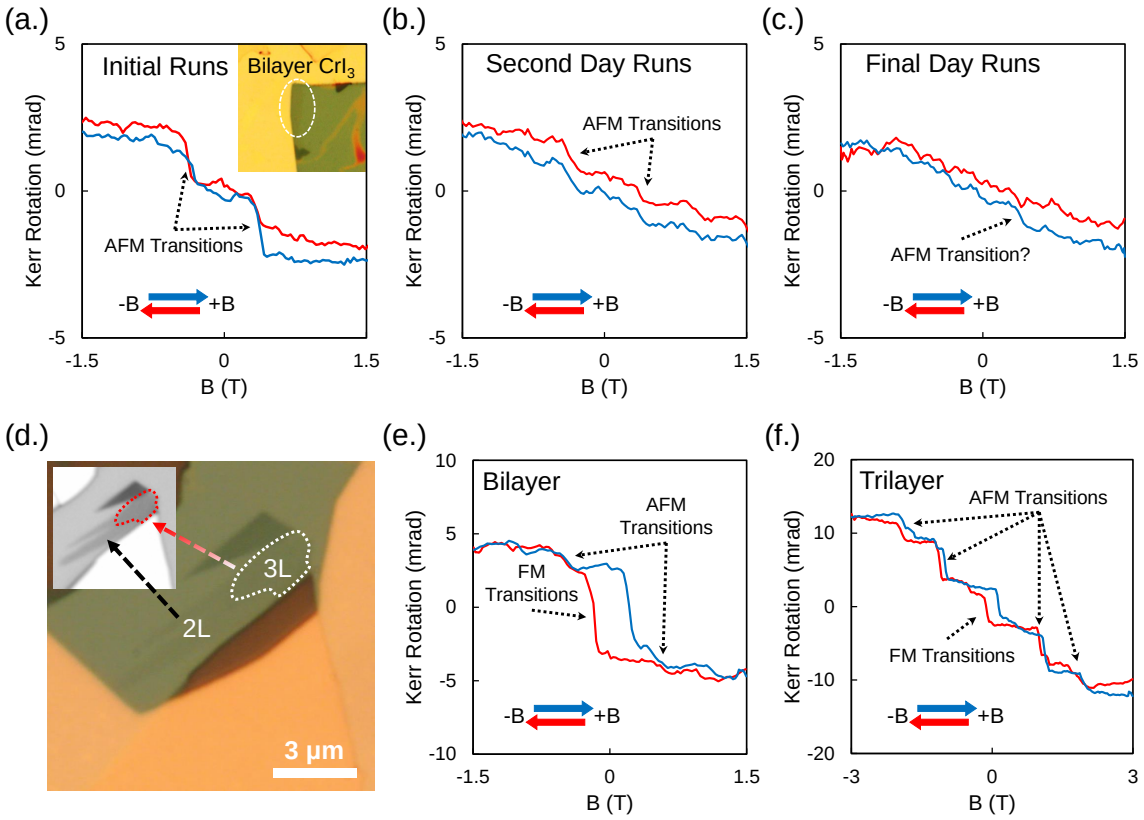

Figure 8.6. Thin layers of CrI_3 under only alumina with no PTCDA buffer layer. Large gold alignment markers help to identify layer location. (a.) Anti-ferromagnetic behavior on initial tests, as expected of bilayer. Inset shows the bilayer. (b.) Behavior on day two, the anti-ferromagnetic behavior has significantly decreased. Suggesting a slow decay of magnetic ordering in the CrI_3 (c.) Near-total loss of anti-ferromagnetic response by the third day. (d.) Optical image of the bilayer and trilayer of the follow-up alumina-only test. White/red lines mark-out the trilayer from the bilayer. (e.) Ferromagnetic response on the bilayer, small anti-ferromagnetic transitions are marked with arrows. Suggesting an n-1 result due to a damaged top layer. (f.) Trilayer showing ferromagnetic response and many anti-ferromagnetic transitions.

most extreme of changes to the layer. There is also no way to remove the passivation layer, preventing more direct and robust looks at the layer such as atomic force microscopy or SEM imaging.

Second, discussing the many-transition trilayer behavior, comparing to results shown in Fig.[8.6**c**] we see familiar FM/AFM behavior around zero but with much smaller hysteresis and the expected transitions are smaller in rotation. As the field increases, we see new AFM switching that was not expected. One explanation for the additional switching as well as lower signal is that the alumina growth, while not as significantly compromising the top layer of the trilayer as in the bilayer case, has created multiple domains resulting in multiple different transitions and a weaker FM response around zero. The bilayer and trilayer were also tested for decay as seen in the cases of the first direct alumina sample, but no decay could be observed. Power was increased multiple-fold (from 10s of μW to hundreds of mW) in an attempt to trigger any decay in the layer but none could be seen. This is likely indicative of little or no trapped water molecules in this case to create significant layer decay under illumination.

In both tested cases, however, it is evident that direct alumina growth results in inconsistent behavior of the layers compared to expected, both from our own work and the literature, results. Conversely, all samples prepared and measured using PTCDA passivation layer showed no significant variance in performance nor signs of damage or decay occurring on lab-scale times. Creating a stable, robust, scale-able protection scheme was ultimately the goal and these results highlight the necessity for the PTCDA capping layer in order to achieve that result.

8.4.1. Wavelength Dependence of MOKE on Chromium Iodide

A final result of interest from the CrI_3 work was that of an observed wavelength dependence on the signal strength of MOKE in Kerr Rotation and Ellipiticity that was highly

dependent on the encapsulating materials used. This again highlights the significance of environmental engineering of these 2D layers, here showing an impact even on magnetic measurements of the material. This result can be seen in Fig.[8.7]. Signal was extracted from the Kerr rotations extracted at approximately 2.5 T, similar to the rotation seen in Fig.[8.3c,d]. The magnitude of this rotation was tracked as the wavelength of the pump laser was tuned from 530 nm to 660 nm (this is the entire range of our visible M2 laser). Error bars were extracted from three runs per wavelength which were averaged before a rotation value was extracted.

The exact origins of this wavelength dependent disparity is not clear at the time of this writing. However, this result does highlight a non-obvious degree of tunability in how a magnetic material responds depending on the superstrate and substrates used. For a brief discussion, a likely contribution is that each of these material sub/superstrates have different permittivity. Slight differences in permittivity will result in slight changes to the speed of light propagation and refractive index. This can have significant impact on the retardation between Left and Right circularly polarized light along the path of propagation, altering the circular birefrigence and as such resultant MOKE shift. More over, these changes can result in slight shifts in polarization at the interfaces of the materials following Fresnel's equations. That said, because the Al_2O_3 appears to lack the same periodicity and uniformity in both Kerr Rotation and Ellipticity to that seen for hBN response as seen in Fig.[8.7], it is possible that a more nuanced magnetic response within the materials, specifically the Al_2O_3, is also at play.

The nature of the substrates and their quality may also play a role in the wavelength dependent differences. hBN is a well known "ideal" substrate for layered materials due

to its smooth, clean surface unlike SiO_2, and likely contributes at least partially to the more periodic signal seen in both hBN spectra in Fig.[8.7b,d]. The alumina capped layers were directly on SiO_2 which is a rough amorphous substrate and may be the origin of the more asymmetric patterns of the data.

To better investigate this result in the future, it would be ideal to test two CrI_3 on hBN substrates with varied superstrates, this would eliminate the unknown effects of the substrate and narrow differences only to the superstrate. Regardless, this result keenly highlights the capabilities of environmental engineering in these materials beyond simply preserving their properties in ambient conditions.

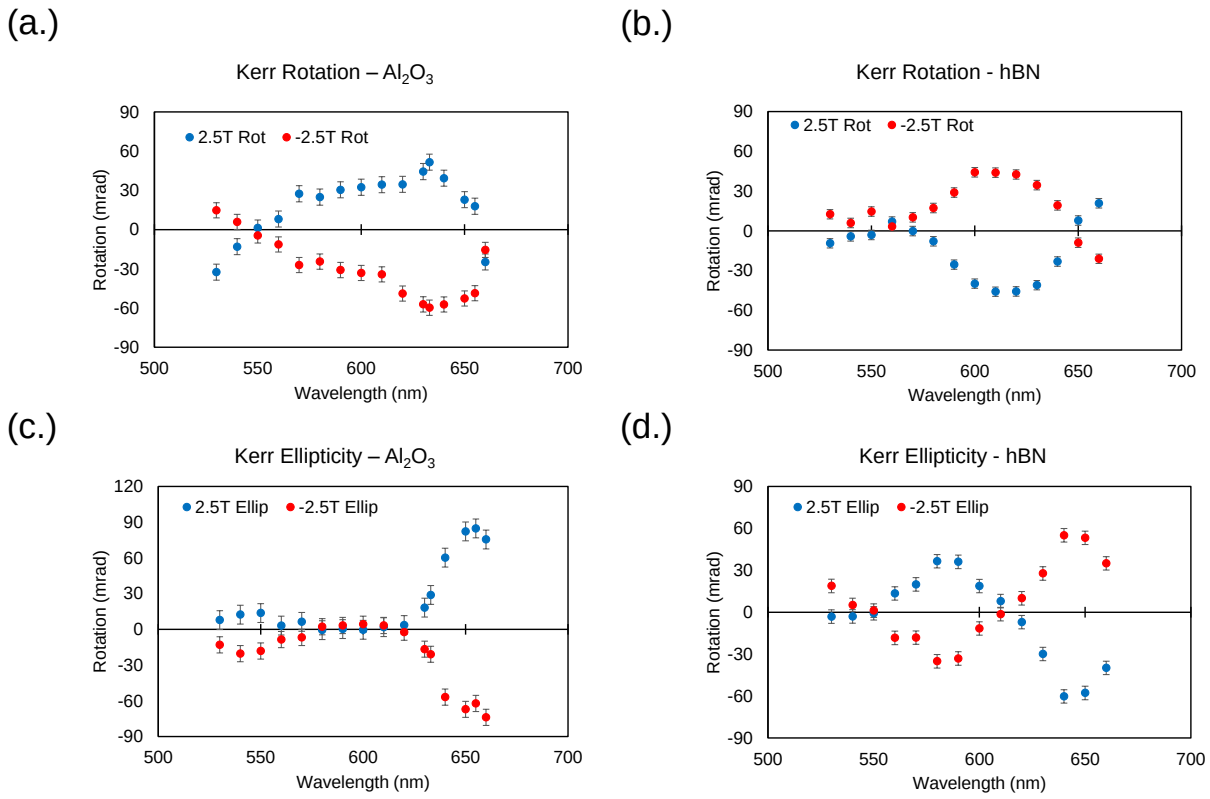

Figure 8.7. Impact of superstrate and substrate on the Kerr Rotation and Ellipticity response of CrI_3 at 2.5 T magnetic field for anti-ferromagnetic bulk. (a-b.) Kerr Rotation of CrI_3 under Al_2O_3 and hBN respectively. It is notable that the largest seen rotations are at different wavelengths. (c-d.) Kerr Ellipticity of CrI_3 under Al_2O_3 and hBN respectively. Notably, in the case of Al_2O_3, there is an extended wavelength region of no observable signal unlike the largely periodic hBN signal.

8.5. Future Work

My successes with CrI_3 MOKE has laid the ground work for studying other known and suspected magnetic materials in the Stern Lab and opening significant new opportunities for collaborations in the pursuit of interesting new physics in magnetic materials.

Some future projects being worked on are materials such as NiI_2 [214, 267], $FeCl_2$, and $CrOCl_3$ which are suspected to have magnetic properties at the monolayer limit. Using passivation techniques presented here and hBN encapsulation, work is underway in testing these materials for MOKE response in our system. Early results from $CrOCl_3$ have been successful on bulk recently, seen in Fig.[8.8] showing AFM behavior in a many-layer system encapsulated by hBN. The new APD detector proved critical in observing this small response but has now laid the ground work for looking at thinner layers and down to a monolayer where ferromagnetic signal might be seen.

Further more, early results for $FeCl_2$ have also been successful in observing MOKE response from many layer flakes protected by hBN via stamping techniques in a glovebox similar to those described in the Appendix. $FeCl_2$ is so aggressively unstable that even minor exposure results in near instantaneous decay, making it a very difficult material to work with. However, as a bimetal it may prove to be an interesting new platform to work with in layered materials unlike previous semiconductors and insulators such as NiI_2 and CrI_3 respectively.

Another project that has recently began in follow-up to the successful work with CrI_3 and the projects surrounding phthalocyanines such as VoPc [268, 269] is an inquiry into the possibility of coupling magnetic dynamics to 2D layers via passivation by magnetic metal core Pc. This project, which combines both layer passivation and manipulation

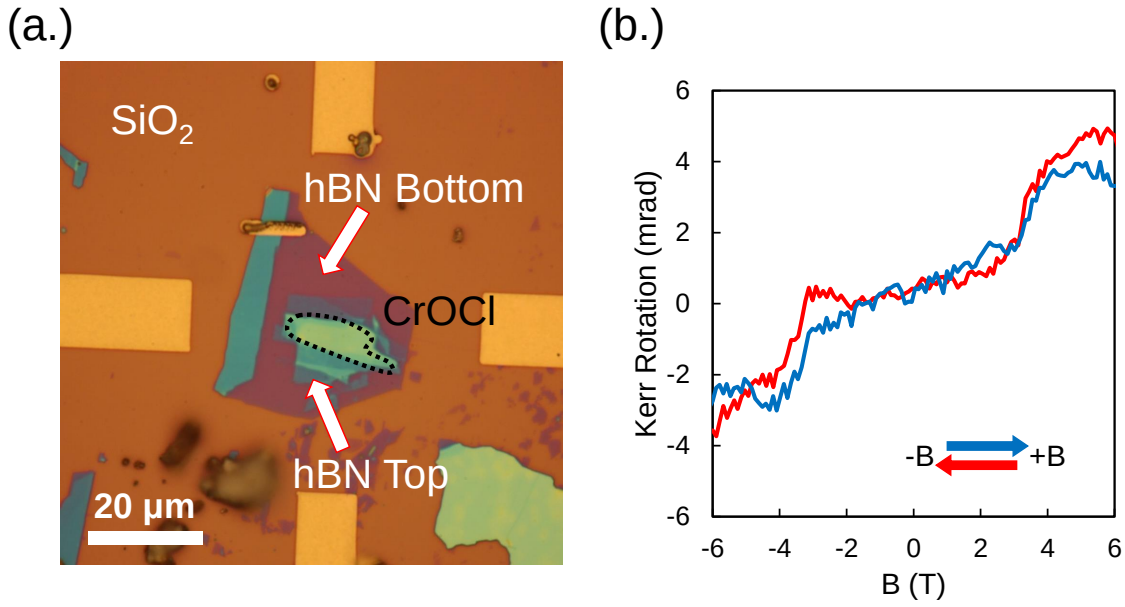

Figure 8.8. (a.) Many layer CrOCl, marked by black dashed line, encapsulated by hBN on both sides. Gold markers are used to help find the sample. (b.) Anti-ferromagnetic switching seen in the CrOCl bulk sample in (a.).

by mixed dimensional interactions with layer protection, was initially brainstormed by Sam Amsterdam and me but has since been picked up by our underclassmen who will hopefully see the projects to completion!

I look forward to results in the future that build off of the framework I have designed.

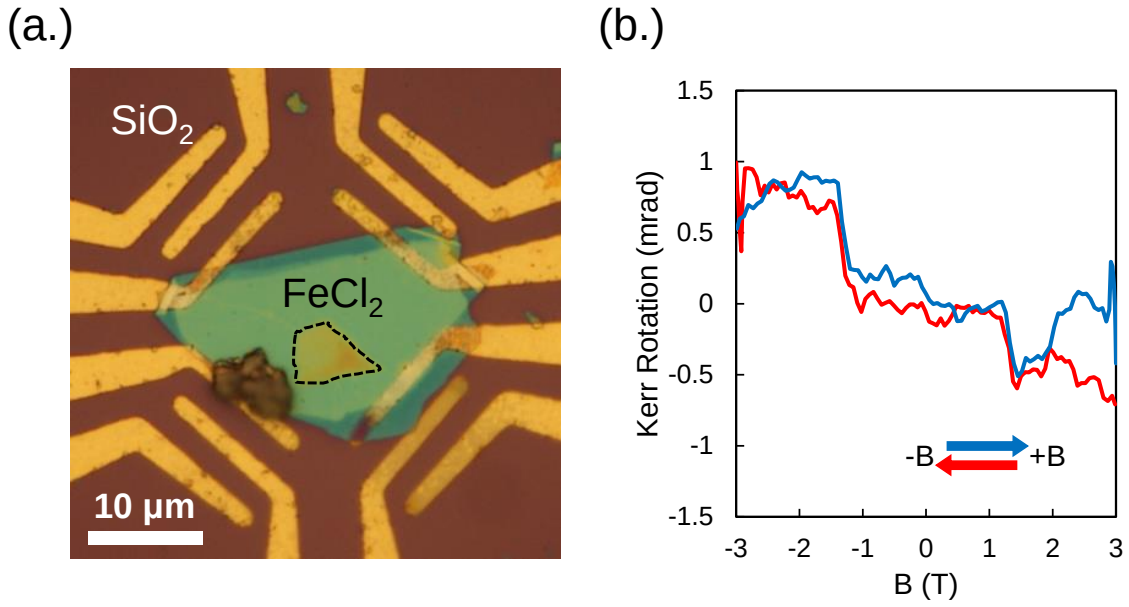

Figure 8.9. (a.) $FeCl_2$ encapsulated in hBN. (b.) Anti-ferromagnetic switching seen in the $FeCl_2$ bulk sample in (a.).

CHAPTER 9

Conclusion

TMDs, and 2D layered materials more generally, are powerful tools for creating novel devices and studying interesting and new physics of these structures. This Thesis has walked through the evolution of usage of layers with interesting confined properties in one-dimension, to creating a wide array of interesting devices: homostructures, heterostructures, and mixed-dimensional heterostructures. I have also detailed how this manipulation can be utilized to control material properties: optical, electronic, magnetic, confinement behavior, and structural preservation.

In Chapter 3, we looked at homostructures built from MoS_2 layers made distinct by their intrinsic layer number (a control "knob" for layered materials), and observed an enhanced 1D channel for conduction form at the interface of monolayer−multilayer junction. This channel offers up future possibility for quantum wires, for example. We also looked at inter- and intra-layer interactions in an external electric field, and an apparent observable and layer dependent Stokes and Starks Shifts in MoS_2 layers.

In Chapter 4, we first developed and tested tunneling contacts in order to tackle a major problem facing sensitive device design. In 2D semiconductors contact resistance can play a major role in device characterization. We showed a notable reduction in contact resistance from alloying and significant device performance increase via use of hBN tunneling barriers. This provided an opportunity to study a lateral-heterojunction and its in-plane interface.

In Chapter 5, focused shifted to hBN-based heterostructuring to test and show its ability to protect 2D materials from radiation damage. This was utilized to realize smaller than previously achieved, directly patterned nanodot arrays as well as create a narrow quantum confined conduction channel.

In Chapter 6 and 7, attention moved from the limits of only-2D layered heterostructures and focused on varied dimensionalities by combining 0D and 2D in so-called mixed dimensional heterostructures. These projects were part of a large scale collaboration at Northwestern under the MRSEC IRG program, and done in partnership with Sam Amsterdam.

In Chapter 6, this was done by combining MoS_2 with a series of metal phthalocyanines and studying a significant enhancement of the Raman of the MPc on MoS_2. Additionally, a novel absorption feature that was discovered and studied extensively. These phenomona were tested for their dependence on both the metal identity of the MPc and the layer number of the MoS_2. Furthermore, we looked at the effects of the MPc on the underlying MoS_2 layer and observed significant, metal-dependent quenching of MoS_2 low temperature defect emission. This shows how these systems can be combined into flexible, platforms for novel optoelectronic devices and has spawned a number of follow-up projects that will continue to make this partnership of groups extremely fruitful.

In Chapter 7, Pentacene, another 0D organic molecule, and how it templates on layered 2D substrates was the main focus. The observed sensitivity of the templating on the substrate (testing MoS_2, WS_2, and hBN) vs. SiO_2 was the main result. The importance of surface quality and cleanliness in realizing these mixed dimensional heterojunctions

was also of major focus as even minor residue from very common processing such as PMMA/MMA contact patterning completely ruined Pentacene templating capabilities.

In Chapter 8, I highlighted my successful realization of MOKE spectroscopy to measure collaborator provided samples that were prepared with novel protective techniques via ALD deposition. The goal was to enable magneto-optical study of magnetic layered, highly reactive 2D materials with an approach that could be scaled to real world applications. We further compared this novel technique to hBN encapsulation of these volatile materials which did show eventual decay after months of exposure. We also observed the impact of different ALD techniques on the magnetic materials, and their impact on magnetic response.

All together, these projects show the flexible and powerful nature of engineering with 2D layered materials, and the ability to probe new and old physics in new ways.

9.1. Future Work and Direction of 2D Engineering

With interest in 2D materials continuing to grow and expand in new directions, the techniques developed here and the results achieved have laid out a groundwork upon which many future directions can build. My methods, outlined in detail in the Appendix, have been put to good use by colleagues in the Stern Group as well as in other groups for projects not covered here. The robustness of my transfer scheme and applicability to a variety of surfaces and shapes has made it a very desirable technique.

One such example of this evolution of my work is attempting to utilize the defect quenching behavior of surface functionalization via organic molecules to isolate strain-induced defect single photon emitters. It may be possible to isolate the SPEs via surface

functionalization that remove all other defect states. MoS_2, for example, has very broad defect states and the layer strain techniques have not been capable of generating defect SPEs that can be measured. By functionalizing the surface and quenching the defects, it may be possible to observe SPEs that would normally be buried in the defect states. Depending on how the functionalization and SPEs interact, it may also be possible to provide new insight into defect SPE formation. This project could be utilized to help in realizing robust, flexible quantum emitter diodes. Potentially, MPc functionalization flexibility by changing the metal core could be applied here to selectively and robustly tune these quantum diode properties.

Another example that is now in the early stages of progress is the previously mentioned twisted angle heterostructures and specifically Moire excitons. Aside from the techniques to construct these heterostructures, I developed the first samples with evidence of Moire potentials and confined interlayer excitons. This is discussed in greater detail with early results in the Appendix. The project will be heralded forward by others in the Stern Group with an initial focus on applying the patterning techniques with hBN protection from Chapter 5 to Moire potentials. Unlike the small Bohr radius of the excitons in TMDs, the artificial Moire pattern is up to an order of magnitude larger. This may make strong confinement a much more easily realized result. Confinement of a Moire potential could lead to the creation of size-controllable quantum states with significant promise in quantum information applications.

My layer manipulation techniques for successfully interfacing thin layers with less conducive systems for transfer, such as waveguides, have become standard practice in related projects in the Stern Group. Waveguides and topological insulator devices do not

have smooth surfaces and are comprised of large structures that tend to tear any layers used for interfacing. But utilizing support layers and suspension-stamps, detailed in the Appendix, it is possible to gently but precisely place layers over these structures. This will help in realizing new experiments with topological systems and waveguides, interfaced with TMDs.

References

[1] Ying Jia, Teodor K. Stanev, Erik J. Lenferink, and Nathaniel P. Stern. Enhanced conductivity along lateral homojunction interfaces of atomically thin semiconductors. *2D Materials*, 4(2):021012, February 2017.

[2] Samuel Amsterdam, Teodor K. Stanev, Qunfei Zhou, Alexander J.-T. Lou, Hadallia Bergeron, Pierre Darancet, Mark C. Hersam, Nathaniel P. Stern, and Tobin J. Marks. Electronic coupling in metallophthalocyanine-transition metal dichalcogenide mixed-dimensional heterojunctions. *ACS Nano*, 13(4):4183–4190, April 2019.

[3] Imen Ben Amara, Emna Ben Salem, and Sihem Jaziri. Optoelectronic response and excitonic properties of monolayer mos2. *Journal of Applied Physics*, 120(5):051707, August 2016.

[4] Majid Shahriari, Abdolmohammad Ghalambor Dezfuli, and Mohammad Sabaeian. Investigation of uniaxial and biaxial strains on the band gap modifications of monolayer mos2 with tight-binding method. *Superlattices and Microstructures*, 125:34–57, January 2019.

[5] Adrien Allain, Jiahao Kang, Kaustav Banerjee, and Andras Kis. Electrical contacts to two-dimensional semiconductors. *Nature Materials*, 14(12):1195–1205, December 2015.

[6] Shi-Jun Liang, Bin Cheng, Xinyi Cui, and Feng Miao. Van der waals heterostructures for high-performance device applications: Challenges and opportunities. *Adv.*

Mater., 32(27):1903800, July 2020.

[7] Deep Jariwala, Tobin J. Marks, and Mark C. Hersam. Mixed-dimensional van der waals heterostructures. *Nature Materials*, 16(2):170–181, February 2017.

[8] Youngbin Lee, Hyunmin Kim, Jinhwan Lee, Seong Hun Yu, Euyheon Hwang, Changgu Lee, Jong-Hyun Ahn, and Jeong Ho Cho. Enhanced raman scattering of rhodamine 6g films on two-dimensional transition metal dichalcogenides correlated to photoinduced charge transfer. *Chem. Mater.*, 28(1):180–187, January 2016.

[9] Akshay Murthy, Teodor K. Stanev, Jeffrey D. Cain, Shiqiang Hao, Trevor LaMountain, Sungkyu Kim, Nathaniel Speiser, Kenji Watanabe, Takashi Taniguchi, Chris Wolverton, Nathaniel P. Stern, and Vinayak P. Dravid. Intrinsic transport in 2d heterostructures mediated through h-bn tunneling contacts. *Nano Lett.*, 18(5):2990–2998, May 2018.

[10] Samuel H. Amsterdam, Trevor LaMountain, Teodor K. Stanev, Vinod K. Sangwan, Rafael Lpez-Arteaga, Suyog Padgaonkar, Kenji Watanabe, Takashi Taniguchi, Emily A. Weiss, Tobin J. Marks, Mark C. Hersam, and Nathaniel P. Stern. Tailoring the optical response of pentacene thin films via templated growth on hexagonal boron nitride. *J. Phys. Chem. Lett.*, 12(1):26–31, January 2021.

[11] Xiao Li and Hongwei Zhu. Two-dimensional mos2: Properties, preparation, and applications. *Journal of Materiomics*, 1(1):33–44, March 2015.

[12] Andres Castellanos-Gomez, Michele Buscema, Rianda Molenaar, Vibhor Singh, Laurens Janssen, Herre S. J. van der Zant, and Gary A. Steele. Deterministic transfer of two-dimensional materials by all-dry viscoelastic stamping. *2D Materials*, 1(1):011002, April 2014.

[13] F. Cadiz, E. Courtade, C. Robert, G. Wang, Y. Shen, H. Cai, T. Taniguchi, K. Watanabe, H. Carrere, D. Lagarde, M. Manca, T. Amand, P. Renucci, S. Tongay, X. Marie, and B. Urbaszek. Excitonic linewidth approaching the homogeneous limit in mos_2-based van der waals heterostructures. *Phys. Rev. X*, 7(2):021026, May 2017.

[14] Liam Britnell, Roman V. Gorbachev, Rashid Jalil, Branson D. Belle, Fred Schedin, Mikhail I. Katsnelson, Laurence Eaves, Sergey V. Morozov, Alexander S. Mayorov, Nuno M. R. Peres, Antonio H. Castro Neto, Jon Leist, Andre K. Geim, Leonid A. Ponomarenko, and Kostya S. Novoselov. Electron tunneling through ultrathin boron nitride crystalline barriers. *Nano Lett.*, 12(3):1707–1710, March 2012.

[15] Yi-Hsien Lee, Xin-Quan Zhang, Wenjing Zhang, Mu-Tung Chang, Cheng-Te Lin, Kai-Di Chang, Ya-Chu Yu, Jacob Tse-Wei Wang, Chia-Seng Chang, Lain-Jong Li, and Tsung-Wu Lin. Synthesis of large-area mos2 atomic layers with chemical vapor deposition. *Adv. Mater.*, 24(17):2320–2325, May 2012.

[16] Yongjie Zhan, Zheng Liu, Sina Najmaei, Pulickel M. Ajayan, and Jun Lou. Large-area vapor-phase growth and characterization of mos2 atomic layers on a sio2 substrate. *Small*, 8(7):966–971, April 2012.

[17] Jaeho Jeon, Sung Kyu Jang, Su Min Jeon, Gwangwe Yoo, Yun Hee Jang, Jin-Hong Park, and Sungjoo Lee. Layer-controlled cvd growth of large-area two-dimensional mos2 films. *Nanoscale*, 7(5):1688–1695, 2015.

[18] Dumitru Dumcenco, Dmitry Ovchinnikov, Kolyo Marinov, Predrag Lazi, Marco Gibertini, Nicola Marzari, Oriol Lopez Sanchez, Yen-Cheng Kung, Daria Krasnozhon, Ming-Wei Chen, Simone Bertolazzi, Philippe Gillet, Anna Fontcuberta i

Morral, Aleksandra Radenovic, and Andras Kis. Large-area epitaxial monolayer mos2. *ACS Nano*, 9(4):4611–4620, April 2015.

[19] Hai Li, Jumiati Wu, Zongyou Yin, and Hua Zhang. Preparation and applications of mechanically exfoliated single-layer and multilayer mos2 and wse2 nanosheets. *Acc. Chem. Res.*, 47(4):1067–1075, April 2014.

[20] Matj Velick, Gavin E. Donnelly, William R. Hendren, Stephen McFarland, Declan Scullion, William J. I. DeBenedetti, Gabriela Calinao Correa, Yimo Han, Andrew J. Wain, Melissa A. Hines, David A. Muller, Kostya S. Novoselov, Hctor D. Abrua, Robert M. Bowman, Elton J. G. Santos, and Fumin Huang. Mechanism of gold-assisted exfoliation of centimeter-sized transition-metal dichalcogenide monolayers. *ACS Nano*, 12(10):10463–10472, October 2018.

[21] Filippo Pizzocchero, Lene Gammelgaard, Bjarke S. Jessen, Jos M. Caridad, Lei Wang, James Hone, Peter Bggild, and Timothy J. Booth. The hot pick-up technique for batch assembly of van der waals heterostructures. *Nature Communications*, 7(1):11894, June 2016.

[22] Zhe Wang, Ignacio Gutirrez-Lezama, Nicolas Ubrig, Martin Kroner, Marco Gibertini, Takashi Taniguchi, Kenji Watanabe, Ata Imamolu, Enrico Giannini, and Alberto F. Morpurgo. Very large tunneling magnetoresistance in layered magnetic semiconductor cri3. *Nature Communications*, 9(1):2516, June 2018.

[23] Gonzalo Abelln, Stefan Wild, Vicent Lloret, Nils Scheuschner, Roland Gillen, Udo Mundloch, Janina Maultzsch, Maria Varela, Frank Hauke, and Andreas Hirsch. Fundamental insights into the degradation and stabilization of thin layer black phosphorus. *J. Am. Chem. Soc.*, 139(30):10432–10440, August 2017.

[24] Yijun Xu, Zhe Shi, Xinyao Shi, Kai Zhang, and Han Zhang. Recent progress in black phosphorus and black-phosphorus-analogue materials: properties, synthesis and applications. *Nanoscale*, 11(31):14491–14527, 2019.

[25] Giuseppe Iannaccone, Francesco Bonaccorso, Luigi Colombo, and Gianluca Fiori. Quantum engineering of transistors based on 2d materials heterostructures. *Nature Nanotechnology*, 13(3):183–191, March 2018.

[26] Yan Wang, Jong Chan Kim, Ryan J. Wu, Jenny Martinez, Xiuju Song, Jieun Yang, Fang Zhao, Andre Mkhoyan, Hu Young Jeong, and Manish Chhowalla. Van der waals contacts between three-dimensional metals and two-dimensional semiconductors. *Nature*, 568(7750):70–74, April 2019.

[27] Dattatray J. Late, Bin Liu, H. S. S. Ramakrishna Matte, Vinayak P. Dravid, and C. N. R. Rao. Hysteresis in single-layer mos2 field effect transistors. *ACS Nano*, 6(6):5635–5641, June 2012.

[28] Mengjian Zhu, Wei Luo, Nannan Wu, Xue-ao Zhang, and Shiqiao Qin. Engineering few-layer mote2 devices by co/hbn tunnel contacts. *Appl. Phys. Lett.*, 112(18):183102, April 2018.

[29] Pasqual Rivera, John R. Schaibley, Aaron M. Jones, Jason S. Ross, Sanfeng Wu, Grant Aivazian, Philip Klement, Kyle Seyler, Genevieve Clark, Nirmal J. Ghimire, Jiaqiang Yan, D. G. Mandrus, Wang Yao, and Xiaodong Xu. Observation of long-lived interlayer excitons in monolayer mose2-wse2 heterostructures. *Nature Communications*, 6(1):6242, February 2015.

[30] Michael Frg, Anvar S. Baimuratov, Stanislav Yu. Kruchinin, Ilia A. Vovk, Johannes Scherzer, Jonathan Frste, Victor Funk, Kenji Watanabe, Takashi Taniguchi, and

Alexander Hgele. Moir excitons in mose2-wse2 heterobilayers and heterotrilayers. *Nature Communications*, 12(1):1656, March 2021.

[31] Shigehiko Sasa, Junji Saito, Kazuo Nanbu, Tomonori Ishikawa, and Satoshi Hiyamizu. Improved 2deg mobility in inverted gaas/n-algaas heterostructures grown by mbe. *Japanese Journal of Applied Physics*, 23(Part 2, No. 8):L573–L575, August 1984.

[32] T. R. Lenka and A. K. Panda. Characteristics study of 2deg transport properties of algan/gan and algaas/gaas-based hemt. *Semiconductors*, 45(5):650–656, May 2011.

[33] M. C. Holland, A. H. Kean, and C. R. Stanley. 250 aa spacer gaas/algaas two dimensional electron gas (2deg) structures with mobilities in excess of 3x10/sup 6/ cm/sup 2/v-1/sub s/-1 at 4 k. In *IEE Colloquium on III-V Compound Semiconductor Materials Growth*, pages 7/1–7/4, 20-2.

[34] Y. Fu, T. H. Wang, and M. Willander. Designing two-dimensional electron gases in gaas/ingaas/algaas, -doped algaas/gaas, and algaas/ingaas/gaas heterostructures for single electron transistor application. *Journal of Applied Physics*, 89(3):1759–1763, February 2001.

[35] Kin Fai Mak, Changgu Lee, James Hone, Jie Shan, and Tony F. Heinz. Atomically thin mos_2: A new direct-gap semiconductor. *Phys. Rev. Lett.*, 105(13):136805, September 2010.

[36] K. S. Novoselov, A. Mishchenko, A. Carvalho, and A. H. Castro Neto. 2d materials and van der waals heterostructures. *Science*, 353(6298):aac9439, July 2016.

[37] Gong Zhang, Huijuan Liu, Jiuhui Qu, and Jinghong Li. Two-dimensional layered mos2: rational design, properties and electrochemical applications. *Energy Environ.*

Sci., 9(4):1190–1209, 2016.

[38] Changli Li, Qi Cao, Faze Wang, Yequan Xiao, Yanbo Li, Jean-Jacques Delaunay, and Hongwei Zhu. Engineering graphene and tmds based van der waals heterostructures for photovoltaic and photoelectrochemical solar energy conversion. *Chem. Soc. Rev.*, 47(13):4981–5037, 2018.

[39] Anna N. Hoffman, Michael G. Stanford, Cheng Zhang, Ilia N. Ivanov, Akinola D. Oyedele, Maria Gabriela Sales, Stephen J. McDonnell, Michael R. Koehler, David G. Mandrus, Liangbo Liang, Bobby G. Sumpter, Kai Xiao, and Philip D. Rack. Atmospheric and long-term aging effects on the electrical properties of variable thickness wse2 transistors. *ACS Appl. Mater. Interfaces*, 10(42):36540–36548, October 2018.

[40] Gioele Mirabelli, Conor McGeough, Michael Schmidt, Eoin K. McCarthy, Scott Monaghan, Ian M. Povey, Melissa McCarthy, Farzan Gity, Roger Nagle, Greg Hughes, Attilio Cafolla, Paul K. Hurley, and Ray Duffy. Air sensitivity of mos2, mose2, mote2, hfs2, and hfse2. *Journal of Applied Physics*, 120(12):125102, September 2016.

[41] Jason W. Christopher, Bennett B. Goldberg, and Anna K. Swan. Long tailed trions in monolayer mos2: Temperature dependent asymmetry and resulting red-shift of trion photoluminescence spectra. *Scientific Reports*, 7(1):14062, October 2017.

[42] Andrzej Taube, Jarosaw Judek, Anna apiska, and Mariusz Zdrojek. Temperature-dependent thermal properties of supported mos2 monolayers. *ACS Appl. Mater. Interfaces*, 7(9):5061–5065, March 2015.

[43] Lei Wang, Xiaohong Ji, Fei Chen, and Qinyuan Zhang. Temperature-dependent properties of monolayer mos2 annealed in an ar diluted s atmosphere: an experimental and first-principles study. *J. Mater. Chem. C*, 5(42):11138–11143, 2017.

[44] Edward P. Randviir, Dale A. C. Brownson, and Craig E. Banks. A decade of graphene research: production, applications and outlook. *Materials Today*, 17(9):426–432, November 2014.

[45] Duyen H. Cao, Constantinos C. Stoumpos, Omar K. Farha, Joseph T. Hupp, and Mercouri G. Kanatzidis. 2d homologous perovskites as light-absorbing materials for solar cell applications. *J. Am. Chem. Soc.*, 137(24):7843–7850, June 2015.

[46] Jingshan S. Du, Donghoon Shin, Teodor K. Stanev, Chiara Musumeci, Zhuang Xie, Ziyin Huang, Minliang Lai, Lin Sun, Wenjie Zhou, Nathaniel P. Stern, Vinayak P. Dravid, and Chad A. Mirkin. Halide perovskite nanocrystal arrays: Multiplexed synthesis and size-dependent emission. *Sci Adv*, 6(39):eabc4959, September 2020.

[47] Eve D. Hanson, Luc Lajaunie, Shiqiang Hao, Benjamin D. Myers, Fengyuan Shi, Akshay A. Murthy, Chris Wolverton, Raul Arenal, and Vinayak P. Dravid. Systematic study of oxygen vacancy tunable transport properties of few-layer moo3x enabled by vapor-based synthesis. *Adv. Funct. Mater.*, 27(17):1605380, May 2017.

[48] Andres Castellanos-Gomez, Leonardo Vicarelli, Elsa Prada, Joshua O. Island, K. L. Narasimha-Acharya, Sofya I. Blanter, Dirk J. Groenendijk, Michele Buscema, Gary A. Steele, J. V. Alvarez, Henny W. Zandbergen, J. J. Palacios, and Herre S. J. van der Zant. Isolation and characterization of few-layer black phosphorus. *2D Materials*, 1(2):025001, June 2014.

[49] Jose . Silva-Guilln, Pablo San-Jose, and Rafael Roldn. Electronic band structure of transition metal dichalcogenides from ab initio and slater-koster tight-binding model, 2016.

[50] K. S. Novoselov, A. K. Geim, S. V. Morozov, D. Jiang, Y. Zhang, S. V. Dubonos, I. V. Grigorieva, and A. A. Firsov. Electric field effect in atomically thin carbon films. *Science*, 306(5696):666, October 2004.

[51] Sunkook Kim, Aniruddha Konar, Wan-Sik Hwang, Jong Hak Lee, Jiyoul Lee, Jaehyun Yang, Changhoon Jung, Hyoungsub Kim, Ji-Beom Yoo, Jae-Young Choi, Yong Wan Jin, Sang Yoon Lee, Debdeep Jena, Woong Choi, and Kinam Kim. High-mobility and low-power thin-film transistors based on multilayer mos2 crystals. *Nature Communications*, 3(1):1011, August 2012.

[52] Kin Fai Mak, Keliang He, Jie Shan, and Tony F. Heinz. Control of valley polarization in monolayer mos2 by optical helicity. *Nature Nanotechnology*, 7(8):494–498, August 2012.

[53] Hualing Zeng, Junfeng Dai, Wang Yao, Di Xiao, and Xiaodong Cui. Valley polarization in mos2 monolayers by optical pumping. *Nature Nanotechnology*, 7(8):490–493, August 2012.

[54] Meng-Lin Tsai, Sheng-Han Su, Jan-Kai Chang, Dung-Sheng Tsai, Chang-Hsiao Chen, Chih-I. Wu, Lain-Jong Li, Lih-Juann Chen, and Jr-Hau He. Monolayer mos2 heterojunction solar cells. *ACS Nano*, 8(8):8317–8322, August 2014.

[55] Jelena Klinovaja and Daniel Loss. Spintronics in mos_2 monolayer quantum wires. *Phys. Rev. B*, 88(7):075404, August 2013.

[56] Andrea Splendiani, Liang Sun, Yuanbo Zhang, Tianshu Li, Jonghwan Kim, Chi-Yung Chim, Giulia Galli, and Feng Wang. Emerging photoluminescence in monolayer mos2. *Nano Lett.*, 10(4):1271–1275, April 2010.

[57] Maurizia Palummo, Marco Bernardi, and Jeffrey C. Grossman. Exciton radiative lifetimes in two-dimensional transition metal dichalcogenides. *Nano Lett.*, 15(5):2794–2800, May 2015.

[58] Malte Selig, Gunnar Berghuser, Archana Raja, Philipp Nagler, Christian Schller, Tony F. Heinz, Tobias Korn, Alexey Chernikov, Ermin Malic, and Andreas Knorr. Excitonic linewidth and coherence lifetime in monolayer transition metal dichalcogenides. *Nature Communications*, 7(1):13279, November 2016.

[59] M. Koperski, K. Nogajewski, A. Arora, V. Cherkez, P. Mallet, J.-Y. Veuillen, J. Marcus, P. Kossacki, and M. Potemski. Single photon emitters in exfoliated wse2 structures. *Nature Nanotechnology*, 10(6):503–506, June 2015.

[60] Benjamin T. Zhou, Katsuhisa Taguchi, Yuki Kawaguchi, Yukio Tanaka, and K. T. Law. Spin-orbit coupling induced valley hall effects in transition-metal dichalcogenides. *Communications Physics*, 2(1):26, March 2019.

[61] Joeson Wong, Deep Jariwala, Giulia Tagliabue, Kevin Tat, Artur R. Davoyan, Michelle C. Sherrott, and Harry A. Atwater. High photovoltaic quantum efficiency in ultrathin van der waals heterostructures. *ACS Nano*, 11(7):7230–7240, July 2017.

[62] Li Song, Lijie Ci, Hao Lu, Pavel B. Sorokin, Chuanhong Jin, Jie Ni, Alexander G. Kvashnin, Dmitry G. Kvashnin, Jun Lou, Boris I. Yakobson, and Pulickel M. Ajayan. Large scale growth and characterization of atomic hexagonal boron nitride layers. *Nano Lett.*, 10(8):3209–3215, August 2010.

[63] Vinod K. Sangwan, Hong-Sub Lee, Hadallia Bergeron, Itamar Balla, Megan E. Beck, Kan-Sheng Chen, and Mark C. Hersam. Multi-terminal memtransistors from polycrystalline monolayer molybdenum disulfide. *Nature*, 554(7693):500–504, February 2018.

[64] Akshay A. Murthy, Teodor K. Stanev, Roberto dos Reis, Shiqiang Hao, Christopher Wolverton, Nathaniel P. Stern, and Vinayak P. Dravid. Direct visualization of electric-field-induced structural dynamics in monolayer transition metal dichalcogenides. *ACS Nano*, 14(2):1569–1576, February 2020.

[65] Sangwan Sim, Jusang Park, Jeong-Gyu Song, Chihun In, Yun-Shik Lee, Hyungjun Kim, and Hyunyong Choi. Exciton dynamics in atomically thin mos_2: Interexcitonic interaction and broadening kinetics. *Phys. Rev. B*, 88(7):075434, August 2013.

[66] Yuxuan Lin, Xi Ling, Lili Yu, Shengxi Huang, Allen L. Hsu, Yi-Hsien Lee, Jing Kong, Mildred S. Dresselhaus, and Toms Palacios. Dielectric screening of excitons and trions in single-layer mos2. *Nano Lett.*, 14(10):5569–5576, October 2014.

[67] Thomas Mueller and Ermin Malic. Exciton physics and device application of two-dimensional transition metal dichalcogenide semiconductors. *npj 2D Materials and Applications*, 2(1):29, September 2018.

[68] M. R. Molas, C. Faugeras, A. O. Slobodeniuk, K. Nogajewski, M. Bartos, D. M. Basko, and M. Potemski. Brightening of dark excitons in monolayers of semiconducting transition metal dichalcogenides. *2D Materials*, 4(2):021003, January 2017.

[69] Ermin Malic, Malte Selig, Maja Feierabend, Samuel Brem, Dominik Christiansen, Florian Wendler, Andreas Knorr, and Gunnar Berghuser. Dark excitons in transition metal dichalcogenides. *Phys. Rev. Materials*, 2(1):014002, January 2018.

[70] C. Robert, B. Han, P. Kapuscinski, A. Delhomme, C. Faugeras, T. Amand, M. R. Molas, M. Bartos, K. Watanabe, T. Taniguchi, B. Urbaszek, M. Potemski, and X. Marie. Measurement of the spin-forbidden dark excitons in mos2 and mose2 monolayers. *Nature Communications*, 11(1):4037, August 2020.

[71] Fengcheng Wu, Fanyao Qu, and A. H. MacDonald. Exciton band structure of monolayer mos_2. *Phys. Rev. B*, 91(7):075310, February 2015.

[72] Kin Fai Mak, Keliang He, Changgu Lee, Gwan Hyoung Lee, James Hone, Tony F. Heinz, and Jie Shan. Tightly bound trions in monolayer mos2. *Nature Materials*, 12(3):207–211, March 2013.

[73] E. Courtade, M. Semina, M. Manca, M. M. Glazov, C. Robert, F. Cadiz, G. Wang, T. Taniguchi, K. Watanabe, M. Pierre, W. Escoffier, E. L. Ivchenko, P. Renucci, X. Marie, T. Amand, and B. Urbaszek. Charged excitons in monolayer wse_2: Experiment and theory. *Phys. Rev. B*, 96(8):085302, August 2017.

[74] J. Jadczak, J. Kutrowska-Girzycka, P. Kapuciski, Y. S. Huang, A. Wjs, and L. Bryja. Probing of free and localized excitons and trions in atomically thin wse2, ws2, mose2 and mos2 in photoluminescence and reflectivity experiments. *Nanotechnology*, 28(39):395702, September 2017.

[75] Erfu Liu, Jeremiah van Baren, Zhengguang Lu, Mashael M. Altaiary, Takashi Taniguchi, Kenji Watanabe, Dmitry Smirnov, and Chun Hung Lui. Gate tunable dark trions in monolayer wse_2. *Phys. Rev. Lett.*, 123(2):027401, July 2019.

[76] D. Liu, Y. Guo, L. Fang, and J. Robertson. Sulfur vacancies in monolayer mos2 and its electrical contacts. *Appl. Phys. Lett.*, 103(18):183113, October 2013.

[77] Jason S. Ross, Sanfeng Wu, Hongyi Yu, Nirmal J. Ghimire, Aaron M. Jones, Grant Aivazian, Jiaqiang Yan, David G. Mandrus, Di Xiao, Wang Yao, and Xiaodong Xu. Electrical control of neutral and charged excitons in a monolayer semiconductor. *Nature Communications*, 4(1):1474, February 2013.

[78] Bairen Zhu, Hualing Zeng, Junfeng Dai, Zhirui Gong, and Xiaodong Cui. Anomalously robust valley polarization and valley coherence in bilayer ws₂. *Proc Natl Acad Sci USA*, 111(32):11606, August 2014.

[79] Jinhua Hong, Zhixin Hu, Matt Probert, Kun Li, Danhui Lv, Xinan Yang, Lin Gu, Nannan Mao, Qingliang Feng, Liming Xie, Jin Zhang, Dianzhong Wu, Zhiyong Zhang, Chuanhong Jin, Wei Ji, Xixiang Zhang, Jun Yuan, and Ze Zhang. Exploring atomic defects in molybdenum disulphide monolayers. *Nature Communications*, 6(1):6293, February 2015.

[80] Lei Liu, Erik J. Lenferink, Guohua Wei, Teodor K. Stanev, Nathaniel Speiser, and Nathaniel P. Stern. Electrical control of circular photogalvanic spin-valley photocurrent in a monolayer semiconductor. *ACS Appl. Mater. Interfaces*, 11(3):3334–3341, January 2019.

[81] Mingxiao Ye, Dongyan Zhang, and Yoke K. Yap. Recent advances in electronic and optoelectronic devices based on two-dimensional transition metal dichalcogenides, 2017.

[82] Britton W. H. Baugher, Hugh O. H. Churchill, Yafang Yang, and Pablo Jarillo-Herrero. Intrinsic electronic transport properties of high-quality monolayer and bilayer mos2. *Nano Lett.*, 13(9):4212–4216, September 2013.

[83] Wenzhong Bao, Xinghan Cai, Dohun Kim, Karthik Sridhara, and Michael S. Fuhrer. High mobility ambipolar mos2 field-effect transistors: Substrate and dielectric effects. *Appl. Phys. Lett.*, 102(4):042104, January 2013.

[84] Jingli Wang, Qian Yao, Chun-Wei Huang, Xuming Zou, Lei Liao, Shanshan Chen, Zhiyong Fan, Kai Zhang, Wei Wu, Xiangheng Xiao, Changzhong Jiang, and Wen-Wei Wu. High mobility mos2 transistor with low schottky barrier contact by using atomic thick h-bn as a tunneling layer. *Adv. Mater.*, 28(37):8302–8308, October 2016.

[85] Wei Wu, Debtanu De, Su-Chi Chang, Yanan Wang, Haibing Peng, Jiming Bao, and Shin-Shem Pei. High mobility and high on/off ratio field-effect transistors based on chemical vapor deposited single-crystal mos2 grains. *Appl. Phys. Lett.*, 102(14):142106, April 2013.

[86] Daichi Kozawa, Rajeev Kumar, Alexandra Carvalho, Kiran Kumar Amara, Weijie Zhao, Shunfeng Wang, Minglin Toh, Ricardo M. Ribeiro, A. H. Castro Neto, Kazunari Matsuda, and Goki Eda. Photocarrier relaxation pathway in two-dimensional semiconducting transition metal dichalcogenides. *Nature Communications*, 5(1):4543, July 2014.

[87] Kin Fai Mak, Di Xiao, and Jie Shan. Light-valley interactions in 2d semiconductors. *Nature Photonics*, 12(8):451–460, August 2018.

[88] Yuan Liu, Jian Guo, Enbo Zhu, Lei Liao, Sung-Joon Lee, Mengning Ding, Imran Shakir, Vincent Gambin, Yu Huang, and Xiangfeng Duan. Approaching the schottky-mott limit in van der waals metal-semiconductor junctions. *Nature*, 557(7707):696–700, May 2018.

[89] Changsik Kim, Inyong Moon, Daeyeong Lee, Min Sup Choi, Faisal Ahmed, Seunggeol Nam, Yeonchoo Cho, Hyeon-Jin Shin, Seongjun Park, and Won Jong Yoo. Fermi level pinning at electrical metal contacts of monolayer molybdenum dichalcogenides. *ACS Nano*, 11(2):1588–1596, February 2017.

[90] Teresa Cusati, Gianluca Fiori, Amit Gahoi, Vikram Passi, Max C. Lemme, Alessandro Fortunelli, and Giuseppe Iannaccone. Electrical properties of graphene-metal contacts. *Scientific Reports*, 7(1):5109, July 2017.

[91] L. Wang, I. Meric, P. Y. Huang, Q. Gao, Y. Gao, H. Tran, T. Taniguchi, K. Watanabe, L. M. Campos, D. A. Muller, J. Guo, P. Kim, J. Hone, K. L. Shepard, and C. R. Dean. One-dimensional electrical contact to a two-dimensional material. *Science*, 342(6158):614, November 2013.

[92] Shengxi Huang, Xi Ling, Liangbo Liang, Jing Kong, Humberto Terrones, Vincent Meunier, and Mildred S. Dresselhaus. Probing the interlayer coupling of twisted bilayer mos2 using photoluminescence spectroscopy. *Nano Lett.*, 14(10):5500–5508, October 2014.

[93] Woosuk Choi, Imtisal Akhtar, Malik Abdul Rehman, Minwook Kim, Dongwoon Kang, Jongwan Jung, Yoon Myung, Jungcheol Kim, Hyeonsik Cheong, and Yongho Seo. Twist-angle-dependent optoelectronics in a few-layer transition-metal dichalcogenide heterostructure. *ACS Appl. Mater. Interfaces*, 11(2):2470–2478, January 2019.

[94] Simone Latini, Kirsten T. Winther, Thomas Olsen, and Kristian S. Thygesen. Interlayer excitons and band alignment in mos2/hbn/wse2 van der waals heterostructures. *Nano Lett.*, 17(2):938–945, February 2017.

[95] Bastian Miller, Alexander Steinhoff, Borja Pano, Julian Klein, Frank Jahnke, Alexander Holleitner, and Ursula Wurstbauer. Long-lived direct and indirect interlayer excitons in van der waals heterostructures. *Nano Lett.*, 17(9):5229–5237, September 2017.

[96] Pasqual Rivera, Hongyi Yu, Kyle L. Seyler, Nathan P. Wilson, Wang Yao, and Xiaodong Xu. Interlayer valley excitons in heterobilayers of transition metal dichalcogenides. *Nature Nanotechnology*, 13(11):1004–1015, November 2018.

[97] Kaihui Liu, Liming Zhang, Ting Cao, Chenhao Jin, Diana Qiu, Qin Zhou, Alex Zettl, Peidong Yang, Steve G. Louie, and Feng Wang. Evolution of interlayer coupling in twisted molybdenum disulfide bilayers. *Nature Communications*, 5(1):4966, September 2014.

[98] Giovanni Scuri, Trond I. Andersen, You Zhou, Dominik S. Wild, Jiho Sung, Ryan J. Gelly, Damien Brub, Hoseok Heo, Linbo Shao, Andrew Y. Joe, Andrs M. Mier Valdivia, Takashi Taniguchi, Kenji Watanabe, Marko Lonar, Philip Kim, Mikhail D. Lukin, and Hongkun Park. Electrically tunable valley dynamics in twisted wse_2/wse_2 bilayers. *Phys. Rev. Lett.*, 124(21):217403, May 2020.

[99] Chunxiao Cong, Chenji Zou, Bingchen Cao, Lishu Wu, Jingzhi Shang, Haomin Wang, Zhijun Qiu, Laigui Hu, Pengfei Tian, Ran Liu, and Ting Yu. Intrinsic excitonic emission and valley zeeman splitting in epitaxial ms2 (m = mo and w) monolayers on hexagonal boron nitride. *Nano Research*, 11(12):6227–6236, December 2018.

[100] T. P. Lyons, S. Dufferwiel, M. Brooks, F. Withers, T. Taniguchi, K. Watanabe, K. S. Novoselov, G. Burkard, and A. I. Tartakovskii. The valley zeeman effect in inter-

and intra-valley trions in monolayer wse2. *Nature Communications*, 10(1):2330, May 2019.

[101] Guohua Wei, David A. Czaplewski, Erik J. Lenferink, Teodor K. Stanev, Il Woong Jung, and Nathaniel P. Stern. Size-tunable lateral confinement in monolayer semiconductors. *Scientific Reports*, 7(1):3324, June 2017.

[102] W. Schottky. Halbleitertheorie der sperrschicht. *Naturwissenschaften*, 26(52):843–843, December 1938.

[103] W. Schottky. Zur halbleitertheorie der sperrschicht- und spitzengleichrichter. *Zeitschrift fr Physik*, 113(5):367–414, May 1939.

[104] Tsuneya Ando, Alan B. Fowler, and Frank Stern. Electronic properties of two-dimensional systems. *Rev. Mod. Phys.*, 54:437–672, Apr 1982.

[105] SooHo Choi, Zhang Shaolin, and Woochul Yang. Layer-number-dependent work function of mos2 nanoflakes. *Journal of the Korean Physical Society*, 64(10):1550–1555, May 2014.

[106] Oliver Ochedowski, Kolyo Marinov, Nils Scheuschner, Artur Poloczek, Benedict Kleine Bussmann, Janina Maultzsch, and Marika Schleberger. Effect of contaminations and surface preparation on the work function of single layer mos2. *Beilstein Journal of Nanotechnology*, 5:291–297, 2014.

[107] Jong Hun Kim, Jinhwan Lee, Jae Hyeon Kim, C. C. Hwang, Changgu Lee, and Jeong Young Park. Work function variation of mos2 atomic layers grown with chemical vapor deposition: The effects of thickness and the adsorption of water/oxygen molecules. *Appl. Phys. Lett.*, 106(25):251606, June 2015.

[108] Zongyou Yin, Hai Li, Hong Li, Lin Jiang, Yumeng Shi, Yinghui Sun, Gang Lu, Qing Zhang, Xiaodong Chen, and Hua Zhang. Single-layer mos2 phototransistors. *ACS Nano*, 6(1):74–80, January 2012.

[109] F. K. Perkins, A. L. Friedman, E. Cobas, P. M. Campbell, G. G. Jernigan, and B. T. Jonker. Chemical vapor sensing with monolayer mos2. *Nano Lett.*, 13(2):668–673, February 2013.

[110] Chung-Chiang Wu, Deep Jariwala, Vinod K. Sangwan, Tobin J. Marks, Mark C. Hersam, and Lincoln J. Lauhon. Elucidating the photoresponse of ultrathin mos2 field-effect transistors by scanning photocurrent microscopy. *J. Phys. Chem. Lett.*, 4(15):2508–2513, August 2013.

[111] D. A. B. Miller, D. S. Chemla, T. C. Damen, A. C. Gossard, W. Wiegmann, T. H. Wood, and C. A. Burrus. Electric field dependence of optical absorption near the band gap of quantum-well structures. *Phys. Rev. B*, 32(2):1043–1060, July 1985.

[112] H. J. Polland, L. Schultheis, J. Kuhl, E. O. Gbel, and C. W. Tu. Lifetime enhancement of two-dimensional excitons by the quantum-confined stark effect. *Phys. Rev. Lett.*, 56(4):404–404, January 1986.

[113] J. Klein, J. Wierzbowski, A. Regler, J. Becker, F. Heimbach, K. Mller, M. Kaniber, and J. J. Finley. Stark effect spectroscopy of mono- and few-layer mos2. *Nano Lett.*, 16(3):1554–1559, March 2016.

[114] Shinichiro Mouri, Yuhei Miyauchi, and Kazunari Matsuda. Tunable photoluminescence of monolayer mos2 via chemical doping. *Nano Lett.*, 13(12):5944–5948, December 2013.

[115] Kuang-Chung Wang, Teodor K. Stanev, Daniel Valencia, James Charles, Alex Henning, Vinod K. Sangwan, Aritra Lahiri, Daniel Mejia, Prasad Sarangapani, Michael Povolotskyi, Aryan Afzalian, Jesse Maassen, Gerhard Klimeck, Mark C. Hersam, Lincoln J. Lauhon, Nathaniel P. Stern, and Tillmann Kubis. Control of interlayer physics in 2h transition metal dichalcogenides. *Journal of Applied Physics*, 122(22):224302, December 2017.

[116] C. R. Dean, A. F. Young, I. Meric, C. Lee, L. Wang, S. Sorgenfrei, K. Watanabe, T. Taniguchi, P. Kim, K. L. Shepard, and J. Hone. Boron nitride substrates for high-quality graphene electronics. *Nature Nanotechnology*, 5(10):722–726, October 2010.

[117] Jingang Wang, Fengcai Ma, and Mengtao Sun. Graphene, hexagonal boron nitride, and their heterostructures: properties and applications. *RSC Adv.*, 7(27):16801–16822, 2017.

[118] Kailiang Zhang, Yulin Feng, Fang Wang, Zhengchun Yang, and John Wang. Two dimensional hexagonal boron nitride (2d-hbn): synthesis, properties and applications. *J. Mater. Chem. C*, 5(46):11992–12022, 2017.

[119] Zhenping Wang, Qirong Yao, Yalei Hu, Chuan Li, Marleen Humann, Ben Weintrub, Jan N. Kirchhof, Kirill Bolotin, Takashi Taniguchi, Kenji Watanabe, and Siegfried Eigler. Influence of sio2 or h-bn substrate on the room-temperature electronic transport in chemically derived single layer graphene. *RSC Adv.*, 9(65):38011–38016, 2019.

[120] Woo Hyun Chae, Jeffrey D. Cain, Eve D. Hanson, Akshay A. Murthy, and Vinayak P. Dravid. Substrate-induced strain and charge doping in cvd-grown monolayer mos2. *Appl. Phys. Lett.*, 111(14):143106, October 2017.

[121] S. Kurabayashi and K. Nagashio. Transport properties of the top and bottom surfaces in monolayer mos2 grown by chemical vapor deposition. *Nanoscale*, 9(35):13264–13271, 2017.

[122] Long Qi, Ying Wang, Lei Shen, and Yihong Wu. Chemisorption-induced n-doping of mos2 by oxygen. *Appl. Phys. Lett.*, 108(6):063103, February 2016.

[123] Jnos Pet, Tams Ollr, Pter Vancs, Zakhar I. Popov, Gbor Zsolt Magda, Gergely Dobrik, Chanyong Hwang, Pavel B. Sorokin, and Levente Tapaszt. Spontaneous doping of the basal plane of mos2 single layers through oxygen substitution under ambient conditions. *Nature Chemistry*, 10(12):1246–1251, December 2018.

[124] Junfeng Xie, Jiajia Zhang, Shuang Li, Fabian Grote, Xiaodong Zhang, Hao Zhang, Ruoxing Wang, Yong Lei, Bicai Pan, and Yi Xie. Controllable disorder engineering in oxygen-incorporated mos2 ultrathin nanosheets for efficient hydrogen evolution. *J. Am. Chem. Soc.*, 135(47):17881–17888, November 2013.

[125] Yongji Gong, Junhao Lin, Xingli Wang, Gang Shi, Sidong Lei, Zhong Lin, Xiaolong Zou, Gonglan Ye, Robert Vajtai, Boris I. Yakobson, Humberto Terrones, Mauricio Terrones, BengKang Tay, Jun Lou, Sokrates T. Pantelides, Zheng Liu, Wu Zhou, and Pulickel M. Ajayan. Vertical and in-plane heterostructures from ws2/mos2 monolayers. *Nature Materials*, 13(12):1135–1142, December 2014.

[126] Kun Chen, Xi Wan, Jinxiu Wen, Weiguang Xie, Zhiwen Kang, Xiaoliang Zeng, Huanjun Chen, and Jian-Bin Xu. Electronic properties of mos2-ws2 heterostructures

synthesized with two-step lateral epitaxial strategy. *ACS Nano*, 9(10):9868–9876, October 2015.

[127] Gwan-Hyoung Lee, Xu Cui, Young Duck Kim, Ghidewon Arefe, Xian Zhang, Chul-Ho Lee, Fan Ye, Kenji Watanabe, Takashi Taniguchi, Philip Kim, and James Hone. Highly stable, dual-gated mos2 transistors encapsulated by hexagonal boron nitride with gate-controllable contact, resistance, and threshold voltage. *ACS Nano*, 9(7):7019–7026, July 2015.

[128] Lingming Yang, Kausik Majumdar, Han Liu, Yuchen Du, Heng Wu, Michael Hatzistergos, P. Y. Hung, Robert Tieckelmann, Wilman Tsai, Chris Hobbs, and Peide D. Ye. Chloride molecular doping technique on 2d materials: Ws2 and mos2. *Nano Lett.*, 14(11):6275–6280, November 2014.

[129] Kun Chen, Xi Wan, Weiguang Xie, Jinxiu Wen, Zhiwen Kang, Xiaoliang Zeng, Huanjun Chen, and Jianbin Xu. Lateral built-in potential of monolayer mos2-ws2 in-plane heterostructures by a shortcut growth strategy. *Adv. Mater.*, 27(41):6431–6437, November 2015.

[130] Xiaoping Hong, Jonghwan Kim, Su-Fei Shi, Yu Zhang, Chenhao Jin, Yinghui Sun, Sefaattin Tongay, Junqiao Wu, Yanfeng Zhang, and Feng Wang. Ultrafast charge transfer in atomically thin mos2/ws2 heterostructures. *Nature Nanotechnology*, 9(9):682–686, September 2014.

[131] Xijiao Mu and Mengtao Sun. Interfacial charge transfer exciton enhanced by plasmon in 2d in-plane lateral and van der waals heterostructures. *Appl. Phys. Lett.*, 117(9):091601, August 2020.

[132] Y. Guo, D. Liu, and J. Robertson. Chalcogen vacancies in monolayer transition metal dichalcogenides and fermi level pinning at contacts. *Appl. Phys. Lett.*, 106(17):173106, April 2015.

[133] Baoshan Tang, Zhi Gen Yu, Li Huang, Jianwei Chai, Swee Liang Wong, Jie Deng, Weifeng Yang, Hao Gong, Shijie Wang, Kah-Wee Ang, Yong-Wei Zhang, and Dongzhi Chi. Direct n- to p-type channel conversion in monolayer/few-layer ws2 field-effect transistors by atomic nitrogen treatment. *ACS Nano*, 12(3):2506–2513, March 2018.

[134] Sarah L. Howell, Deep Jariwala, Chung-Chiang Wu, Kan-Sheng Chen, Vinod K. Sangwan, Junmo Kang, Tobin J. Marks, Mark C. Hersam, and Lincoln J. Lauhon. Investigation of band-offsets at monolayer-multilayer mos2 junctions by scanning photocurrent microscopy. *Nano Lett.*, 15(4):2278–2284, April 2015.

[135] Anupum Pant, Zafer Mutlu, Darshana Wickramaratne, Hui Cai, Roger K. Lake, Cengiz Ozkan, and Sefaattin Tongay. Fundamentals of lateral and vertical heterojunctions of atomically thin materials. *Nanoscale*, 8(7):3870–3887, 2016.

[136] Velveth Klee, Edwin Preciado, David Barroso, Ariana E. Nguyen, Chris Lee, Kristopher J. Erickson, Mark Triplett, Brandon Davis, I.-Hsi Lu, Sarah Bobek, Jessica McKinley, Joseph P. Martinez, John Mann, A. Alec Talin, Ludwig Bartels, and Franois Lonard. Superlinear composition-dependent photocurrent in cvd-grown monolayer mos2(1-x)se2x alloy devices. *Nano Lett.*, 15(4):2612–2619, April 2015.

[137] Michele Buscema, Maria Barkelid, Val Zwiller, Herre S. J. van der Zant, Gary A. Steele, and Andres Castellanos-Gomez. Large and tunable photothermoelectric effect in single-layer mos2. *Nano Lett.*, 13(2):358–363, February 2013.

[138] Zhaogang Nie, Run Long, Linfeng Sun, Chung-Che Huang, Jun Zhang, Qihua Xiong, Daniel W. Hewak, Zexiang Shen, Oleg V. Prezhdo, and Zhi-Heng Loh. Ultrafast carrier thermalization and cooling dynamics in few-layer mos2. *ACS Nano*, 8(10):10931–10940, October 2014.

[139] Eric Parzinger, Martin Hetzl, Ursula Wurstbauer, and Alexander W. Holleitner. Contact morphology and revisited photocurrent dynamics in monolayer mos2. *npj 2D Materials and Applications*, 1(1):40, November 2017.

[140] Ya Yi, Changming Wu, Hongchao Liu, Jiali Zeng, Hongtao He, and Jiannong Wang. A study of lateral schottky contacts in wse2 and mos2 field effect transistors using scanning photocurrent microscopy. *Nanoscale*, 7(38):15711–15718, 2015.

[141] Deepesh Gopalakrishnan, Dijo Damien, Bo Li, Hemtej Gullappalli, Vijayamohanan K. Pillai, Pulickel M. Ajayan, and Manikoth M. Shaijumon. Electrochemical synthesis of luminescent mos2 quantum dots. *Chem. Commun.*, 51(29):6293–6296, 2015.

[142] Joohoon Kang, Jung-Woo T. Seo, Diego Alducin, Arturo Ponce, Miguel Jose Yacaman, and Mark C. Hersam. Thickness sorting of two-dimensional transition metal dichalcogenides via copolymer-assisted density gradient ultracentrifugation. *Nature Communications*, 5(1):5478, November 2014.

[143] Daniel S. Fox, Yangbo Zhou, Pierce Maguire, Arlene ONeill, Cormac Coilein, Riley Gatensby, Alexey M. Glushenkov, Tao Tao, Georg S. Duesberg, Igor V. Shvets, Mohamed Abid, Mourad Abid, Han-Chun Wu, Ying Chen, Jonathan N. Coleman, John F. Donegan, and Hongzhou Zhang. Nanopatterning and electrical tuning of mos2 layers with a subnanometer helium ion beam. *Nano Lett.*, 15(8):5307–5313,

August 2015.

[144] Michael G. Stanford, Pushpa R. Pudasaini, Nicholas Cross, Kyle Mahady, Anna N. Hoffman, David G. Mandrus, Gerd Duscher, Matthew F. Chisholm, and Philip D. Rack. Tungsten diselenide patterning and nanoribbon formation by gas-assisted focused-helium-ion-beam-induced etching. *Small Methods*, 1(4):1600060, April 2017.

[145] Pei Zuo, Lan Jiang, Xin Li, Mengyao Tian, Chenyang Xu, Yongjiu Yuan, Peng Ran, Bo Li, and Yongfeng Lu. Maskless micro/nanopatterning and bipolar electrical rectification of mos2 flakes through femtosecond laser direct writing. *ACS Appl. Mater. Interfaces*, 11(42):39334–39341, October 2019.

[146] A. P. Sunitha, P. Hajara, Manu Shaji, M. K. Jayaraj, and K. J. Saji. Luminescent mos2 quantum dots with reverse saturable absorption prepared by pulsed laser ablation. *Journal of Luminescence*, 203:313–321, November 2018.

[147] Xiang-Xiang Song, Di Liu, Vahid Mosallanejad, Jie You, Tian-Yi Han, Dian-Teng Chen, Hai-Ou Li, Gang Cao, Ming Xiao, Guang-Can Guo, and Guo-Ping Guo. A gate defined quantum dot on the two-dimensional transition metal dichalcogenide semiconductor wse2. *Nanoscale*, 7:16867–73, Oct 2015.

[148] Theodore Manouras and Panagiotis Argitis. High sensitivity resists for euv lithography: A review of material design strategies and performance results, 2020.

[149] Anda E. Grigorescu, Marco C. van der Krogt, and Cees W. Hagen. Sub-10-nm structures written in ultra-thin HSQ resist layers using electron-beam lithography. In Qinghuang Lin, editor, *Advances in Resist Materials and Processing Technology XXIV*. SPIE, mar 2007.

[150] Hannu-Pekka Komsa, Jani Kotakoski, Simon Kurasch, Ossi Lehtinen, Ute Kaiser, and Arkady V. Krasheninnikov. Two-dimensional transition metal dichalcogenides under electron irradiation: defect production and doping. *Physical review letters*, 109:035503, Jul 2012.

[151] Gerardo Algara-Siller, Simon Kurasch, Mona Sedighi, Ossi Lehtinen, and Ute Kaiser. The pristine atomic structure of mos2 monolayer protected from electron radiation damage by graphene. *Appl. Phys. Lett.*, 103(20):203107, November 2013.

[152] Recep Zan, Quentin M. Ramasse, Rashid Jalil, Thanasis Georgiou, Ursel Bangert, and Konstantin S. Novoselov. Control of radiation damage in mos2 by graphene encapsulation. *ACS Nano*, 7(11):10167–10174, November 2013.

[153] T. Lehnert, O. Lehtinen, G. Algara-Siller, and U. Kaiser. Electron radiation damage mechanisms in 2d mose2. *Appl. Phys. Lett.*, 110(3):033106, January 2017.

[154] Chitraleema Chakraborty, Kenneth M. Goodfellow, and A. Nick Vamivakas. Localized emission from defects in mose2 layers. *Opt. Mater. Express*, 6(6):2081–2087, June 2016.

[155] Takao Wada and Kyoichiro Yasuda. Mechanism of electron-beam doping in semiconductors. *Phys. Rev. B*, 53(8):4770–4781, February 1996.

[156] Yangbo Zhou, Jakub Jadwiszczak, Darragh Keane, Ying Chen, Dapeng Yu, and Hongzhou Zhang. Programmable graphene doping via electron beam irradiation. *Nanoscale*, 9(25):8657–8664, 2017.

[157] Tingyan Luo, Baojun Pan, Kenan Zhang, Youqing Dong, Chao Zou, Zhiyang Gu, and Lijie Zhang. Electron beam lithography induced doping in multilayer mote2. *Applied Surface Science*, 540:148276, February 2021.

[158] Jakob Wierzbowski, Julian Klein, Florian Sigger, Christian Straubinger, Malte Kremser, Takashi Taniguchi, Kenji Watanabe, Ursula Wurstbauer, Alexander W. Holleitner, Michael Kaniber, Kai Mller, and Jonathan J. Finley. Direct exciton emission from atomically thin transition metal dichalcogenide heterostructures near the lifetime limit. *Scientific Reports*, 7(1):12383, September 2017.

[159] Di Wu, Xiao Li, Lan Luan, Xiaoyu Wu, Wei Li, Maruthi N. Yogeesh, Rudresh Ghosh, Zhaodong Chu, Deji Akinwande, Qian Niu, and Keji Lai. Uncovering edge states and electrical inhomogeneity in mos2 field-effect transistors. *Proceedings of the National Academy of Sciences of the United States of America*, 113:8583–8, Aug 2016.

[160] Grace G. D. Han, Kun-Hua Tu, Farnaz Niroui, Wenshuo Xu, Si Zhou, Xiaochen Wang, Vladimir Bulovi, Caroline A. Ross, Jamie H. Warner, and Jeffrey C. Grossman. Photoluminescent arrays of nanopatterned monolayer mos2. *Adv. Funct. Mater.*, 27(45):1703688, December 2017.

[161] Alejandra Garcia, Andres M. Raya, Marcelo M. Mariscal, Rodrigo Esparza, Miriam Herrera, Sergio I. Molina, Giovanni Scavello, Pedro L. Galindo, Miguel Jose-Yacaman, and Arturo Ponce. Analysis of electron beam damage of exfoliated mos2 sheets and quantitative haadf-stem imaging. *Ultramicroscopy*, 146:33–38, November 2014.

[162] Aniello Pelella, Osamah Kharsah, Alessandro Grillo, Francesca Urban, Maurizio Passacantando, Filippo Giubileo, Laura Iemmo, Stephan Sleziona, Erik Pollmann, Lukas Madau, Marika Schleberger, and Antonio Di Bartolomeo. Electron irradiation of metal contacts in monolayer mos2 field-effect transistors. *ACS Appl. Mater.*

Interfaces, 12(36):40532–40540, September 2020.

[163] Paul Masih Das and Marija Drndi. In situ 2d mos2 field-effect transistors with an electron beam gate. *ACS Nano*, 14(6):7389–7397, June 2020.

[164] Alexander Epping, Luca Banszerus, Johannes Gttinger, Luisa Krckeberg, Kenji Watanabe, Takashi Taniguchi, Fabian Hassler, Bernd Beschoten, and Christoph Stampfer. Quantum transport through mos2 constrictions defined by photodoping. *Journal of Physics: Condensed Matter*, 30(20):205001, April 2018.

[165] Riccardo Pisoni, Yongjin Lee, Hiske Overweg, Marius Eich, Pauline Simonet, Kenji Watanabe, Takashi Taniguchi, Roman Gorbachev, Thomas Ihn, and Klaus Ensslin. Gate-defined one-dimensional channel and broken symmetry states in mos2 van der waals heterostructures. *Nano Lett.*, 17(8):5008–5011, August 2017.

[166] Jianping Shi, Xiebo Zhou, Gao-Feng Han, Mengxi Liu, Donglin Ma, Jingyu Sun, Cong Li, Qingqing Ji, Yu Zhang, Xiuju Song, Xing-You Lang, Qing Jiang, Zhongfan Liu, and Yanfeng Zhang. Narrow-gap quantum wires arising from the edges of monolayer mos2 synthesized on graphene. *Adv. Mater. Interfaces*, 3(17):1600332, September 2016.

[167] Xi Ling, Wenjing Fang, Yi-Hsien Lee, Paulo T. Araujo, Xu Zhang, Joaquin F. Rodriguez-Nieva, Yuxuan Lin, Jin Zhang, Jing Kong, and Mildred S. Dresselhaus. Raman enhancement effect on two-dimensional layered materials: Graphene, h-bn and mos2. *Nano Lett.*, 14(6):3033–3040, June 2014.

[168] Jingjing Lin, Liangbo Liang, Xi Ling, Shuqing Zhang, Nannan Mao, Na Zhang, Bobby G. Sumpter, Vincent Meunier, Lianming Tong, and Jin Zhang. Enhanced raman scattering on in-plane anisotropic layered materials. *J. Am. Chem. Soc.*,

137(49):15511–15517, December 2015.

[169] Lin Quan, Yuqing Song, Yue Lin, Guanghui Zhang, Yanmeng Dai, Yukun Wu, Ke Jin, Huaiyi Ding, Nan Pan, Yi Luo, and Xiaoping Wang. The raman enhancement effect on a thin gase flake and its thickness dependence. *J. Mater. Chem. C*, 3(42):11129–11134, 2015.

[170] Ying Yin, Peng Miao, Yumin Zhang, Jiecai Han, Xinghong Zhang, Yue Gong, Lin Gu, Chengyan Xu, Tai Yao, Ping Xu, Yi Wang, Bo Song, and Song Jin. Significantly increased raman enhancement on mox2 (x = s, se) monolayers upon phase transition. *Adv. Funct. Mater.*, 27(16):1606694, April 2017.

[171] Yu Huang, Fuwei Zhuge, Junxian Hou, Liang Lv, Peng Luo, Nan Zhou, Lin Gan, and Tianyou Zhai. Van der waals coupled organic molecules with monolayer mos2 for fast response photodetectors with gate-tunable responsivity. *ACS Nano*, 12(4):4062–4073, April 2018.

[172] Cyril Muehlethaler, Christopher R. Considine, Vinod Menon, Wei-Cheng Lin, Yi-Hsien Lee, and John R. Lombardi. Ultrahigh raman enhancement on monolayer mos2. *ACS Photonics*, 3(7):1164–1169, July 2016.

[173] Jinsu Pak, Jingon Jang, Kyungjune Cho, Tae-Young Kim, Jae-Keun Kim, Younggul Song, Woong-Ki Hong, Misook Min, Hyoyoung Lee, and Takhee Lee. Enhancement of photodetection characteristics of mos2 field effect transistors using surface treatment with copper phthalocyanine. *Nanoscale*, 7(44):18780–18788, 2015.

[174] Tejas A. Shastry, Itamar Balla, Hadallia Bergeron, Samuel H. Amsterdam, Tobin J. Marks, and Mark C. Hersam. Mutual photoluminescence quenching and photovoltaic effect in large-area single-layer mos2-polymer heterojunctions. *ACS Nano*,

10(11):10573–10579, November 2016.

[175] Nikolaos Balis, Emmanuel Stratakis, and Emmanuel Kymakis. Graphene and transition metal dichalcogenide nanosheets as charge transport layers for solution processed solar cells. *Materials Today*, 19(10):580–594, December 2016.

[176] Kyungjune Cho, Jinsu Pak, Seungjun Chung, and Takhee Lee. Recent advances in interface engineering of transition-metal dichalcogenides with organic molecules and polymers. *ACS Nano*, 13(9):9713–9734, September 2019.

[177] Yu Li Huang, Yu Jie Zheng, Zhibo Song, Dongzhi Chi, Andrew T. S. Wee, and Su Ying Quek. The organic-2d transition metal dichalcogenide heterointerface. *Chem. Soc. Rev.*, 47(9):3241–3264, 2018.

[178] Stephanie Bettis Homan, Vinod K. Sangwan, Itamar Balla, Hadallia Bergeron, Emily A. Weiss, and Mark C. Hersam. Ultrafast exciton dissociation and long-lived charge separation in a photovoltaic pentacene-mos2 van der waals heterojunction. *Nano Lett.*, 17(1):164–169, January 2017.

[179] Noa Marom, Oded Hod, Gustavo E. Scuseria, and Leeor Kronik. Electronic structure of copper phthalocyanine: A comparative density functional theory study. *J. Chem. Phys.*, 128(16):164107, April 2008.

[180] O. I. Arillo-Flores, M. M. Fadlallah, C. Schuster, U. Eckern, and A. H. Romero. Magnetic, electronic, and vibrational properties of metal and fluorinated metal phthalocyanines. *Phys. Rev. B*, 87(16):165115, April 2013.

[181] Sean R. Wagner, Bing Huang, Changwon Park, Jiagui Feng, Mina Yoon, and Pengpeng Zhang. Growth of metal phthalocyanine on deactivated semiconducting surfaces steered by selective orbital coupling. *Phys. Rev. Lett.*, 115(9):096101, August

2015.

[182] Frank J. Adrian. Charge transfer effects in surfaceenhanced raman scatteringa). *J. Chem. Phys.*, 77(11):5302–5314, December 1982.

[183] Floyd W. Hilty, Andrew K. Kuhlman, Fabian Pauly, and Alexey T. Zayak. Raman scattering from a molecule-semiconductor interface tuned by an electric field: Density functional theory approach. *J. Phys. Chem. C*, 119(40):23113–23118, October 2015.

[184] Max E. Lippitsch. Ground-state charge transfer as a mechanism for surface-enhanced raman scattering. *Phys. Rev. B*, 29(6):3101–3110, March 1984.

[185] John R. Lombardi and Ronald L. Birke. Theory of surface-enhanced raman scattering in semiconductors. *J. Phys. Chem. C*, 118(20):11120–11130, May 2014.

[186] Seth M. Morton and Lasse Jensen. Understanding the moleculesurface chemical coupling in sers. *J. Am. Chem. Soc.*, 131(11):4090–4098, March 2009.

[187] Nicholas Valley, Nathan Greeneltch, Richard P. Van Duyne, and George C. Schatz. A look at the origin and magnitude of the chemical contribution to the enhancement mechanism of surface-enhanced raman spectroscopy (sers): Theory and experiment. *J. Phys. Chem. Lett.*, 4(16):2599–2604, August 2013.

[188] Xiaolong Liu, Itamar Balla, Hadallia Bergeron, Gavin P. Campbell, Michael J. Bedzyk, and Mark C. Hersam. Rotationally commensurate growth of mos2 on epitaxial graphene. *ACS Nano*, 10(1):1067–1075, January 2016.

[189] Xu Cui, En-Min Shih, Luis A. Jauregui, Sang Hoon Chae, Young Duck Kim, Baichang Li, Dongjea Seo, Kateryna Pistunova, Jun Yin, Ji-Hoon Park, Heon-Jin Choi, Young Hee Lee, Kenji Watanabe, Takashi Taniguchi, Philip Kim, Cory R.

Dean, and James C. Hone. Low-temperature ohmic contact to monolayer mos2 by van der waals bonded co/h-bn electrodes. *Nano Lett.*, 17(8):4781–4786, August 2017.

[190] Hong Wang, Fucai Liu, Wei Fu, Zheyu Fang, Wu Zhou, and Zheng Liu. Two-dimensional heterostructures: fabrication, characterization, and application. *Nanoscale*, 6(21):12250–12272, 2014.

[191] Engineering quantum confinement in semiconducting van der waals heterostructure k. wang1, t. taniguchi2, k. watanabe2, p. kim1 * 1department of physics, harvard university, cambridge, 02138, ma, us 2national institute for materials science, namiki 1-1, ibaraki 305-0044, japan *email: pkim@physics.harvard.edu spatial confinement and manipulation of charged carriers in semiconducting nanostructures are essential for realizing quantum electronic devices [1-3]. gate-defined nanostructures made of two-dimensional (2d) semiconducting transition metal dichalcogenides (tmdcs) have the potential to add a unique additional control of quantum degrees of freedom owing to valley-spin locking of confined carriers near the band edges [4-13]. however, due to prevailing inhomogeneities in the conducting channels, it has been difficult to realize quantum confinement in 2d tmdcs with well-controlled tunnel-coupling strength [14-16]. here we demonstrate quantum transport in lateral gate-defined 2d electron quantum dots formed in atomically thin tmdc heterostructures. utilizing micro- fabricated local contact gates, encapsulation in 2d dielectrics and light illumination at low temperatures, we show that the quality of tmdc 2d electron gases (2degs) can be improved, rendering them suitable for mesoscopic quantum transport measurements. we observe quantized conductance in quantum point contact (qpc)

channels controlled by gate-tunable confinement. we also demonstrate single electron transport in tmdc quantum dots (qd) with tunable tunnel-coupling. our observation holds promise for the quantum manipulation of spin and valley degrees of freedom in engineered tmdc nanostructures, enabling versatile 2d quantum electronic devices. 0213.

[192] Guang Yi Jia, Yue Liu, Jing Yu Gong, Dang Yuan Lei, Dan Li Wang, and Zhen Xian Huang. Excitonic quantum confinement modified optical conductivity of monolayer and few-layered mos2. *J. Mater. Chem. C*, 4(37):8822–8828, 2016.

[193] Nan Zhang, Alessandro Surrente, Micha Baranowski, Duncan K. Maude, Patricia Gant, Andres Castellanos-Gomez, and Paulina Plochocka. Moir intralayer excitons in a mose2/mos2 heterostructure. *Nano Lett.*, 18(12):7651–7657, December 2018.

[194] Zhiwei Ding, Qing-Xiang Pei, Jin-Wu Jiang, and Yong-Wei Zhang. Manipulating the thermal conductivity of monolayer mos2 via lattice defect and strain engineering. *J. Phys. Chem. C*, 119(28):16358–16365, July 2015.

[195] Andrey N. Enyashin, Maya Bar-Sadan, Lothar Houben, and Gotthard Seifert. Line defects in molybdenum disulfide layers. *J. Phys. Chem. C*, 117(20):10842–10848, May 2013.

[196] Xiaolong Liu, Itamar Balla, Hadallia Bergeron, and Mark C. Hersam. Point defects and grain boundaries in rotationally commensurate mos2 on epitaxial graphene. *J. Phys. Chem. C*, 120(37):20798–20805, September 2016.

[197] Nihit Saigal and Sandip Ghosh. Phonon induced luminescence decay in monolayer mos2 on sio2/si substrates. *Appl. Phys. Lett.*, 107(24):242103, December 2015.

[198] Haining Wang, Changjian Zhang, and Farhan Rana. Ultrafast dynamics of defect-assisted electron-hole recombination in monolayer mos2. *Nano Lett.*, 15(1):339–345, January 2015.

[199] Z. X. Gan, L. Z. Liu, H. Y. Wu, Y. L. Hao, Y. Shan, X. L. Wu, and Paul K. Chu. Quantum confinement effects across two-dimensional planes in mos2 quantum dots. *Appl. Phys. Lett.*, 106(23):233113, June 2015.

[200] Subhrajit Mukherjee, Rishi Maiti, Ajit K. Katiyar, Soumen Das, and Samit K. Ray. Novel colloidal mos2 quantum dot heterojunctions on silicon platforms for multifunctional optoelectronic devices. *Scientific Reports*, 6(1):29016, June 2016.

[201] Chih-Pin Lu, Guohong Li, Jinhai Mao, Li-Min Wang, and Eva Y. Andrei. Bandgap, mid-gap states, and gating effects in mos2. *Nano Lett.*, 14(8):4628–4633, August 2014.

[202] Kirby K. H. Smithe, Andrey V. Krayev, Connor S. Bailey, Hye Ryoung Lee, Eilam Yalon, zgr Burak Aslan, Miguel Muoz Rojo, Sergiy Krylyuk, Payam Taheri, Albert V. Davydov, Tony F. Heinz, and Eric Pop. Nanoscale heterogeneities in monolayer mose2 revealed by correlated scanning probe microscopy and tip-enhanced raman spectroscopy. *ACS Appl. Nano Mater.*, 1(2):572–579, February 2018.

[203] Sake Wang, Hongyu Tian, Chongdan Ren, Jin Yu, and Minglei Sun. Electronic and optical properties of heterostructures based on transition metal dichalcogenides and graphene-like zinc oxide. *Scientific Reports*, 8(1):12009, August 2018.

[204] Xin He, Hai Li, Zhiyong Zhu, Zhenyu Dai, Yang Yang, Peng Yang, Qiang Zhang, Peng Li, Udo Schwingenschlogl, and Xixiang Zhang. Strain engineering in monolayer ws2, mos2, and the ws2/mos2 heterostructure. *Appl. Phys. Lett.*, 109(17):173105,

October 2016.

[205] Tom Vincent, Vishal Panchal, Tim Booth, Stephen R. Power, Antti-Pekka Jauho, Vladimir Antonov, and Olga Kazakova. Probing the nanoscale origin of strain and doping in graphene-hbn heterostructures. *2D Materials*, 6(1):015022, December 2018.

[206] Yan-Hong Zhou, Jing Zeng, Li-Ming Tang, Ke-Qiu Chen, and W. P. Hu. Giant magnetoresistance effect and spin filters in phthalocyanine-based molecular devices. *Organic Electronics*, 14(11):2940–2947, November 2013.

[207] C. Barraud, K. Bouzehouane, C. Deranlot, D. J. Kim, R. Rakshit, S. Shi, J. Arabski, M. Bowen, E. Beaurepaire, S. Boukari, F. Petroff, P. Seneor, and R. Mattana. Phthalocyanine based molecular spintronic devices. *Dalton Trans.*, 45(42):16694–16699, 2016.

[208] L. L. Tao and J. Wang. Giant magnetoresistance and perfect spin filter effects in manganese phthalocyanine based molecular junctions. *Nanoscale*, 9(34):12684–12689, 2017.

[209] A. Atxabal, M. Ribeiro, S. Parui, L. Urreta, E. Sagasta, X. Sun, R. Llopis, F. Casanova, and L. E. Hueso. Spin doping using transition metal phthalocyanine molecules. *Nature Communications*, 7(1):13751, December 2016.

[210] Emilia Annese, Giovanni Di Santo, Fadi Choueikani, Edwige Otero, and Philippe Ohresser. Iron phthalocyanine and ferromagnetic thin films: Magnetic behavior of single and double interfaces. *ACS Omega*, 4(3):5076–5082, March 2019.

[211] Trevor LaMountain, Hadallia Bergeron, Itamar Balla, Teodor K. Stanev, Mark C. Hersam, and Nathaniel P. Stern. Valley-selective optical stark effect probed by kerr

rotation. *Phys. Rev. B*, 97(4):045307, January 2018.

[212] Bevin Huang, Genevieve Clark, Efrn Navarro-Moratalla, Dahlia R. Klein, Ran Cheng, Kyle L. Seyler, Ding Zhong, Emma Schmidgall, Michael A. McGuire, David H. Cobden, Wang Yao, Di Xiao, Pablo Jarillo-Herrero, and Xiaodong Xu. Layer-dependent ferromagnetism in a van der waals crystal down to the monolayer limit. *Nature*, 546:270–273, Jun 2017.

[213] Tiancheng Song, Xinghan Cai, Matisse Wei-Yuan Tu, Xiaoou Zhang, Bevin Huang, Nathan P. Wilson, Kyle L. Seyler, Lin Zhu, Takashi Taniguchi, Kenji Watanabe, Michael A. McGuire, David H. Cobden, Di Xiao, Wang Yao, and Xiaodong Xu. Giant tunneling magnetoresistance in spin-filter van der waals heterostructures. *Science*, 360(6394):1214, June 2018.

[214] Kin Fai Mak, Jie Shan, and Daniel C. Ralph. Probing and controlling magnetic states in 2d layered magnetic materials. *Nature Reviews Physics*, 1(11):646–661, November 2019.

[215] Suyog Padgaonkar, Samuel H. Amsterdam, Hadallia Bergeron, Katherine Su, Tobin J. Marks, Mark C. Hersam, and Emily A. Weiss. Molecular-orientation-dependent interfacial charge transfer in phthalocyanine/mos2 mixed-dimensional heterojunctions. *J. Phys. Chem. C*, 123(21):13337–13343, May 2019.

[216] Chul-Ho Lee, Theanne Schiros, Elton J. G. Santos, Bumjung Kim, Kevin G. Yager, Seok Ju Kang, Sunwoo Lee, Jaeeun Yu, Kenji Watanabe, Takashi Taniguchi, James Hone, Efthimios Kaxiras, Colin Nuckolls, and Philip Kim. Epitaxial growth of molecular crystals on van der waals substrates for high-performance organic electronics. *Adv. Mater.*, 26(18):2812–2817, May 2014.

[217] Hiroyuki Yoshida, Kazuto Yamada, Jun'ya Tsutsumi, and Naoki Sato. Complete description of ionization energy and electron affinity in organic solids: Determining contributions from electronic polarization, energy band dispersion, and molecular orientation. *Phys. Rev. B*, 92(7):075145, August 2015.

[218] Beomjin Park, Kyunghun Kim, Jaesung Park, Heeseon Lim, Phung Thi Lanh, A.-Rang Jang, Chohee Hyun, Chang Woo Myung, Seungkyoo Park, Jeong Won Kim, Kwang S. Kim, Hyeon Suk Shin, Geunsik Lee, Se Hyun Kim, Chan Eon Park, and Jin Kon Kim. Anomalous ambipolar transport of organic semiconducting crystals via control of molecular packing structures. *ACS Appl. Mater. Interfaces*, 9(33):27839–27846, August 2017.

[219] Y. . Lin, D. J. Gundlach, S. F. Nelson, and T. N. Jackson. Stacked pentacene layer organic thin-film transistors with improved characteristics. *IEEE Electron Device Letters*, 18(12):606–608, 1997.

[220] Mark W. B. Wilson, Akshay Rao, Bruno Ehrler, and Richard H. Friend. Singlet exciton fission in polycrystalline pentacene: From photophysics toward devices. *Acc. Chem. Res.*, 46(6):1330–1338, June 2013.

[221] C. Kim, A. Facchetti, and T. J. Marks. Gate dielectric microstructural control of pentacene film growth mode and field-effect transistor performance. *Adv. Mater.*, 19(18):2561–2566, September 2007.

[222] Rui He, Nancy G. Tassi, Graciela B. Blanchet, and Aron Pinczuk. Intense photoluminescence from pentacene monolayers. *Applied Physics Letters*, 96(26):127, 2010.

[223] Daniel Faltermeier, Bruno Gompf, Martin Dressel, Ashutosh K. Tripathi, and Jens Pflaum. Optical properties of pentacene thin films and single crystals. *Phys. Rev. B*, 74(12):125416, September 2006.

[224] Ricardo Ruiz, Devashish Choudhary, Bert Nickel, Tullio Toccoli, Kee-Chul Chang, Alex C. Mayer, Paulette Clancy, Jack M. Blakely, Randall L. Headrick, Salvatore Iannotta, and George G. Malliaras. Pentacene thin film growth. *Chem. Mater.*, 16(23):4497–4508, November 2004.

[225] Jan Gtzen, Daniel Kfer, Christof Wll, and Gregor Witte. Growth and structure of pentacene films on graphite: Weak adhesion as a key for epitaxial film growth. *Phys. Rev. B*, 81(8):085440, February 2010.

[226] Kwanpyo Kim, Elton J. G. Santos, Tae Hoon Lee, Yoshio Nishi, and Zhenan Bao. Epitaxially grown strained pentacene thin film on graphene membrane. *Small*, 11(17):2037–2043, May 2015.

[227] Leonard von Helden, Tobias Breuer, and Gregor Witte. Anisotropic thermal expansion in pentacene and perfluoropentacene: Effects of molecular packing motif and fixation at the interface. *Applied Physics Letters*, 110(14):141904, 2017.

[228] Deep Jariwala, Sarah L. Howell, Kan-Sheng Chen, Junmo Kang, Vinod K. Sangwan, Stephen A. Filippone, Riccardo Turrisi, Tobin J. Marks, Lincoln J. Lauhon, and Mark C. Hersam. Hybrid, gate-tunable, van der waals p–n heterojunctions from pentacene and MoS2. *Nano Letters*, 16(1):497–503, dec 2015.

[229] J. Helzel, S. Jankowski, M. El Helou, G. Witte, and W. Heimbrodt. Temperature dependent optical properties of pentacene films on zinc oxide. *Appl. Phys. Lett.*, 99(21):211102, November 2011.

[230] Yoshinobu Hosoi, Daniel Martnez Deyra, Kazuhiro Nakajima, and Yukio Furukawa. Micro-raman spectroscopy on pentacene thin-film transistors. *null*, 491(1):317–323, September 2008.

[231] Keisuke Seto and Yukio Furukawa. Study on solid structure of pentacene thin films using raman imaging. *J. Raman Spectrosc.*, 43(12):2015–2019, December 2012.

[232] Mark W. B. Wilson, Akshay Rao, Jenny Clark, R. Sai Santosh Kumar, Daniele Brida, Giulio Cerullo, and Richard H. Friend. Ultrafast dynamics of exciton fission in polycrystalline pentacene. *J. Am. Chem. Soc.*, 133(31):11830–11833, August 2011.

[233] Rui He, X. Chi, Aron Pinczuk, D. V. Lang, and A. P. Ramirez. Extrinsic optical recombination in pentacene single crystals: Evidence of gap states. *Appl. Phys. Lett.*, 87(21):211117, November 2005.

[234] T. AOKI-MATSUMOTO, K. FURUTA, T. YAMADA, H. MORIYA, K. MIZUNO, and A. H. MATSUI. Excitonic photoluminescence in pentacene single crystal. *Int. J. Mod. Phys. B*, 15(28n30):3753–3756, December 2001.

[235] Demetris N. Bikiaris and George P. Karayannidis. Thermomechanical analysis of chain-extended pet and pbt. *J. Appl. Polym. Sci.*, 60(1):55–61, April 1996.

[236] B. Yates, M. J. Overy, and O. Pirgon. The anisotropic thermal expansion of boron nitride. *null*, 32(4):847–857, October 1975.

[237] I. Blech and U. Cohen. Effects of humidity on stress in thin silicon dioxide films. *Journal of Applied Physics*, 53(6):4202–4207, June 1982.

[238] Sefaattin Tongay, Joonki Suh, Can Ataca, Wen Fan, Alexander Luce, Jeong Seuk Kang, Jonathan Liu, Changhyun Ko, Rajamani Raghunathanan, Jian Zhou, Frank

Ogletree, Jingbo Li, Jeffrey C. Grossman, and Junqiao Wu. Defects activated photoluminescence in two-dimensional semiconductors: interplay between bound, charged and free excitons. *Scientific Reports*, 3(1):2657, September 2013.

[239] D. Kaplan, K. Mills, J. Lee, S. Torrel, and V. Swaminathan. Excitation intensity dependent photoluminescence of annealed two-dimensional mos2 grown by chemical vapor deposition. *Journal of Applied Physics*, 119(21):214301, June 2016.

[240] Xiaoting Huang, Yang Gao, Tianqi Yang, Wencai Ren, Hui-Ming Cheng, and Tianshu Lai. Quantitative analysis of temperature dependence of raman shift of monolayer ws2. *Scientific Reports*, 6(1):32236, August 2016.

[241] Duan Zhang, Ye-Cun Wu, Mei Yang, Xiao Liu, Cormac . Coilein, Hongjun Xu, Mourad Abid, Mohamed Abid, Jing-Jing Wang, Igor V. Shvets, Haonan Liu, Zhi Wang, Hongxing Yin, Huajun Liu, Byong Sun Chun, Xiangdong Zhang, and Han-Chun Wu. Probing thermal expansion coefficients of monolayers using surface enhanced raman scattering. *RSC Adv.*, 6(101):99053–99059, 2016.

[242] Lenan Zhang, Zhengmao Lu, Youngsup Song, Lin Zhao, Bikram Bhatia, Kevin R. Bagnall, and Evelyn N. Wang. Thermal expansion coefficient of monolayer molybdenum disulfide using micro-raman spectroscopy. *Nano Lett.*, 19(7):4745–4751, July 2019.

[243] Zhongtao Lin, Wuguo Liu, Shibing Tian, Ke Zhu, Yuan Huang, and Yang Yang. Thermal expansion coefficient of few-layer mos2 studied by temperature-dependent raman spectroscopy. *Scientific Reports*, 11(1):7037, March 2021.

[244] I. Maximov, A. A. Zakharov, T. Holmqvist, L. Montelius, and I. Lindau. Investigation of polymethylmethacrylate resist residues using photoelectron microscopy.

Journal of Vacuum Science & Technology B: Microelectronics and Nanometer Structures Processing, Measurement, and Phenomena, 20(3):1139–1142, May 2002.

[245] D. S. Macintyre, O. Ignatova, S. Thoms, and I. G. Thayne. Resist residues and transistor gate fabrication. *Journal of Vacuum Science & Technology B: Microelectronics and Nanometer Structures Processing, Measurement, and Phenomena*, 27(6):2597–2601, November 2009.

[246] Yuehui Jia, Xin Gong, Pei Peng, Zidong Wang, Zhongzheng Tian, Liming Ren, Yunyi Fu, and Han Zhang. Toward high carrier mobility and low contact resistance: Laser cleaning of pmma residues on graphene surfaces. *Nano-Micro Letters*, 8(4):336–346, October 2016.

[247] Ethan C. Ahn. 2d materials for spintronic devices. *npj 2D Materials and Applications*, 4(1):17, June 2020.

[248] Yanping Liu, Cheng Zeng, Jiahong Zhong, Junnan Ding, Zhiming M. Wang, and Zongwen Liu. Spintronics in two-dimensional materials. *Nano-Micro Letters*, 12(1):93, April 2020.

[249] Vertikasari P. Ningrum, Bowen Liu, Wei Wang, Yao Yin, Yi Cao, Chenyang Zha, Hongguang Xie, Xiaohong Jiang, Yan Sun, Sichen Qin, Xiaolong Chen, Tianshi Qin, Chao Zhu, Lin Wang, and Wei Huang. Recent advances in two-dimensional magnets: Physics and devices towards spintronic applications. *Research*, 2020:1768918, June 2020.

[250] Giang D. Nguyen, Jinhwan Lee, Tom Berlijn, Qiang Zou, Saban M. Hus, Jewook Park, Zheng Gai, Changgu Lee, and An-Ping Li. Visualization and manipulation of magnetic domains in the quasi-two-dimensional material Fe_3GeTe_2. *Phys. Rev. B*,

97(1):014425, January 2018.

[251] Guanxing Guo, Gang Bi, Chunfeng Cai, and Huizhen Wu. Effects of external magnetic field and out-of-plane strain on magneto-optical kerr spectra in cri(3) monolayer. *Journal of physics. Condensed matter : an Institute of Physics journal*, 30:285303, Jul 2018.

[252] Bevin Huang, Genevieve Clark, Dahlia R. Klein, David MacNeill, Efrn Navarro-Moratalla, Kyle L. Seyler, Nathan Wilson, Michael A. McGuire, David H. Cobden, Di Xiao, Wang Yao, Pablo Jarillo-Herrero, and Xiaodong Xu. Electrical control of 2d magnetism in bilayer cri3. *Nature Nanotechnology*, 13(7):544–548, July 2018.

[253] John Kerr. Xliii. on rotation of the plane of polarization by reflection from the pole of a magnet. *The London, Edinburgh, and Dublin Philosophical Magazine and Journal of Science*, 3(19):321–343, 1877.

[254] Anatoli Konstantinovich Zvezdin and Viacheslav Alekseevich Kotov. *Modern magnetooptics and magnetooptical materials*. CRC Press, 1997.

[255] Jeffrey McCord. Progress in magnetic domain observation by advanced magneto-optical microscopy. *Journal of Physics D: Applied Physics*, 48(33):333001, 2015.

[256] Tomoya Higo, Huiyuan Man, Daniel B. Gopman, Liang Wu, Takashi Koretsune, Olaf M. J. van t Erve, Yury P. Kabanov, Dylan Rees, Yufan Li, Michi-To Suzuki, Shreyas Patankar, Muhammad Ikhlas, C. L. Chien, Ryotaro Arita, Robert D. Shull, Joseph Orenstein, and Satoru Nakatsuji. Large magneto-optical kerr effect and imaging of magnetic octupole domains in an antiferromagnetic metal. *Nature Photonics*, 12(2):73–78, February 2018.

[257] Yilv Guo, Shijun Yuan, Bing Wang, Li Shi, and Jinlan Wang. Half-metallicity and enhanced ferromagnetism in li-adsorbed ultrathin chromium triiodide. *J. Mater. Chem. C*, 6(21):5716–5720, 2018.

[258] Hyun Ho Kim, Shengwei Jiang, Bowen Yang, Shazhou Zhong, Shangjie Tian, Chenghe Li, Hechang Lei, Jie Shan, Kin Fai Mak, and Adam W. Tsen. Magneto-memristive switching in a 2d layer antiferromagnet. *Adv. Mater.*, 32(2):1905433, January 2020.

[259] Kyle L. Seyler, Ding Zhong, Dahlia R. Klein, Shiyuan Gao, Xiaoou Zhang, Bevin Huang, Efrn Navarro-Moratalla, Li Yang, David H. Cobden, Michael A. McGuire, Wang Yao, Di Xiao, Pablo Jarillo-Herrero, and Xiaodong Xu. Ligand-field helical luminescence in a 2d ferromagnetic insulator. *Nature Physics*, 14(3):277–281, March 2018.

[260] Dmitry Shcherbakov, Petr Stepanov, Daniel Weber, Yaxian Wang, Jin Hu, Yanglin Zhu, Kenji Watanabe, Takashi Taniguchi, Zhiqiang Mao, Wolfgang Windl, Joshua Goldberger, Marc Bockrath, and Chun Ning Lau. Raman spectroscopy, photocatalytic degradation, and stabilization of atomically thin chromium tri-iodide. *Nano Lett.*, 18(7):4214–4219, July 2018.

[261] Gabriel C. Constantinescu and Nicholas D. M. Hine. Multipurpose black-phosphorus/hbn heterostructures. *Nano Lett.*, 16(4):2586–2594, April 2016.

[262] Michael Seitz, Patricia Gant, Andres Castellanos-Gomez, and Ferry Prins. Long-term stabilization of two-dimensional perovskites by encapsulation with hexagonal boron nitride, 2019.

[263] Joshua D. Wood, Spencer A. Wells, Deep Jariwala, Kan-Sheng Chen, EunKyung Cho, Vinod K. Sangwan, Xiaolong Liu, Lincoln J. Lauhon, Tobin J. Marks, and Mark C. Hersam. Effective passivation of exfoliated black phosphorus transistors against ambient degradation. *Nano Lett.*, 14(12):6964–6970, December 2014.

[264] Marta Galbiati, Victor Zatko, Florian Godel, Pomme Hirschauer, Aymeric Vecchiola, Karim Bouzehouane, Sophie Collin, Bernard Servet, Andrs Cantarero, Frdric Petroff, Marie-Blandine Martin, Bruno Dlubak, and Pierre Seneor. Very long term stabilization of a 2d magnet down to the monolayer for device integration. *ACS Appl. Electron. Mater.*, 2(11):3508–3514, November 2020.

[265] Justice M. P. Alaboson, Qing Hua Wang, Jonathan D. Emery, Albert L. Lipson, Michael J. Bedzyk, Jeffrey W. Elam, Michael J. Pellin, and Mark C. Hersam. Seeding atomic layer deposition of high-k dielectrics on epitaxial graphene with organic self-assembled monolayers. *ACS Nano*, 5(6):5223–5232, June 2011.

[266] J. Tyler Gish, Dmitry Lebedev, Teodor K. Stanev, Shizhou Jiang, Leonidas Georgopoulos, Thomas W. Song, Gilhwan Lim, Ethan S. Garvey, Luk Valdman, Oluwaseyi Balogun, Zdenk Sofer, Vinod K. Sangwan, Nathaniel P. Stern, and Mark C. Hersam. Ambient-stable two-dimensional cri3 via organic-inorganic encapsulation. *ACS Nano*, 15(6):10659–10667, June 2021.

[267] Haining Liu, Xinsheng Wang, Juanxia Wu, Yuansha Chen, Jing Wan, Rui Wen, Jinbo Yang, Ying Liu, Zhigang Song, and Liming Xie. Vapor deposition of magnetic van der waals nii2 crystals. *ACS Nano*, 14(8):10544–10551, August 2020.

[268] M. Fronk, C. Schubert, F. Haidu, C. Scarlat, K. Dorr, M. Albrecht, D. R. T. Zahn, and G. Salvan. Characterization of organic thin films on ferromagnetic substrates

by spectroscopic ellipsometry and magneto-optical kerr effect spectroscopy. *IEEE Transactions on Magnetics*, 48(11):2777–2780, Nov.

[269] M. Fronk, B. Bruer, J. Kortus, O. G. Schmidt, D. R. T. Zahn, and G. Salvan. Determination of the voigt constant of phthalocyanines by magneto-optical kerr-effect spectroscopy. *Phys. Rev. B*, 79(23):235305, June 2009.

APPENDIX A

Layer Exfoliation, Preparation, and Engineering

The appendix will describe in detail the various fabrication techniques used to realize two-dimensional based heterostructures and devices. It will also provide images and schematics of specifically, custom designed hardware. This will be organized as follows.

First, exfoliation techniques used to find two-dimensional layers will be explained with step-by-step instructions. My work has produced several techniques in evolution from literature and of my own design. Second, a detailed overview of the transfer processes used will be provided with instructions for reproduction. This will detail how stacked heterostructures of 2D materials are realized, how suspended TEM-devices were made, and how waveguide coupled layers were achieved.

A.1. Exfoliation Techniques

A.1.1. Micromechanical Exfoliation - The Scotch Tape Method

Popularized by the Nobel Prize winning graphene monolayer isolation, micromechanical exfoliation or "The Scotch Tape" method is the go to standard exfoliation technique. While this process appears simple, achieving high yield and large size monolayers is no trivial task and can take hours or days of tedium to identify a suitable monolayer.

The standard procedure is as follows:

(1) Source crystals are gently padded onto the adhesive side of scotch tape. This is spread across a portion of the tape.

(2) The tape is folded over such that the segment of material touches an empty part of adhesive, and pressed together gently.

(3) The tape is slowly and gently peeled apart.

(4) The process of folding and peeling is repeated with the initial segment such that the length of tape has a good coverage of material.

(5) If this process is done too quickly, resulting layer exfoliation will be small and granular. Layers will be torn up.

(6) Pieces of thermal oxide wafer or wafer of choice are placed face-down (polished side SiO_2 down) onto the material and pressed to ensure uniform surface contact.

(7) The tape is then peeled (again slowly) from the thermal oxide, leaving behind a coating of exfoliated material on the wafer.

(8) This process can be repeated many times with the same tape. As the quality of the material on the tape wears down, the size of the exfoliated pieces will be visibly smaller. A new tape is then made.

This process is demonstrated in in part Fig.[A.1] and with a personalized twist in Fig.[A.2] that will be detailed shortly. For the Stern Group, the wafer of choice is most commonly thermal oxide (285 nm SiO_2 on p-doped Si). This wafer provides a good adhesion for monolayers, good contrast for identification of monolayers, and good electrical isolation of the layer from the Si for electrical device fabrication and back-gating. Our group has also used SiN wafer and Si wafers but these have proven to have worse adhesion of the monolayer and thus lower yields.

While the process detailed will eventually yield monolayers, I developed my own "twist" on these steps that have proven to result in much higher yields at the cost of a longer period of time needed to exfoliate a given wafer. (This technique has also proved popular with other groups at Northwestern and I have shared it with many other graduate students who have also found it to be very successful.)

The process is similar to the one from above up to step 6. The details below follow after step 6:

(1) (Previously Step 6, provided for reference) Pieces of thermal oxide wafer or wafer of choice are placed face-down onto the material and pressed to ensure surface contact.

(2) A soft flat guiding tool is used to gently rub the non-adhesive side of the tape down onto the wafer. This is done in smooth gliding strokes from one end of the tape to the other, and back. This process can be repeated and is one of "feel".

(3) Tape and wafers can be left like this for days without adverse effects or can be immediately prepped for exfoliation as follows.

(4) The wafers with tape and material still attached are then moved to a hot-plate. The hot-plate is set to approximately 50 to 70C and left to heat for an hour.

(5) Using the guiding tool, the wafer and tape are once again gently rubbed back and forth (still on the hotplate). This is done one or twice every 15 to 30 minutes for one to two hours.

(6) While still hot, the tape is slowly peeled from the wafer. The wafers are then removed from the hotplate and left to cool for a minute.

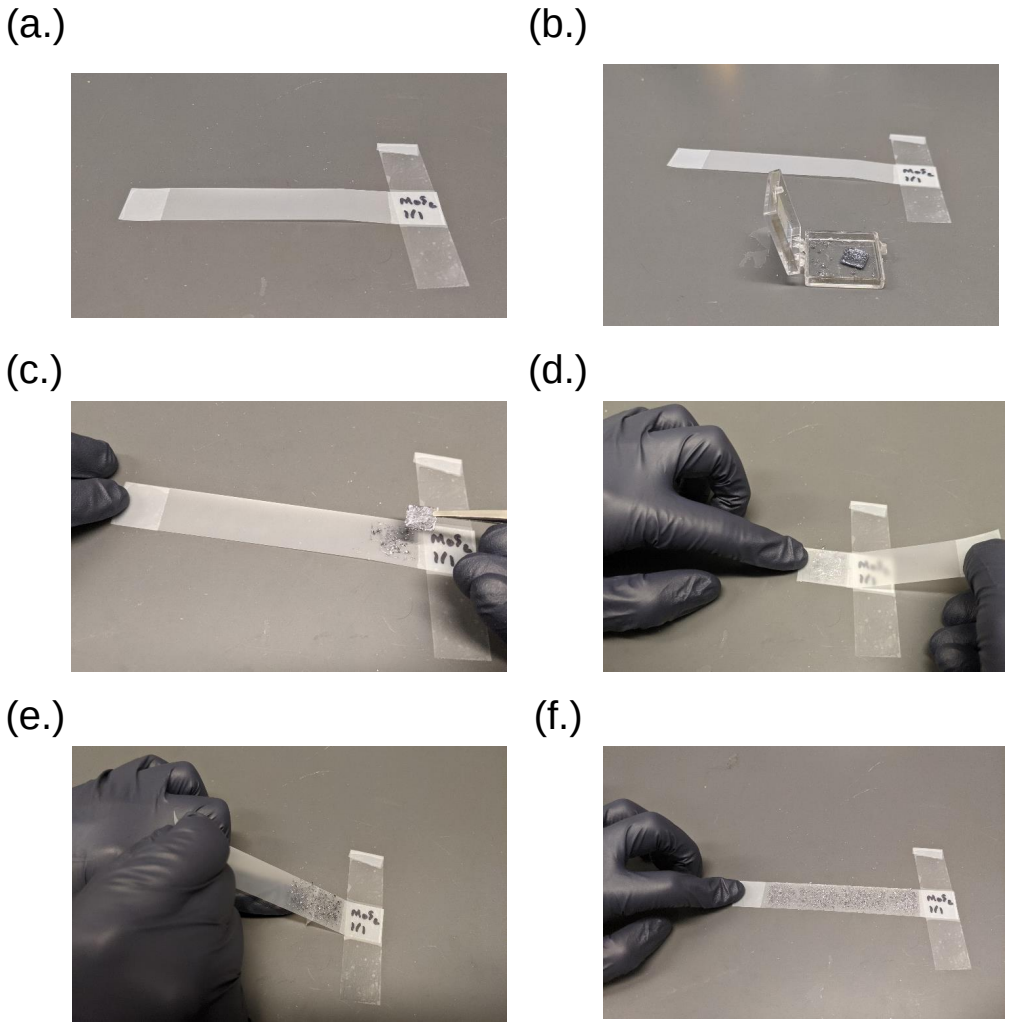

Figure A.1. Common preparation of micromechanical exfoliation tape, follows steps as described in the section list. (a.) Blank tape with folded edges for points of contact with gloved hands, helps to keep tape orderly and clear from contact residue. (b.) TMD crystal (MoS_2 pictured). (c.) The TMD crystal is pressed and pulled from the tape, leaving behind pieces of material residue. (d.) Tape is folded over on itself. (e.) The tape is slowly pulled apart, leaving two portions of tape with cleaved TMD layers. (f.) The process in (e.) is repeated until the material has covered the whole tape.

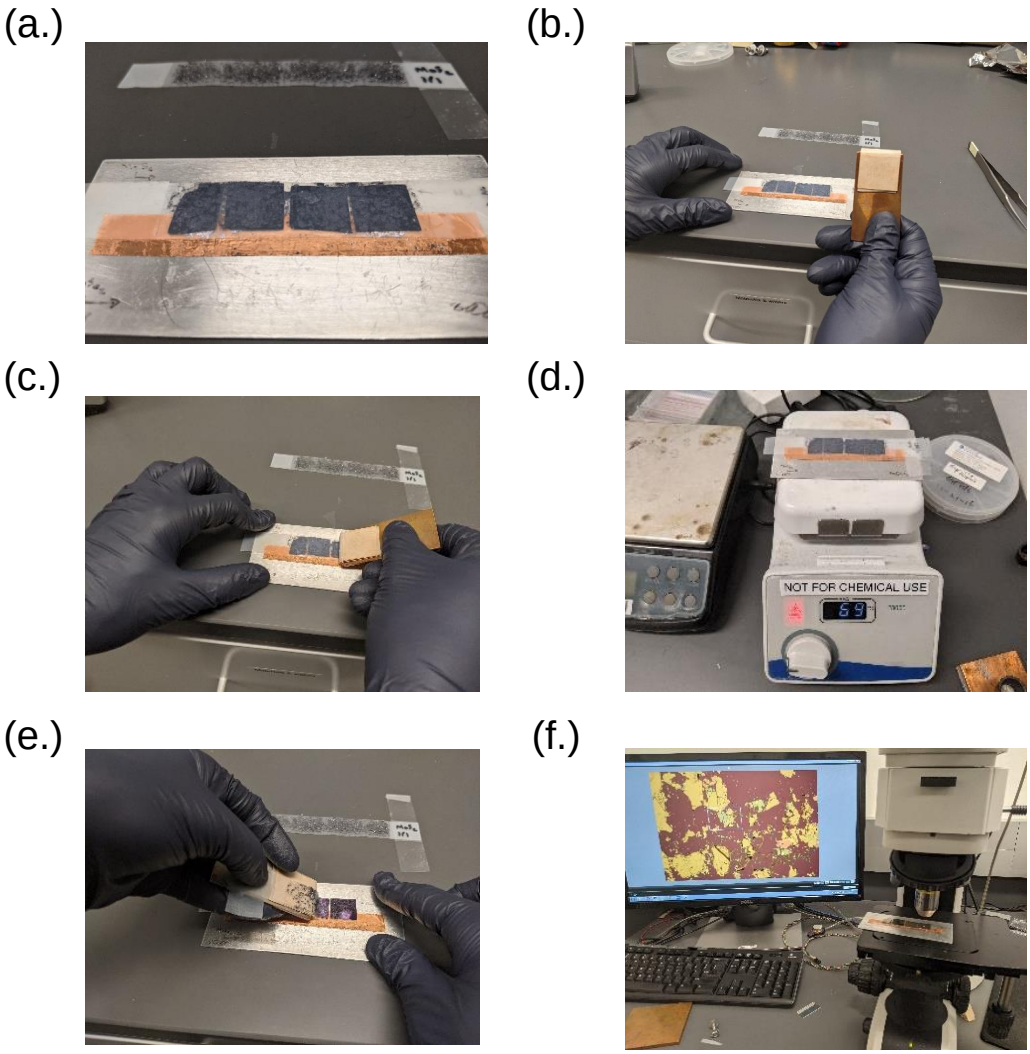

Figure A.2. Heat and massage treated exfoliation for higher yield. (a.) A tape identical to the one made in Fig.[A.1] is placed atop wafer of SiO_2 thermal oxide of 285 nm thickness on p-doped Si. (b.) The soft guiding tool used to rub the backside of the tape. (c.) Gentle rubbing of the back side of the tape, done in strokes across the whole length of chips. A base plate as shown here made of aluminum is ideal for keeping chips from sliding or the tape from tearing. It is also a good thermal conductor for the healing step and prevents the tape from directly melting touching (contaminating) the hotplate. (d.) Samples are moved to a hotplate and heated at approx. 70 C for an hour or more. (e.) After treatment as described in this section, the tape is peeled off while still warm. (f.) The samples are moved to the microscope and can now be carefully examined for layers of desired thicknesses either through the eye-pieces or through a digital camera live-feed.

While this process takes considerably more preparation over that of rapidly exfoliating layers, it has proven to yield large (over 50 um length) monolayers as well as produce usable (15-30 um) layers at near unity with the number of wafers used. This makes the technique considerably less wasteful of source material, wafers, and a graduate student's time.

Both of these methods are applicable to hBN exfoliation. Because hBN is not necessarily needed as large monolayers, the standard micromechanical method works suitably for finding large, thick layers to use as part of hBN-TMD sandwiches. If monolayers (such as those needed for tunneling contact designs) are needed, then the second method is more advantageous.

After a wafer is exfoliated onto, the wafer is moved to the optical microscope and scanned at 10x or 20x magnification under top-down white light illumination in search of monolayers or layers of desirable thickness. Exfoliated layer examples can be seen Fig.[A.3] where exfoliation results are shown for MoS_2 and hBN. It is possible to identify layers of different thicknesses here due to the different contrasts of different layer thicknesses on the oxide wafer. The contrast to layer number association was established via careful atomic force microscopy study of many exfoliated layers, this was done in tandem with Erik J. Lenferink through our tenure together, for TMDs and hBN. TMDs, in general, at monolayer are slightly off-color of the surrounding wafer (the exact contract varies by material type) and become darker (and bluer or purple, again dependent on material type) with increasing layer number until bulk. Bulk MoS_2 is a bright yellow. hBN has a different trend that loops in color and can be quite confusing at a glance on how many layers are being observed. Monolayer to few layer is similar to TMDs but with an

even lower contrast from the surrounding oxide (an orange light filter helps distinguish monolayers more easily than with white light). To better establish a reference guide for thicker hBN, which the Stern Group uses routinely for heterostructures, a color contrast to thickness (from AFM) guide was made in a joint effort with Erik. This can be seen in Fig.[A.4].

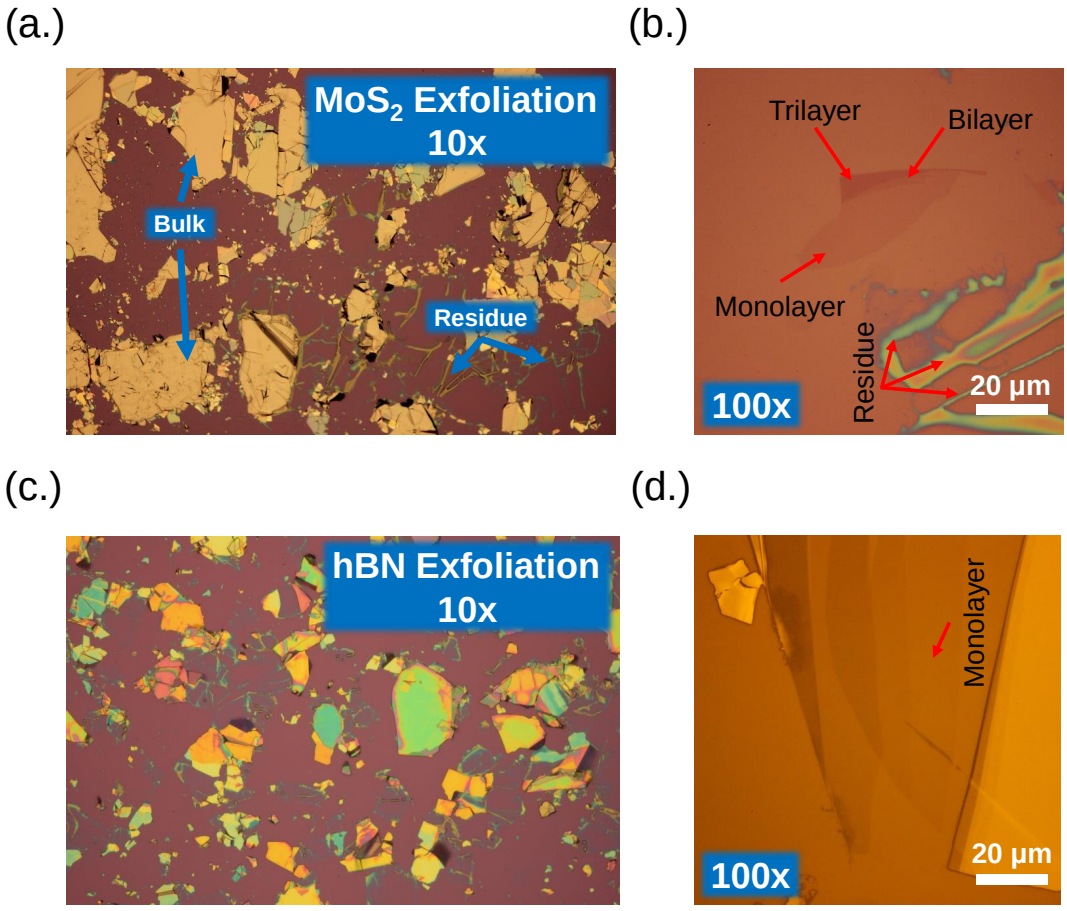

Figure A.3. Exfoliation result from Fig.[A.2]. (a.) The same image as seen in the video feed of the previous figure. At 10x, majority of the field is covered in large bulk crystals and visible tape residue. (b.) After careful searching, a large monolayer (roughly 20 x 40 microns) can be found. Attached bilayer and trilayer segments are also labeled. The slight contrast changes set apart the different layer thicknesses. Residue is labeled again for instructive show at 100x magnification. This residue will burned away in annealing. (c.) hBN exoliation. The bulk has a more distinct rainbow coloring. (d.) An example monolayer of hBN is shown under an orange filter. This filter is necessary to find hBN monolayers are their contrast under standard white light is too faint to notice.

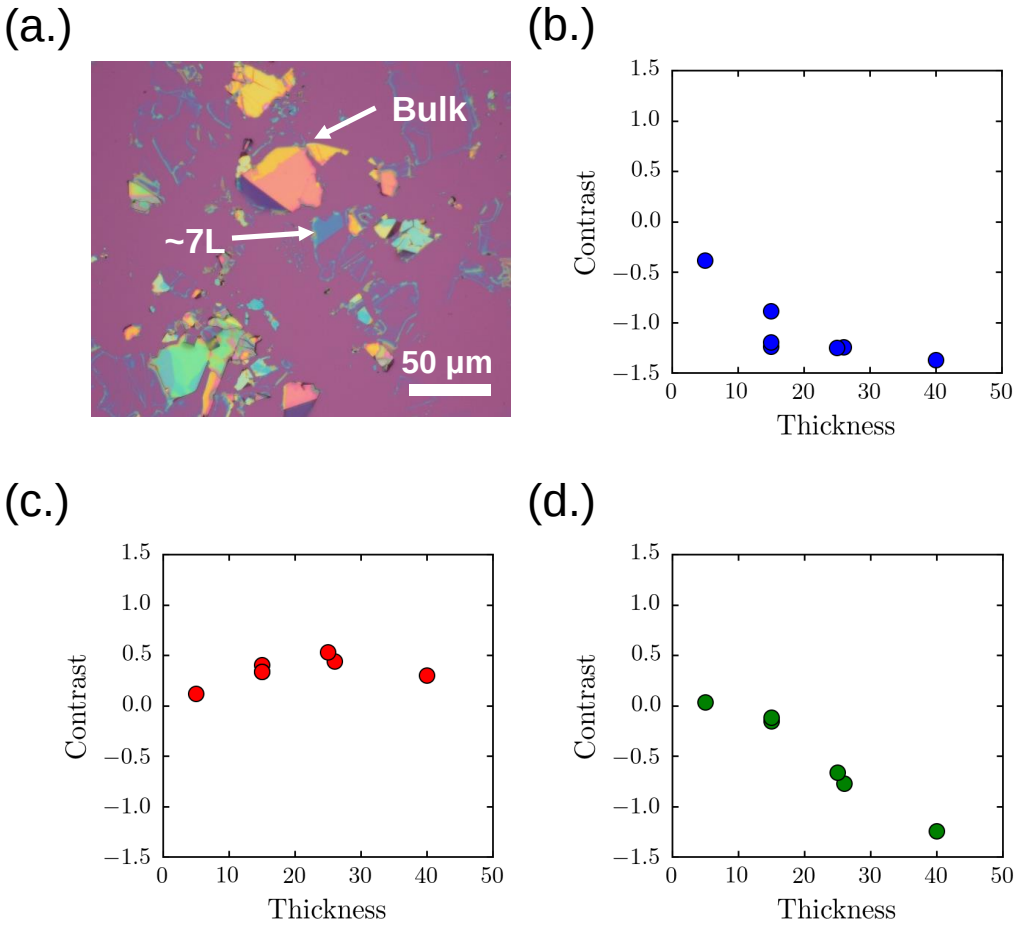

Figure A.4. hBN exfoliation and characterization. (a.) Tape exfoliated hBN layers (and tape residues visible). The layer contrast can be seen, signifying the different potential thicknesses of the layers. (b.-d.) Contrast RGB analysis of the layer colors relative to the SiO_2 substrate to determine approximate thicknesses of the layers. This thickness comparison was achieved by correlating hBN color contrast to AFM results over many layers.

Following exfoliation and identification, layers of interest can be annealed to clean off tape-adhesive residues. While both processes detailed above are expected to leave behind residue, the longer the second process is used for a given wafer, the more residue is expected to remain on the wafer. If there is an extreme excess of tape residue on

the wafer, it is recommended to add at least an extra hour of annealing. The anneal process explained here is the same for all exfoliation and transfer techniques and will be referenced in subsequent sections. Samples are annealed for 3 hours (2 hours annealing, 30 minutes ramping and 30 minutes cooling), in an Ar/H_2 rich environment (600/200 sccm, respectively). This is done to protect the oxygen sensitive layers (such as MoS_2 or WS_2 from oxygen-induced damage, for hBN-only annealing the hydrogen is unnecessary.

A.1.2. Gel Method Exfoliation - Fast, Large Layer Yield

Where the micromechanical techniques detailed previously produce very high quality layers, there are situations where fast and large yield is more desirable even with caveats. To that end, a secondary technique for achieving large monolayers of TMDs was used, aka the "gel" method. This method functions similarly to the micromechanical method and has some similar steps which will be detailed shortly. This technique has high yields of large monolayers but is prone to key issue such as: PDMS residue (requires use of an aggressive cleaning to remove), layer wrinkles, and tearing. Wrinkles and tearing are often minor issues and can be iterated through, but the PDMS residue is an overarching issue with this method and can result in issues with spin-coating resists (such as those needed for contact writing or patterning).

The procedure is as follows:

(1) A low adhesion tape is used as the exfoliation target.

(2) Source crystals are exfoliated onto a corner of the tape and stamping is done to spread the material across the length of the tape in a method identical to the one described in the previous section for micromechanical exfoliation.

(3) Squares of PDMS Gels are cut out and the soft cover is peeled away leaving behind a hard plastic-backed gel stamp.

(4) The gel-side is placed onto to the tape and pressed down to make good contact with the exfoliated bulk crystals.

(5) Similar squares of gel can be placed along the length of the tape.

(6) Let the gel stamp sit on the exfoliation tape for roughly 15 minutes to let the gel to relax.

(7) The gel is then slowly, and carefully peeled from the tape without letting the gel warp in the process. If the tape adhesive is too strong the gel will partially stick to the tape and stretch (this can also happen at times even with low adhesion tapes), this can and will cause exfoliated layers to tear apart on the gel.

(8) This process can be repeated many times with the same tape. The gels are only one time use and must be disposed of once used.

This process is demonstrated pictorially in Fig.[A.5] and layer identification in Fig.[A.6]. The transfer process hardware will be detailed in the following section where the transfer stage is introduced. However, I will show a transferred layer in this section "completing" the exfoliation steps of the gel-method.

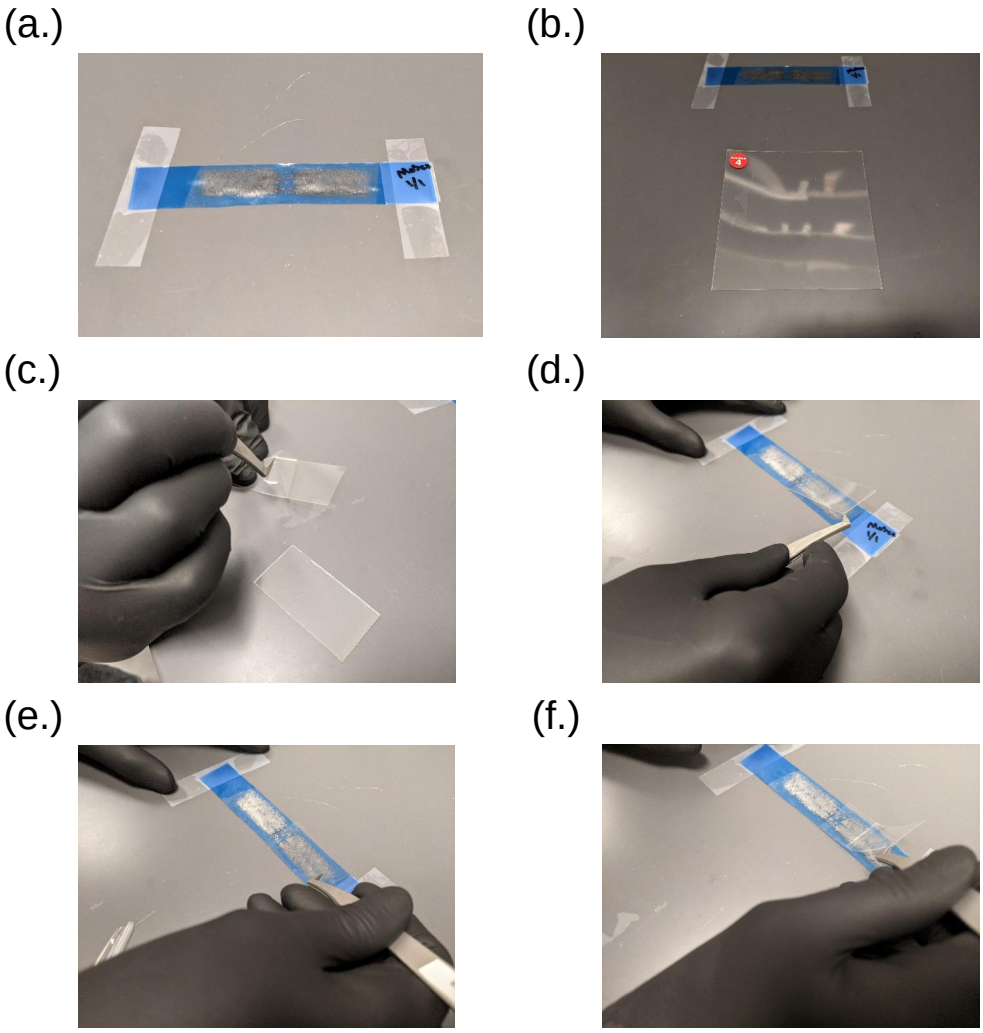

Figure A.5. Gel exfoliation, analogous to the tape exfoliation method, as detailed in the procedure in this section. (a.) Low adhesion tape is prepared with MoS_2 flakes (or other TMDs) from bulk crystals. (b.) Example of gel used, the level 4 adhesion of the gel is important to avoid higher levels (hard to remove from tape or target chip, less likely to release the exfoliated TMD) or lower levels (too weak adhesion to pick up layers from the tape). (c.) Soft protection plastic is removed from the gel. (d.-e.) Gel is placed atop the exfoliated TMD on the tape, and pressed down gently to create a smooth interface with no bubbles. (f.) The gel is peeled off slowly and carefully, picked up.

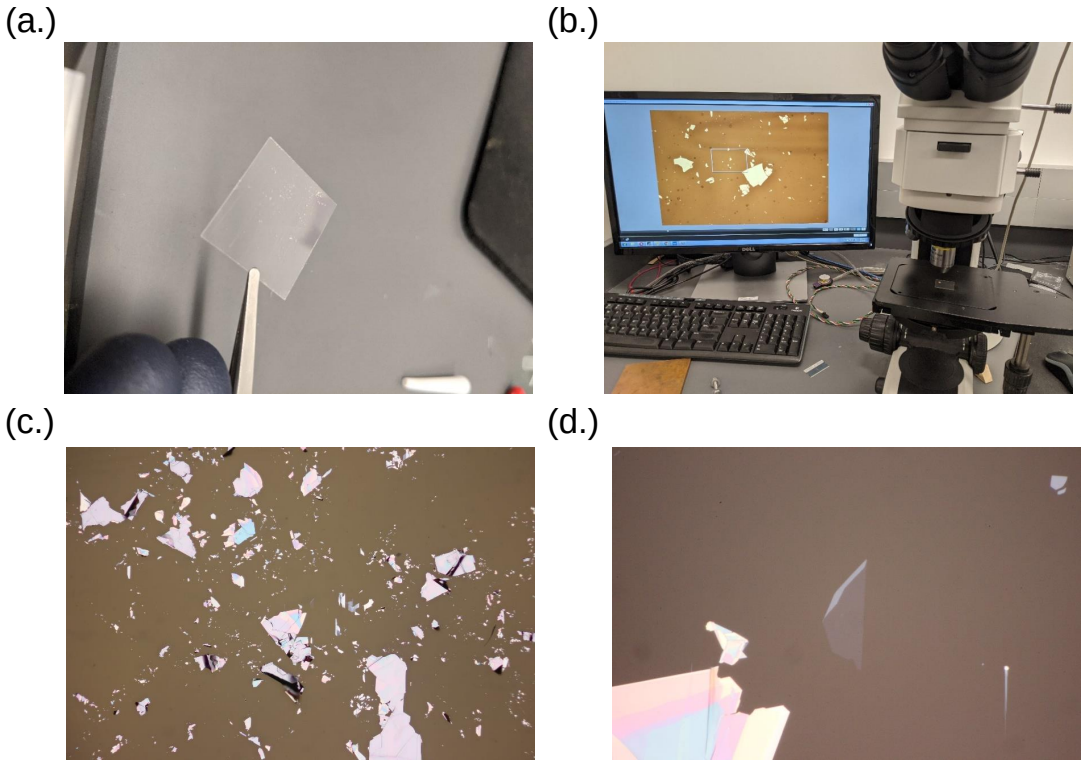

Figure A.6. Final steps of gel exfoliation preparation. (a.) Gel with visible pieces of bulk MoS_2 as exfoliated from the blue tape in Fig.[A.5]. (b.) The gel piece being observed under a microscope, the bulk pieces being very visible as large yellow blocks. The gel is carefully scanned for monolayers. (c.) Direct image of bulk and other pieces of MoS_2 at 10x magnification. (d.) Monolayer of MoS_2 on gel at 100x magnification.

After a layer is exfoliated onto a gel piece and identified Fig.[A.6], the gel is inverted and anchored to the transfer stage platform as seen in Fig.[A.7] and positioned over a sample of interest where the identified layer is desired to be placed. The entire set-up is then moved to the microscope and focus is put on the bottom-side of the gel, putting the layers of interest into view above the target sample. This can be seen in Fig.[A.8], where for this example an easy to see bulk piece at the center (marked) is transferred from the gel onto a target chip of SiO_2 with pre-patterned contact pads. An advantage of the gel method, aside from size, is that the bulk and other visible residues are often left on the gel rather than transferred as well as can be seen in this example. The large bulk is difficult to displace from the adhesion of the gel, making for a very clean transfer technique. Monolayer of MoS_2 is also shown in Fig.[A.6] on gel, note the very different contrast from that shown in tape exfoliated monolayers in the previous section.

Upon successful transfer of the layer, the transferred layer and chip are annealed using the same conditions as discussed in the previous section about tape exfoliation. After an anneal, for the gel method only, the sample is submerged into dynasolve for 15 minutes at 60 C. After 15 minutes, the layer is put into acetone at 60 C for 5 minutes then triple rinsed with acetone and IPA. This is done to dissolve remnants of the gel polymer as it will otherwise cause adhesion problems of resists such as PMMA and MMA. It can also interfere with layer transfer or introduction of molecular coats for mixed dimensional heterostructures.

(a.)

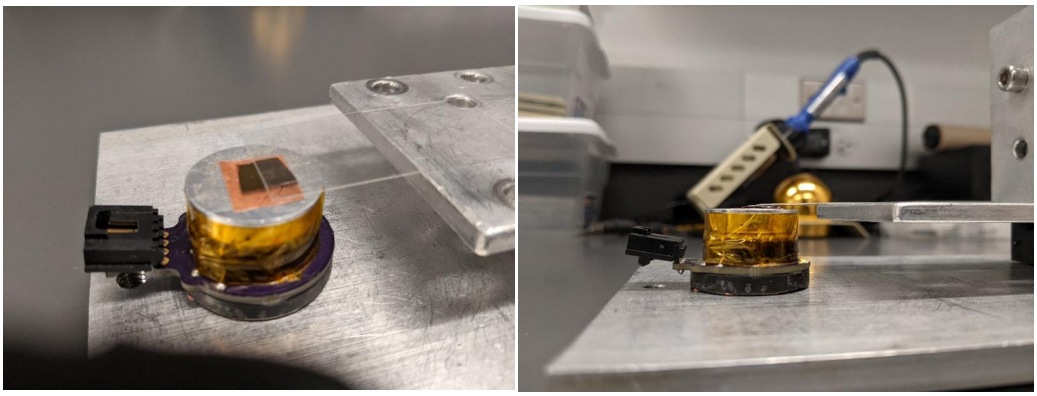

(b.)

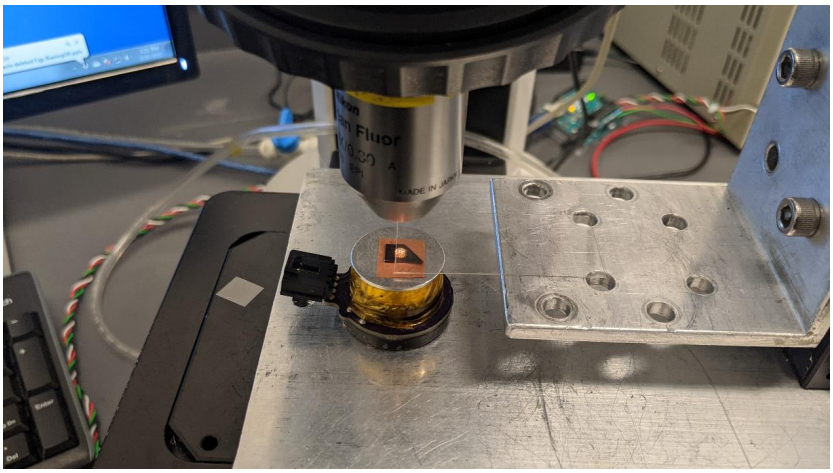

Figure A.7. (a.) Left and right show two different perspectives of the gel, inverted, anchored to the transfer platform and suspended over a target sample of interest where the exfoliated layer is to be placed. (b.) The entire stage under the microscope so that the layer can be found and positioned over the target area of interest on the target chip.

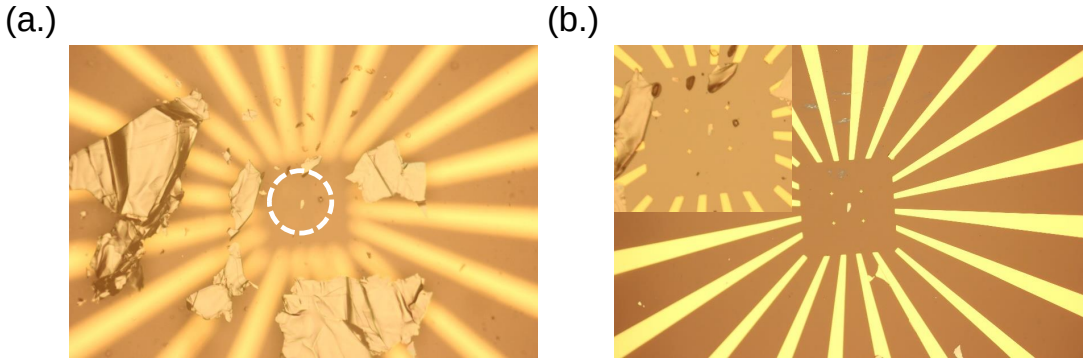

Figure A.8. Gel method final steps. (a.) An example piece of bulk (marked) that is easy to see is aligned over the area of interest for its placement. This view is the gel hanging above the target chip, with the focus through the back of the gel on the layers stuck to the gel. (b.) (Inset) The gel, layers, and chip target all in contact. (Outset) The bulk piece transferred cleanly to the target chip at the center of alignment marks, an ideal placement for subsequent electrical or device patterning.

A.2. Layer Transfer Techniques

Here I will detail the techniques used throughout the main thesis section that enabled the realization of many of the devices presented. These techniques have become a ubiquitous part of the Stern Lab's sample prep routine and has even been adapted by other labs!

A.2.1. Hardware Design

The transfer stages presented here are used in all processes that involved transfer of layers (using the polycarbonate stamp method, which will be detailed after this section) or the gel method. These pieces of equipment were pivotal in much of my research.

The transfer stage was built from a combination of Newport parts and machine alumina components (using the Northwestern Student Machine Shop). The XYZ stage is a standard manual linear positioner (1 inch travel) system with three axes, the specific part is discontinued but an equivalent Newport 460P-XYZ-05 part can be found or replaced with any rough equivalent. This component can be seen, axes labeled, in Fig.[A.9a]. An L-bracket aluminum was machined with suitable through-holes for screws to mount the L-bracket into the XYZ positioner front as seen in Fig.[A.9b]. Additional through-holes were machined on the other half of the L-bracket in mirrored sets as seen in Fig.[A.9b], these holes were used to create platforms for transfers such as with the glass slide as shown. As shown in the gel-exfoliation section, gel pieces can be directly mounted to the L-bracket and used for transfer.

Using the XYZ control and a microscope, it is possible to transfer a layer to a precise position on a target as shown in Fig.[A.8]. The example presented was bulk but monolayers can be transferred in similar fashion. Some examples of potential targets are: blank wafers, patterned wafers (as in the example with contacts), waveguides, and other layers (for heterostructures).

An equivalent but motorized system was built for the Stern Group glovebox, with the intent of layer assembly and transfer in a safe environment for more volatile materials such as InSe and CrI_3. This set up can be seen in Fig.[A.10], including the glovebox, with an overall similar arrangement built within the glovebox with a Nikon microscope connected to an external computer for imaging. Here, ThorLabs components were used, the motorized 3-axis unit (PT3-Z8) with suitable K-Cube controllers (KDC101) are controlled by the external computer that also controls the Nikon microscope. The sample mounting is not done with a simple L-bracket as tilt degrees of freedom are needed to be able to be controlled specifically to compensate for potential sample unevenness. Instead, a 2" mirror mount is retrofitted into a mounting platform using two-sided tape to mount a glass side to the bottom of the mirror mount (KM200). The bore control knobs are used to adjust tilt and improve surface contact.

Both systems have sample platforms with heating elements. These are connected to external power supplies that are controlled by Arduino logic and attached thermistors to control temperature and heating rate. This allows for the use of heat in sample transfers and placements, with very similar logic to that presented in tape exfoliation. Heating the substrate has shown to improve surface adhesion of layers and as such improve the success of layer placement/transfer.

(a.)

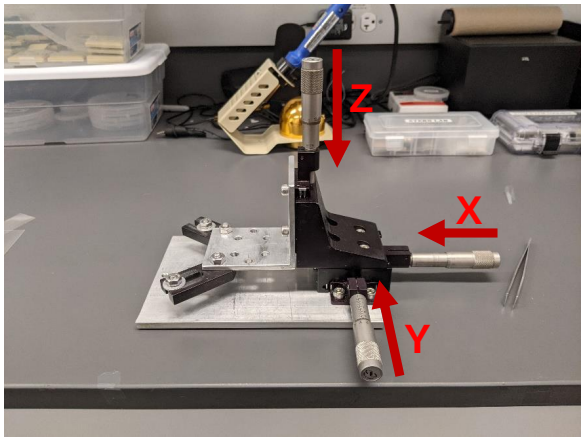

(b.)

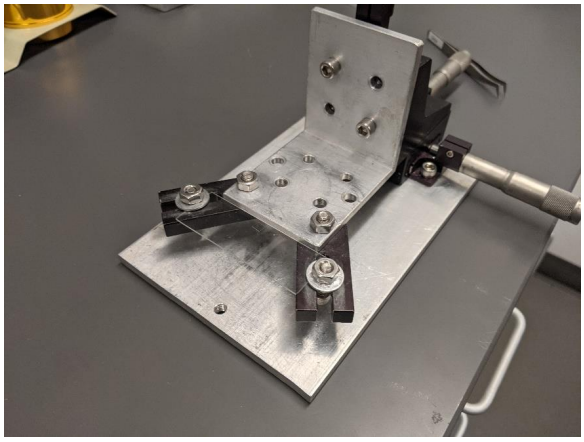

Figure A.9. Gel method final steps. (a.) An example piece of bulk (marked) that is easy to see is aligned over the area of interest for its placement. This view is the gel hanging above the target chip, with the focus through the back of the gel on the layers stuck to the gel. (b.) (Inset) The gel, layers, and chip target all in contact. (Outset) The bulk piece transferred cleanly to the target chip at the center of alignment marks, an ideal placement for subsequent electrical or device patterning. (c.) Example of exfoliated MoS_2 on the gel. (d.) A monolayer of MoS_2 on the gel.

(a.)

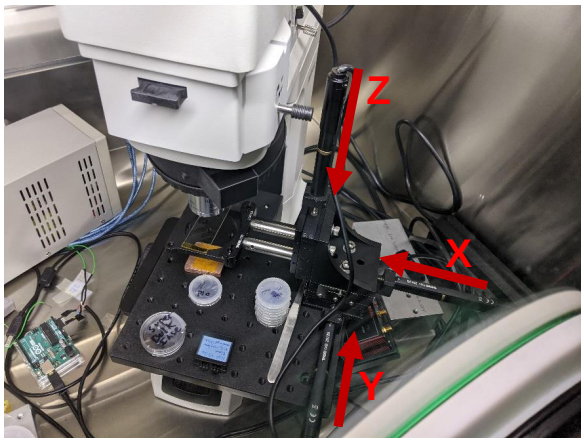

(b.)

Figure A.10. Gel method final steps. (a.) An example piece of bulk (marked) that is easy to see is aligned over the area of interest for its placement. This view is the gel hanging above the target chip, with the focus through the back of the gel on the layers stuck to the gel. (b.) (Inset) The gel, layers, and chip target all in contact. (Outset) The bulk piece transferred cleanly to the target chip at the center of alignment marks, an ideal placement for subsequent electrical or device patterning. (c.) Example of exfoliated MoS_2 on the gel. (d.) A monolayer of MoS_2 on the gel.

A.2.2. Polycarbonate Transfer Method

This section is a brief overview of the polycarbonate (PC) transfer method which will go over the broad details of preparing the PC solution and using it for general applications of layer transfer. Specific applications of this technique, such as to TEM grid, waveguides, or for making complex heterostructure stacks will be dealt with in greater detail in the subsequent sections.

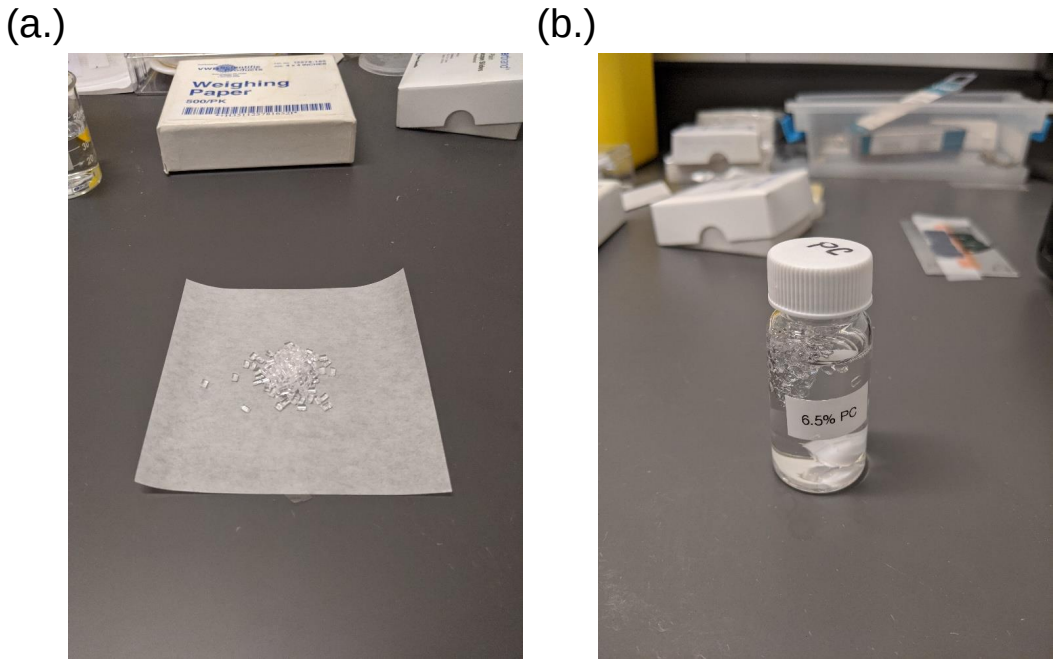

Figure A.11. (a.) Polycarbonate pieces in their solid form. (b.) Polycarbonate dropped into chloroform with a magnetic stirrer visible at the bottom, the ratio is 6.5 percent PC to Chloroform by weight.

Polycarbonate is initially brewed into a liquid solution. This process is done by weighing approximately 6.5 percent PC to chloroform by weight, and then mixed as seen in Fig.[A.11]. The mixing process is done over several hours of 1200 RPM stirring with a

magnetic stirrer on a stirring hotplate at 60 C, creating the PC brew. The PC brew should be checked for no floating pieces of PC solids in the solution, if any are visible the brew is not yet ready and needs more time stirring. It is ideal to then test the brew, this is done by taking a blank SiO_2 wafer of about 1 cm x 1 cm and using a pipette to cover the surface with a few drops of the liquid brew. The chip is then spun 2000 RPM for 60 seconds, the film should create a smooth film surface on top of the SiO_2 that is semi-transparent. If the film has a rough/granular appearance, the PC brew is not yet sufficiently dissolved and should be spun longer. Achieving an ideal film state significantly improves transfer success rates as the film is smoother and forms better surface contact with layer for transfer. High quality, transparent films with out PC chunks creating roughness is also much easier to focus through with the microscope objectives and see layers of interest for transfer, the latter is of great important when creating heterostructures.

The simplest application of the PC transfer method is to pick up exfoliated monolayers (via the tape method) or CVD grown layers, and placing them on another wafer such as one pre-patterned with contacts.

This process is done as follows:

(1) (If PC is not freshly brewed) Heat and stir the PC brew on a hotplate for 5 to 10 minutes. If the solution appears viscous and thick, add small quantities of chloroform and stir for 30 minutes to an hour. Chloroform has evaporated and needs to be replenished in the brew.

(2) Place sample in a spincoater and using a clear pipette, deposit enough drops to cover the surface of the chip.

(3) Spin at 2000 RPM for 60s.

(4) Move your sample with its thin coat of PC to a hotplate and heat at 120 C for 60 s. Heating for too long is not overly problematic but can make the eventual film very thin and prone to bunch up due to statics.

(5) (1) For exfoliated layers, it is possible to manually peel off the PC from the chip, picking up the layer.

(6) (2) For CVD grown layers, it is necessary to submerge the chip and film in water. Using tweezers, break the edges of the film to let water seep between the wafer surface and film, let this process naturally break the surface contact between the film and the wafer. The film will float up and can be removed from the water.

(7) (2.1) Let the wet film dry.

(8) Regardless of which method, (1) or (2), the film is placed onto a glass slide and checked for the layer that was desired to be picked up on a microscope.

(9) If the layer is confirmed, the film is moved to a glass slide with a gel piece on it, and the film is placed onto the gel (the non-layer side in contact with the gel), avoid bubbles.

(10) If the layer is not confirmed, repeat the process.

(11) The gel and PC stamp can now be cut down using a razor blade edge (press directly down with the blade edge, creating clean cuts) to reduce the size of the overall stamp, this helps limit any macroscopic unevenness from preventing the the stamp from making good, consistent contact.

(12) The glass slide and stamp are then placed into the transfer stage and stamped down on a target chip in a method very similar to the one showed for the gel method in Fig.[A.7] and Fig.[A.8].

(13) Once the stamp is in full contact with the chip surface, the sample is heated to 150 C until the PC film has melted down onto the wafer (can heat up to 180 C). This will cause it to release from the gel which is left attached to the glass slide, the gel can be discarded.

(14) The new stamped sample with melted-on PC stamp is placed in chloroform overnight to dissolve the PC stamp, leaving behind the layer. The long soak in chloroform was found to be ideal to remove remnant carbon residues from the PC stamp, confirmed by SEM and TEM work.

(15) The sample is cleaned with triple rinse of IPA and acetone, and then annealed using standard methods detailed previous.

This method can also be used to create a blank stamp (useful for picking up layers for heterostructures) with nominally the same steps as listed above but using a clean, blank wafer as the starting chip. In this method, dry pickup is sufficient and water steps are unneeded. The process to achieve a blank stamp (but identical to the process of picking up an exfoliated layer) is shown roughly step by step in image form in Fig.[A.12] and finalized in Fig.[A.13].

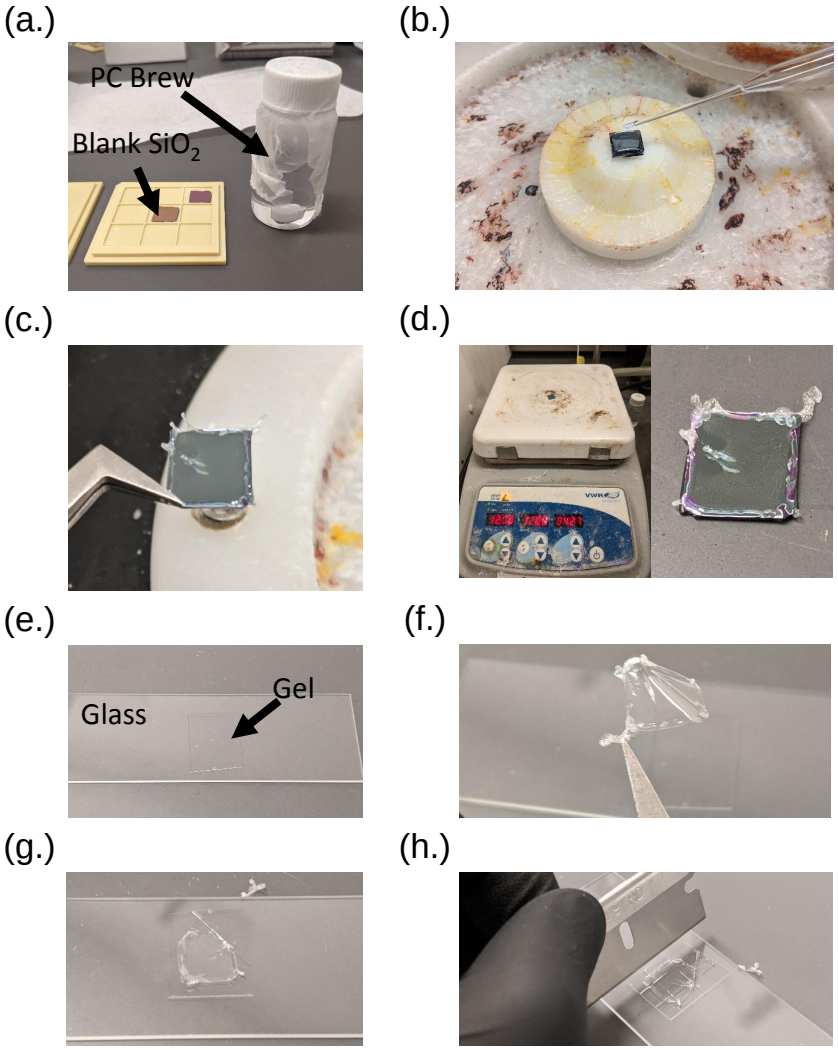

Figure A.12. (a.) Prepared PC brew and blank SiO_2 to spin a stamp. (b.) SiO_2 wafer is put in a spincoater and PC solution is deposited over the surface, to cover the surface, with a pipette. (c.) Sample is spun for 60s at 2000 RPM, the defect at the middle of the chip was caused by a chunk of undissolved PC. (d.) Chip is heated on hotplate (left), and the sample after heating (right) shows a clear and mostly uniform film aside from the defect chunk. (e.) Gel is prepared on a glass slide. (f.) Film is peeled from the SiO_2 by hand, for stamping and picking up exfoliated monolayers this is sufficient. (g.) Film is placed on gel, to improve uniformity the edges are cut off. (h.) The stamp is cut down to a small square, this allows for the removal of the defect chunk, leaving only a clean, uniform stamp ready for use.

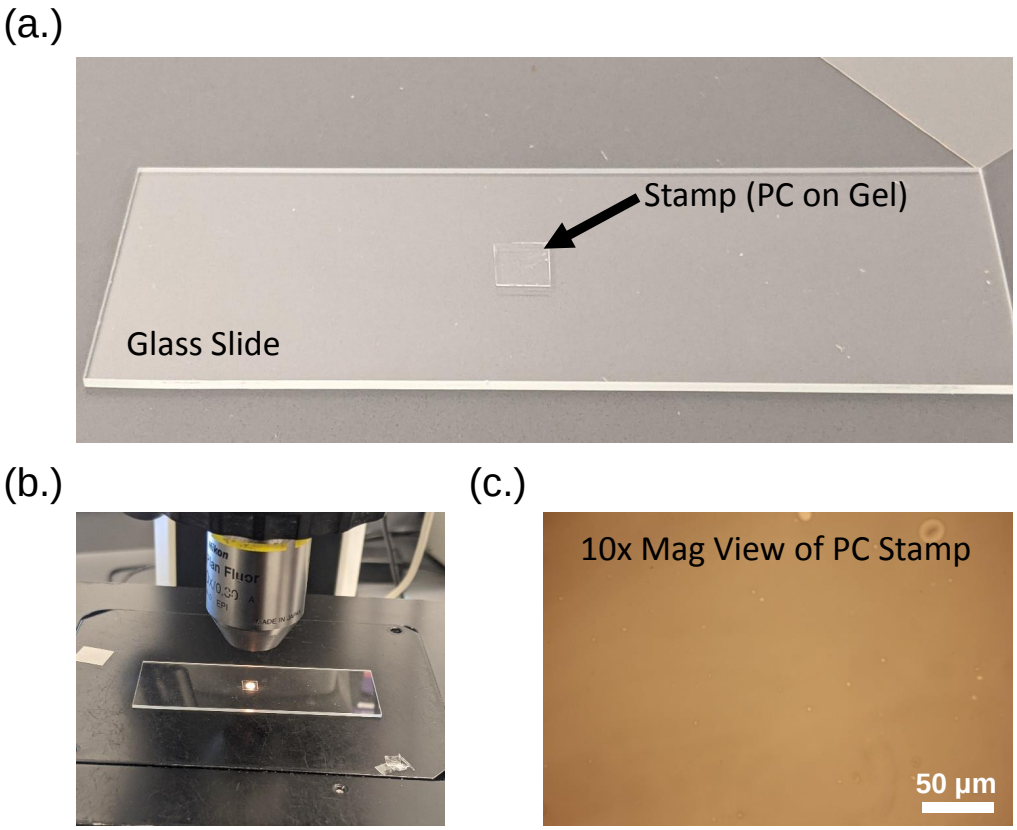

Figure A.13. (a.) Cut down stamp on glass slide, anchored with gel. Note the transparency and lack of trapped bubbles. (b.) Stamp under the microscope. (c.) Stamp as seen by the microscope, note the uniform, transparent nature of it with no visible chunks of PC.

A.2.3. Heterostructures

The ability to build complex structures from layered 2D materials is a pivotal component of the work discussed throughout my thesis. Here I will outline how the transfer process was utilized in a step-by-step fashion. The techniques presented here are expanded further into specific, more deliberate applications in following two sections.

For the purposes of creating layered heterostructures, there are two methods of approaching the problem with their own advantages and disadvantages. These methods are layer-by-layer assembly on a target chip, or a stamped pick up of all layers of interest. An example of the latter can be seen in Fig.[A.14] where a heterostructure is built through sequential pick-up onto a stamp and then placed on a target (in the figure another layer is used as the target but anything can be a target: a bare wafer, contacts, gratings, waveguides, etc.).

Layer-by-layer Assembly:

- **Advantage:** This method has limited risk of failure for the overall heterostructure. Even if a layer fails to pick up or tears in processing, it can be discarded without compromising the remaining heterostructure.
- **Disadvantage:** This method requires an anneal between each step of layer stacking. For n-layer heterostructure this means n-anneals.
- **Advantage:** Conducive to fine-adjustment in relative angle stacking of layers such as the need for a 1-2deg rotation between layers for Moire Patterns.
- **Advantage:** Can pattern between layer additions, such as patterning specific shapes or introducing contacts, before adding further layers.
- **Disadvantage:** Time consuming.

- **Disadvantage:** Due to the need for constant annealing steps, this method is not suitable for glovebox assembly (such as for volatile layers) unless the glovebox is capable of internal annealing.
- **Disadvantage:** Contaminants between layer steps may ruin the heterostructure, layers must be kept clean through the process. The stamp may leave residue between each step and must be cleaned thoroughly.

Stamped Heterostructure:

- **Advantage:** This process is done in sequence with no breaks, and only requires a final anneal.
- **Disadvantage:** If a layer tears or breaks in the pick-up process on the stamp, it can ruin the entire structure and require a complete reset.
- **Advantage:** Conducive with projects that need suspended materials (see subsequent sections on TEM and waveguide layer work).
- **Advantage:** Conducive to working within a glovebox environment.
- **Advantage:** Layers are pristine from exfoliation and have clean interfaces through the whole process.

As described, both methods have their merits and the proper method must be decided on based on the needs of a given situation. The methodology, however, is functionally identical between the two methods. To begin, the process starts from a stamp identical to the one demonstrated in Fig.[A.13], this stamp can be either bare or have already been used to pick up a layer. For the purposes of layer-by-layer assembly, either option is viable, however for the stamped heterostructure approach it is ideal to begin with a blank stamp.

The PC stamping process is done as follows:

(1) Prepare a stamp as detailed in the previous section and shown in Fig.[A.13].

(2) Align the stamp using the micromechanical transfer stage with the target layer of interest.

(3) Put down the stamp onto the layer, once in contact heat to 60-70 degC and heat for 15 minutes. This helps the layer release from the SiO_2 substrate and stick to the stamp.

(4) After 15 minutes, while still warm, peel the stamp from the wafer at a steady rate. Any rate changes can cause the layer to tear.

(5) For a stamped heterostructure, repeat steps (2-4) for each layer that is to be picked up to create the stamped heterostructure.

(6) Once the desired layer is picked up or the stamped heterostructure is assembled, align the stamp with the desired put-down location.

(7) Bring the stamp down into contact with the target sample, heat the sample to 150 degC, this will cause the PC stamp to begin to melt and release from the gel-backing.

(8) Slowly pull back the gel-backing and glass slide, make sure that you do not accidentally rip up the PC stamp.

(9) Increase the heating temperature to 170 degC, this will fully melt the PC (if the gel were still there, it would cause the gel to also begin to melt and stick to the wafer) and release any possible trapped gas bubbles. Heat for 10 to 15 minutes.

(10) With the PC stamp fully melted down, turn off the heat and let the sample cool to room temperature.

(11) Once cooled, transfer the sample to a chloroform bath and let it soak overnight, up to 24 hours, to dissolve the PC stamp. After the soak, clean off the chloroform residue with IPA and acetone rinses. If the sample is delicate, not use a rinse but instead dip the sample into IPA and acetone baths repeatedly.

(12) Anneal in a 95%/5% Ar/H_2 environment at atmospheric pressure at 400deg C for 3 hours.

(13) If doing layer-by-layer assembly, repeat the process n-times for n-layers.

This process is shown, approximately, in visual form in Fig.[A.14].

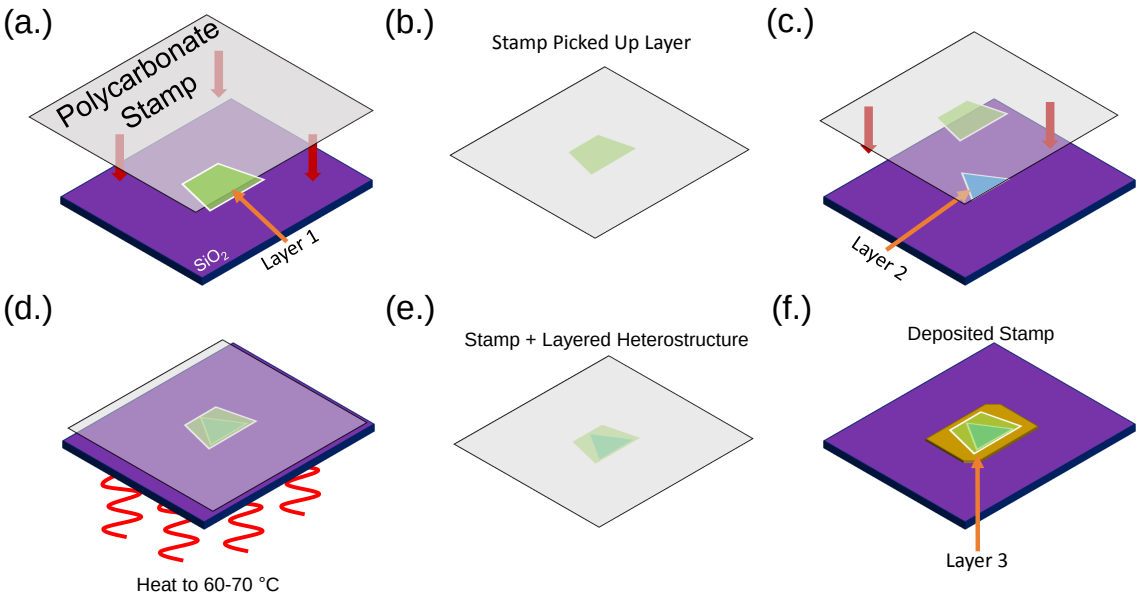

Figure A.14. (a.) General scheme of the transfer process of a stamped heterostructure. The general premise can be applied to layer by layer assembly by repeating steps (a-b) and (f.) over and over as needed for n-layers. (a.) PC stamp is used to pick up the first layer of interest such as "top" hBN or MoS_2 for a heterostructure of TMDs. (b.) Stamp is lifted from the SiO_2 picking up the layer of interest. (c.) Stamp is positioned with micromechanical XYZ-positioners and aligned with the second of n-layers of interest to be picked up onto the stamped heterostructure. (d.) Stamp+layer 1 are brought into contact with layer 2, and heated to 60-70 degC, and peeled off slowly after heating for 10-15 minutes (e.) Picked up stamped heterostructure. (f.) Stamped heterostructure is placed onto a target bottom layer 3, (c-e) can be repeated n-times for n-layers as needed for the desired heterostructure. The stamp is put onto the target layer or substrate and heated to 170 degC to melt down the stamp. Chloroform is used to wash of the stamp with an overnight soak.

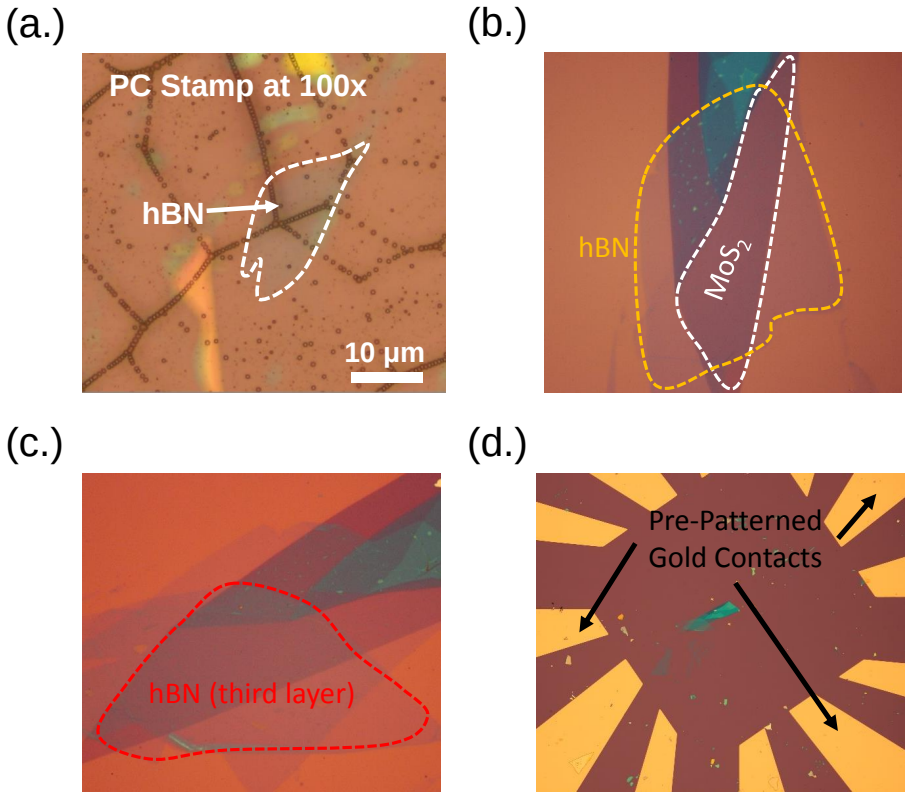

Figure A.15. Layer-by-layer assembly of an hBN/MoS_2/hBN heterostructure. (a.) hBN layer picked up on a PC stamp, white dashed line highlights the location of the hBN for ease of viewing. (b.) hBN/MoS_2 structure assembled, MoS_2 is on top of the hBN. Orange/white dashed lines highlight the hBN and MoS_2 respectively. (c.) Third hBN is added to the stack creating a heterostructure sandwich of hBN/MoS_2/hBN, red dashed line outlines newly added hBN. (d.) The heterostructure was built at the center of pre-patterned gold contacts, highlighting the flexibility of where a sample is built. Potentially, contacts could be added to this stacked structure to create an electrical device.

A.2.4. Moire Heterostructures - Twist Angle Control and Construction

Mentioned briefly in the introduction and in Chapter 5's Future Work section, I will now discuss the methods of creating twisted angle heterostructures. I will also show some of the early results of the work I did and the groundwork I have laid out for the future. This work takes the ideas of confinement from Chapter 5 and hopes to apply them to these superlattice structures and much larger potentials than the tightly bound exciton.

Structures built in this section employ the Layer-By-Layer assembly process but use the transfer stage with an additional component. The updated design can be seen in Fig.[A.16]. The large axis arm, pivoted under or near the sample, is used such that a large shift of the arm results in only small angular rotation at the sample. The length also lowers the required input force from the user to torque the sample, allowing for a more precise control down to fractions of a degree. Accuracy of the system is limited by the camera pixel resolution though can be improved in the future with a higher magnification objective or higher pixel density censor camera.

A model example of the desired superlattice formation from layer twisting can be seen in Fig.[A.17]. This structure is realized via the upgraded transfer stage. A successfully built Moire twisted bilayer, of $MoSe_2$ and WSe_2 monolayers within an hBN encapsulating sandwich, can be seen in Fig.[A.18]. Utilizing naturally occurring 60 degree corners of exfoliated flakes, it was possible to identify the lattice axis of the crystal flakes and align them within 2 degrees of each other along the axis. This 2 degree angle is often considered the "magic angle" and well known for observation of Moire behavior.

As such, for the purposes of creating these precise twisted angle heterostructures, exfoliated flakes require specific shapes that display an obvious crystal corner and 30 or

(a.)

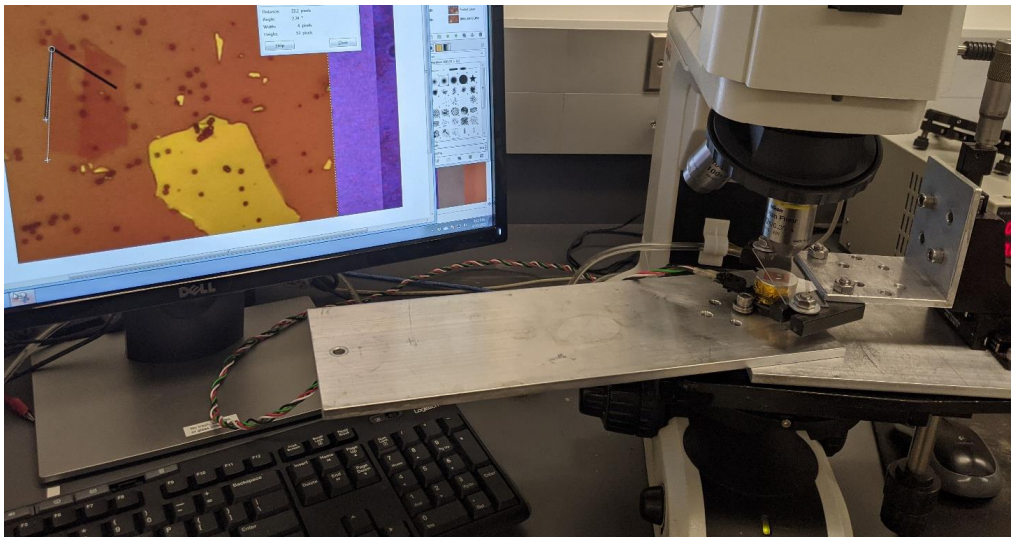

(b.)

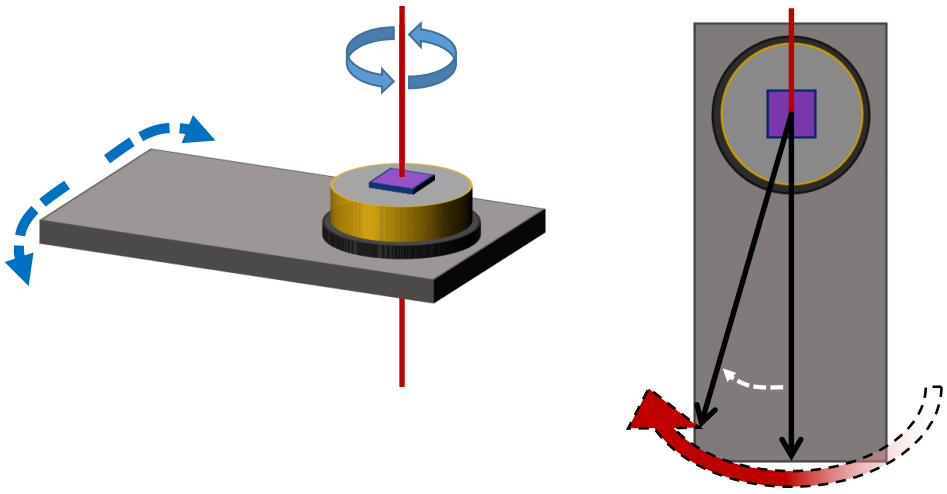

Figure A.16. Rotation update of the transfer stage. (a.) A large aluminum arm was designed to be modular to the transfer stage. The large lever arm provides a lower needed force to turn the sample by small degrees, providing for much higher accuracy and control of sample angles. This set up rotates the sample, not the film. (b.) Model representation of the pivot arm from a side and top-down view respectively.

60 degree angles. This makes exfoliation more demanding but provides for high quality, high certainty twisted angle control. From experience, I have found that freshly prepared exfoliation tapes utilizing the heat treated exfoliation method are the best source for these desirable layers.

Following the device creation, room temperature PL mapping was used to confirm the strong interlayer coupling which can be seen in the strong quenching of PL at the heterostructure due to strong charge dissociation. The indivual layers parts that are not overlapped remain bright, confirming that quenching was not a feature of the individual layers but of the heterostructure. $MoSe_2$ is naturally darker than WSe_2 at room temperature (inverse at low temperatures) but it is a brighter emitter still than the heterostructure region which is dark like the surrounding hBN.

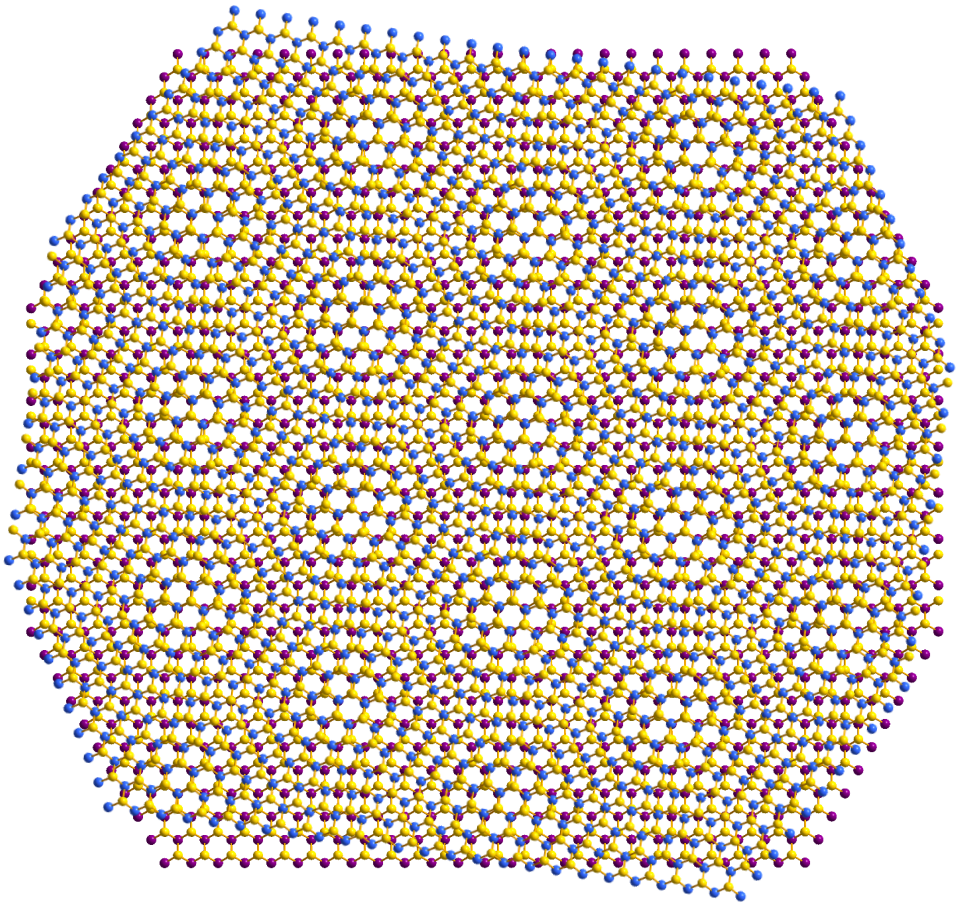

Figure A.17. Simple representation of a twisted bilayer structure forming a Moire Superlatice with periodic potentials much larger than the constituent layers.

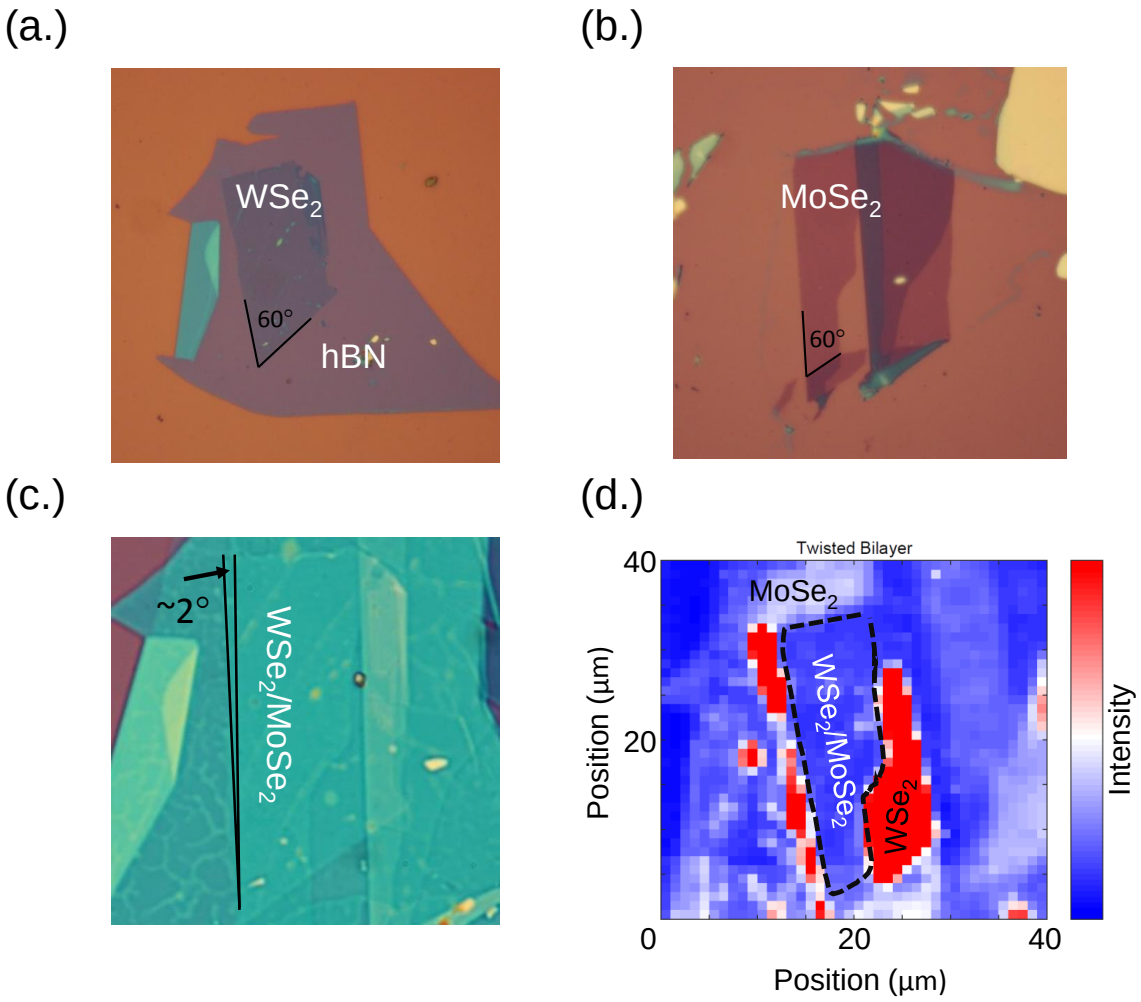

Figure A.18. Realizing a Moire heterostructure. (a.), (b.) WSe_2 (on hBN) and $MoSe_2$ monolayers with identifiable 60 degree edges, identifying the crystal axis with only optical microscopy. (c.) Completed heterostructure within an hBN sandwhich of the parts from (a.) and (b.), the degree is marked at the edge of approximately 2 degrees twist. (d.) 2D PL map of the heterostructure and surrounding material, the independent layers still luminescent and bright but the heterostructure region is dark, indicating strong couply and charge dissociation.

In a "traditional" heterobilayer of TMD layers, interlayer excitons form due to the formation of type-II band alignments between the layers, recall Fig.[2.9] from Chapter 2.

These bilayers are considered arbitrarily stacked and have random angles which are usually not conducive to forming any Moire Superlattice. However, given the proper "magic angle" twist, it becomes possible for these interlayer excitons to experience confinement potentials localized at Moire potentials. This leads to the formation of multiple interlayer excitons of differing energy levels. Comparing arbitrary "traditional" interlayers to Moire interlayers can be seen in Fig.[A.19]. The "traditional" interlayer is a low emission state with a single broad feature. Conversely, in the Moire interlayers, the interlayers are have defined multiple peak features, likely owing to different energy levels of confinement of the interlayer exciton. It is further important to note that the intralayer excitons (of $MoSe_2$ and WSe_2 used here) are quenched in the Moire structure but not in the arbitrary one.

These Moire potentials are physical locations and can themselves be nanopatterned similar to the techniques presented in Chapter 5. While they cannot be specifically targeted for patterning with current techniques and those utilized in Chapter 5, it is possible to create nanodots of several tens of nanometers in size that are likely to contain at least one Moire potential. Furthermore, unlike the very small Bohr radius of TMDs which limits any confinement effects due to current lower limits on patterning still being over an order of magnitude larger, the Moire potentials are several to upwards of ten nanometers large (depending on the angle). A theoretical confinement of a 10 nm Moire potential within a 50 nm nanodot is of the same order and may experience strong confinement interaction. This may result in significant energy shifts of the interlayer excitons or new interlayer energy states by the secondary confinement.

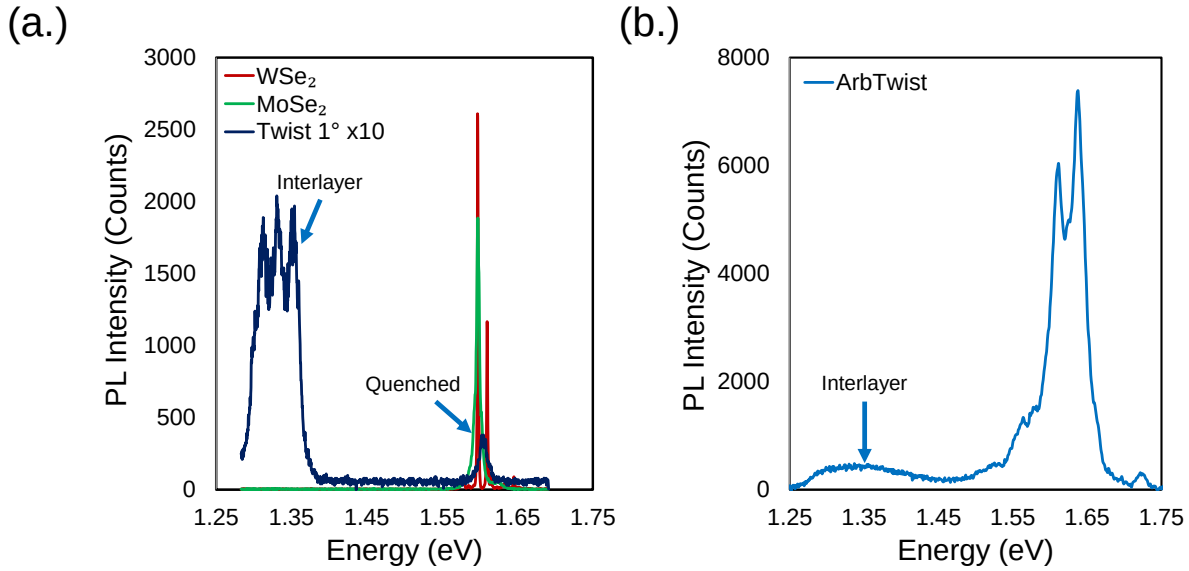

Figure A.19. (a.) Moire interlayer exciton emission and $MoSe_2$ and WSe_2 emission from parts of the flakes not part of the heterostructure. The Moire exciton has three distinctly defined features indicating three species of interlayer exciton. The $MoSe_2$ and WSe_2 emission of the heterostructure is nearly totally quenched compared to the stand alone segments. (b.) Arbitrary twist angle heterostructure. The interlayer emission is broad and undefined, and the $MoSe_2$ and WSe_2 emission remains bright even in the heterostructure.

While I won't be able to see this project to further fruition beyond realization of Moire excitons, I look forward to a successful conclusion. It has been left in more than capable hands. I have laid the ground work and others can follow.

A.2.5. TEM Electrical Contacts and Layer Suspension

The techniques presented in this transfer scheme can be applied to gold contact transfer to achieve electrical biasing in regimes where standard lithography does not work. TEM is one such case, where it is not possible to write contacts with lithography over the gaps of a TEM-wafer. It is possible to create contacts on the periphery or use much smaller conductive TEM-wafers but these cases have limitations. In the former, this requires very large layers of over several hundred microns to millimeters in length which is difficult to achieve and use for thin layers. In the latter, the conduction is everywhere and cannot be reliably applied only to the areas of interest. To solve this problem, in collaboration with Akshay Murthy in the Dravid Group, I set about to create a method of achieving an electrical device suspended entirely over a TEM-grid.

To achieve this, first a gold electrode structure was iterated upon until settled at a 75 nm thick structure similar to the one shown in Fig.[A.20] with inter-digitated contacts that have spacing of roughly 1 to 2 microns. These contacts are written on a standard 300 nm SiO_2/Si substrate. The patterned substrate is then coated with our polycarbonate solution (5% polycarbonate to 95% chloroform by weight) at 2000 RPM for 60 seconds and, subsequently, baked immediately at 120deg C for 60 seconds. After cooling, the substrate was then placed into DI Water until the film began to naturally detach from the substrate (if this process does not take after several seconds, force can be applied to the edges of the chip with tweezers while submerged in order to break the surface between the film and the substrate at the edges). After several seconds to a minute, the film will naturally lift from the substrate, picking up the gold contacts. This process must be left to occur naturally and smoothly to avoid folds and bends in the gold contacts. Once

the film has lifted, it naturally floats to the surface of the water and can be retrieved with tweezers. The polycarbonate stamp is then removed and placed gold-side up on a microscope slide and left to dry naturally for ten to fifteen minutes.

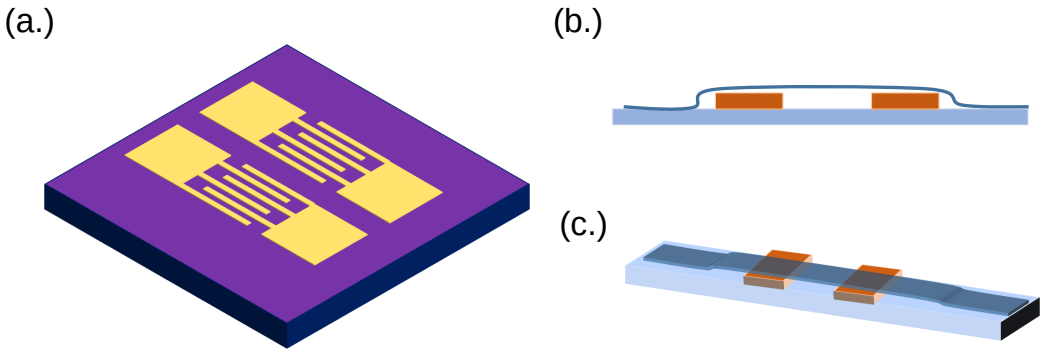

Figure A.20. (a.) Gold contact design on SiO_2 wafer. (b.-c.) PMDS (orange) is placed on standard microscope glass slide (blue), and the polymer film is suspended over the PDMS, suspending it a small distance from the glass slide (dark blue).

When the stamp is dry, it is transferred atop two strips of PDMS gel on a microscope glassslide, suspending the section of the film with gold 1 mm over above the glass. This is done intentionally to avoid any back-pressure placed on the film as it is put over the TEM grid. Any pressure would break the film and gold contacts over the holes of the TEM-grid. Using our XYZ-transfer stage, the gold+film is aligned over a TEM hole and slowly brought down an into contact with the grid. Heat is then applied gradually up to 150deg C, causing the polycarbonate stamp to begin melting and stick to the TEM grid surface and release from the PDMS stamp. The PDMS stamp is withdrawn and the heat is slowly raised up to 170deg C to completely melt the film and release any bubbles that may have trapped under the film. The film is then baked in this position for 15 minutes.

After cooling, the sample is moved into a small crucible filled with chloroform and then transferred into a large beaker with chloroform. This is done to allow for easy recovery of the TEM grid. The sample is allowed to sit for 12 to 24 hours in chloroform to dissolve and remove film residue from the grid and contacts. Following, the crucible is removed from the acetone and moved to an IPA bath for several minutes. Once completed and the contacts successfully suspended, the process is repeated for MoS_2 or layers of interest. The completed structure of gold+layer+grid is then annealed in a 95%/5% Ar/H_2 environment at atmospheric pressure at 200deg C for 2 hours plus a 45 minute cooldown. This was done to remove any remaining carbon residue from the polycarbonate film from the layer and contacts. Wirebonding to finalize the electrical device and facilitate biasing was done with small indium globule melted onto the tips of gold wires and pressed down onto the gold contacts. This whole process is shown from beginning to end in Fig.[A.21].

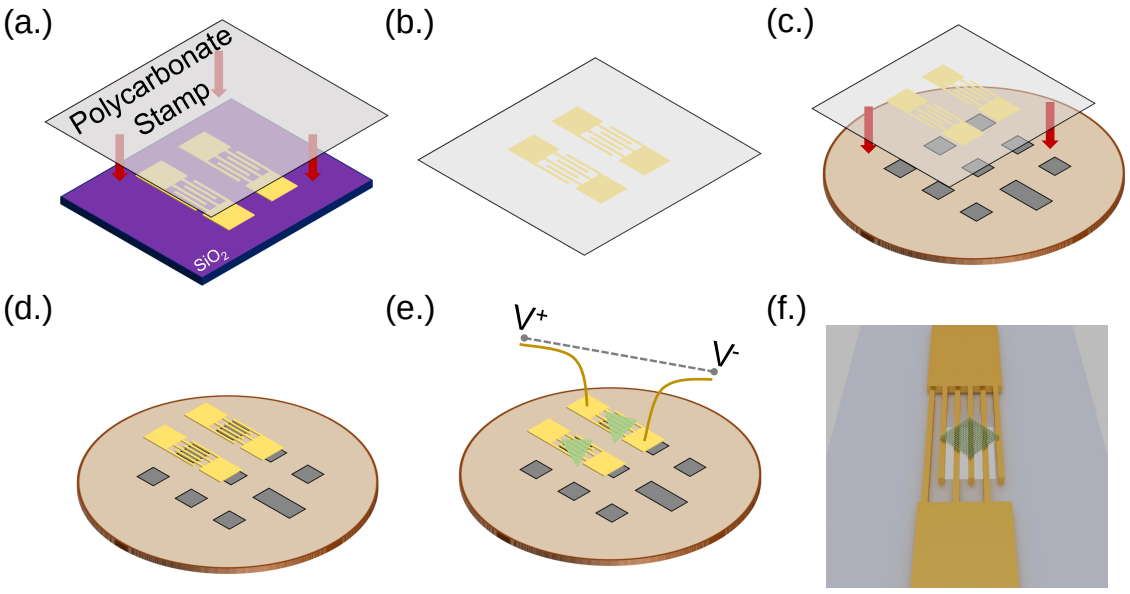

Figure A.21. General scheme of the transfer process onto a TEM grid with 1 mm holes. (a.) Gold contacts are patterned with standard lithography on a wafer, and spun-coated with a polycarbonate stamp. (b.) Stamp is lifted with the gold contacts attached to the stamp. (c.) Stamp is positioned with micromechanical XYZ-positioners and aligned with the TEM holes of interest and placed down gently. (d.) Gold contacts are left behind on the TEM grid. (e.) Monolayers or layer of interest are transferred in the same way onto the transferred gold contacts. Biasing can be applied to these devices in a TEM setting. (f.) 3D render of the contacts and layer over a TEM gap.

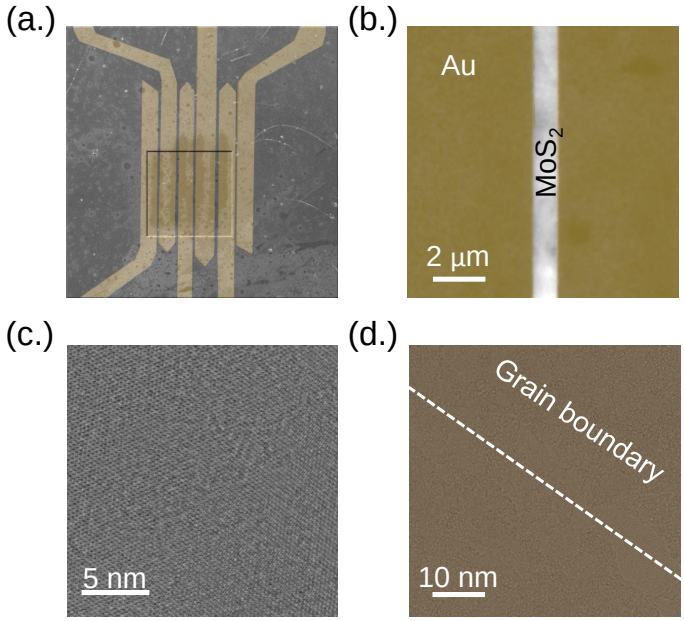

Figure A.22. Images of a successfully created gold+MoS_2 structure on a TEM window. (a.) Gold and MoS_2 suspended over a TEM window (indentation) using SEM imaging. (b.) Lower resolution zoom in on area between gold contacts showing the MoS_2 under TEM imaging. (c.) MoS_2 crystal structure of suspended material. (d.) Grain boundary in the MoS_2 as imaged, the white line is to guide the eye.

This work can be seen in our publication: Murthy, A. A.; Stanev, T. K.; dos Reis, R.; Hao, S.; Wolverton, C.; Stern, N. P.; Dravid, V. P., Direct Visualization of Electric Field Induced Structural Dynamics in Monolayer Transition Metal Dichalcogenides. *ACS Nano* 4 (2), **2020**, 1569-1576. Successes of this work are sampled in Fig.[A.22].

A.2.6. Waveguide Layer Suspension

Here I will detail two methods for layer suspension over waveguides.

The fist method uses techniques very similar to those presented in the gel method section, refer to that section for how to exfoliate to a piece of gel. MoS_2 or a TMD of choice is exfoliated onto gel layer, and monolayers or layers of n-desired layers are identified. The gel should then be cut such that the area of the layer of interest ideally on the far end of the eventual fulcrum-point of the gel that will be used to mount the gel to the transfer stage, a simple layout of this is presented in Fig.[A.23a]. The reason to create this long arm is to be able to have a slow, steady put down and subsequent peel of the gel from the surface of the target waveguide.

The gel+layer should be carefully positioned over the waveguide (again, see gel methods for this process) with sufficient coverage of material on either side of the waveguide (to create structural support, if the layer is not supported on both sides it will simply fall into the waveguide or not leave the gel) as seen in Fig.[A.23b-c]. Once the layer is properly positioned, the gel+layer should be brought down slowly until the gel begins to touch the surface of the target wafer. At this point, the gel should be brought down extremely slowly such that the rate of gel coming into contact with the wafer is very slow, if the rate is too fast when it reaches the monolayer it is likely to cause the monolayer to break where it is to be suspended over the waveguide. It is not necessary but generally helpful to heat the chip at this stage to 60 C for 5 to 10 minutes to improve adhesion of the monolayer to the surface of the wafer, but too much heat may cause the layer roll up over the suspended region (for layers other than MoS_2 this critical temperature may vary and should be considered). Regardless of heating, after 15 minutes the gel should slowly be peeled from the surface of the chip at a steady rate using the positioner system. If the

rate of peel is too fast, it is common for the unsupported segments of the layer to simply break off, leaving only material that has stuck to the uninteresting parts of the wafer.

A successfully transferred layer can be seen in Fig.[A.24a]. A 2D PL map can confirm the suspended layer (though it is optically visible for this case of SiN waveguides) as the suspended region is expected to be much brighter than the areas in contact with the wafer around it as seen in Fig.[A.24b].

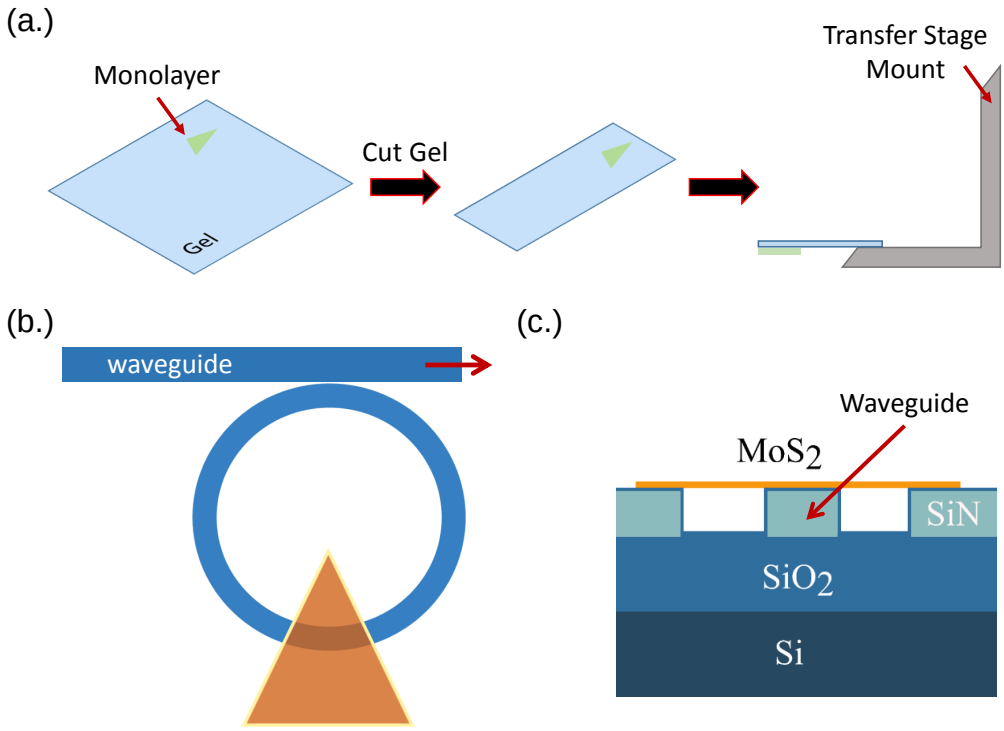

Figure A.23. (a.) Example of prep for a gel with identified layer of interest. The gel is cut such that the layer is far from the point where the gel is mounted to the transfer stage. This is done for better control over gel put down and peel off rates. (b.) Top view of how a layer needs to be positioned over a waveguide (visualized ring resonator waveguide). (c.) Side view of the monolayer across the waveguide. The layer needs to be anchored on material on either end of the waveguide for structural integrity.

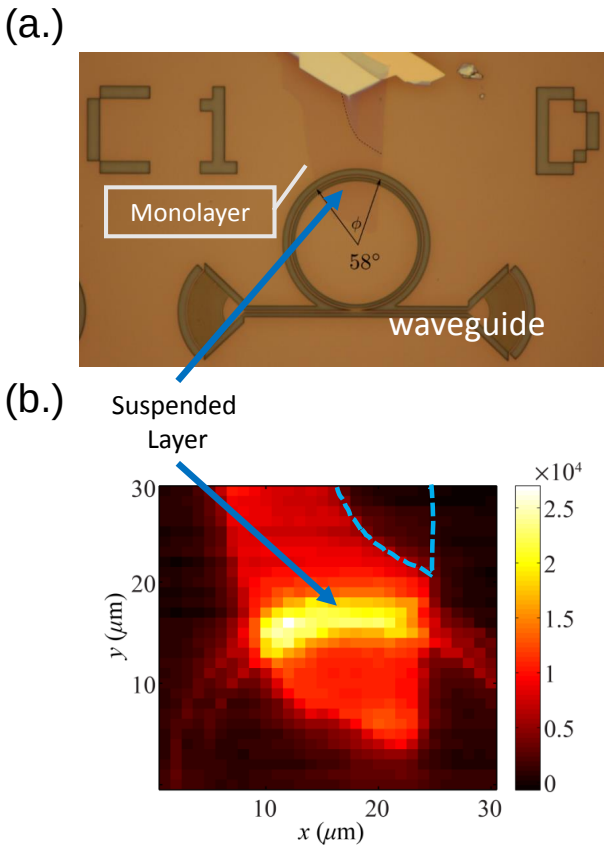

Figure A.24. (a.) Successfully transferred monolayer over a ring resonator. (b.) A 2D PL maps showing the bright suspended layer.

This work can be seen in our publication: Guohua Wei,Teodor K. Stanev, David A. Czaplewski, Il Woong Jung, and Nathaniel P.Stern: DSilicon-nitride photonic circuits interfaced with monolayer MoS_2. *APPLIED PHYSICS LETTERS* 107 (2), **2015**.

The second method for waveguide with monolayer integration utilizes techniques informed by the methods from the building of TEM suspended layers and contacts as well as general heterostructure building. Here, an hBN layer of reasonable thickness (5-10L) is picked up via a PC stamp (such as that seen in Fig.[A.13]). The reason for a thicker

hBN (but not too thick to be optically opaque) is to create a rigid structural support for a more fragile monolayer.

To pick up the layer of hBN, the PC stamp is brought into contact with the hBN+substrate, and the whole system is heated to approximately 60 to 70 C for 5 minutes. This temperature is not high enough to melt the PC stamp but does improve the hBN adhesion to the PC stamp. The stamp is then rapidly retreated from the surface of the wafer (by rapid turns of the z-control on the transfer stage). This step should be done smoothly and continuously, and if done correctly will peel the hBN from the surface of the substrate without creating wrinkles in the hBN. If the process does not pick up the hBN it can be repeated again.

The picked up hBN+stamp is then used in a similar fashion on a target monolayer, and the process is repeated. Now creating a stack of PC stamp/hBN/monolayer. In analogue to the considerations of placing material over a gap in the TEM section of transfer, we must use a suspended stamp approach for placing the stamped heterostructure over the waveguide. For details on this see Fig.[A.20b-c]. As before, this is done intentionally to avoid any pressure on the film as it is put over the waveguide channel, otherwise there is a high probability of breakage of the heterostructure and potential ruining of the waveguide. Using our XYZ-transfer stage, the heterostructure stamp is aligned over the target waveguide and slowly brought down an into contact. Heat is then applied gradually up to 150deg C, causing the polycarbonate stamp to begin melting and eventually release from the gel backing. The gel+glass slide are then withdrawn and the heat is slowly raised up to 170deg C to completely melt the film and release any bubbles that may have trapped under the film. The film is then baked in this position for 15 minutes.

After cooling, the sample is moved into a bath of chloroform. The sample is allowed to sit for 12 to 24 hours in chloroform to dissolve and remove film residue. Subsequently, the sample is moved to an IPA bath and gently swirled for several seconds. Rinsing the sample should be avoided as it will likely break the suspended layers. Once completed, the sample should be annealed in a 95%/5% Ar/H_2 environment at atmospheric pressure at 200deg C for 2 hours plus a 45 minute cooldown. This will remove any remaining carbon residue from the polycarbonate film and other potential solvent residues. A rough approximation of this process is shown from beginning to end in Fig.[A.25], and a completed suspension over a waveguide in Fig.[A.26].

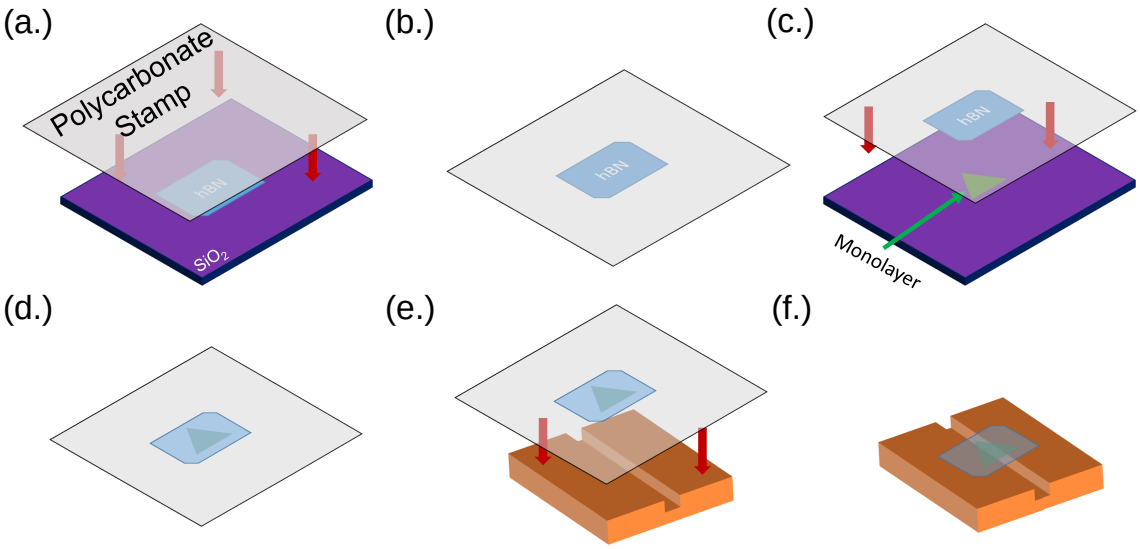

Figure A.25. General scheme of the transfer process onto a waveguide or channel using PC method. (a.) hBN (5-10 layer thick) is picked up, this is the support structure for a monolayer. (b.) Stamp is lifted hBN attached to the stamp. (c.) hBN is positioned with micromechanical XYZ-positioners and aligned with the monolayer of interest. (d.) Monolayer is picked up with the hBN, creating a stamped heterostructure. (e.) The stamped heterostructure is aligned over a waveguide or channel (f.) The resulting suspended heterostructure over a waveguide or channel. The hBN support structure greatly improves the success rate of successfully spanning the waveguide or channel with a monolayer.

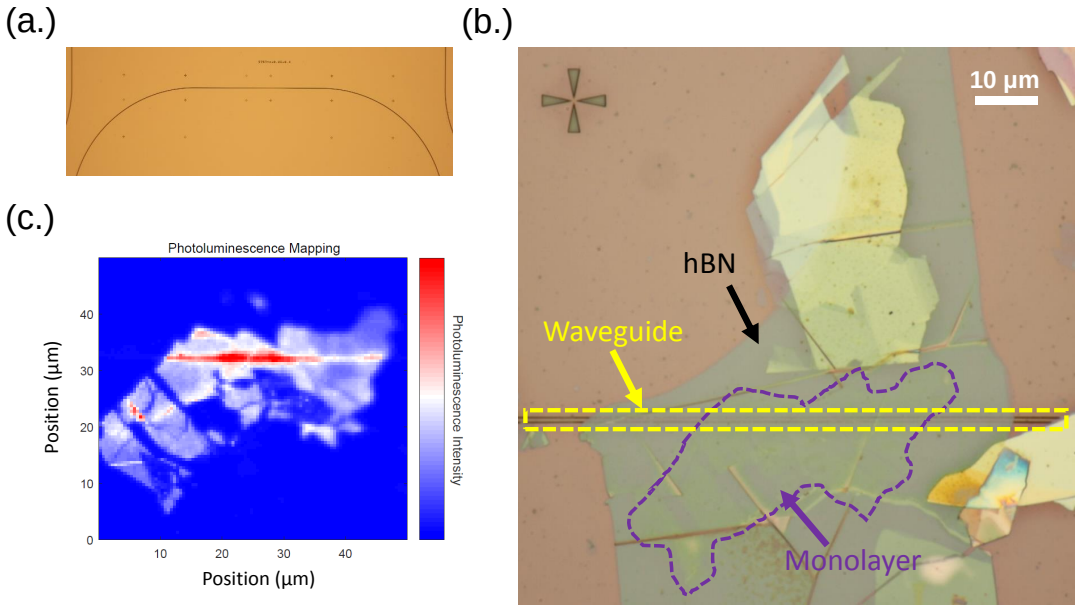

Figure A.26. (a.) An example waveguide, pristine. (b.) Waveguide with hBN-backed monolayer MoS_2 suspended over the waveguide. Outlines (yellow, waveguide and purple, monolayer) marked the layers for ease of viewing under the hBN. (c.) 2D PL map showing the monolayer under the hBN and the bright suspended region over the waveguide. Much like with the gel-method, the suspended layer region is much brighter than the surrounding areas.

APPENDIX B

Magneto-Optical Kerr Effect Measurements

This section will detail the hardware development and evolution for realization of MOKE; the problems initially encountered and the clever solutions to work around them.

B.1. Achieving MOKE Spectroscopy

In this section, I will be discussing how MOKE was realized in the Stern Lab, the experimental set-up, and various steps needed along the way to achieving the high quality results and successes shown in the MOKE section previously. The work presented here were of critical importance to the successes with MOKE spectroscopy.

While MOKE was of particular interest in the Stern Lab for sometime, equipment truly suitable for it (with sufficiently high fields, and low temperatures) was only a recent development. Early work was limited a cryostat (Montana Instruments) with temperature capabilities down to to 7 to 10 K, and fields of only roughly 500 mT with a very limited working area and limited, to-no ability to move the sample or use small spotsizes. This was tenable for large films or magnetic particle solutions, but less than ideal for small samples such as those of exfoliated layered materials which are usually only a few microns in size.

The work presented so far has operated at temperatures of roughly 1.6 K and observed magnetic dynamics from 0.5 T to upwards of 4 T, well outside of the original capabilities

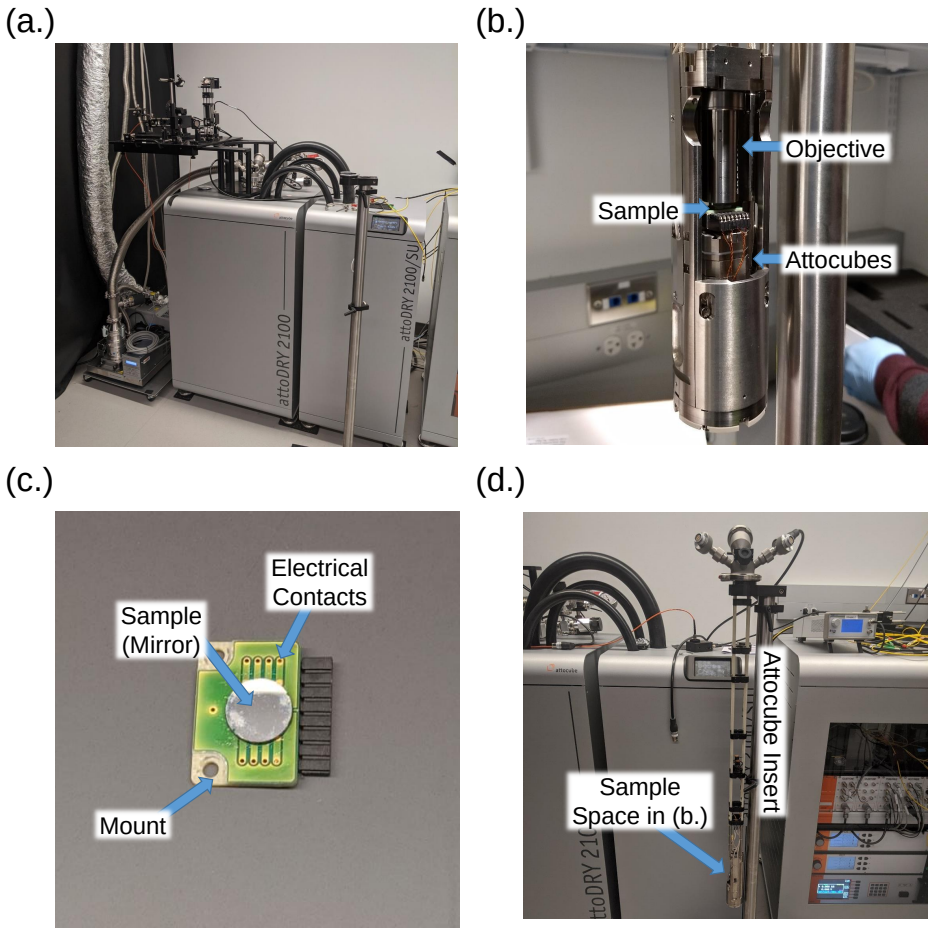

Figure B.1. (a.) The AttoDry 2100 Cryostat installed in the Stern Lab. (b.) The sample mounting scheme within the AttoDry, visible and marked points of importance: objective for confocal microscopy (offering a very high NA of 0.95 with sub-micron spot-sizes), attocube stacks for XYZ sample motion (up to 3 mm in each direction), sample for measurement with electrical wiring options). (c.) Sample mount with a silver mirror placed as an example and used for calibrations. Electrical pads are built into the sample mount. (d.) Stick insert that holds the sample area, objective, and attocubes. The sample space from (b.) is marked out at the bottom and the stick is presented in front of the AttoDry for size comparison. Optical access is at the top of the insert.

available on the older system. This was all made possible by the previously mentioned AttoDry 2100 cryostat and its 1.6 K, 9 T capabilities. The system can be seen in Fig.[B.1a].

Additionally, the AttoDry offered the ability to move the sample within the magnetic field and at low temperatures. This was accomplished by the Attocube stacks shown in Fig.[B.1b], offering approx 3 mm of XYZ travel of the sample. This was of utmost importance in facilitating work with small, layered structures such as those of CrI_3.

Measuring of the magnetic response of materials through MOKE was done with the optical set-up shown in Fig.[B.2]. A simplified design of this layout was shown in Fig.[8.1b] but with the full path and all optics now included.

Initially, the Attocube provided microscope objective (can be seen in Fig.[B.1b] and simple cage-mounts were utilized to attempt basic MOKE spectroscopy on YIG samples as calibration but several problems arose that were critically detrimental to our measurement capabilities. First and most critical, the compound microscope objective proved to have much too high of a Verdet Constant and was susceptible to significant Faraday influences from the magnetic field. This resulted in a sine-like background of many hundreds of mrad on any attempted MOKE measurement, completely burying any signal and making it nigh impossible to observe signal on YIG. This large, unwanted background signal can be seen in Fig.[B.3a] as collected on a silver mirror like the one shown in Fig.[B.1c], showing a background approaching nearly an entire rad of background signal with a sine-like shape. This would have made attempting to detect signals such as the monolayer, only of a few mrad as shown previously, nigh-impossible to observe.

To rectify this problem, a new objective had to be made that had a much lower response to the field and as such limiting the impact on data collection. Of the main concerns in making this objective were: a small spotsize of at most a micron but preferably less than a micron (similar to what was possible with the Atto-Objective), limited magnetic response

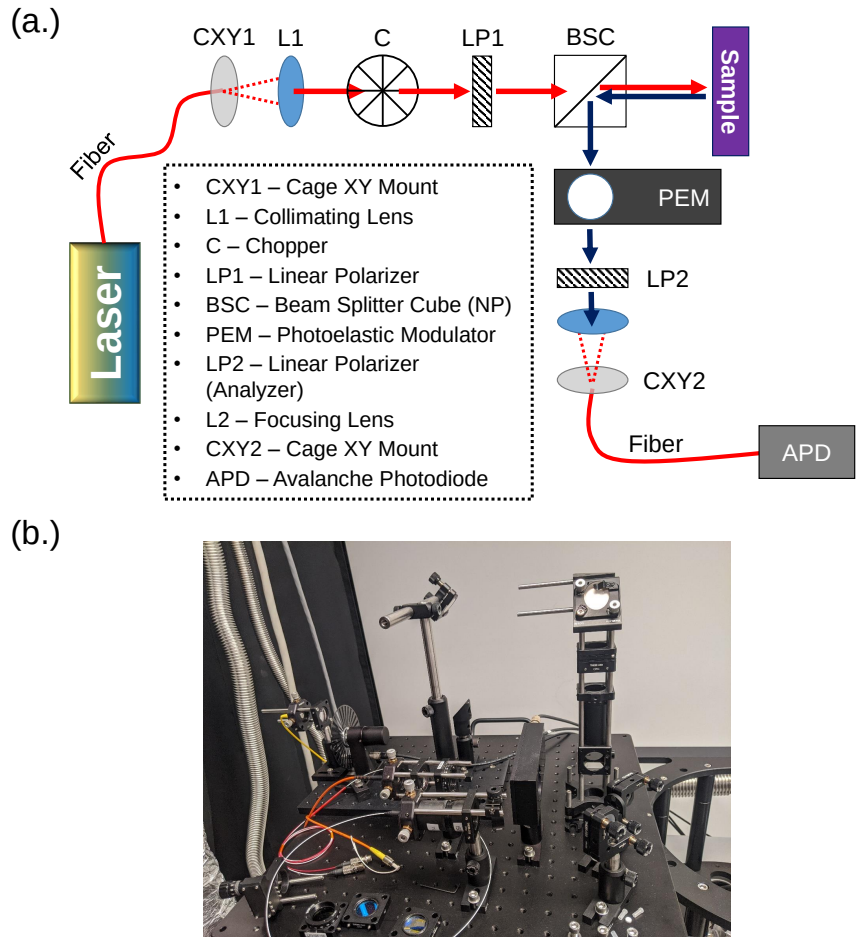

Figure B.2. (a.) Design of the optical path for MOKE measurement within the AttoDry shown in Fig.[B.1] with the beam path after the beam splitter cube to the sample (and back from the sample) being along the insert shown in Fig.[B.1d]. Red and blue lines are used only to show path of the beam to sample (red) and from sample (blue). (b.) The set-up as realized atop of the AttoDry on a breadboard.

of the optics, could fit within the working space of atto-insert. For achieving a small spotsize with minimal magnetic response and able to fit within the small working area of the sample insert, an apsheric lens (A375TM-A from Thorlabs) was chosen. But in order to use this lens, a brand new housing needed to be made. Using non-magnetic and impurity-free aluminum, the objective-mount was handmade at the Northwestern Student

Machine Shop. The design can be seen with the aspheric lens installed in Fig.[B.3b]. The final work, can be seen in Fig.[B.3c] after being mounted into the AttoDry and with a green laser passed through and focused on a test target.

A test identical to the one performed for the Attocube objective was done on a silver mirror with results shown in **Fig.[B.3d]**. Unlike the sine-shape of the atto-objective, the new objective shows only a linear background and an order of magnitude less rotation signal. While there is still a significant "background" of tens of millirad, it proved manageable in our experiments. The background was accounted for through both direct subtraction or fit-out from the data of a sample. Both approaches provided to have similar results.

To then test our new objective and the Atto system as a whole on a well understood magnetic material to confirm are capability to see actual magnetic material response, MOKE was again attempted on YIG. The sample is shown in Fig.[B.4a] and its result in Fig.[B.4b], showing the expected ferromagnetic response for a thin film of YIG.

While the result is quite simple and noisy, this was our first observation of magnetic response in a material within our system, and laid the groundwork for all work presented with regards to MOKE spectroscopy.

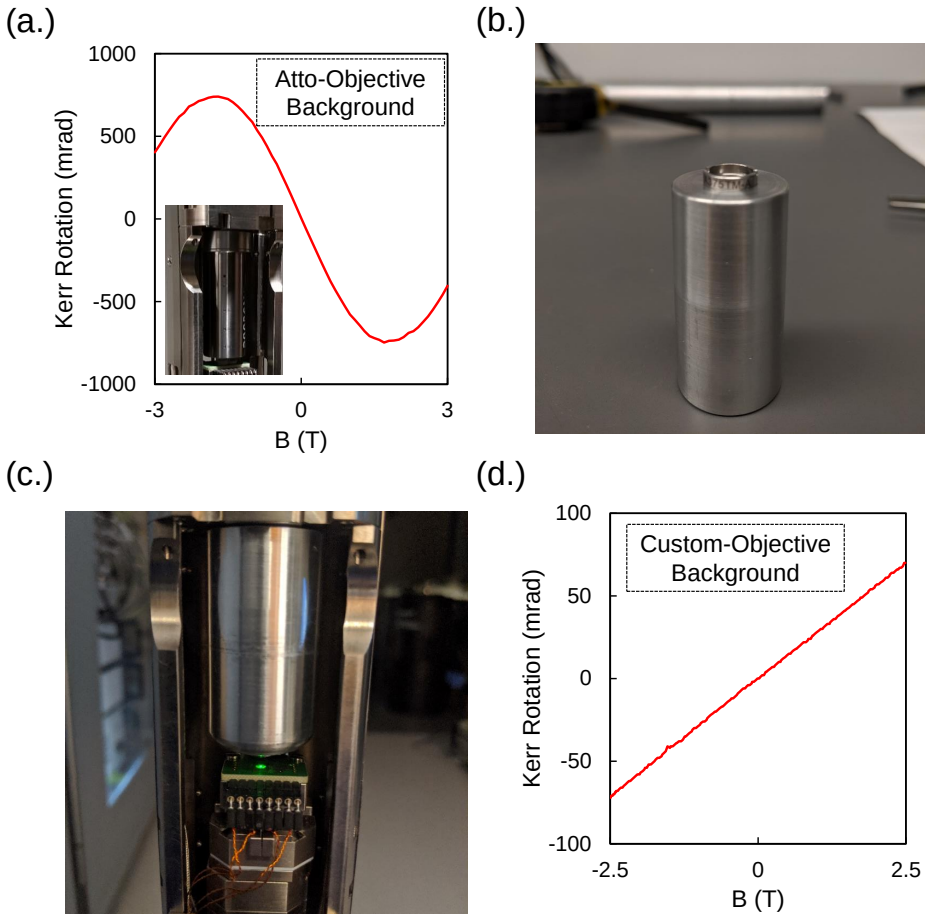

Figure B.3. (a.) The Atto-Objective being used for MOKE spectroscopy on a calibration silver mirror. Large magnetic response is observed coming from the objective as it is exposed to high fields. (b.) New objective being created from aluminum with an aspheric lens mounted. (c.) The completed objective, mounted into the AttoDry sample area replacing theh Atto-objective. A green laser is shone through the new objective and onto a sample mount for testing. (d.) The new objective with aspheric lens tested on a silver mirror, the background has been significantly reduced in magnitude and is now linear. This linearity was tested out to the maximum of the AttoDry of 9 T and was consistent.

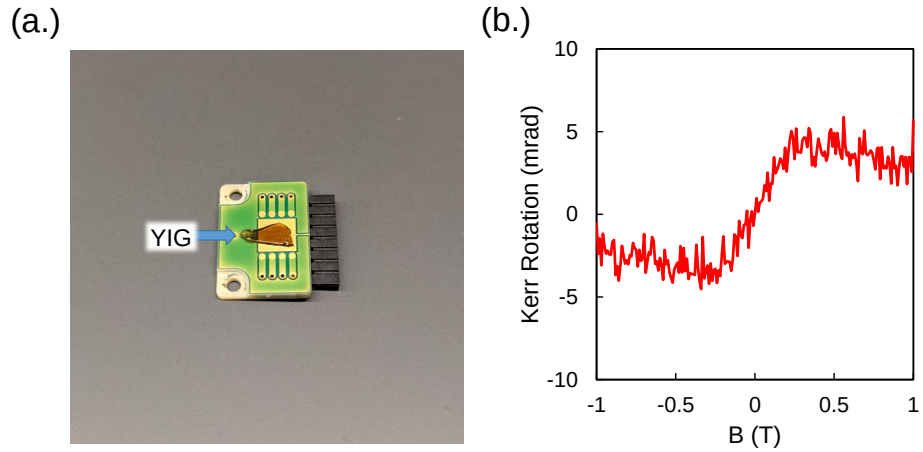

Figure B.4. (a.) YIG thin film on sapphire substrate, mounted onto an atto mount. (b.) Kerr reponse of the sample in our system, showing anticipated ferromagnetic response.